Super-resolution ultrasound imaging using a lensed row-column array

Øygard, Sigrid Husebø

Publication date:
2022

Document Version
Publisher's PDF, also known as Version of record

DTU Health Tech
Center for Fast Ultrasound Imaging

Super-resolution ultrasound imaging using a lensed row-column array

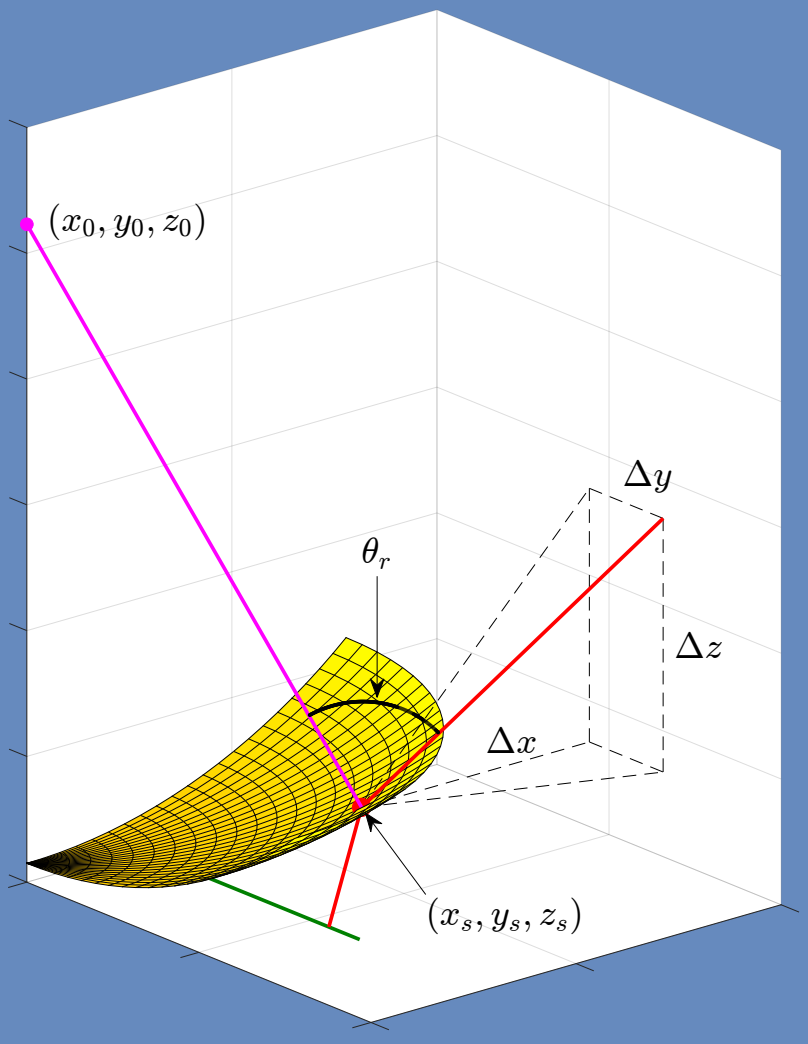

Ph.D. thesis by Sigrid Husebø Øygard

Supervised by: Prof. Jørgen Arendt Jensen, Ph.D., Dr. Techn.
Co-supervised by: Assoc. Prof. Matthias Bo Stuart, Ph.D.

Center for Fast Ultrasound imaging (CFU)
DTU Health Tech
Department of Health Technology
Technical University of Denmark
Ørsteds Plads
Building 349
2800 Kgs. Lyngby, Denmark

Preface

This Ph.D. thesis has been submitted to the Department of Health Technology at Technical University of Denmark (DTU) in partial fulfillment of the requirements for acquiring the Ph.D. degree. The research providing the foundation for this thesis has been conducted for three years, from January 15th, 2019 to January 14th, 2022, at the Center for Fast Ultrasound Imaging (CFU), Department of Health Technology. The project has been supervised by Prof. Jørgen Arendt Jensen, Ph.D., Dr. Techn., and co-supervised by Assoc. Prof. Matthias Bo Stuart, Ph.D.

Sigrid Husebø Øygard
Kgs. Lyngby, Denmark
January 2022

Contents

Summary

Ultrasound imaging provides a noninvasive and accessible form of medical imaging, but has been fundamentally limited by both the diffraction limit and 2D images. Recently, super-resolution ultrasound imaging (SRUI) has surpassed the diffraction limit, offering macroscopic resolution. Similarly, volumetric imaging with row-column arrays (RCAs) can be used to make 3D images, and has the potential for clinical application due to the low number of connecting channels in the transducer. Designing an RCA using capacitive micromachined ultrasonic transducer (CMUT) technology offer several advantageous features for SRUI, such as wide bandwidth and narrow inter-element pitch. However, the usable field of view (FOV) of an RCA is limited, and the inclusion of an acoustic lens is therefore useful. It is hypothesized that if combined, these four modern ultrasound techniques has the potential to create a practical tool for imaging microvascular structures in whole organs, with microscopic resolution and macroscopic FOVs. However, several developmental steps remain before this proposal can be tested and applied.

Firstly, the minor sequences used for contrast enhanced ultrasound (CEUS) imaging in SRUI are studied theoretically. It is shown algebraically that pulse inversion (PI) and amplitude modulation (AM) can be used to eliminate linear back-scattering while preserving the nonlinear back-scattering from microbubbles. Furthermore, by applying the Marmottant et al. (2005) model governing nonlinear scattering from microbubbles, examples of the back-scattering from the contrast agent SonoVue are modeled and used to validate the efficiency of the two sequences. This theoretical validation method is explored in order to also theoretically validate the use of CMUTs for the CEUS. When CMUTs emit sound, the harmonic content in the sound is nonlinearly dependent on the applied voltage to the transducer. It is found that CMUTs can be used for CEUS imaging without loss of image quality, if a three-pulse AM sequence is applied. In this thesis, this is validated theoretically. Moreover, measurements of the contrast-to-tissue ratio (CTR) of images of microbubble contrast agents acquired using a CMUT and a comparable lead zirconate titanate (PZT) array show that the average enhancement of contrast, compared with B-mode images, was 37.4 dB for the CMUT and 49.9 dB for the PZT array. The discrepancy is attributed to the CMUT achieving a poorer signal-to-noise ratio.

Secondly, the use of a RCA for 3D SRUI is demonstrated. In preparation, the beamformation of signals created by an RCA is studied and implemented, and examples of the point-spread-function of an RCA emitting a single-element synthetic aperture sequence are simulated. Then, an experimental set-up using a 3D printed microflow phantom is designed and used to collect images of flowing SonoVue. The images are collected using a 62 + 62 element PZT RCA. From these, ultrasound localization microscopy is performed. The microbubble localization precision is found to be 15.4 µm and 16.0 µm. Whether this fulfills the true definition of super-resolution is discussed, but, regardless, the resulting 3D imaging indicates that RCAs can be used for SRUI.

Lastly, the transmission of sound from an RCA through a lens is studied. When the sound is emitted and received, its paths are refracted by the lens, and this makes the prediction of the time of flight (TOF) complicated. The TOF is needed to beamform images from the received signals, and errors in the prediction lead to lower image quality. A simplification of the problem is offered by the thin lens model, which assumes that the lens is infinitely thin and has a single focal point. An RCA with an infinitely thin lens

is simulated by making the elements of the transducer curved. The thin lens model is used to predict the TOF of emissions from the transducer, and comparison with simulations of the emitted field indicate that no phase errors are introduced by the model. However, real lenses have a finite thickness and the simulations do not validate that the model is applicable to real lenses, due to the underlying assumptions in the model. Therefore, a ray tracing model is presented, which does not make simplifying assumptions about the geometry of the lens. How accurately the thin lens model and the ray tracing model can predict the TOF of an emitted wave is quantified by comparison of the predictions with the emitted field simulated using finite element method modeling of a lens with finite thickness. The accuracy of the prediction affects the usable FOV, which for four example cases is found to be higher or equal to the FOV when the TOF is predicted by the ray tracing model. For the case with the biggest discrepancy, the ray tracing model increased the FOV by 25.1°. Furthermore, the ray tracing model is validated by comparison of its predicted TOF with measurements of the emitted field from a 128 + 128 element RCA through a concave silicone lens. This resulted in a maximum phase difference of 0.19 λ, despite errors in the alignment of the hydrophone. Lastly, the usable transmitted FOV of the 128 + 128 element RCA is quantified using the ray tracing model. The FOV is found to be 37.2 cm $\times$ 12.1 cm at 9 cm to 10 cm depth, which is large enough to image a whole human kidney. Thus, it is indicated that the lensed array has the capability of making 3D SRUI of whole organs.

Resumé

Ultralyd afbildning tilbyder en ikke-invasiv og tilgængelig måde at lave medicinske bilder, men har været fundamentalt begrænset af diffraktionsgrænsen og 2D billeder. For nyligt har superopløsningsultralyd afbildning (SOUA) brudt diffraktionsgrænsen, og opnår dermed mikroskopisk opløsning. Tilsvarende, har 3D billeddannelse med række-søjle arrays (RSAs) vist potentiale for klinisk applikationer grundet transduceren lave antal kanaler. Et RSA, designet ved brug af kapacitivt mikromaskineret ultrasonisk transducer (KMUT) teknologi, tilbyder flere fordelagtige funktioner for SOUA, såsom et bredt båndbredte og et smalt inter-elementafstand. Men det brugbare synsfelt for en RSA er begrænset, og det er derfor nyttigt, at kunne tilføje en akustisk linse. Det er påstået, at hvis disse fire moderne ultralydsteknikker kombineres, kan der potentielt skabes et praktisk værktøj til afbildning af mikrovaskulaturer i hele organet, med mikroskopisk opløsning og makroskopisk synsfelt. Der er dog flere udviklingstrin tilbage, før denne påstand kan afprøves og anvendes.

Først bliver de mindre sekvenser som bruges til kontrastfremhævende ultralyd (KFU) afbilding i SOUA studeret teoretisk. Først vises algebraisk, at pulsinversion (PI) og amplitudemodulation (AM) kan bruges til at eliminere lineær tilbagespredning, mens den ikke-lineære tilbagespredning fra mikrobobler bevares. Desuden, ved anvendelse af Marmottant et al. (2005) modellen, som beskriver den ikke-lineære tilbagespredning fra mikrobobler, bliver det moduleret eksempler på tilbagespredning fra kontraststoffet SonoVue, som bruges til at validere effektiviteten af de to sekvenser. Denne teoretiske valideringsmetode er udforsket for at også teoretisk validere brugen af KMUTer for KFU. Når KMUTer udsender lyd, har den harmoniske indhold af lyden et ikke-lineært forhold til den elektriske spænding tilføjet til transduceren. Det er vist, at KMUTer kan bruges til KFU afbildning uden tab af billedkvalitet, hvis der anvendes en tre-impuls AM-sekvens. Dette valideres teoretisk. Desuden, viser målinger af kontrast-til-vævsforholdet til billeder af mikroboble-kontraststof optaget med KMUT og en sammenlignelig PZT-array, at den gennemsnitlige kontrastforbedring, sammenlignet med B-mode billeder, var 37.4 dB med KMUTen og 49.9 dB med PZT arrayet. Forskellen kan forklares ved KMUTen's lavere signal-støjforhold.

Dernæst var brugen af RSA til 3D SOUA demonstreret. Til forberedelse, studeres og implementeres stråleformingen af et signal optaget med en RSA, og simulerede eksempler på en punktspredningsfunktion fra en RSA, der udsender en enkelt-element syntetisk apparatursekvens, vises. Derefter vises design af et eksperimentelt set-up med et 3D-printet mikroflow-fantom, lavet til optagelse af gennemstrømmende SonoVue. Billederne optages med en 62 + 62 element PZT RSA. Fra disse bliver ultralydlokaliseringsmikroskopi udført. Mikroboblelokaliseringspræcisionen blev bestemt til at være 15.4 µm og 16.0 µm. Om dette opfylder den sande definition på super-opløsning, bliver diskuteret, men, uafhængig af dette, indikerer de resulterende 3D-billeder, at RSAer kan bruges til SOUA.

Til sidst er transmission af lyd fra en RSA gennem en linse studeret. Når lyden er emitteret og modtaget brudes lydudbredelsen af linsen, og dette gør prædiktion af rejsetiden, som bruges til at stråleforme billederne fra de modtaget signaler, kompliceret. En simplificering af dette problem tilbydes af tynd-linsemodellen, som antager at linsen er uendelig tynd og har et enkelt fokalpunkt. En RSA med en uendelig tynd linse er simuleret ved at lave elementerne i transduceren kurvede. Tynd-linsemodellen bruges til at prædiktere rejsetiden af udsendinger fra transduceren, og sammenligning med simuleringer af det

udsendte lydfelt indikerer, at ingen fasefejl introduceres af modellen. Men ægte linser har en tykkelse, og simuleringer validerer ikke, at modellen er brugbar for ægte linser. Derfor bliver en strålesporingsmodel præsenteret, som ikke bruger forenklede antagelser om linsegeometrien. Hvor nøjagtig tynd-linsemodellen og strålesporingsmodellen kan prædiktere rejsetiden kvantificeres ved at sammenligne de prædikterede tider med det udsendte lydfelt, simuleret med finite-elementmetode-modellering af en linse med endelig tykkelse. Nøjagtigheden af prædiktionerne påvirker det brugbare synsfelt, som for fire eksempler bliver vist at være lig eller højere, når rejsetiden prædikteres af strålesporingsmodellen. I eksemplet med højest forskel, øger strålesporingsmodellen synsfeltet med 25.1°. Desuden valideres strålesporingsmodellen yderligere ved at sammenligne dens prædikterede rejsetid med målinger af det udsendte lydfelt fra en 128 + 128 element RSA gennem en konkav silikonelinse. Dette resulterede i maksimalt 0.19° faseforskel, trods fejl i positioneringen af hydrofonen. Til sidst blev det brugbare udsendte synsfelt til 128 + 128 element RSAen kvantificeret ved at bruge strålesporingsmodellen. Det vises at synsfeltet er 37.2 cm × 12.1 cm ved 9 cm til 10 cm dybde, hvilket er stort nok til at afbillede en menneskenyre. Dermed er det indikeret at arrayet med linsen, er i stand til at skabe 3D SOUA af hele organer.

Acknowledgments

I would like to express my gratitude to my supervisors Prof. Jørgen A. Jensen and Prof. Matthias B. Stuart for all our discussions. Your guidance and drive has taught me how to approach scientific questions with a combination of rigor and realism. Your knowledge has shaped my understanding of ultrasound and research, and given me confidence in my own scientific understanding.

At DTU I have also received tremendous support from our technical staff, the academics in our collaborating research groups, and my PhD candidate colleagues. Firstly, I would like to thank Borislav G. Tomotov for your ceaseless technical support in the CFU lab. Without your detailed understanding of the inner workings of the ultrasound scanners, none of the experimental work presented in this thesis could have been done. Thank you to Prof. Erik V. Thomsen for very fruitful discussions about my articles. Thank you for taking the time to unofficially supervise me, across the parking lot. Your detailed knowledge and pedagogic approach has made it possible for me to study the complicated workings of capacitive micromachined transducers, without getting lost in the details. Finally, thank you to all my colleagues, past and current, at CFU, at the MEMS group, and at Copenhagen University. Thank you for always answering all my numerous questions. And thank you for making the day to day life as a PhD candidate fun and hyggelig. Thank you for all the numerous coffee breaks, for the times you let me plan meals for us outside the university, for all the beers and for all the times you listened to me complain. Without such a great group of friends around me through the years spent at DTU, this PhD would not have been completed. Thanks in particular to Mikkel Schou for always having an answer to all my questions and for many fruitful discussions. Thank you to Martin L. Ommen for always being helpful and flexible when I broke the 3D printed phantoms. And thank you to Jihwan Youn and Lars Ørsøe for being my office buddies and making office 210 a warm and cozy place to work. I will always remember you.

I have also been blessed to receive academic support from outside my home university, and I would in particular like to thank the host of my external research stay and my former supervisors at my alumni university. First of all, thank you to Prof. Andreas Austeng for hosting me during an external research stay at the University of Oslo. Although the COVID-19 pandemic limited the physical presence at the university, your support, digital teaching and supervision was valuable and greatly appreciated. Being included in your signal processing course and getting a fresh point of view on my research project broadened my understanding of ultrasound and gave me the confidence to approach it more theoretically. Your support encouraged me to dig into the geometric details of lenses, and resulted in the creation of the ray tracing theory presented in Chapter 7. Secondly, thank you to Prof. Timothy Leighton for first introducing me to the wonderful realm of bubble acoustics at the University of Southampton. Thank you, together with Prof. Paul White, for your supervision in my early years as an acoustics student. You sparked my interest in bubbles and laboratory research. Your continued support and encouragement has lead me to appreciate research and given me the confidence to eventually apply for this PhD.

I am blessed to have an abundance of tremendously gifted friends and family with technical educations who have engaged in my research questions and helped me understand my work. I would like to thank my acoustics support network, Greg White, Dylan Morgan, and Charlie House for always answering my bright and my dumb questions about acoustics and signal processing. Thank you for your continued availability

through the years. Thank you to Knut Bjarte Haus for your impressive mathematical support. Thank you for always trying to answer my questions, even when I didn't know what I needed, and for always putting in so much effort in solving the geometrical riddles I presented. Lastly, thank you to everyone who contributed to proofreading my work; Greg White, Jihwan Youn, Lasse T. Jørgensen, Mikkel Schou, my family and Andreas.

Finally, I would like to thank those who have supported me outside the university. Thank you to my Norwegian gang in Copenhagen, Daan Hottentot, Benedicte Desirée, Rebecca Lin, and Solveig Joy for making moving to yet another country for my studies less daunting. Most importantly, thank you to my biggest support, my partner Andreas Stusvik Haug. Thank you for always listening to me talk on and on about work, both when I've been excited and when I've been frustrated. Thank you for grounding me. Thank you for letting me set up my university-exchange-from-home office in your 31 m^2 apartment. Your continued emotional support and mathematical insight has lightened my workload and lessened my stress unquantifiably. Finally, thank you to my loving family: Mor, Far and Birgit. For always supporting me, for always helping me, and for always being there when I need anything at all.

List of Figures

List of Tables

Abbreviations

AM	Amplitude modulation
CEUS	Contrast enhanced ultrasound
CMUT	Capacitive micromachined ultrasonic transducer
CTR	Contrast-to-tissue ratio
DAS	Delay-and-sum
DOF	Distance of flight
FEM	Finite element method
FOV	Field of view
FWHM	Full width at half maximum
HRI	High resolution image
LRI	Low resolution image
PI	Pulse inversion
PNP	Peak-negative-pressure
PSF	Point-spread-function
PZT	Lead zirconate titanate
RCA	Row-column array
RF	Radio-frequency

SA	Synthetic aperture
SARUS	Synthetic aperture real-time ultrasound system
SF_6	Sulphur hexafluoride
SNR	Signal-to-noise ratio
SRU	Super-resolution ultrasound
SRUI	Super-resolution ultrasound imaging
TOF	Time of flight
ULM	Ultrasound localization microscopy
VS	Virtual source

Symbols

a	Amplitude ratio
a	End-point of a curved element
a_n	Coefficient of polynomial expansion
A	End-point of a virtual source line
A_{el}	Area of CMUT cell
b	Number of cycles
b	End-point of a curved element
B	End-point of a virtual source line
c_A	Speed of sound in material A
c_B	Speed of sound in material B
c_l	Speed of sound in the liquid
c_L	Speed of sound in the lens
c_m	Speed of sound in image medium
C	End-point of a receiving element
$\mathbf{C_{el}}$	Center of curvature of a curved element
d	Some distance variable
d^*	Cross-correlation reference position
$d_{\mathrm{VS}\to\mathbf{P}}$	Distance from a virtual source to a image point
D	End-point of a receiving element
e	Element index
E	Total number of elements
E_{sub}	Number of active elements in the sub-array
f	Some function describing the position of the refracted wavefront
f_{prf}	Pulse repetition frequency
f_0	Fundamental frequency

F	F-number
F_{el}	Electrostatic force on CMUT plate
F_L	Focal point of the lens
g	Some function describing the time of flight through a refracting lens to an image point
h	Harmonic index
h_{gap}	CMUT gap height
i	Emission order
I	Incident pressure wave
k	Parameterization variable
l	Lag
L	Line between emitting element and origo of the lens
L_H	Lens height
L_T	Lens thickness
m	Mass of the mass-spring system governing the displacement og a CMUT cell
n	Index giving the term in polynomial expansion
N	Number of low resolution images
p	Element pitch
p_H	Harmonic components of pressure wave emitted by a CMUT
p_i	Intersection points of the SNR criterion
p_L	Linear component of pressure wave emitted by a CMUT
p_0	Ambient pressure
p*	Reference point for the SNR criterion
P	Acoustic pressure
$\mathbf{P}$	Image point
P_B	Power of signal scattered by microbubbles
P_T	Power of signal scattered by tissue
$\mathbf{P}'$	Projected image point
P_0	Acoustic pressure amplitude
r	Cross-correlation
R	Received signal
r_B	Radius of bubble
$r_{\text{Break-up}}$	Break-up radius of the bubble

r_{Buckling}	Buckling radius of the bubble
r_c	Chord radius of the lens
r_{el}	Radius of curvature of a curved element
r_p	Radius of surface at some plane intersecting the lens
r_0	Equilibrium radius of bubble
R_{AM}	Amplitude modulation signal
R_L	Spherical radius of the lens
R_{PI}	Pulse inversion signal
S	Scattered pressure wave
S_f	Shell friction coefficient
S_p	Shell stiffness coefficient
t	Time
T	Transmitted signal
V	Voltage
V_{AC}	AC voltage
V_{DC}	DC voltage
V_0	Initial amplitude of applied AC voltage
w	Weights
$\mathbf{W}$	Position of the wavefront
x_{el}	Element position
$x_i(t)$	Incident wave
x_p	Image point position
x_{pl}	Position of a plane parallel with the y-axis
x_s	Position of the lens surface
x_{vs}	Virtual source position
x_w	Position of the emitted wavefront
$x^{\prime}$	Projected image point position
x_0	Origo of the lens surface
Δx	Distance traveled after refraction
y_{el}	Element position
$y_{el,\,j}$	Position of sub-element
y_p	Image point position
y_{pl}	Position of a plane parallel with the x-axis

y_s	Position of the lens surface
y_w	Position of the emitted wavefront
y_0	Origo of the lens surface
Δy	Distance traveled after refraction
z_p	Image point position
z_s	Position of the lens surface
z_{vs}	Virtual source position
z_w	Position of the emitted wavefront
z_0	Origo of the lens surface
Δz	Distance traveled after refraction
$\|\|\ \|\|$	Euclidean norm
$\times$	Cross-product
$\star$	Cross-correlation
$\cdot$	Dot-product
α	Emitting angle of sound ray
α_e	Limit to the emitting angle due to the ray hitting the edge of the lens
α_g	Limit to the emitting angle due to the ray grazing the curvature of the lens
α_h	Pressure amplitude of harmonic h
α_x	Emitting angle in the x-z plane
α_y	Emitting angle in the y-z plane
β	Angle between the line between the emitting element and the origo of the lens, and the emitted ray
γ	Polytropic gas exponent of gas core
Γ	Pixel intensity value
δ	Damping of the mass-spring system governing the displacement og a CMUT cell
Δ	Delay
$\Delta\phi$	Phase difference
ϵ_0	Permittivity of vacuum
ζ	Angle between the horizontal and the line between the emitting element and the origo of the lens
η	CMUT membrane displacement

κ	Stiffness of the mass-spring system governing the displacement og a CMUT cell
θ_i	Incident angle
θ_r	Refracted angle
λ	Wavelength
μ	Dynamic viscosity of the liquid
μ_S	Viscosity of the bubble wall material
ρ_l	Density in the liquid
σ_l	Surface tension of the liquid
$\sigma(r_B)$	Surface tension on the bubble wall, as a function of radius
τ	Time of flight
τ_{TX}	Transmission time of flight
ϕ_h	Phase of harmonic h
χ	Propagation direction of sound ray
χ_B	Shell elasticity modulus
χ_x	Propagation direction of sound ray in the x-z plane
χ_y	Propagation direction of sound ray in the y-z plane
ω	Angular frequency
ω_0	Applied angular frequency
Ω	Angular field-of-view

Defined terms

Frame	A sequence of all defined emissions
High resolution image	A focused image made by coherently adding several beamformed low resolution images
Low resolution image	An unfocused image made by beamforming the received signal from one or more emissions from a single virtual source
Minor sequence	The sequence of emissions emitted consequtively from a single virtual source
Virtual source	An imaginary point at the center of the wavefront arc of a single emission

CHAPTER 1

Introduction

Medical ultrasound imaging is one of the most widely used noninvasive imaging modalities. It outperforms other common modalities, such as computed tomography imaging and magnetic resonance imaging, in terms of cost, portability, and complexity, and it does not require the use of any toxic contrast agents or radiation (Szabo 2014). However, since it was initially proposed, over 70 years ago (Edler and Hertz 1954; Howry and Bliss 1952; Wild 1950), commercial ultrasound has been fundamentally limited in two aspects: resolution and dimensionality. Firstly, the resolution of common ultrasound images are limited by diffraction, meaning that if two scatters are positioned closer than half a wavelength apart, they cannot be separated in the image (Rayleigh 1945). Secondly, linear ultrasound transducers produce 2D images, which makes it both challenging to precisely identify the desired image plane within the body, and to account for out-of-plane tissue motion. Recently, both of these limitations have been addressed: the diffraction limit has been surpassed using super-resolution ultrasound imaging (SRUI) (Christensen-Jeffries et al. 2015; Errico et al. 2015), and 2D images have evolved to 3D imaging with the introduction of matrix arrays (Smith et al. 1991; von Ramm et al. 1991) and row-column arrays (RCAs) (Morton and Lockwood 2003; Rasmussen and Jensen 2013). Although the implementation SRUI and the use of RCAs remain largely pre-clinical, the methods offer great potential to evolve the use of ultrasound for vascular imaging, especially when combined.

3D ultrasound imaging was first proposed using matrix arrays in the 1990s (Smith et al. 1991; von Ramm et al. 1991). The arrays offer volumetric imaging by individually controlling a matrix of elements. If the matrix has E elements along each side, the total number of elements in the array is $E \times E$, which each require a cable for data transfer. Consequently, the arrays suffer from a high channel count, which is often impossible to implement using commercial ultrasound scanners. Sparsely populated arrays have been proposed as a compromise, but the reduction in channel count comes at the expense of higher side-lobe levels (Davidsen et al. 1994). Instead, RCAs have been proposed to overcome the issue of high channel count, while maintaining the same emitting surface area. For an RCA with E elements along each side, the total number of elements, and thus also channels, is $E + E$ (Morton and Lockwood 2003; Rasmussen et al. 2015; Sampaleanu et al. 2014; Seo and Yen 2009). Moreover, due to the large element size, RCAs benefit from large penetration depth. For instance, by quantifying the signal-to-noise ratio (SNR) of a 62 + 62 element lead zirconate titanate (PZT) RCA on a tissue-mimicking phantom, Bouzari et al. (2019) found its penetration depth to be 14 cm for single element emissions and 30 cm using focused emissions. Recently, RCAs have been employed for volumetric Doppler flow estimation (Holbek et al. 2015; Sauvage et al. 2018), functional brain imaging (Sauvage et al. 2020), as well as time-varying 3D velocity estimation using transverse oscillations (Schou et al. 2020).

SRUI can be used to image microvasculature beyond the diffraction limit, thus achieving significantly higher resolution than other ultrasound imaging methods. In recent years, the number of studies exploring SRUI have increased rapidly. The most notable works include the seminal demonstration of SRUI *in vivo* by Errico et al. (2015) who imaged a rat brain, and Christensen-Jeffries et al. (2015) who imaged a mouse ear and validated the imaged structures by comparing with optical images. SRUI is achieved using four stages: first a number of consecutive image frames are captured while microbubbles flow through the blood-stream and some contrast-enhancing technique, such as contrast enhanced ultrasound (CEUS) or singular-value decomposition, is used to remove scattering from the tissue surrounding the microvessels. Secondly a motion-correction algorithm is typically applied (Hingot et al. 2017; Taghavi et al. 2021),

before ultrasound localization microscopy (ULM) is used to localize the positions of microbubbles in each image (Couture et al. 2011). This consists of using the point-spread-function (PSF) caused by the microbubble to localize their position using for instance centroid-detection (Siepmann et al. 2011) or deconvolution (Errico et al. 2015). Finally, the localized microbubble positions can be used to form density images of the vessel structure, or tracked through consecutive images to create velocity maps of the blood flow. Several algorithms have been proposed for tracking of the microbubbles (Ackermann and Schmitz 2016; Hansen et al. 2016; Song et al. 2018; Taghavi et al. 2020).

During the ULM stage of SRUI, it is vital to obtain a precise position for the microbubbles in each image. Failure to adequately localize the microbubbles can lead to blurring of the resulting image and errors in the velocity estimation (Hingot et al. 2021). Therefore, in some implementations of ULM, some bubble-scattering signals, deemed to be of low quality or to have overlapping PSFs, are rejected before the remaining signals are used for localization (Ackermann and Schmitz 2016; Christensen-Jeffries et al. 2015; O'Reilly and Hynynen 2013). Too high concentrations of microbubbles within each image will lead to poor localization, because the PSF of adjacent microbubbles will overlap, making it impossible to accurately localize their respective centers (Christensen-Jeffries et al. 2020). Therefore, in most implementations of ULM, the concentration of microbubbles is limited so that the number of microbubbles is low within each captured image. Thereby, the distance between each microbubble is likely high enough to avoid overlapping PSFs. However, limiting the concentration of microbubbles means that a high number of images need to be captured to build a single super-resolution ultrasound (SRU) image, since the total number of localized microbubbles determines the resolution of the final SRU image (Hingot et al. 2021) and the size of the smallest vessels that can be reconstructed in the SRU image (Hingot et al. 2019). This severely prolongs the required acquisition time for SRUI. For example, in the seminal study on SRUI by Errico et al. (2015), one SRU image was produced using 75 000 images at 500 frames per second, yielding a total acquisition time of 2.5 min. This is far from adequate if real-time imaging is to be achieved, and it is practically impossible for the patient to lay still enough for this duration, as even small amounts of movement will introduce errors in the image. Thus, there exists a trade-off between acquisition time and the number of microbubbles localized in each image.

1.1 Motivation and objectives

Blood-flow in the vascular network of vessels smaller than 100 µm is known as microcirculation, and dysfunctionality of this blood-flow is often indicative of illness (Lenasi 2016). For instance, disease of the microvasculature is a known precursor for diabetic nephropathy, which is one of the leading causes of renal failure (Fowler 2011). Such disease is also known to elevate the risk of amputation of outer extremities (Beckman et al. 2019). Moreover, one of the early indicators of cancer occur in the microvasculature; as tumors grow the microvasculature experience angiogenesis, causing excessive branching and distorted and enlarged vessels (Hanahan and Weinberg 2011). Cancer is most commonly diagnosed using biopsy of the tumor (Niederhuber et al. 2020), and non-invasive imaging of the microvasculature could therefore potentially provide advantages for both screening, diagnosis, and monitoring during treatment. The microvasculature include capillaries that can be less than 10 µm wide (Lenasi 2016), and observation of these structures has been impossible with conventional diffraction-limited ultrasound. SRUI has been proposed to image and separate blood-vessels that lay closer than the diffraction limit (Christensen-Jeffries et al. 2020). Imaging and extraction of information, such as blood-flow velocity, tortuosity, and microvessel density, from these structures has the potential to revolutionize the access to information about the human microvasculature and its disease.

Making SRU images of the microvasculature in 3D improves the clinical applicability of the technique because it will enable simultaneous imaging of a whole volume of the organ. In addition to giving the clinician access to more information, this also solves some fundamental problems associated with SRUI. The technique suffers from three problems when a linear array is used: inaccurate positioning

in the elevation plane, out-of plane movement of the microbubbles, and out-of plane tissue movement (Christensen-Jeffries et al. 2020). When using a linear array, localization of the microbubbles in the elevation plane of the transducer is limited by the elevation focus, which means that any microbubble laying within the width of the elevation focus will be taken to have the same azimuthal position. The vessel network typically imaged using SRUI often lay closer than the elevation focus of a typical linear array, and separation of these vessels is thus not possible (Foiret et al. 2017). Consequently, these vessels will appear to lay in the same plane in the resulting 2D SRUI image. Christensen-Jeffries et al. (2015) compared SRU images and optical images of the vasculature in a mouse ear, and found that the width of the elevation focus caused some vessels to appear to lay in the imaged plane, when, in fact, the optical image showed that they laid further into the ear tissue. Such miss-localization of vessel structure will impact the clinical usability of SRU images, and can be alleviated by making 3D images. Furthermore, in 2D SRU images, the microbubbles will flow in and out of the imaged plane, making their tracking either discontinuous or erroneous. This will likely cause errors in the velocity estimation (Ackermann and Schmitz 2016). Imaging of the 3D structure of the microvasculature is especially essential when applied to tumors where angiogenesis is a known marker for disease. Lin et al. (2017) first demonstrated 3D SRUI imaging of complex microvascular patterns in rat tumors, and hypothesized that with further development of this technique, it can be used to detect and quantify malignant biomarkers in the microvasculature. Lastly, when using a 1D array, motion-correction can only be applied in the dimension parallel to the transducer. Thus, the motion in the orthogonal direction is ignored, and this will degrade both the contrast of the images and the precision of the microbubble localization. Therefore, for volumetric SRUI, motion-correction should be applied in 3D, as demonstrated by Harput et al. (2018).

Ideally, an RCA used for SRUI should have a large surface area to provide high resolution, a large field of view (FOV) and deep penetration. In any ultrasound imaging technique, the size of the array is inversely proportional to the resolution (Szabo 2014). And although this resolution does not translate directly to the lateral resolution of the final SRU images (Hingot et al. 2021), it does affect the acquisition time of the image, which is prolonged by low resolution in the collected images due to the trade-off between acquisition time and the number of localized microbubbles (Hingot et al. 2019). Thus, a large surface area contributes to lower the needed acquisition time. Moreover, a larger surface area also increases the usable FOV of the RCA. Unfortunately, the foot-print of the imaged volume captured by an RCAs is limited to the shape of the transducer apertures (Bouzari et al. 2017). In many of the seminal works on RCAs, the transducer is made of PZT and have fairly small foot-prints of only $\sim 1\,\text{cm}$ to $2\,\text{cm}$ width (Bouzari et al. 2016; Holbek et al. 2015; Sauvage et al. 2018). As an example for comparison, the median size of a left kidney in an adult human is $11.2\,\text{cm} \times 5.8\,\text{cm} \times 4.6\,\text{cm}$ (Emamian et al. 1993), and imaging the whole organ with an RCA thus requires an increased aperture size. Moreover, with a large surface area, more energy is emitted from the transducer, thus making it possible to image deeper into the tissue. This is vital to make SRUI a functional tool for clinicians, as imaging beyond $10\,\text{cm}$ is needed to image entire organs (Christensen-Jeffries et al. 2020).

For SRUI the trade-off between acquisition time and the number of localized microbubbles in each image means that a high resolution is desirable. This can be achieved by using a large aperture, giving a high lateral resolution, and emitting a high frequency. For any ultrasound imaging technique, the axial resolution is proportional to the emitted frequency (Szabo 2004). However, this puts some strict constraints on the design and production of the array. The size of an RCA is given by the number of elements times the inter-element pitch, which is restricted by the smallest wavelength in the emitted field (Jensen 2002). To avoid grating lobes in the image region, the pitch must be $< \frac{\lambda}{2}$, where λ is the wavelength of the emitted pulse (Szabo 2004). If a high frequency is employed to increase the axial resolution, to keep the pitch smaller than $\frac{\lambda}{2}$ and the size of the aperture the same, the number of elements must be increased. Producing such an array comes with some challenges. The elements are typically separated by dicing the PZT (Sauvage et al. 2018), and if the required pitch is too small this becomes unfeasible (Yeh et al. 2005).

On the other hand, producing a high frequency RCA using capacitive micromachined elements is

attainable (Yeh et al. 2005). Here, the elements are separated using etching, and smaller pitches and kerfs are thus attainable. Capacitive micromachined ultrasonic transducers (CMUTs) have recently emerged as a viable alternative to more conventional PZT arrays (Haller and Khuri-Yakub 1994; Oralkan et al. 2002). Production of CMUTs is cheaper than PZT transducers, and the process offers great design flexibility (Kamaya et al. 2013), enabling features which are especially suitable for SRUI. For example, the array can be designed to have a low emitted pressure, while maintaining a high receive sensitivity (Savoia et al. 2012). The low emitted pressure is suitable for imaging microbubbles without destroying them (Eckersley et al. 2005), and the high receive sensitivity allows for even weak bubble signals to be received and preserved through the CEUS process. Moreover, the array can also be designed to have a wide bandwidth (Kamaya et al. 2013), which gives a high axial resolution, giving the potential for a lower acquisition time. However, the emission from CMUT arrays is nonlinearly related to its driving voltage, and weather CMUTs can be used for CEUS imaging has therefore been questioned (Martin et al. 2014). To achieve contrast-enhancement with a CMUT, careful consideration of the combination of the inherent nonlinearity of the array with the nonlinear nature of the microbubbles is required.

Moreover, production of large CMUTs is also challenging and puts high demands on the robustness of the manufacturing process (Grass et al. 2020; Ommen et al. 2021). Ultimately, manufacturing of the array sets a limit for how large the active surface area can be, while maintaining a suitable pitch and emitted frequency. Therefore, it has been suggested that the usable FOV of an RCA should be increased using an acoustic lens (Bouzari et al. 2017; Joyce and Lockwood 2014). This will increase the volume of the image, without the need to increase the aperture of the transducer. In addition to bypassing the aforementioned production challenges, this also enables the transducer to capture a larger image through the gap between the ribs. Enlarging the FOV of an RCA without increasing the size of aperture was first proposed by Démoré et al. (2009), who curved the elements of an RCA on a hemisphere and simulated the resulting radiation pattern. Ferin et al. (2018) later proposed a manufacturing technique for such an array, but noted that the process was complex and doubted its commercial applicability. Contrarily, a simple casting method has been proposed to produce such acoustic lenses for RCA (Bouzari et al. 2018; Engholm et al. 2018), and these can be mounted onto flat RCAs. Adding an acoustic lens in front of RCAs was first proposed by Joyce and Lockwood (2014), who showed that the energy from an RCA could be spread out to 45° by adding a bowl-shaped piezoceramic in front of the aperture. However, Joyce and Lockwood (2014) also noted that the addition of the material introduces a non-trivial complexity to the calculation of the delays used to beamform and compose the ultrasound images. Precise calculation of these delays is the main challenge remaining before lensed RCA can be progressed to clinical use.

Thus, the advancement of clinical ultrasound towards microscopic resolution using SRUI has several important potential diagnostic applications. The performance of this technique can be improved by making the images in 3D with an RCA, and, a macroscopic FOV can be achieved by using an acoustic lens. The key advantage of these techniques lie in their potential combination. It is hypothesized that non-invasive imaging of the microvasculature with microscopic resolution and a macroscopic FOV is attainable by combining the four modern ultrasound techniques: SRUI, CMUT array design, RCA imaging, and an acoustic lenses. Several developmental steps remain before this hypothesis can be tested *in vivo*, and several of these steps will be explored in this thesis.

1.2 Delay-and-sum beamforming

Medical ultrasound images are created by emitting ultrasound from a transducer, and receiving the signal scattered by media in the image domain. The received signals are beamformed to create an image from the acoustic signals, and this technique forms the back-bone of all acoustic imaging. Although more advanced beamforming methods, such as adaptive beamforming (Rindal et al. 2019), are regularly proposed and studied, most commercial ultrasound imaging scanners use a delay-and-sum (DAS) beamformer. The aim

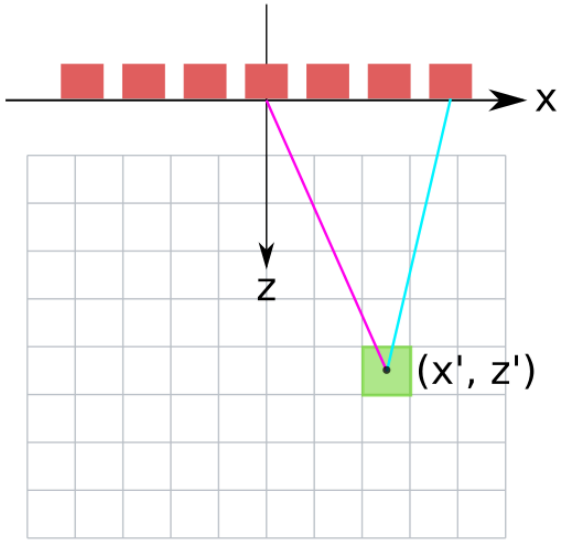

Figure 1.1: An illustration of a uniform linear array and how the DOF is calculated in the simplest form. The red rectangles are elements in the array, the green square is the pixel position which is being beamformed, the magenta line is the DOF$_{tx}$, and the cyan line is the DOF$_{rc}$.

of DAS is to delay the signals received on each element in the transducer so that they are in phase and can be summed coherently.

For a uniform, linear array with E elements, the output of a DAS beamformer for a single emission is

$$\Gamma = \sum_{e=0}^{E-1} w_e \, R_e(\tau_e). \tag{1.1}$$

Here, Γ is the pixel value at the beamformed point, e is the element index, w is the weight applied to each element, R_e is the signal received on element number e, and τ is the time of flight (TOF). The TOF is calculated based on the distance traveled to and from the image pixel, and accurate prediction of this time is what makes coherent summation possible. Fig. 1.1 shows a simple example of the geometry used to calculate τ. Here, a single element in the middle of the transducer emits sound, and the resulting received signal on all receiving elements can be beamformed for the image pixel at $\mathbf{P} = (x_p, z_p)$. The TOF is calculated from the distance traveled by the sound from the emitting element to the image pixel and back to each of the receiving elements, and can in this scenario be expressed as

$$\tau(m) = \frac{\text{DOF}_{tx}(e) + \text{DOF}_{rc}(e)}{c_m} \tag{1.2}$$

where c_m is the speed of sound in the image medium, DOF is the distance of flight, and the subscripts tx and rc denote transmit and receive, respectively. In the example drawn in Fig. 1.1, the magenta line is the DOF from the emitting element to the image pixel, and the cyan line is the DOF from the image pixel to element number $e = E$. To compose a full ultrasound image using a DAS beamformer, eq. (1.1) must be applied for every image pixel. Much of the theoretical work on using lenses on RCAs, which will be further discussed in Chapters 6 and 7, revolves around predicting this TOF, so that a DAS beamformer can

be accurately implemented.

1.3 Synthetic aperture ultrasound imaging

The synthetic aperture (SA) imaging technique improves contrast and resolution of the ultrasound image by dynamically implementing precise calculations of τ for each image pixel. SA imaging uses coherent compounding of several emitted diverging waves to achieve an image which is dynamically focused both in transmit and receive (Jensen et al. 2006). The SA technique was first introduced in radar technology in the 1950s (Jensen et al. 2006; Soumekh 1999). In radar, typically, a single element array is used to transmit and receive pulses while it is moved across the image domain. When the received pulses are delayed and summed coherently, this creates a virtual array. Combined with high pulse repetition frequency, this also enables a higher frame-rate, as fewer emissions are required to achieve the same image-quality (Jensen et al. 2010). The same principle is applied in ultrafast plane-wave imaging (Tanter and Fink 2014), which is essentially the same as SA imaging, but with plane waves rather than diverging waves. Both techniques are ideal for SRUI, where long acquisition time is one of the most crucial drawbacks. Moreover, when using a diverging or plane wave, the emitted acoustic energy is spread across a large section of the imaged medium, and the peak pressure experienced by the contrast agents is therefore restricted. This is ideal for imaging of microbubbles, which are destroyed or degraded at too high insonification pressures (de Jong et al. 2009).

1.3.1 Implementing synthetic aperture ultrasound imaging

In this section, the implementation of SA imaging for medical ultrasound used throughout this thesis is described, in order to define all terms associated with the method. The implementation is based on Jensen et al. (2006).

SA images are created by emitting waves which diverge while propagating through the image domain. This is achieved by applying a delay, Δ, to the emitting elements so that the profile of the wavefront is circular. The point laying in the center of this circle is referred to as the virtual source (VS). An example of the geometry of the SA set-up is shown in Fig. 1.2. The DOF_{tx} is in this case predicted based on the position of the VS, as if the wave was emitted from the VS before $t = 0$. Here, $t = 0$ is referring to the time instance when the first element starts to emit sound. Thus, the DOF is predicted as

$$\text{DOF}_{tx} = \sqrt{(z_p - z_{VS})^2 + (x_{VS} - x_p)^2} - z_{VS}, \tag{1.3}$$

$$\text{DOF}_{rc} = \sqrt{(x_p - x_{el,\,e})^2 + (z_p)^2}. \tag{1.4}$$

Here, (x_{vs}, z_{vs}) is the position of the VS, and $x_{el,\,e}$ is the position of the receiving element number e. Having calculated the DOFs, eq. (1.2) is applied to calculate τ. DAS beamforming can be applied to all image pixels to create a whole image from only this one emission. Because this is created using an unfocused emission, the image is not focused, and is referred to as a low resolution image (LRI).

The emission from a VS is made from a sub-set of the elements in the array, called a sub-array. In Fig. 1.2, the active elements in the sub-array are drawn in solid color, while the other elements are drawn as unfilled boxes. The F-number gives the relation between the z position of the VS and the width of the sub-array, as

$$\text{F} = \frac{z_{vs}}{p \cdot M_{sub}}, \tag{1.5}$$

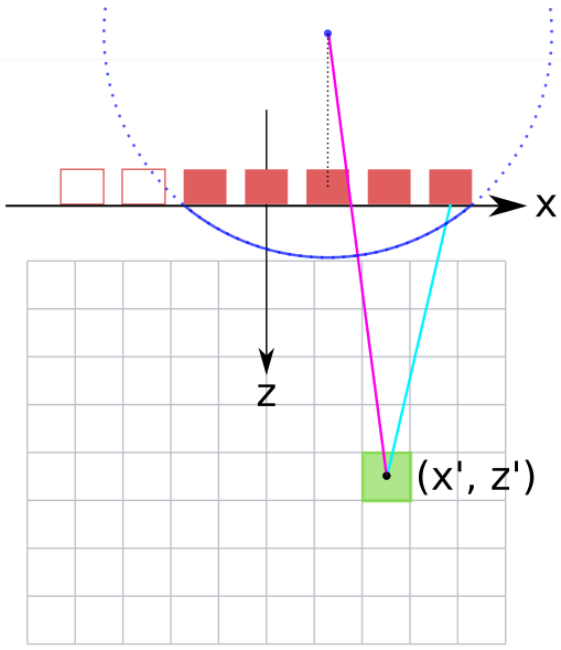

Figure 1.2: An illustration of how TOF is predicted from a virtual source (VS) to an image pixel in SA imaging. The red rectangles are the active elements in the array, the white rectangles with red borders are not active, the green square is the pixel position which is being beamformed, the magenta line is the distance from the VS to the image pixel, the cyan line is the DOF$_{rc}$, the blue dot is the VS and the blue curve is the emitted wavefront.

where p is the element pitch and E_{sub} is the number of active elements in the sub-array. A negative F-number indicates that the VS lays behind the transducer surface. This configuration is commonly used to ensure that a large area of the image domain is insonified by a single emission.

Several emissions are used to create a full SA image. A sequence of several consecutive emissions is defined as a frame, and this referrers to a sequence of emissions, emitted from both constant and consecutive VS. The VSs are typically placed along the transducer aperture, so that the emissions seemingly slide across the aperture. The emission from each VS are received and beamformed to create a set of LRIs. Then, to form a focused image, the LRIs are all summed to form a high resolution image (HRI), as

$$\text{HRI} = \text{LRI}_1 + \text{LRI}_2 + ... + \text{LRI}_N, \tag{1.6}$$

where N is the total number of LRIs used in the HRI. Normally, the number of LRIs is equivalent with the number of VSs, and equivalent with the number of transmissions. However, occasionally, more than a single emission is emitted from a VS. This is, for instance, the case in CEUS imaging, which is the topic of Chapter 2. In CEUS imaging, several consecutive emissions from the same VS are combined to enhance the contrast of nonlinearly scattering reflectors in the image domain. In this case, the emissions emitted consecutively, from a single VS, are referred to as the minor sequence. These emissions can be combined to create one or more LRIs, and thus several ultrasound images can result from a single frame.

1.4 Scientific Contribution

A list of published papers and papers in preparation during this Ph.D. project is shown below. The listed papers can be found in the appendix.

1.4.1 Papers included in the thesis

Paper 1

Title: History and latest advances in flow estimation technology: from 1-D in 2-D to 3-D in 4-D

Authors: Jørgen Arendt Jensen, Svetoslav Ivanov Nikolov, Kristoffer Lindskov Hansen, Matthias Bo Stuart, Carlos A. Villagomez Hoyos, Mikkel Schou, Martin Lind Ommen, **Sigrid Husebø Øygard**, Lasse Thurmann Jørgensen, Marie Sand Traberg, Tin-Quoc Nguyen, Erik Vilain Thomsen, Niels Bent Larsen, Christopher Beers, Borislav Gueorguiev Tomov, and Michael Bachmann Nielsen

Published in: *IEEE Int. Ultrason. Symp.*, pp. 1041-1050, 2019

Contributions: Took part in designing and operating one of the experimental set-ups used to produce the 3D SRU image presented in the article.

Paper 2

Title: 3-D super-resolution imaging using a 62+62 elements row-column array

Authors: Jørgen Arendt Jensen, Mikkel Schou, Martin Lind Ommen, **Sigrid Husebø Øygard**, Thomas Sams, Matthias Bo Stuart, Erik Vilain Thomsen, Niels Bent Larsen, Christopher Beers, and Borislav Gueorguiev Tomov

Published in: *IEEE Int. Ultrason. Symp.*, pp. 1838-1841, 2019

Contributions: Took part in designing and operating the experimental set-up used to produce the 3D SRU image presented in the article and contributed in revising the manuscript.

Paper 3

Title: Three-dimensional super-resolution imaging using a row-column array

Authors: Jørgen Arendt Jensen, Martin Lind Ommen, Mikkel Schou, **Sigrid Husebø Øygard**, Thomas Sams, Matthias Bo Stuart, Christopher Beers, Erik Vilain Thomsen, Niels Bent Larsen, and Borislav Gueorguiev Tomov

Published in: *IEEE Transactions on Ultrasonics, Ferroelectrics, and Frequency Control*, pp. 538-546, 2019

Contributions: Took part in designing and operating the experimental set-up used to produce the 3D SRU image presented in the article and contributed in revising the manuscript.

Paper 4

Title: Investigating a CMUT's ability to achieve non-linear contrast enhancement

Authors: **Sigrid Husebø Øygard**, Martin L. Ommen, Mathias Engholm, Mikkel Schou, Søren E. Diederichsen, Erik V. Thomsen, Matthias Bo Stuart, and Jørgen Arendt Jensen

Published in: *IEEE Int. Ultrason. Symp.*, pp. 1-4, 2020

Contributions: Lead the formulation of the conceptual framework and the planning of the design of the study, carried out all experiments and data collection, and is main author of the manuscript.

Paper 5

Title: Contrast-enhanced ultrasound imaging using capacitive micromachined ultrasonic transducers

Authors: **Sigrid Husebø Øygard**, Martin L. Ommen, Borislav G. Tomov, Søren E. Diederichsen, Erik V. Thomsen, Niels B. Larsen, Matthias B. Stuart, and Jørgen A. Jensen

In review: *BMC Medical Imaging*, 2021

Contributions: Lead the formulation of the conceptual framework and the planning of the design of the study, carried out all experiments and data collection, as well as theoretical derivations, and is main author of the manuscript.

Paper 6

Title: Prediction of transmission through a lensed row-column addressed array

Authors: **Sigrid Husebø Øygard**, Mélanie Audoin, Andreas Austeng, Erik V. Thomsen, Matthias B. Stuart, and Jørgen A. Jensen

In review: *The Journal of the Acoustical Society of America*, 2021

Contributions: Lead the formulation of the conceptual framework and the planning of the design of the study, carried out theoretical derivations, as well as interpretation of the simulated results, and is main author of the manuscript.

1.4.2 Papers excluded from the thesis

Paper 7

Title: Tracking performance in ultrasound super-resolution imaging

Authors: Iman Taghavi, Sofie B. Andersen, Carlos A. Villagomez Hoyos, Mikkel Schou, **Sigrid Husebø Øygard**, Fredrik Gran, Kristoffer L. Hansen, Charlotte M. Sørensen, Michael B. Nielsen, Matthias Bo Stuart, and Jørgen Arendt Jensen

Published in: *IEEE Int. Ultrason. Symp.*, pp. 1-4, 2020

Contributions: Participated in formulation of experimental design and revision of the manuscript.

1.5 Outline

The theory of CEUS imaging and the nonlinear acoustic properties of microbubbles is described in Chapter 2. The chapter includes descriptions of the CEUS image sequences used throughout the thesis, as well as theoretic and simulated proofs of their effectiveness. In Chapter 3, the theoretic study of the CEUS sequences is expanded to include the nonlinear emissions from CMUTs. The sequences are then applied and experimental results on their contrast enhancement are presented. The chapter validates that CEUS imaging with a CMUT is attainable and concludes on the appropriate choice of the minor CEUS sequence to use when making contrast-enhanced images with a nonlinearly emitting CMUT.

The theory of RCA imaging is presented in Chapter 4. A beamformer for RCAs, implemented by the author, is described, and its performance is evaluated using simulations. The chapter also goes through the status and flaws of the RCAs which have been available throughout this project. One of the RCAs has been used to make 3D SRUI of a microflow phantom, and these results are presented and discussed in Chapter 5.

In Chapter 6, the thin lens theory proposed by Bouzari et al. (2017) is introduced and implemented. The implementation of the model is validated using simulations of the emitted field from a lensed RCA. Moreover, the chapter discusses how the beamforming of simulated data from a lensed RCA can be made using the thin lens model, and simulated example images are presented. Moreover, the assumptions and limitations of the model are discussed.

Finally, a model for predicting the TOF through a lensed RCA, without making the simplifying assumptions of the thin lens model are presented in Chapter 7. The theory of this model is presented and its performance is compared with the thin lens model. The performance of the model is further evaluated by comparing its TOF prediction with both simulated and measured emitted fields. Finally, the model is applied to evaluate the usable FOV of a 128 + 128 element RCA with a concave lens.

CHAPTER 2

Contrast-enhanced ultrasound imaging

This chapter gives theoretic proofs of how the CEUS sequences amplitude modulation and pulse inversion cancels linearly scattered signals and preserves nonlinearly scattered signals. The chapter also introduces the modeling of the acoustic model for bubble vibration by Marmottant et al. (2005) and the response of SonoVue microbubbles to insonification by the CEUS sequences are simulated using the model.

SRUI is made using intravascular microbubble contrast agents. The acoustic properties of the microbubbles make it possible to separate their scattered signals from the surrounding linearly scattering tissue (Christensen-Jeffries et al. 2020). This occurs because bubbles in liquids scatter sound nonlinearly. This means that when a bubble is insonified with some frequency f_0, the scattered sound contains harmonics to this frequency: $2f_0$, $3f_0$, etc (Leighton 1994). Additionally, since the bubbles have a remarkable compressibility, their scattering cross-section is significantly greater than their geometrical cross-section, and bubbles are thus very efficient sound scatterers (Jong et al. 1991). Both these features are utilized in CEUS, where micro-sized bubbles are injected into the blood-stream and imaged as they travel through the blood-vessels. Such techniques can be utilized to study blood flow using parameters such as the wash-in and wash-out time in the heart and liver (Dietrich et al. 2018), and the time-intensity curves of blood-flow in the organs (M. X. Tang et al. 2011).

Several microbubble-pharmaceuticals have been approved for clinical use, and these microbubbles are commonly constructed using a thin shell surrounding a gas core. The shell is formed of lipids or proteins and serves the role of protecting the gas core from too rapid diffusion (M. X. Tang et al. 2011). Ultrasonic insonification of microbubbles induces both radial and surface mode vibrations (Leighton 1994), which contribute to the efficient scattering of the incident sound. The coating affects the dynamics of how the bubble responds to insonification, and several authors have attempted to describe these dynamics theoretically by extending the Rayleigh-Plesset equation (Church 1995; Hoff et al. 2000; Jong et al. 1994; Morgan et al. 2000). Currently, the most advanced model is that by Marmottant et al. (2005), who describes the nonlinear behavior of the bubble and its shell. Marmottant et al. (2005) found that when the microbubble undergoes drastic compression, its lipid shell will buckle and fold. When a large rarefaction causes the bubble to become larger than the surface area of the lipids, they break up and expose areas of the gas core to direct contact with the surrounding liquid. This affects the surface tension experienced by the bubble, and a model for how the surface tension of the bubble wall varies with the radius of the bubble is used as initial conditions for the bubble motion:

$$\sigma(r_B) = \begin{cases} 0, & r_B \leqslant r_{\text{Buckling}}, \\ \chi_B \left(\frac{{r_B}^2}{r_{\text{Buckling}}} - 1 \right), & r_{\text{Buckling}} \leqslant r_B \leqslant r_{\text{Break-up}}, \\ \sigma_l, & r_B \geqslant r_{\text{Break-up}}. \end{cases} \tag{2.1}$$

Here, r_B is the radius of the bubble, $\sigma(r_B)$ is the surface tension on the bubble wall as a function of radius, σ_l is the surface tension of the surrounding liquid, χ_B is the elasticity modulus of the shell, r_{Buckling} is the

radius at which the shell starts to buckle, and $r_{\text{Break-up}}$ is the radius at which the shell starts to break up. By extending the Rayleigh-Plesset equation Marmottant et al. (2005) found that when insonified with some time-varying acoustic pressure, P, the radial motion of the bubble suspended in a liquid is determined by

$$\rho_l \left(r_B \ddot{r}_B + \frac{3}{2} \dot{r}_B^2 \right) = \left[P_0 + \frac{2\sigma(r_0)}{r_0} \left(\frac{r_B}{r_0} \right)^{-3\gamma} \left(1 - \frac{3\gamma}{c_l} \dot{r_B} \right) - P_0 \frac{2\sigma(r_B)}{r_B} - \frac{4\mu \dot{r}_B}{r_B} - 4 \frac{\mu_S \dot{r_B}}{{r_B}^2} - P(t) \right], \quad (2.2)$$

where r_0 is the equilibrium radius of the bubble, ρ_l is the density in the liquid, p_0 is the ambient pressure in the liquid, c_l is the speed of sound in the liquid, μ is the dynamic viscosity of the liquid, γ is the polytropic gas exponent of the gas core, and μ_S is the viscosity of the bubble wall material. The notations $\dot{r}_B$ and $\ddot{r}_B$ represent the first-order and second-order derivation with respect to time. Solving eq. (2.2) for the variation in r_B with respect to time reveals the harmonic content of the bubble wall movement.

CEUS is made using specific sequences which utilize the nonlinear scattering from the microbubbles to enhance contrast. Details on how the quality of the resulting images can be quantified are given in Section 2.1. The theory of the most commonly used CEUS sequences will be described in Section 2.2. As previously discussed, the emission from CMUTs is also nonlinear, and detailed understanding of how the CEUS technique utilize the nonlinearity of the microbubbles is therefore needed to successfully use a CMUT for CEUS imaging. Therefore, Section 2.2 also includes theoretic proofs of the abilities of the sequences to preserve nonlinear reflections while eliminating linear reflections, as well as simulations of the acoustic response from microbubbles to insonification by the sequences.

2.1 Theory: Assessing image quality

When making SRU images, the nonlinear scattering of the microbubbles is utilized to distinguish the microbubbles from the surrounding tissue. The number of contrast-enhanced images needed to create a SRU image depends on how many microbubbles that can be detected in each image, and this is dependent on both the contrast and resolution of the contrast-enhanced images (Brown and Hoyt 2021).

Resolution is often quantified by the size of the PSF, and during ULM, the size of the PSF directly impacts how many microbubbles that can be separated within each image. Thus, this is a decisive factor for the acquisition time, and ultimately clinical applicability of SRUI. The size of the PSF is affected by the geometry of the array, the spatial impulse response of the imaging system, and by the accuracy of the TOF used for beamforming. The width of the PSF can be quantified by its full width at half maximum (FWHM), which is defined as:

> **Definition 2.1:** The FWHM is the total lateral width between the points where the intensity has decreased by 6 dB compared with the maximum value of the PSF, on both sides of the maximum value.

The FWHM is found by identifying the position of maximum amplitude in the PSF and the position corresponding to the image pixel on a lateral line from the peak amplitude position which has 6 dB lower image intensity than the peak. In conventional line-by-line ultrasound imaging, with emission at some frequency corresponding to a wavelength λ, the lateral width of the PSF is expected to equal the two-way beam width, given by

$$\text{FWHM} = F\lambda, \quad (2.3)$$

with the expectation of some improvement in the width when using SA imaging (Jensen et al. 2010; Rasmussen and Jensen 2013). However, when imaging with an RCA, only one-way focusing is attainable in each dimension, and therefore the beam-width is expected to be higher. According to Bouzari et al. (2019), the FWHM of an RCA can be estimated as

$$\text{FWHM} = 1.208 \cdot F\lambda. \tag{2.4}$$

Contrast enhancement is often quantified using contrast-to-tissue ratio (CTR), which, according to Bouakaz et al. (2002), is the ratio of scattered power from the enhanced signal, to the power scattered by the minimized signal. For CEUS imaging the enhanced signal is the signal scattered nonlinearly by the microbubbles and the minimized signal is the signal scattered linearly, often taken to be from the tissue surrounding the microbubbles. Thus, the ratio can be expressed as

$$\text{CTR} = \frac{P_B}{P_T}. \tag{2.5}$$

Here, P_B is the power of the signal scattered by the microbubble and P_T is the power of the signal scattered by the tissue.

2.2 Theory and simulations: CEUS sequences

In the first stage of making SRU images, a CEUS sequence is used to create images with high contrast, so that the injected microbubbles can more easily be distinguished from the surrounding tissue. This is achieved by emitting image sequences where several emissions are combined to form a single image line or low-resolution image, where the signal from the tissue is canceled out, while the signal scattered by the microbubbles are preserved (Eckersley et al. 2005). The emissions which are combined are referred to as the minor sequence, throughout this thesis, while a series of combined emissions are referred to as the major sequence. Both the chosen minor sequence and the number of emissions in the major sequence affect the contrast of the image (Brown and Hoyt 2021; Couture et al. 2012). The most commonly used minor CEUS sequences are amplitude modulation (AM) and pulse inversion (PI). These techniques preserve the nonlinear scattering from microbubbles, while filtering out the linear scattering from the surrounding tissue.

2.2.1 Amplitude modulation

The AM technique was first introduced in a patent by Brock-Fischer et al. (1996) and has later been used in many seminal works on SRUI (Christensen-Jeffries et al. 2015; Foiret et al. 2017; Hansen et al. 2016). In conventional AM, the minor sequence consists of two emissions where the second has half the pressure amplitude of the first. For example, take the incident signal on the microbubble to be equal to the transmitted signal, $T_i(t)$, from emission number i. For an AM-sequence, the emitted minor sequence is

$$T_1(t) = P_0 \sin(\omega_0 t), \tag{2.6}$$
$$T_2(t) = 0.5 P_0 \sin(\omega_0 t), \tag{2.7}$$

where ω_0 is the emitted angular frequency, t is time, P_0 is the pressure amplitude of the transmitted wave, and this is for simplicity set to $P_0 = 1$ here. As shown by Eckersley et al. (2005), the resulting nonlinear scattering from the microbubble can be modeled as a polynomial expansion of the incident waveforms:

$$S_i(t) = a_1 I_i + a_2 {I_i}^2 + a_3 {I_i}^3 \ldots \tag{2.8}$$

Here, $I_i(t)$ and $S_i(t)$ are the incident and scattered signals from emission i, respectively, a_n are coefficients giving the amplitude of each term, and n is the term index. The expansion is here given to the third order only. Any term which starts with a_1 is a linear reflection, while any term with $a_{n>1}$ is nonlinear. By assuming that the emitted signals propagate linearly to the microbubble, one can equate the incident pressure with the emitted pressure, $I_i = T_i$, and the minor AM sequence given in eq. (2.6) and eq. (2.7) can be applied, giving

$$S_1(t) = a_1\left(\sin\left(\omega_0 t\right)\right) + a_2\left(\sin\left(\omega_0 t\right)\right)^2 + a_3\left(\sin\left(\omega_0 t\right)\right)^3, \tag{2.9}$$

$$\begin{aligned} &= a_1 \sin\left(\omega_0 t\right) + \frac{a_2}{2}\Big[1 - \sin\left(2\omega_0 t + \frac{\pi}{2}\right)\Big] \\ &\quad + a_3\Big[\frac{3}{4}\sin\left(\omega_0 t\right) - \frac{1}{4}\sin\left(3\omega_0 t\right)\Big], \end{aligned} \tag{2.10}$$

$$\begin{aligned} S_2(t) &= a_1\left(\frac{1}{2}\sin\left(\omega_0 t\right)\right) + a_2\left(\frac{1}{2}\sin\left(\omega_0 t\right)\right)^2 \\ &\quad + a_3\left(\frac{1}{2}\sin\left(\omega_0 t\right)\right)^3, \end{aligned} \tag{2.11}$$

$$\begin{aligned} &= \Big[\frac{a_1}{2}\sin\left(\omega_0 t\right) - \frac{a_2}{8}\Big[1 - \sin\left(2\omega_0 t + \frac{\pi}{2}\right)\Big] \\ &\quad + \frac{a_3}{32}\Big[3\sin\left(\omega_0 t\right) - \sin\left(3\omega_0 t\right)\Big]\Big]. \end{aligned} \tag{2.12}$$

To cancel out all linear terms, the AM technique uses

$$R_{AM} = R_1 - 2 \cdot R_2, \tag{2.13}$$

Ambient pressure (p_0)	101 325 Pa
Surface tension of water (σ_l)	0.073 N m^{-1}
Dynamic viscosity of water (μ)	0.001 Pa s^{-1}
Bubble radius* (r_B)	1.25 µm
Polytropic exponent of SF_6† (γ)	1.095
Buckling radius† (r_{Buckling})	0.975×10^{-6} m
Elasticity modulus‡ of the phospholipid monolayer (χ_B)	0.55 N m^{-1}
Shell viscosity‡ (μ_S)	7.2×10^{-9} kg s^{-1}
Initial surface tension§ ($\sigma(R_0)$)	0.063 N m^{-1}

Table 2.1: The physical properties of SonoVue and water used to implement the Marmottant bubble-motion models.

The sources of the properties in Table 2.1 are:

* Bracco Imaging S.p.A. (2001).

† Marmottant et al. (2005).

‡ Given as shell stiffens (S_p) and friction coefficient (S_f) by Gorce et al. (2000) and converted as $S_p = 2\chi_B$ and $S_f = 12\pi\kappa_s$ (Marmottant et al. 2005).

§ Estimated as $\sigma_0 = 0.5 \cdot P_0 R_0$, assuming an initial tensionless state (de Jong et al. 2009).

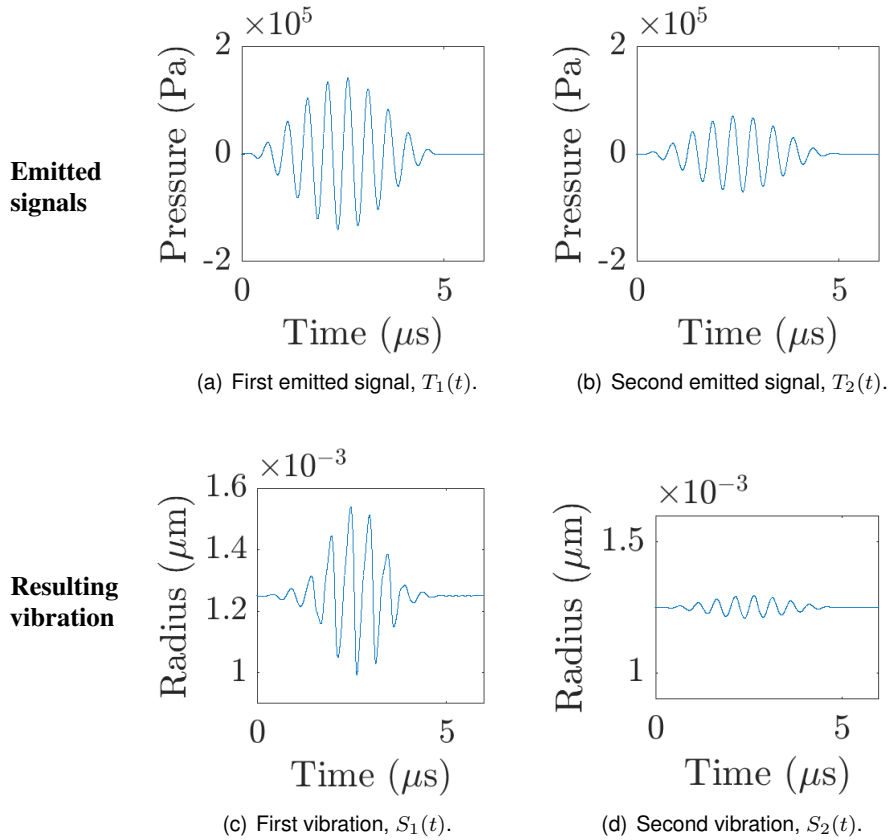

(a) First emitted signal, $T_1(t)$. (b) Second emitted signal, $T_2(t)$.

(c) First vibration, $S_1(t)$. (d) Second vibration, $S_2(t)$.

Figure 2.1: The emitted signals and the resulting bubble vibration using an AM sequence.

where R_i is the signal received from emission number i, and R_{AM} is the radio-frequency (RF) signal used to beamform a single low resolution image in a CEUS image. By assuming that the signal scattered by the bubble propagates linearly to the receiving element, one can take $R_i = S_i$ and fill in the expanded signals eq. (2.10) and eq. (2.12) in eq. (2.13):

$$\begin{aligned} R_{AM}(t) = a_1 \sin(\omega_0 t) + \frac{a_2}{2}\big[1 - \sin(2\omega_0 t + \frac{\pi}{2})\big] \\ + a_3\big[\frac{3}{4}\sin(\omega_0 t) - \frac{1}{4}\sin(3\omega_0 t)\big] \\ - 2 \cdot \Big[\frac{a_1}{2}\sin(\omega_0 t) - \frac{a_2}{8}\big[1 - \sin(2\omega_0 t + \frac{\pi}{2})\big] \\ + \frac{a_3}{32}\big[3\sin(\omega_0 t) - \sin(3\omega_0 t)\big]\Big] \end{aligned} \tag{2.14}$$

$$= \frac{a_2}{4}\sin(2\omega_0 t + \frac{\pi}{2}) + \frac{9\,a_3}{16}\sin(\omega_0 t) - \frac{3a_3}{16}\sin(3\omega_0 t). \tag{2.15}$$

This reveals an interesting feature of AM imaging; all linear scattering components are canceled out, yet the remaining signal contains energy at the emitted frequency ω_0.

This result is also supported by the bubble-motion model by Marmottant et al. (2005). As an example,

eq. (2.2) is here implemented using the physical properties of the commercial contrast agent SonoVue, which are given in Table 2.1. SonoVue is coated with phospholipids and has a core of sulphur hexafluoride (SF_6) (Schneider 1999). The microbubble is insonified with the minor sequence of AM, given in eq. (2.6) and eq. (2.7), and it is assumed that the emitted signal is equal to the incident pressure wave on the bubble, so that $P_i(t) = T_i(t)$. Each emission is a 10-cycle Hanning-windowed pulse at $f_0 = 2\,\text{MHz}$, with peak-negative-pressure $P_0 = 100\,\text{kPa}$. The incident waveforms on the microbubble are shown in Fig. 2.1(a) and (b). By solving eq. (2.2) with respect to $r_B(t)$, the variation in radial movement of the bubble wall resulting from the incident sound, is found. For each of the two incident pulses, the resulting bubble wall movement are shown in Fig. 2.1(c) and (d). These responses are then compounded according to eq. (2.13) to reveal the nonlinear response of the microbubble, shown in Fig. 2.2(b). For comparison,

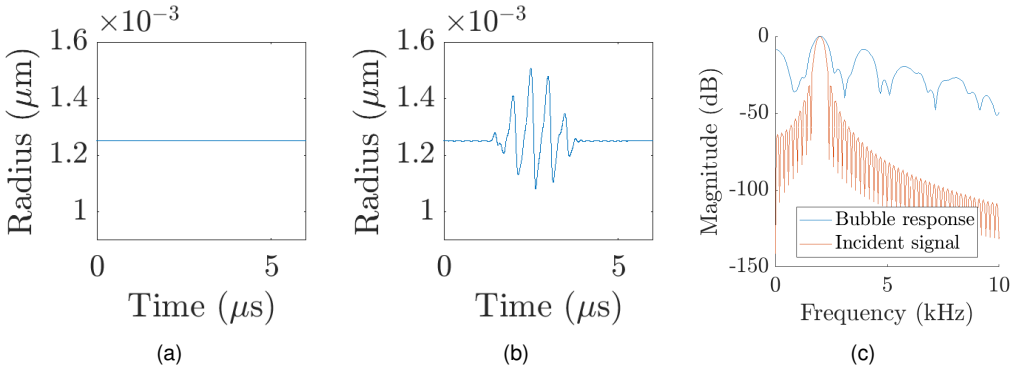

Figure 2.2: The result of AM compounding the bubble responses, when (a) assuming the response is linear and (b) response is modeled using eq. (2.2). The normalized frequency response of the bubble signal (b) and the incident signal (Fig. 2.1(a)) are shown in (c).

Fig. 2.2(a) shows the result of compounding only the linear reflections caused by the emitted signal using eq. (2.13). Here, it is clearly seen that the AM sequence can suppress any linear reflections from the tissue surrounding the microbubble. The frequency content of the incident signal and of the nonlinear bubble response are plotted together in Fig. 2.2(c). Here, it is again clear that the nonlinear content of the bubble response contains energy at the incident frequency, as was seen in eq. (2.14).

2.2.2 Pulse inversion

It is also possible to make CEUS images using PI, although this modality is less commonly used for SRUI. The principal aim of PI is the same as for AM; the linear component of the scattered signal must be suppressed, while some nonlinear component is kept. In PI, the second harmonic frequency to the emitted frequency is preserved. This is achieved by emitting two pulses of opposite polarity:

$$T_1(t) = P_0 \sin(\omega_0 t), \tag{2.16}$$
$$T_2(t) = -P_0 \sin(\omega_0 t), \tag{2.17}$$

where $P_0 = 1$ for simplicity. Again, by assuming that $I_i = T_i$, the resulting scattered signals can be expanded to

$$S_1(t) = a_1\left(\sin\left(\omega_0 t\right)\right) + a_2\left(\sin\left(\omega_0 t\right)\right)^2 + a_3\left(\sin\left(\omega_0 t\right)\right)^3 \ldots \tag{2.18}$$

$$= a_1 \sin\left(\omega_0 t\right) + a_2 \sin^2\left(\omega_0 t\right) + a_3 \sin^2\left(\omega_0 t\right) \ldots \tag{2.19}$$

$$S_2(t) = a_1\left(-\sin\left(\omega_0 t\right)\right) + a_2\left(-\sin\left(\omega_0 t\right)\right)^2 + a_3\left(-\sin\left(\omega_0 t\right)\right)^3 \ldots \tag{2.20}$$

$$= -a_1 \sin\left(\omega_0 t\right) + a_2 \sin^2\left(\omega_0 t\right) - a_3 \sin^2\left(\omega_0 t\right) \ldots \tag{2.21}$$

To cancel the linear terms, the two received signals are added, and assuming $R_i = S_i$, this gives

$$R_{PI}(t) = R_1 + R_2, \tag{2.22}$$

$$= a_1\left(\sin\left(\omega_0 t\right)\right) + a_2\left(\sin\left(\omega_0 t\right)\right)^2 + a_3\left(\sin\left(\omega_0 t\right)\right)^3 - a_1 \sin\left(\omega_0 t\right) + a_2 \sin^2\left(\omega_0 t\right) - a_3 \sin^2\left(\omega_0 t\right)$$

$$= 2\, a_2 \sin^2(\omega_0 t),$$

$$= a_2\left(1 - \sin\left(2\omega_0 t + \frac{\pi}{2}\right)\right). \tag{2.23}$$

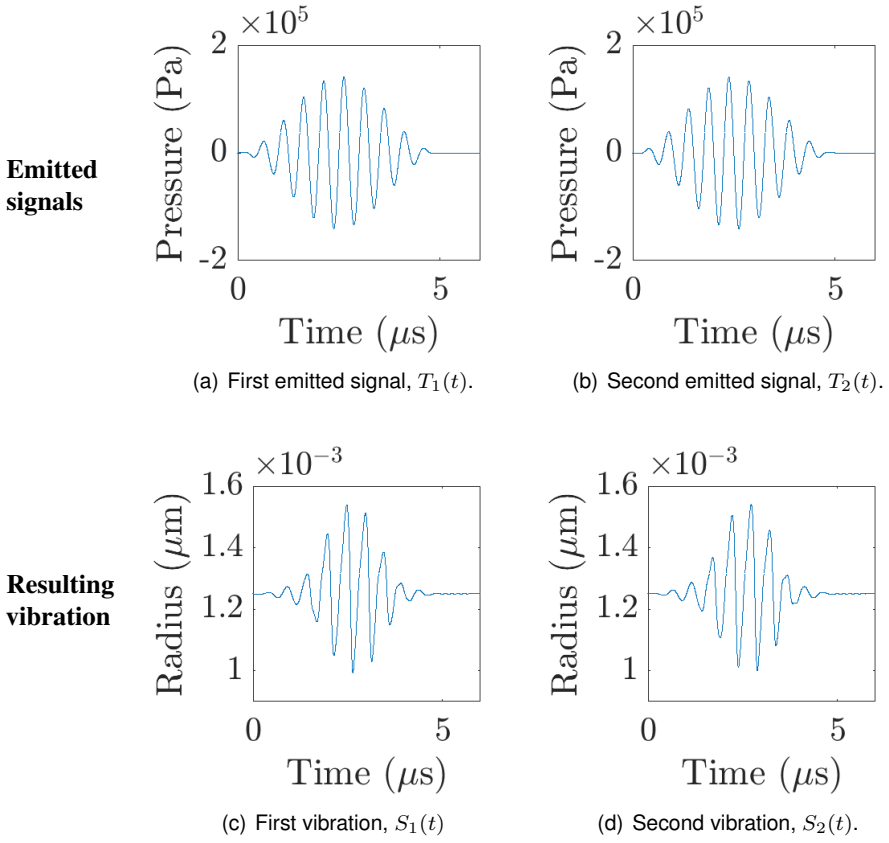

(a) First emitted signal, $T_1(t)$.

(b) Second emitted signal, $T_2(t)$.

(c) First vibration, $S_1(t)$

(d) Second vibration, $S_2(t)$.

Figure 2.3: The emitted signals and the resulting bubble vibration using a PI sequence.

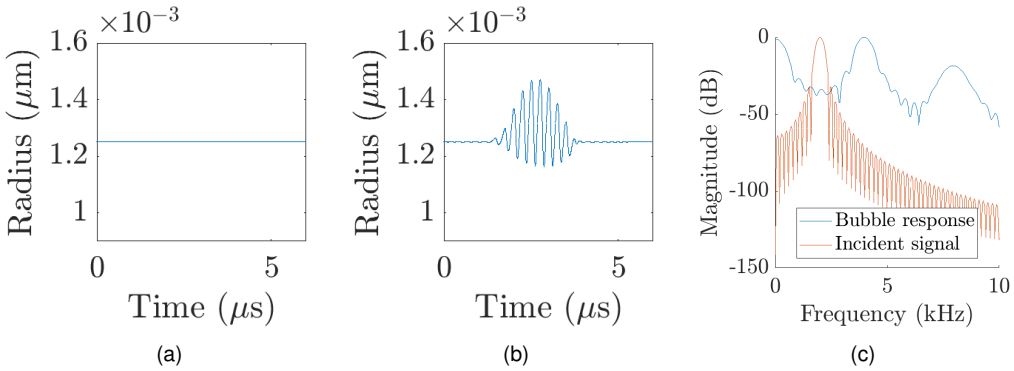

Figure 2.4: The result of PI compounding the bubble responses, when (a) assuming the response is linear and (b) response is modeled using eq. (2.2). The normalized frequency response of the bubble signal (b) and the incident signal (2.3(a)) are shown in (c).

As expected, here, the resulting signal contains energy at twice the fundamental frequency, while any energy at the fundamental frequency is removed.

The theoretical explanation of PI is also supported by the Marmottant model. To demonstrate this, the differential equation governing the vibration of the bubble wall, eq. (2.2), is applied for a SonoVue bubble, with the parameters given in Table 2.1. The minor PI sequence, given in eq. (2.16) and eq. (2.17) are applied with the same first emission as that used in Section 2.2.1. The two incident waveforms and the resulting bubble vibration are shown in Fig. 2.4. The two scattered signals are compounded according to eq. (2.22) to reveal the nonlinear response of the bubble, shown in Fig. 2.4(b). As with the AM sequence, if only the linear response to the two emitted signals in the PI sequence are compounded, all of the energy is canceled out, as shown in Fig. 2.4(a). The frequency content of the compounded bubble vibration resulting from the PI sequence is shown in Fig. 2.4(c), together with the frequency content of the first emission in the sequence. Here, it is also seen that the frequency content of the bubble response contains energy at the second harmonic to the incident frequency.

2.3 Discussion

Utilizing the unique scattering properties of microbubbles is the foundation of both CEUS and its more recent development SRUI. The nonlinear back-scattering from microbubbles makes it possible to remove linear scattering from tissue and thus map out the movement of microbubble through the microvasculature. As seen in sections 2.2.1 and 2.2.2, both AM and PI can be used to perform the cancellation of the linear signals. In 2.13 and 2.22, polynomial expansion of the compounded scattered signals have shown that both CEUS techniques can remove all linear scattering, demonstrating that both techniques are suitable for SRUI. However, the two techniques offer slightly different approaches; as seen in Fig. 2.2(c) and 2.4(c), the PI method cancels out all energy at the incident frequency, while the AM method preserves the nonlinear component at the incident frequency. The peak in the frequency content of the PI signal lays at the second harmonic to the incident signal. Thus, when using PI to perform CEUS imaging, a matched filter for the second harmonic should be used before beamforming. Using PI demands that the transducer has a bandwidth wide enough to effectively receive the second harmonic frequency. This limitation might explain why few recent publications on SRUI have opted to use PI.

CHAPTER 3

Capacitive micromachined ultrasonic transducers

This chapter introduces a three-pulse AM sequence and gives theoretic proof that its performance is unaffected by the nonlinear emissions from CMUTs. The performance of the three-pulse AM is then investigated experimentally. The theory and results presented in this chapter are based on Paper 4 and Paper 5.

CMUTs consist of a substrate etched with a distribution of small micrometer sized cavities. A few micrometers thick plate is suspended on top of the substrate and the plate can be set in motion by applying a time-varying voltage potential across the gap. The resulting electrostatic force vibrates the plate, making the CMUTs emit a sound pressure wave. The electrostatic force vibrating the plate is dependent on the applied voltage as

$$F_{el} = \frac{1}{2}\epsilon_0 A_{el} \frac{V^2}{(h_{gap} - \eta)^2}, \tag{3.1}$$

where ϵ_0 is the permittivity of vacuum, A_{el} is the surface area of the CMUT cell, η is the static displacement of the CMUT cell membrane (Novell et al. 2009). In addition to the AC voltage, a DC voltage is applied across the cell gap to increase its sensitivity (Jin et al. 2001). Thus, the applied voltage, V, consists of two components;

$$V = V_{AC} + V_{DC} \tag{3.2}$$

The sound wave emitted by the CMUT cell depends on the displacement of the cell (Kinsler et al. 1982), which can be modeled as a damped mass-spring system;

$$m\ddot{\eta} + \delta\dot{\eta} + \kappa\eta = -F_{el}. \tag{3.3}$$

where m is the system mass, δ is the system damping, κ is the system stiffness, and the first and second derivative with respect to time is denoted as $\dot{\eta}$ and $\ddot{\eta}$, respectively (Lohfink and Eccardt 2005). Analytic evaluation of this nonlinear differential equation is not straight forward, but several authors have studied the relationship numerically (Certon et al. 2005; Lohfink and Eccardt 2005; Meynier et al. 2010). It has been shown that the emitted sound pressure from CMUTs contain harmonics to the applied excitation frequency (Lohfink and Eccardt 2005; Novell et al. 2009). Moreover, the amount of harmonic distortion caused by the CMUT is proportional to the applied AC voltage (Novell et al. 2008). This poses a great challenge to SRUI using CEUS techniques, because, as was described in Chapter 2, these techniques require that the amplitude or polarity of the applied AC voltage varies between the emissions in the minor sequence. Thus, since the emissions in the minor sequence do not contain the same spectral content when using a CMUT, it will not be possible to eliminate linearly scattered components from the resulting image. This undermines the key quality of CEUS imaging, and some therefore claim that CMUTs cannot be used for CEUS imaging (Martin et al. 2014). However, Fouan and Bouakaz (2016) have proposed an alternative to conventional AM which is designed to overcome the nonlinearity of the CMUT. They

proposed that instead of making the halved emission by lowering the excitation amplitude, an emission of half the amplitude can be created by using only every second element. Thereby, the same AC voltage is applied to each element, and the amount of harmonic distortion is constant.

The theory of the three-pulse AM sequence will be presented in Section 3.1. This includes a theoretic proof that three-pulse AM imaging with a CMUT is attainable, despite the emission of harmonics, using the same bubble acoustics theory as in Section 2.2.1. Section 3.2 will then present experimental results, quantifying the performance of the three-pulse sequence using a CMUT and comparing it to two-pulse AM and PI, as well as three-pulse AM using a PZT transducer.

3.1 Theory: Three-pulse amplitude modulation

The minor sequence of the alternative AM proposed by Fouan and Bouakaz (2016) consists of three excitation, and is therefore here referred to as the three-pulse AM sequence. Fouan and Bouakaz (2016) demonstrates that the sequence outperforms the conventional AM and PI sequences at a particular applied AC voltage, using both hydrophone recordings and quantification of CTR of CEUS images of microbubles. Here follows a derivation of a theoretical proof of the effectiveness of the sequence by applying the polynomial expansion technique by Eckersley et al. (2005), previously introduced in Section 2.2. The derivation is also presented in Section 2 and the Appendix of Paper 5, but it is repeated in full here, using the same nomenclature as in the introduction of the conventional CEUS techniques presented in Section 2.2.

Let the time-varying voltage applied to the CMUT during the minor sequence be

$$V_{AC}(t) = V_0 \sin(\omega_0 t), \tag{3.4}$$

where V_0 is the voltage amplitude and ω_0 is the applied angular frequency. The resulting transmitted signal depends on the electrostatic force applied to the CMUT cells and is known to contain the applied frequency content, as well as harmonics. This can be described as

$$T_i(t) = \alpha_{i,\,h=1} \sin(\omega_0 t) + \sum_{h=2}^{\infty} \alpha_{i,\,h} \sin(h\omega_0 t + \phi_h), \qquad \begin{cases} h \in \mathbb{Z}, \\ \alpha_h \in \mathbb{R}, \end{cases} \tag{3.5}$$

$$= p_L(t) + \sum_{h=2}^{\infty} p_H(t) \tag{3.6}$$

Here, the index h gives the harmonic number, α_h is the pressure amplitude of each harmonic, and ϕ_h is the phase of each harmonic. This notation is applicable to emitted signals containing all or some of the harmonics to the fundamental frequency, since the amplitude, α_h, can be any real number, including zero. A compact form of eq. (3.5) is given in eq. (3.6) for convenience when using the emitted pressure wave in further algebraic expressions. Here, p_L is the linear part of the signal and p_H contains the harmonics.

3.1.1 Amplitude modulation using a CMUT

To cancel the linearly scattered terms using the three-pulse AM sequence, an alternative form of eq. (2.13) is used;

$$R_{AM} = R_1 - R_2 - R_3 \tag{3.7}$$

where R_i is the signal received from emission number i. Here, it will be shown that this compounding removes linearly scattered signals despite the nonlinear emission from a CMUT. This mathematical proof is the same as that presented in the appendix of Paper 5.

When using the three-pulse AM sequence with a CMUT, the 3 emissions can be expressed as

$$T_1(t) = \alpha_{1,1} \sin(\omega_0 t) + \sum_{h=2}^{\infty} \alpha_h \sin(h\omega_0 t + \phi_h), \tag{3.8}$$

$$T_2(t) = 0.5 \left[\alpha_{1,1} \sin(\omega_0 t) + \sum_{h=2}^{\infty} \alpha_h \sin(h\omega_0 t + \phi_h) \right], \tag{3.9}$$

$$T_3(t) = 0.5 \left[\alpha_{1,1} \sin(\omega_0 t) + \sum_{h=2}^{\infty} \alpha_h \sin(h\omega_0 t + \phi_h) \right]. \tag{3.10}$$

The factor of 0.5 in T_2 and T_3 occurs because only half the elements in the active aperture have been employed for these emissions. Considering an active aperture of elements numbered from 1 to E_{sub}, the first halved emission uses the odd numbered elements, whereas the second halved emission uses the even numbered elements. Accordingly, in eq. (3.9) the factor 0.5 is produced by using the odd numbered elements, while in eq. (3.10) it is caused by using the even numbered elements. If assuming that the propagation in the image medium is linear, the 3 emitted signals will be incident on the microbubbles and scattered nonlinearly. As shown in eq. (2.8), the scattered signal by microbubbles can be expressed as a polynomial expansion of the incident signal (Eckersley et al. 2005). Thus, the combination of the 3 received signals can be expressed as

$$\begin{aligned} R_{AM} =& a_1 T_1 + a_2 {T_1}^2 + a_3 {T_1}^3 - a_1 T_2 - a_2 {T_2}^2 \\ & - a_3 {T_2}^3 - a_1 T_3 - a_2 {T_3}^2 - a_3 {T_3}^3 \end{aligned} \tag{3.11}$$

The compact form of eq. (3.8) - eq. (3.8) is substituted in to give

$$\begin{aligned} R_{AM} =& a_1 \left(p_L + \sum_{h=2}^{\infty} p_H \right) + a_2 \left(p_L + \sum_{h=2}^{\infty} p_H \right)^2 + a_3 \left(p_L + \sum_{h=2}^{\infty} p_H \right)^3 \\ & - a_1 \left(0.5 p_L + 0.5 \sum_{h=2}^{\infty} p_H \right) - a_2 \left(0.5 p_L + 0.5 \sum_{h=2}^{\infty} p_H \right)^2 \\ & - a_3 \left(p_L + \sum_{h=2}^{\infty} p_H \right)^3 - a_1 \left(0.5 p_L + 0.5 \sum_{h=2}^{\infty} p_H \right) \\ & - a_2 \left(0.5 p_L + 0.5 \sum_{h=2}^{\infty} p_H \right)^2 - a_3 \left(p_L + \sum_{h=2}^{\infty} p_H \right)^3 \end{aligned} \tag{3.12}$$

Canceling terms and expanding the parenthesis gives

$$\begin{aligned} R_{AM} = & 0.5\,a_2\,{p_L}^2 + 0.5\,a_2\left(\sum_{h=2}^{\infty} p_H\right)^2 + a_2\,p_L\left(\sum_{h=2}^{\infty} p_H\right) \\ & + 2.25\,a_3\,p_L\left(\sum_{h=2}^{\infty} p_H\right)^2 + 2.25\,a_3\,{p_L}^2\left(\sum_{h=2}^{\infty} p_H\right) \\ & + 0.75\,a_3\left(\sum_{h=2}^{\infty} p_H\right)^3 + 0.75\,a_3\,{p_L}^3 \end{aligned} \tag{3.13}$$

Then, p_L and p_H are replaced by the long form of eq. (3.8) - eq. (3.10), where $\alpha_{1\,,1}$ is set to 1 for simplicity;

$$\begin{aligned} R_{AM} = & 0.5\,a_2\sin(\omega_0 t)^2 + 0.5\,a_2\left(\sum_{h=2}^{\infty}\alpha_h\sin(h\omega_0 t+\phi_h)\right)^2 \\ & + a_2\,\sin(\omega_0 t)\left(\sum_{h=2}^{\infty}\alpha_h\sin(h\omega_0 t+\phi_h)\right) \\ & + 2.25\,a_3\,\sin(\omega_0 t)\left(\sum_{h=2}^{\infty}\alpha_h\sin(h\omega_0 t+\phi_h)\right)^2 \\ & + 2.25\,a_3\sin(\omega_0 t)^2\left(\sum_{h=2}^{\infty}\alpha_h\sin(h\omega_0 t+\phi_h)\right) \\ & + 0.75\,a_3\left(\sum_{h=2}^{\infty}\alpha_h\sin(h\omega_0 t+\phi_h)\right)^3 + 0.75\,a_3\sin(\omega_0 t)^3. \end{aligned} \tag{3.14}$$

Finally, the last term of eq. (3.14) is expanded to give

$$\begin{aligned} R_{AM} = & 0.5\,a_2\sin(\omega_0 t)^2 + 0.5\,a_2\left(\sum_{h=2}^{\infty}\alpha_h\sin(h\omega_0 t+\phi_h)\right)^2 \\ & + a_2\,\sin(\omega_0 t)\left(\sum_{h=2}^{\infty}\alpha_h\sin(h\omega_0 t+\phi_h)\right) \\ & + 2.25\,a_3\,\sin(\omega_0 t)\left(\sum_{h=2}^{\infty}\alpha_h\sin(h\omega_0 t+\phi_h)\right)^2 \\ & + 2.25\,a_3\sin(\omega_0 t)^2\left(\sum_{h=2}^{\infty}\alpha_h\sin(h\omega_0 t+\phi_h)\right) \\ & + 0.75\,a_3\left(\sum_{h=2}^{\infty}\alpha_h\sin(h\omega_0 t+\phi_h)\right)^3 \\ & - 0.1875\,a_3\,\sin(3\omega_0 t) + 1.5\,a_3\,\sin(\omega_0 t). \end{aligned} \tag{3.15}$$

It can be seen here, as in eq. (2.14), that no linear scattering coefficients remain, yet, the last term of eq. (3.15) contains energy at the emitted frequency, ω_0. From this, it can be concluded that the inclusion of the emitted harmonics has not hampered the ability to cancel linearly scattered terms.

3.2 Contrast enhancement imaging using a CMUT

The theoretic derivation in Section 3.1 shows that CEUS imaging using a CMUT is attainable if the appropriate sequence is used. The application of different sequence designs for CEUS imaging using a CMUT has been studied in Paper 4 and Paper 5 using a 4.8 MHz CMUT produced by Diederichsen (2020). The studies were conducted using a 1D transducer, for simplicity, but the findings are fully transferable to 3D SRUI.

Firstly, the contrast-enhancement using a two-pulse AM and PI was compared to B-mode imaging at different applied voltages, in Paper 4. Secondly, the three-pulse sequence proposed by Fouan and Bouakaz (2016) was applied, and its performance was compared to the two-pulse AM sequence and B-mode, in Paper 5. The results from these measurements are presented in Section 3.2.1 and 3.2.2, respectively. In addition to examining the choice of the appropriate minor sequence, these measurements investigate the effect of changing the voltage applied to the CMUT. Increasing the applied voltage leads to more harmonic distortion of the emitted signal (Novell et al. 2009). It is hypothesized that these harmonics will degrade the contrast enhancement attainable with PI, but that the contrast-enhancement achieved with the three-pulse AM sequence is independent of the amount of harmonic distortion.

3.2.1 Methods and results: Two-pulse amplitude modulation and pulse inversion

The CTR of CEUS images acquired with a 1D CMUT was studied at different applied AC voltages. Images were acquired of a microflow phantom where diluted SonoVue microbubble contrast agents flowed through a 3D printed channel phantom, which was placed on top of a block of tissue-mimicking material. The minor sequence consisted of three emissions, with positive, half, and negative pressure amplitude, as given by eq. (2.6), eq. (2.7), and eq. (2.17), respectively. The half amplitude scaling of the second emission was made by only employing every second element in each sub-aperture. B-mode images were beamformed using the positive emission, two-pulse AM images were beamformed after applying eq. (2.13) using the positive and half-amplitude emissions, and PI images were beamformed after applying eq. (2.22) using the positive and negative amplitude emissions. The CTR was calculated using eq. (2.5) by taking the power from a region around the channel to be P_B, and the power from a region in the tissue-mimicking phantom to be P_T. The CTR was calculated for the two-pulse AM images, PI images, and B-mode images. At each applied voltage, the resulting peak-negative-pressure (PNP) was recorded using a hydrophone. Further descriptions of the experimental equipment, set-ups and methods are given in Paper 2. The resulting variation in CTR with PNP is given in Fig. 3.1

During the acquisition of the CEUS images, it was observed that the CMUT probe was sensitive to external noise sources. When other equipment in the laboratory was operating, prominent noise arcs occurred in the CEUS image, especially when the transducer was operated at low V_{AC} values. Fig. 3.2 shows an example of a two-pulse AM image of the microflow phantom without infusion of SonoVue, collected at $V_{AC} = 24\,\mathrm{V}$. In the image, the top and the bottom of the phantom can be seen as straight lines, and a number of arcs occur throughout the image. It is likely that these arcs occur because of electromagnetic inference noise on the receive channels. Such noise would occur simultaneously on all channels, and will therefore look like arcs in the beamformed image. It was also observed that the arc positions shifted seemingly randomly through consecutive image acquisitions. While the frames used to calculate the CTR presented in Fig. 3.1 were collected, all equipment in the laboratory that was not in use was turned off, and the images were visually inspected to rule out significant noise inference. However,

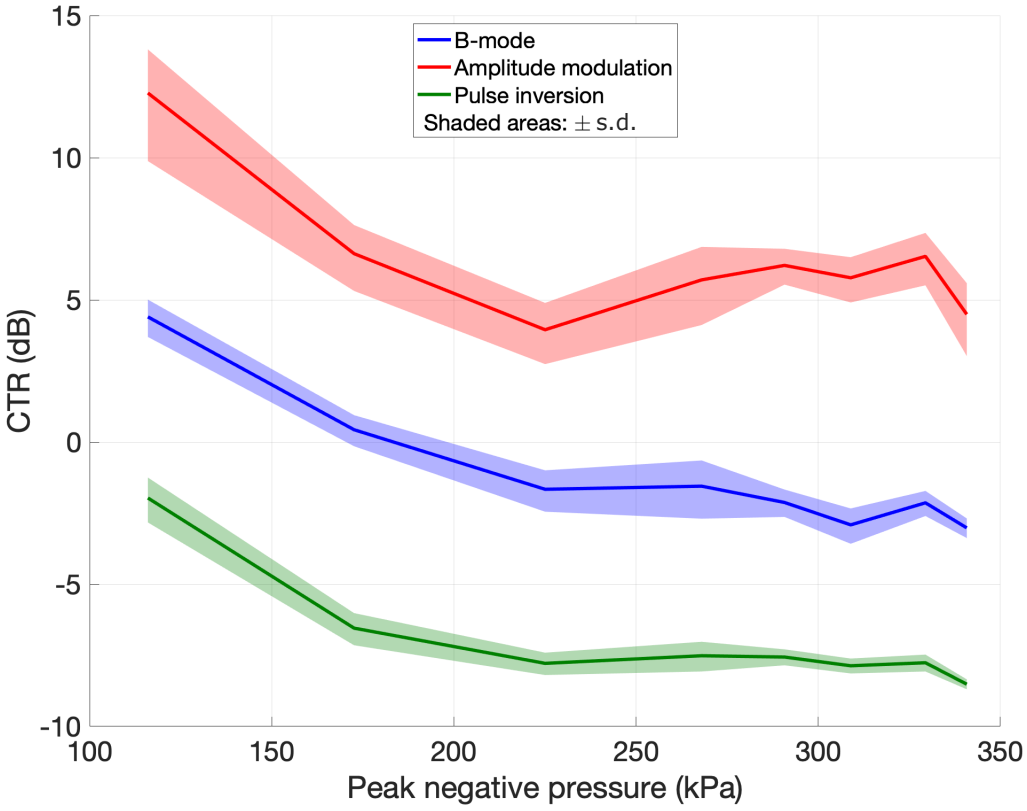

.

Figure 3.1: The CTR of images of a microflow phantom infused with SonoVue acquired using a CMUT. The variation with peak-negative-pressure is induced by varying the applied V_{AC}. Both the AM and the PI imaging are performed with two pulses in the minor sequence. The shaded areas indicate $\pm$ one standard deviation.The figure is moderated and reprinted from Paper 4.

one cannot conclude that electromagnetic noise pollution, even from the ultrasound scanner itself, has not corrupted the images to some degree.

3.2.2 Methods and results: Tree-pulse amplitude modulation

Quantification of CTR was also done in Paper 5, where the contrast-enhancement achieved by two-pulse AM and three-pulse AM images made using a CMUT were compared. In addition, the same quantification was performed using a PZT probe with equivalent design specifications as the CMUT. This gives reference values, where the emitted signal harmonics are not affected by the applied voltage. The method used to make the quantification of CTR are given in Sections 3.1 - 3.3 of Paper 5, and descriptions of the measurement of the corresponding PNP are given in Section 3.4 of Paper 5. The minor sequence used was the three-pulse AM emissions defined in eq. (3.8) to eq. (3.10). Three-pulse AM images were beamformed after applying eq. (3.7), two-pulse AM images were beamformed after applying eq. (2.13), and B-mode images were beamformed from the first emission in the minor sequence. The CTR of both the three-pulse AM images, two-pulse AM images, and B-mode images was quantified at varying V_{AC} values, applied to both the CMUT and the PZT transducer. The resulting variation in CTR with the

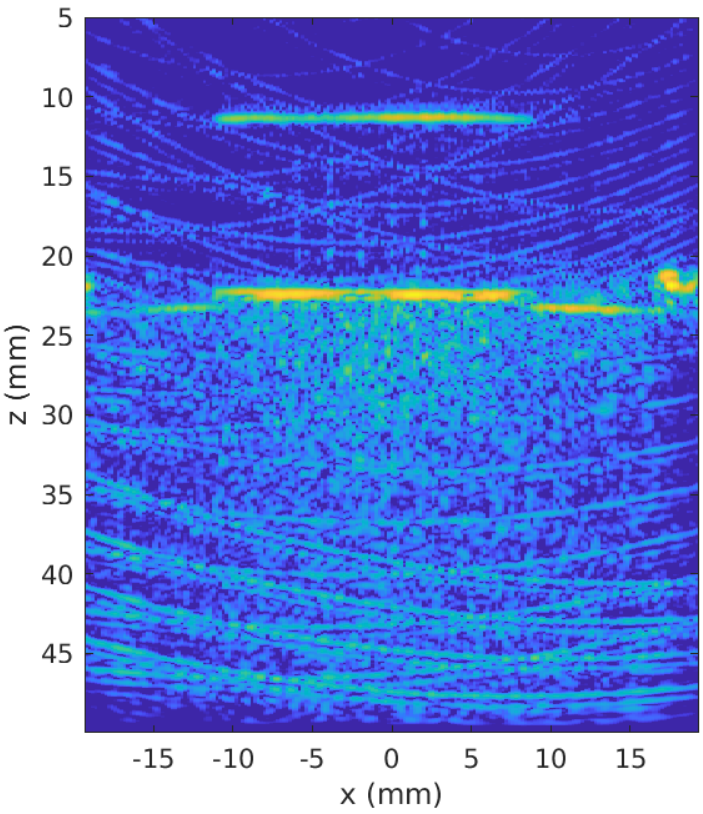

Figure 3.2: An example of a noisy two-pulse AM image of the microflow phantom, without contrast agents, collected with the CMUT.

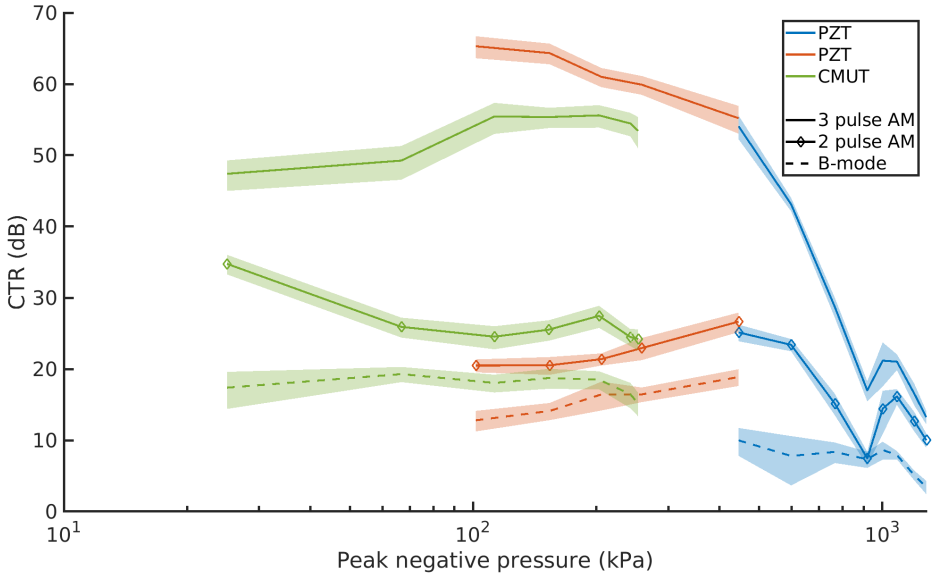

Figure 3.3: Variation in CTR as the applied V_{AC} to the PZT transducer and CMUT is varied. The variation is plotted as a function of the resulting emitted PNP. The figure is reprinted from Paper 5.

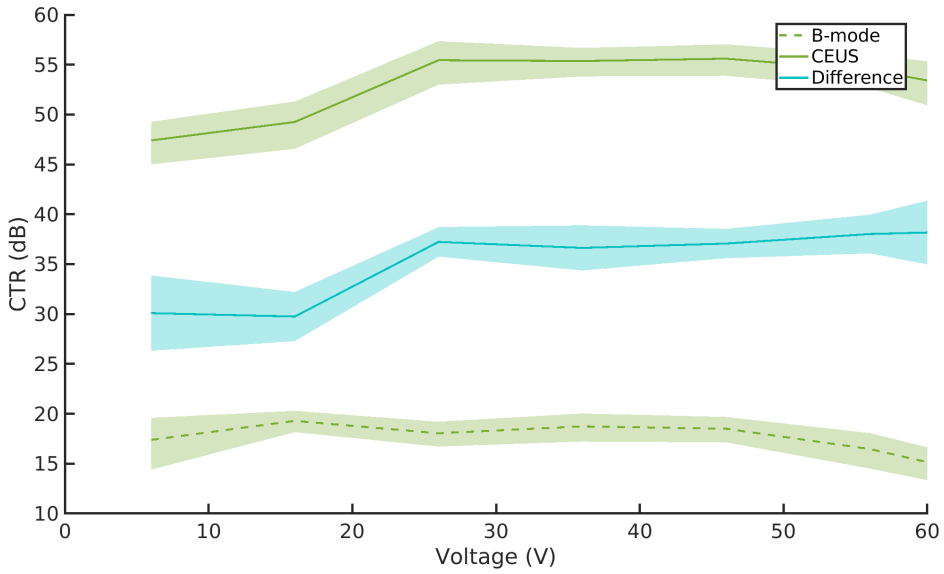

Figure 3.4: Variation in CTR of three-pulse AM images and B-mode images as the V_{AC} applied to a CMUT was varied. The figure is reprinted from Paper 5.

corresponding emitted PNP is plotted in Fig. 3.3.

As shown in eq. (3.15), the theoretic derivation of the combined received signals from the three-pulse AM sequence shows that the emitted harmonics does not hamper the cancellation of the linearly scattered signals. To validate this, in Paper 5, the CTR of the images collected with the CMUT are also plotted as a function of the applied V_{AC}, as shown in Fig. 3.4. Here, it is seen that the difference between the CTR of the CEUS images and the B-mode images does not decline as V_{AC} increases.

3.3 Discussion

The CTR of the acquired CEUS images shown in Fig. 3.1 and Fig. 3.3 demonstrate that the three-pulse AM sequence is superior to both the two-pulse AM and the PI sequence. While the PI sequence has resulted in a reduction in contrast, as compared with the CTR of the B-mode images, the two-pulse AM sequence achieves a minor improvement in contrast. In Fig. 3.3, the two-pulse AM sequence obtains an average of 9.1 dB improvement in the CTR across the applied voltages, compared with the B-mode. On the other hand, the three-pulse AM sequence achieves an improvement of 35.3 dB, and is clearly the preferable minor sequence when using a CMUT for CEUS imaging. However, this introduces a third emission in the minor sequence, which in turn decreases the frame rate. This is an inconvenience for SRUI, which is restricted by a long acquisition time. Yet, the increase in contrast attained with the three-pulse AM sequence outweighs this drawback, as contrast enhancement and removal of the signal scattered by the tissue is a key component of making *in vivo* imaging of microbubbles possible. The difference in performance of the two-pulse and three-pulse AM sequence can be explained by the choice of transmitting elements used to compose the images. When using only two emissions in the minor AM sequence, the signals which are subtracted in eq. (2.13) are transmitted on only some of the elements in each sub-aperture. When using three emissions, the signals which are subtracted in eq. (3.7) are in total transmitted on all elements in each sub-aperture. For two-pulse AM this means that the first emission and the subtracted emission do not contain the same transmitting elements, and this can result in poor cancellation of the

linear components in the received signal, if the performance of the emitting elements are not perfectly similar. On the other hand, any differences in the performance of the emitting elements will not affect the cancellation of linear terms for the three-pulse AM sequence, because the signals transmitted on all elements are subtracted from the signal transmitted on the same elements.

The reason why three-pulse AM imaging with as CMUT is superior to PI is because its contrast enhancement is unaffected by the emission of harmonics from the transducer. This has been shown both in eq. (3.15), as previously discussed, and in Fig. 3.4. Here, the difference between the CTR of the CEUS images and the B-mode images does not decline as the V_{AC} increases, despite the increase in emitted harmonic content this leads to (Novell et al. 2008). This happens regardless of the decline in the CTR of the three-pulse AM images, which is caused by a decrease in the scattered power from the microbubbles, due to rupturing, diffusion, or fragmentation (Chomas et al. 2001; P. Dayton et al. 1999; Thomas et al. 2012).

Moreover, comparison of the CTR of the three-pulse AM images acquired with the CMUT and the PZT transducer show a comparable performance. In the region in Fig. 3.3 where both transducers produce the same PNP, the difference between the CTR of the tree-pulse AM images and the B-mode images is 49.9 dB for the PZT transducer and 37.4 dB for the CMUT. As discussed in Paper 6, the difference in contrast enhancement between the two probes could be attributed to the CMUT's lower SNR. This is likely caused by insufficient shielding. The production of the CMUT probe is described in Chapter 8 of Diederichsen (2020), where the probe is referred to as Tabla VI. The production of the probe is part of a research project on probe assembly, and it is therefore not expected that the performance of the probe is comparable to commercial grade probes, such as the PZT transducer used in Paper 5. Diederichsen (2020) explains that an aluminized polymer foil is included in the transducer to provide electromagnetic shielding. The thickness of the foil was chosen as a compromise between the acoustic performance of the probe and the shielding ability of the foil.

The variation of CTR in Fig. 3.3 also indicates the optimal pressure to use for SRUI. The back-scattering ability of microbubbles is dependent on the incident pressure, and affects both the amplitude and the spectral content of the signal received by the ultrasound probe (Marmottant et al. 2005). When interpreting CTR it is important to keep in mind that when applied to B-mode images, the fraction seen in eq. (2.5) is comprised of the total scattered powers, whereas when eq. (2.5) is applied to CEUS images, only the components of the powers which remain after compounding the pulses of the minor sequence are included, and this will be dominated by nonlinear back-scattering from the microbubbles. Also, CTR is a ratio of two powers, therefore, when CTR increases with pressure this indicates that the rate at which P_B grows is higher than for P_T. Thus, the maximum observed CTR indicates at what incident pressure the nonlinear back-scattering from the microbubbles is high, while the annihilation of power from the tissue is also high. This can be seen in Fig. 3.3, where the CTR first increases with PNP, before decreasing at higher PNPs. At lower pressures, the increase in CTR is due to the increase in nonlinear response from the microbubbles with applied PNP (de Jong et al. 2009; Marmottant et al. 2005). At higher pressures the microbubbles are disrupted by the incident pressure (Chomas et al. 2001; P. Dayton et al. 1999; Thomas et al. 2012) and, as discussed in Paper 5, the annihilation of power is inhibited by nonlinear propagation in the image medium. Therefore, an optimal pressure for SRUI excists, and in Fig. 3.3 this occurs between 100 kPa to 200 kPa. This corresponds to a mechanical index of 0.01 to 0.05, which is within the range suggested for CEUS by M. X. Tang et al. (2011).

The findings of Paper 4 and Paper 5 show that CEUS imaging with a CMUT is possible, despite the nonlinear emission from the transducer, if the appropriate minor sequence is chosen. This further reinforces that using CMUT technology of volumetric SRUI imaging is appropriate. Seemingly, the only notable drawback found in Paper 5 is the SNR of the transducer. Having a high SNR is a vital for SRUI, because fewer bubbles can be localized if the noise level is high (Christensen-Jeffries et al. 2020). Therefore, when designing a CMUT RCA for volumetric SRUI, care should be taken to design adequate noise shielding.

CHAPTER 4

Imaging using row-column addressed arrays

This chapter introduces beamforming using RCAs and presents beamformed PSFs to validate the author's implementation of the beamforming theory. The chapter also goes through the conditions of the physical RCAs which were available for study during the development of this PhD thesis.

In the past decades, using RCAs for volumetric ultrasound imaging has emerged as a viable alternative to the more conventional 2D arrays, such as fully populated matrix arrays and sparse matrix arrays (Christiansen et al. 2015; Démoré et al. 2009; Morton and Lockwood 2003; Rasmussen et al. 2015; Sampaleanu et al. 2014; Yen et al. 2009). Volumetric imaging offers the clinician access to more information at a single time instance, and when applied to SRUI, it solves some fundamental issues posed by the technique, namely inaccurate positioning, and out-of-plane movement of the microbubbles and tissue. However, to successfully use an RCA for SRUI, it is vital that the collected frames have been beamformed correctly. Beamforming RF channel data acquired using an RCA requires careful consideration of the transducer geometry. In conventional DAS beamforming for 2D imaging, the transmitting and receiving elements are commonly though of as point-sources when calculating the TOF used in eq. (1.1). However, Rasmussen et al. (2015) showed that this introduces significant phase errors for RCAs, which in turn will lead to geometrical distortion of the beamformed image. Instead, Rasmussen et al. (2015) suggests that the emissions from a row or column element should be thought of as a line source. This means that the emitted wave is cylindrical, and as illustrated in Fig. 4.1, it appears as a plane wave in the plane laying along the emitting element and as a circle in the plane orthogonal to the element. In Fig. 4.1, the emitting element is referred to as a column element, and throughout this thesis the relationship between the element geometry and the coordinate system is defined as:

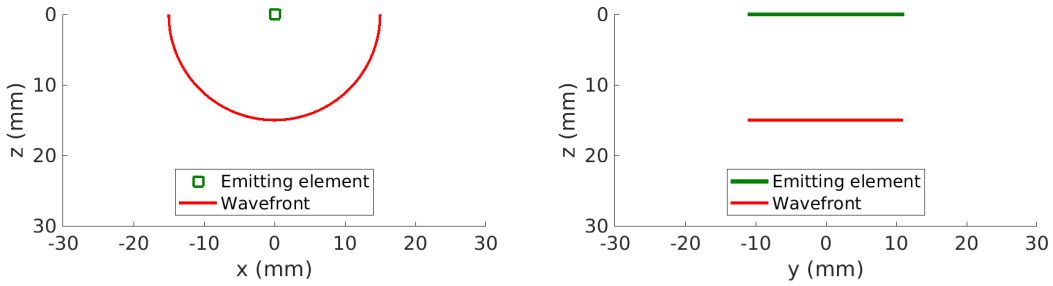

(a) (b)

Figure 4.1: Illustrations of the shape of the emitted wavefront from a column element, (a) in a plane orthogonal to the emitting element and (b) in the plane along the emitting element.

Definition 4.1: A column is an emitting element, and the length of the column lays along the y-axis.

Definition 4.2: A row is a receiving element, and the length of the row lays along the x-axis.

Correct implementation of this geometry in the calculation of τ will be especially important when a diverging lens is added in front of the RCA, which will be the topic of Chapter 6 and 7.

Rasmussen et al. (2015) presents a method for calculating τ for a sequence with focused emissions. In Section 4.1, the technique for calculating τ using the geometry suggested by Rasmussen et al. (2015) is described for defocused emission and dynamic receive focusing. In Chapter 7, this geometry and methodology will be expanded on to describe the calculation of the transmit TOF for a lensed RCA. Therefore, to first validate that the geometry of an unlensed RCA has been implemented correctly, the theory is used to beamform an example PSF in Section 4.2.

4.1 Theory: Beamforming using a row-column array

The basic principle of DAS beamforming, introduced in Chapter 1, is also applied when beamforming RF signals produced by an RCA. Since the elements are elongated, when using a SA sequence the VS is a line. Following the methodology presented by Rasmussen et al. (2015), for an defocused emission, the transmit DOF is found using the shortest distance between the VS line and the image voxel. Fig. 4.2(a) illustrates the distance between a VS line and an image point, and this distance is referred to as $d_{\text{VS}\to\mathbf{P}}$. The VS line is defined by the points **A** and **B** and lays at $z = z_{vs}$. The shortest distance between this line and the image point, **P** is

$$d_{\text{VS}\to\mathbf{P}} = \frac{\|(\mathbf{A}-\mathbf{B})\times(\mathbf{B}-\mathbf{P})\|}{\|\mathbf{A}-\mathbf{B}\|}, \tag{4.1}$$

where $\times$ denotes the cross-product, and $\|\ \|$ denotes the Euclidean norm (Rasmussen et al. 2015; Stuart et al. 2019). The DOF used to calculate the TOF is thus

$$\text{DOF}_{\text{tx}} = d_{\text{VS}\to\mathbf{P}} - z_{vs}. \tag{4.2}$$

When receiving the sound on the RCA, the same principle is applied; the DOF is given by the shortest distance between the image point and the mid-line in the receiving element. This line is defined by its end-points, **C** and **D**, as shown in Fig. 4.2(b), and the DOF is given by

$$\text{DOF}_{\text{rc}} = \frac{\|(\mathbf{C}-\mathbf{D})\times(\mathbf{D}-\mathbf{P})\|}{\|(\mathbf{C}-\mathbf{D})\|}. \tag{4.3}$$

Thus, eq. (1.2) can be applied to give the total TOF, and eq. (1.1) can be used to beamform the image pixel.

4.2 Simulation: Beamforming a PSF using a row-column array

The derivation of τ, presented in Section 4.1, was implemented in MATLAB® so that RF channel data from an RCA can be beamformed. This implementation is made to validate the interpretation of the beamforming theory presented by Rasmussen et al. (2015), and is an important initial step towards calculating the TOF from a lensed RCA, which will be further discussed in Chapter 6 and 7.

4.2.1 Simulating RF data

The RF data channel received on the 62 + 62 element RCA were simulated using Field II (Jensen 1996). Details on the transducer are given in Table 4.1. The single element SA sequence with 62 emissions

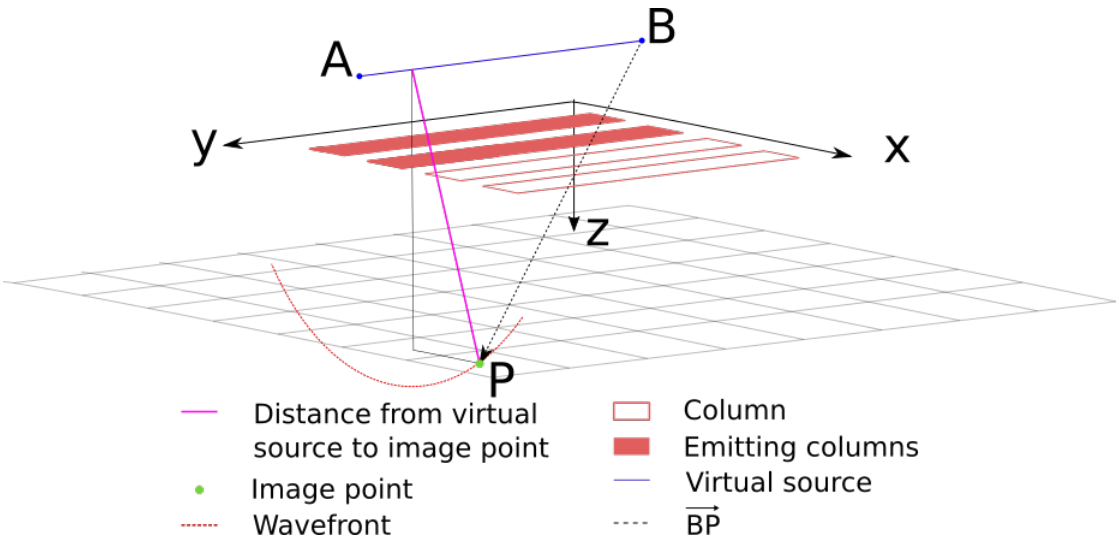

(a) Illustration of the shortest distance between the VS line and the image point, **P**. The end-points on the VS line are given by **A** and **B**, and the vector between **B** and **P** is illustrated as a dotted line.

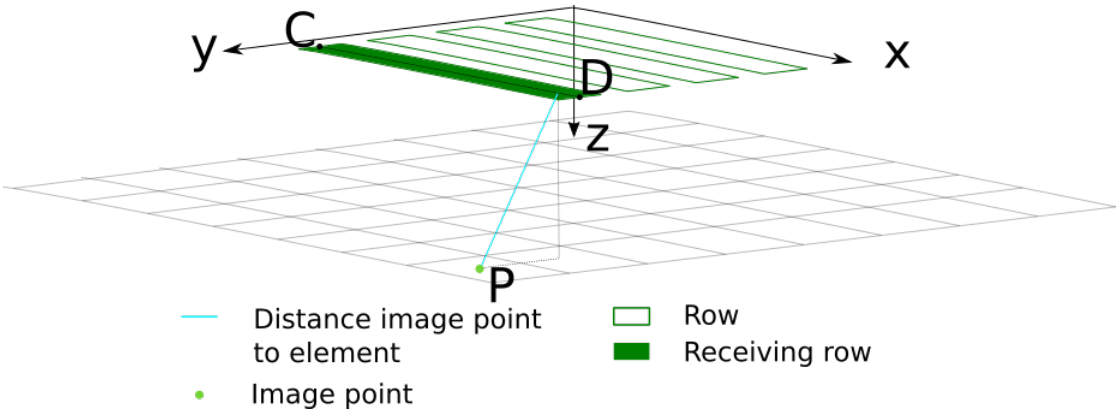

(b) Illustration of the shortest distance between the image point and the receiving column element.

Figure 4.2

proposed by Bouzari et al. (2019) was implemented. Each emission utilizes one transmitting column element, and no transmit delay is applied. The sequence slid across the transducer, so that each element emitted once. A scatterer was placed at $(x,\, y,\, z) = (0,\, 0,\, 20\,\mathrm{mm})$ and for each transmission from a VS, the resulting RF data received on all row elements was simulated.

4.2.2 Beamformation

The simulated RF data was beamformed using scripts implemented both by the author and by Rasmussen et al. (2015), with their permission. To implement the beamformation script, the theory presented in Section 4.1 was used to calculate the TOF to and from all points in two $4\,\mathrm{mm} \times 12\,\mathrm{mm}$ image grids around the scatterer, placed both along the x- and along the y-axis. For each transmission, eq. (1.1) gave the

pixel intensity of each image point in the LRI. To calculate the weights used in eq. (1.1), the dynamic apodization scheme proposed by Stuart et al. (2019) was implemented with a receive F-number of 1 and Hanning window weights. Finally, the beamformed LRI were combined to form the HRI, according to eq. (1.6), and a Hilbert transform was used to find the envelope. The same image points and apodization scheme was used when beamforming the RF data using the script by Rasmussen et al. (2015).

4.2.3 Results: PSFs

The beamformed images of the point-scatterer are shown in Fig. 4.3. The FWHM of these PSFs have been calculated using Definition 2.1, and were found to be 0.86 mm in the x-z plane and 1.35 mm in the y-z plane. The FWHM was identical for Fig. 4.3(a) and Fig. 4.3(c), as well as for Fig. 4.3(b) and Fig. 4.3(d), and visually the plots confirm that the two beamforming implementations have produced the same result. As seen in 4.3(b), as expected, the weighting applied in the dynamic receive apodization scheme has increased the width of the main lobe (Szabo 2004) and decreased the energy in the side-lobes. And since apodization weights have not been applied to the transmit events this has resulted in an anisotropic PSF and significant side-lobes in the x-z plane. These side-lobes stem from edge-waves off of the transmitting array (Szabo 2014) and could have been reduced by applying a synthetic apodization weight to each LRI before summation to a HRI (Schou 2020). The FWHM predicted by the theoretical estimate in eq. (2.4) was 0.71 mm for this transducer and sequence. This is lower than the FWHMs of the simulated PSFs because the equation does not account for the effect of apodization weights or variation in the spatial impulse response on the size of the PSF.

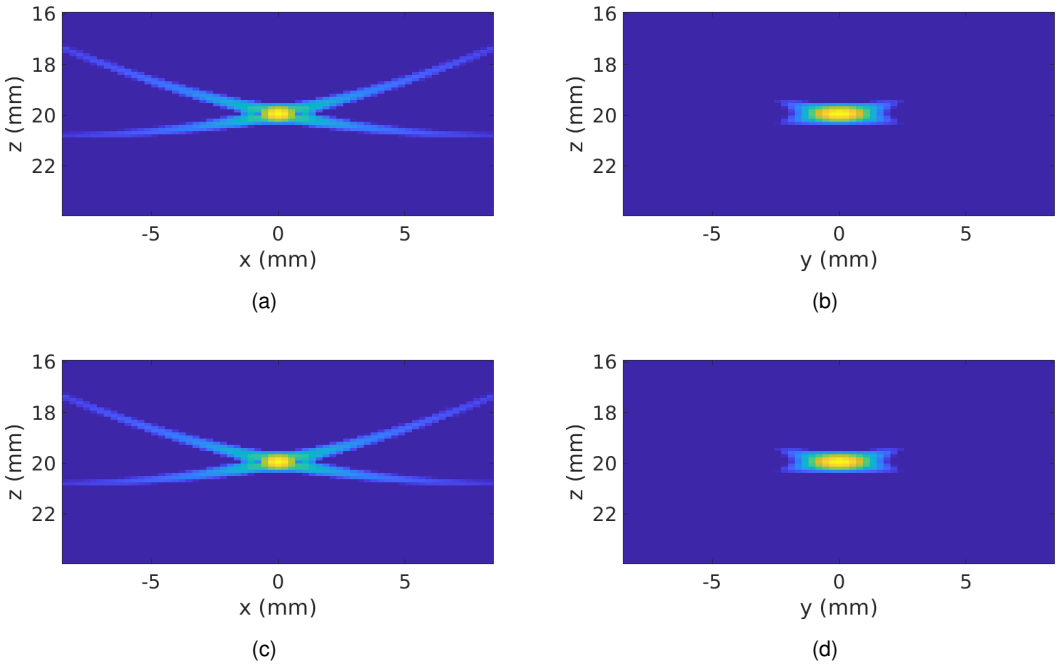

Figure 4.3: Simulated PSFs of the unlensed 62 + 62 element RCA, using a single column transmission SA sequence. Fig. (a) and (b) are beamformed using the author's implementation, while Fig. (c) and (d) have been beamformed using the implementation by Rasmussen et al. (2015).

4.3 Using prototype RCAs

Several RCAs have been used for simulations and measurements through the development of this thesis. In Table 4.1, the dimensions and defining parameters of the RCA are presented for those transducers which have been used to produce results presented in this thesis.

Number of elements	62 + 62	62 + 62	94 + 94	128 + 128
Technology	PZT	CMUT	CMUT	PZT
Center frequency	3 MHz	3 MHz	4.5 MHz	6 MHz
Kerf	25 µm	25 µm	5 µm	20 µm
Pitch	270 µm	270 µm	180 µm	200 µm
Length of physical apodization region	4.05 mm	4.05 mm	2.7 mm	None
Element length	24.84 mm	24.84 mm	22.315 mm	25.6 mm

Table 4.1: Geometry and defining parameters for the RCAs used to produce the results presented in this thesis. Throughout the thesis, the RCAs are referred to by their respective number of elements and technology type.

Part of the challenge of studying super-resolution imaging using RCAs lays inherent in the transducer hardware itself; during this PhD all of the available transducers were prototypes. Therefore, in addition to researching the theory and algorithms needed to create 3D super-resolved images, some issues caused by the manufacturing of the hardware itself have also been met. The fabrication of RCAs is complex and the techniques lay at the current forefront of science (Grass et al. 2019; Grass et al. 2020; Havreland et al. 2019a) Therefore, mass-production of RCAs has not yet occurred, and during this study, the supply of fully functional arrays has been limited. Moreover, unexpected faults in the available RCAs has been uncovered throughout their usage, and to some extent correctly identifying these problems has been a study in itself. Four prototype RCAs were attempted used in this PhD, and here follows a brief summary of some of the issues which were encountered.

The 62 + 62 PZT RCA, used by the author in Paper 2 and Paper 3, was manufactured in 2015 and characterized in its original state by Engholm et al. (2018b). And, as expected, its functionality has declined over time. In Fig. 4.4 the RF signals captured on both row and column elements from a single emission onto a wire phantom is shown in two versions. Fig. 4.4(a) and (b) are captured in May 2019 and 4.4(c) and (d) are captured in August 2019. Vertical lines in the images indicate that an element is not correctly receiving the incoming signal, and the number of malfunctioning elements drastically increases from May to August. Moreover, hydrophone recording of the transmitted signal from the array revealed another debilitating defect; when emission from a constant VS was repeated, the power of the signal received on a hydrophone placed beneath the transducer varied dramatically at a seemingly random pace. The cause of this issue is not known. The variation makes the transducer unsuitable for CEUS imaging, which relies on consecutive emissions having scalable output.

A prototype 62 + 62 CMUT RCA (Christiansen et al. 2015) was also available for testing. The transducer was used to procure the needed hardware, such as DC power supplies and appropriate adapters, for using a CMUT RCA with the synthetic aperture real-time ultrasound system (SARUS) (Jensen et al. 2013). However, using the transducer to produce SRU images proved challenging, as the transducer is excessively susceptible to picking up electromagnetic noise from external sources. To uncover this issue, the SARUS was programmed to receive signal from the transducer while it was not emitting any power. Fig. 4.5 shows an example of the resulting data while the transducer was held next to a flow pump which was running. Significant noise spikes can be seen in the data, and, unfortunately, such noise was

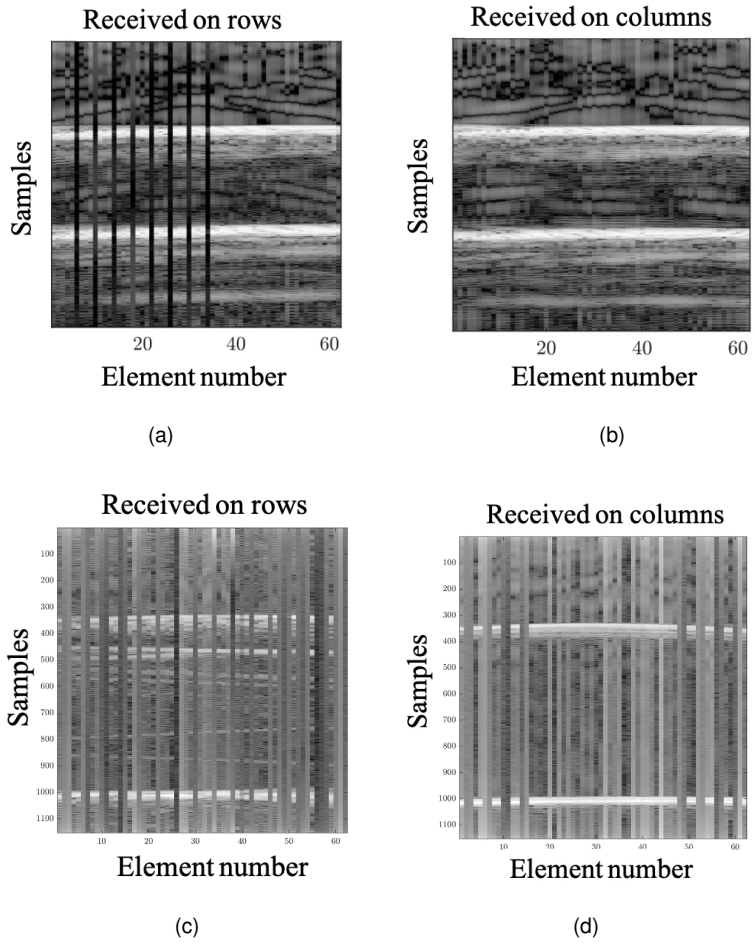

Figure 4.4: RF signal received on all elements from a single emission onto a wire phantom with two wires. Fig. (a) and (b) were captured in May 2019, while Fig. (c) and (d) were captured in August 2019. Re-printed from Jørgensen (2019), with permission.

detrimental to the transducers SNR, rendering it unfit for further use.

The susceptibility of a transducer to include noise on the recorded signal can limit its applicability to SRUI. The SNR affects the precision of localization of microbubbles, and, therefore also the ultimate resolution of the SRU images the probe can produce. Both the 62 + 62 CMUT RCA and the linear CMUT used in Paper 2 and Paper 3 have been shown to suffer from noise pick-up. In the case of the linear CMUT this was shown by measurement and calculation of its SNR in Paper 3. Generally, CMUTs are slightly more prone to noise than PZT transducers due to the particularities of their design. CMUTs commonly have a pre-amplifier inside its transducer body (Engholm et al. 2015). It is placed here to reduce effects of parasitic capacitance on the cable between the receiving elements and the pre-amplifier (Bhuyan et al. 2013). This means that if electromagnetic inference noise is picked up by the receivers, it will be magnified more in a CMUT than in a PZT transducer. The receive circuitry is protected from input inference noise by shielding around the transducer, but, as previously mentioned, the thickness of the shielding foil in front of the active aperture introduces a trade-off between the effectiveness of the shielding and its acoustic

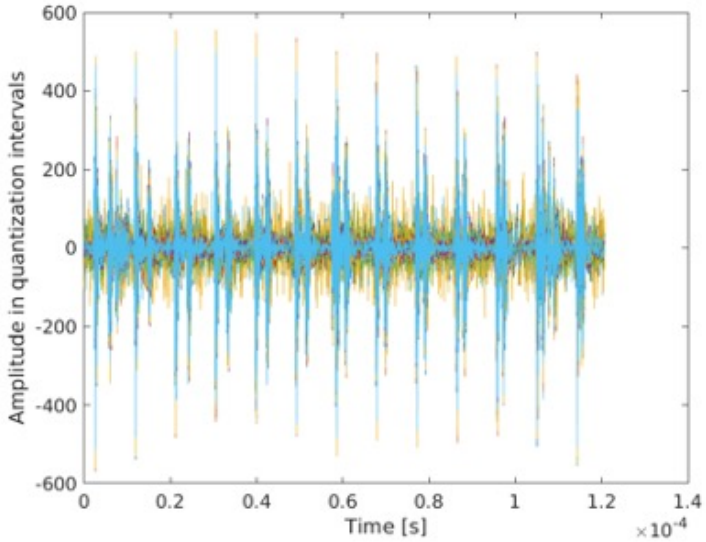

Figure 4.5: The RF data received on the 62 + 62 element CMUT RCA while it was not emitting any power. Spikes in the data are cause by noise pick-up from a nearby flow pump.

transparency (Diederichsen 2020). Moreover, the CMUTs used in this study were all designed and built as part of university research (Christiansen 2015; Diederichsen 2020; Engholm 2018), and it is therefore not expected that their noise performance is comparable to those of commercially developed transducers.

A flat 94 + 94 CMUT RCAs was produced in the development of the lensed RCA presented by Engholm et al. (2018). The bottom electrode of these transducers are known to suffer from high resistivity along the elements (Havreland et al. 2019b), and can therefore not be used for pulse-echo imaging. Yet, not all hardware faults make the transducer completely unusable. The top electrode of the transducers have adequate resistivity and the transducer was thus used to study the transmitted field from lensed RCAs, discussed in Section 7.4.2.

Finally, a commercially produced 128 + 128 PZT RCA became available for study at the end of this PhD project. It does not have any integrated apodization on the elements, and according to Rasmussen et al. (2015), without integrated apodization, the transducer will suffer from edge effects. Even so, the transducer was the only available RCA with pulse-echo capacity, and it was therefore used during the study of transmission through a lensed RCAs in Chapter 7, in the hopes that this work will in the future be developed to also include refraction though the lens while receiving.

CHAPTER 5

3D super-resolution ultrasound imaging

This chapter presents 3D SRUI of a 3D printed microflow phantom, based in Paper 2 and Paper 3. The chapter discusses validation of the SRU images using the known dimensions of the phantom, as well as the definition of super-resolution.

3D volumetric imaging is a welcome improvement of SRUI, and as discussed in Chapter 1, the volumetric imaging addresses some of the main limitations of SRUI, such as out-of plane motion, 3D bubble tracking, and the slice thickness caused by the elevation focus. Volumetric visualization of SRU images was first achieved by Lin et al. (2017) and Zhu et al. (2019) by mechanically translating a 1D array across the imaged volume. Although this approach produces volumetric information about the imaged vasculature, the images still suffer from the aforementioned limitations, since the volume is stitched together from many 2D images. Christensen-Jeffries et al. (2017) created 3D SRU images using a pair of orthogonal 1D arrays. This was one of the first demonstrations of 3D SRUI, before the publication of Paper 2 (Jensen et al. 2019), where volumetric SRUI of a microflow phantom was presented. Since, volumetric SRUI has been demonstrated using a fully populated matrix array (Heiles et al. 2019) and a sparse matrix array (Harput et al. 2020), both presenting images of phantoms. And Chavignon et al. (2020) presented 3D *in vivo* ULM images of a rat brain, using a multiplexed matrix array, but did not discuss weather these images were super-resolved.

Chavignon et al. (2020) attempted to validate the imaged structures by comparing the ULM images with high resolution micro-computed tomography images of the rat brain. Although visual inspection of the images reveal similarities, quantitative validation could not be achieved. Similarly, several of the authors who presented SRUI of flow phantoms used merely estimates of the internal dimensions of the phantom in an attempt to validate the performances of their SRU imaging (Christensen-Jeffries et al. 2017; Harput et al. 2020; Heiles et al. 2019). Currently, Paper 2 and Paper 3 are the only demonstrations of 3D SRUI where true knowledge of the grown-truth of the imaged structure is known. This was achieved by using a 3D printed micro-flow phantom. Using a 3D printed microflow phantom enables quantitative validation of the SRUI, because both the inner dimensions of the imaged vasculature and its precise location is known. This is not attainable with other commonly used methods, such as cellulose tubes (Christensen-Jeffries et al. 2017) and chicken embryos (Huang et al. 2019). As was specified in Section 1.4, the author's contributions to Paper 2 and Paper 3 was the development of the experimental set-up using the 3D printed phantom, and this will therefore be the focus in this chapter.

5.1 3D super-resolution imaging of a microflow phantom

This section is based on Paper 2 and Paper 3, which demonstrated 3D SRUI using a 62 + 62 element PZT RCA. The probe was used to image a 3D printed microflow phantom, which was designed and manufactured explicitly for the purpose of 3D SRUI by Ommen (2020). The method used to produce and validate the 3D SRU images are outlined in Section 5.1.1. The resulting SRU images and their quantitative

validation are presented in Section 5.1.2, before the results are discussed in Section 5.1.3. Here, further work on the design of 3D printed microflow phantoms for validation of SRUI is also discussed.

5.1.1 Methods: 3D super-resolution imaging

To demonstrate SRUI in 3D, first, a functional phantom set-up had to be designed. A flow phantom was 3D printed using stereolithography (Ommen et al. 2018), similarly to the phantom used in Paper 5. The microflow phantom, seen in Fig. 5.1(a), was designed to have an internal flow channel which bends twice to give an internal 3D vessel structure. The internal dimensions of the phantom are given in Fig. 5.1(b). The phantom was placed in a water bath and fastened on top of an acoustically absorbing mat using a brace. The inlet of the phantom was connected with a flow pump which pumped a flow of SonoVue microbubbles diluted 1:10 with NaCl solution into the phantom. The 62 + 62 element RCA was fastened directly above the phantom. The dimensions of the probe are given in Table 4.1 in Chapter 4.

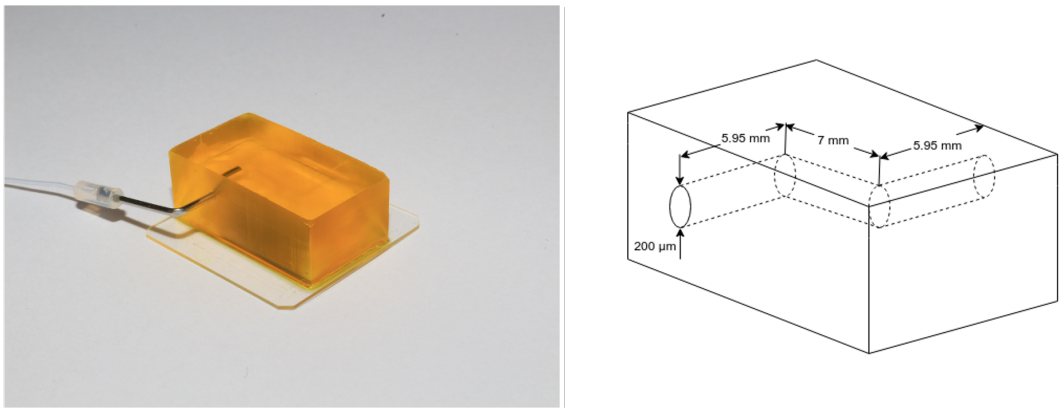

(a) (b)

Figure 5.1: Photo (a) and illustration (b) of the microflow phantom.

Care was taken to decide an appropriate flow rate for the measurement set-up, because trial and error indicated that at some flow rates an adequate number of microbubbles did not survive the journey from the infusion pump to the phantom. This has also been reported by Talu et al. (2008) and Barrack and Stride (2009). To investigate how the flow rate settings affected the bubbles a digital microscope (Q-Scope QS.80200-P) was used to visually inspect the microbubbles as they were pumped out of the flow pump, and as they were pumped out of the tube connecting the flow pump to the phantom. Fig. 5.2 shows an example of a microscope photo of the microbubbles after they have been pumped out of the flow pump without significant destruction. Based on trial and error, the flow rate was set to $1.6\,\mu\mathrm{L\,s^{-1}}$.

The set-up was imaged using a SA sequence designed to optimize the B-mode performance of the 62 + 62 RCA by Schou (2020). The sequence contained 32 VSs, each using 32 active elements, and emitting diverging waves with a F-number = -1. A Hanning window weighting was applied to the active elements to reduce side-lobes. To create CEUS images, a PI minor sequence with two emissions, as specified in eq. (2.16) and eq. (2.17), was emitted by each VS. Each emission was a two-cycle sinusoid with a $f_0 = 3\,\mathrm{MHz}$ center frequency. The pulse repetition frequency was $f_{\mathrm{prf}} = 10\,\mathrm{kHz}$ and a 10 ms pause was inserted between each major sequence to prolong the acquisition time to enable perfusion in the entire phantom.

The RCA was connected to the SARUS research scanner and used to acquire 400 frames. First, the acquisitions in each minor sequence were added according to eq. (2.22), and then the resulting signals were beamformed (Rasmussen et al. 2015) and summed to form CEUS images. ULM was performed by

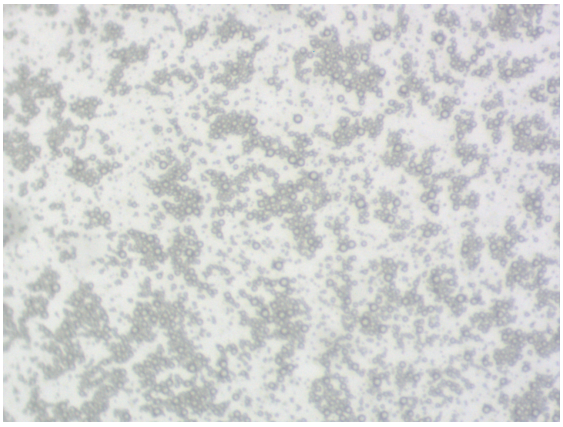

Figure 5.2: Example of a microscope photo of diluted SonoVue microbubble having been successfully expelled from the flow pump, without significant destruction of the microbubbles.

localizing and accumulating all microbubble positions in all images. Localization was achieved by fitting a second-order polynomial to the data in each image and localizing the peak position in the interpolated result.

5.1.2 Results

The localized microbubble positions accumulated over all collected images are plotted in Fig. 5.3. As seen, the localized microbubble positions clearly follow the shape of the internal channel in the microflow phantom. The microbubbles have been localized in three dimensions, thus confirming that ULM in 3D is attainable with an RCA.

Further quantification of the localization accuracy based on the known internal dimensions of the flow phantom, as well as the size of the PSF of the image set-up, was performed by Jensen et al. (2020), but this theory lays beyond the scope of this thesis. It was found that the FWHM of the PSF was ($FWHM_x$, $FWHM_y$, $FWHM_z$) = (0.58 mm, 1.05 mm, 0.31 mm), and that the precision of the microbubble localization was 15.4 µm in the y-z plane and 16.0 µm in the x-z plane. Based on this, Jensen et al. (2020) concluded that the image was super-resolved.

5.1.3 Discussion and further work

The imaging of microbubble flowing through the microflow phantom presented in Section 5.1.2 confirms that the ULM technique used for SRUI is attainable in 3D using an RCA. This confirmation marks the first step towards 3D *in vivo* SRUI using RCAs. However, although ULM, a commonly used technique for SRUI, has been employed, Fig. 5.3 does not necessarily show a super-resolved image. The definition of super-resolution has been subject to some discussion, which is a natural consequence of the fact that SRUI is a rather new and rapidly evolving technique. Jensen et al. (2020) concludes that Fig. 5.3 is super-resolved because the estimated localization precision is lower than the size of the PSF. Similarly, other authors have also concluded that their images are super-resolved because the spatial resolution of the SRUI image is smaller than the diffraction limit (Chen et al. 2020; Lowerison et al. 2020). However, as pointed out by Hingot et al. (2021), since SRU images are not beamformed images, but rather collections of microbubble localization positions or tracks, looking at the resolution of the resulting SRU image does not necessarily indicate the clarity of the image. For instance, a SRU image might have high localization precision of the microbubble, and thus technically a high resolution, yet errors in the data acquisition, such as motion, might adversely affect the accuracy of the localization. In turn, this might make it impossible

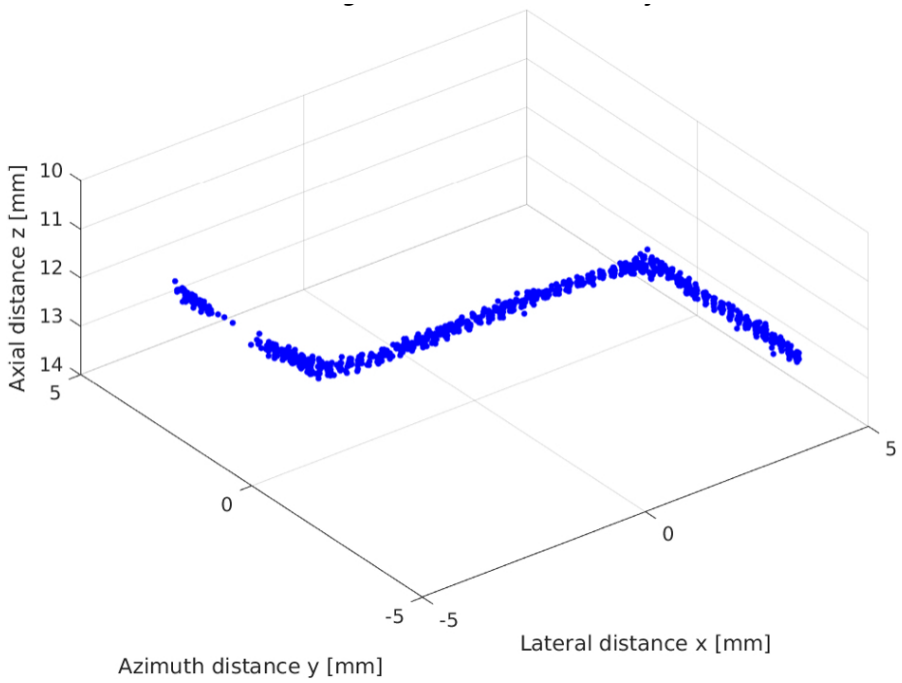

Figure 5.3: 3D plot of all localized microbubble positions inside the microflow phantom. The figure is modified from Paper 3 (Jensen et al. 2020).

to distinguish two microvessels laying further apart than the resolution. Therefore, in their review on SRUI, Christensen-Jeffries et al. (2020) defined super-resolution as the capacity to distinguish two imaged objects beyond the diffraction limit. Other authors have tried to quantify this definition by employing auto-correlation (Descloux et al. 2019) and Fourier-ring correlation (Banterle et al. 2013). Because there are not two objects laying closer than the diffraction limit in the micro-channel phantom used to create Fig. 5.3, one cannot conclude that it is super-resolved, following the definition by Christensen-Jeffries et al. (2020). This is not to say that super-resolution cannot be achieved with the technique used by Jensen et al. (2020), but rather that it has in this case not been demonstrated. Having said this, the fact that the known design of the flow channel is so clearly recognizable in Fig. 5.3 and the fact that the quantified localization precision is an order of magnitude smaller than the size of the PSF indicates that had the method been applied to a structure with flow channels laying closer than the diffraction limit, super-resolution would have been achieved.

Therefore, the construction of the microflow phantom was further developed to include a design where super-resolution could be demonstrated, and where the limit of the attainable resolution could be quantified. The architecture of the phantom was designed by the author in collaboration with Schou (2020), and the design was implemented and manufactured by Ommen (2020). The design includes three "V"-shaped flow channels positioned in three orthogonal planes, and is therefore referred to as the 3V-phantom. Illustrations of the inner structure of the phantom are given in Fig. 5.4. Three "V"-shapes have been included in order to quantify resolution in all three dimensions, since the resolution of RCA imaging can be anisotropic (Schou 2020). In each of the planes, the three "V"-shapes initially have a maximum separation of 270 µm, and moving along the shape the separation decreases before reaching the vertex. At the vertex the minimum separation between the two channels in the "V"-shape is 10.8 µm. Comparably, using the center frequency of the 62 + 62 element PZT RCA, the diffraction limit is

$$\frac{\lambda}{2} = \frac{1}{2}\frac{c_w}{f_0} = \frac{1}{2}\frac{1480\,\mathrm{m\,s^{-1}}}{3\,\mathrm{MHz}} = 246.7\,\mu\mathrm{m}. \tag{5.1}$$

Thus, if SRUI is performed on the 3V-phantom using the 62 + 62 element PZT RCA at some point along the "V"-shapes the diffraction limit will be reached, and super-resolution can be demonstrated. Moreover, since the distance between the two channels in the "V"-shapes vary, the improvement in resolution of the SRUI technique, compared with conventional imaging, can be quantified. Unfortunately, due to the hardware limitations specified in Section 4.3, SRUI of the 3V-phantom has not been achieved at the current time.

The success of the development of a clinical application for 3D SRUI relies on effective ways of validating that the SRU images portray the microvasculature authentically. The development of the 3D printed microflow phantom is an important step towards creating a validation method. Knowledge of the inner dimensions of the phantom, together with the fact that the channels can be placed closer than the diffraction limit, makes it possible to produce truly super-resolved SRUI images and validate that the images truly portray the imaged structure. Lack of ground-truth is a limitation in many current publications on SRUI, and this poses a major question on reliability before SRUI, either in 2D or 3D, can be used clinically. This issue is addressed with the use of 3D printed microflow phantoms and the experimental set-up designed for Paper 3. As seen in Fig. 5.3 there is good concurrence between the structure in the SRUI and the structure of the phantom shown in Fig. 5.1(b), demonstrating not only that 3D SRUI with an RCA is possible, but also that the resulting images are accurate.

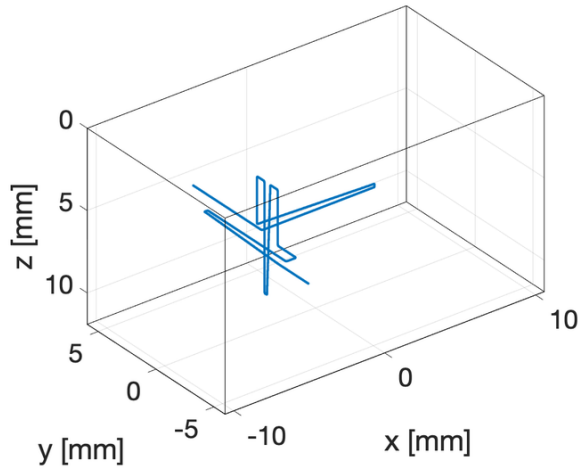

(a) Isometric view

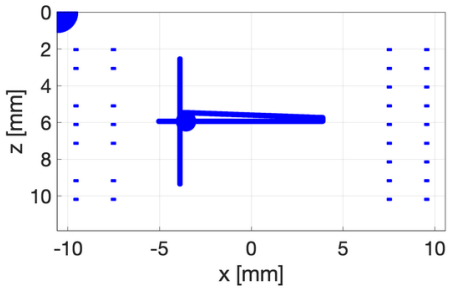

(b) x-z plane

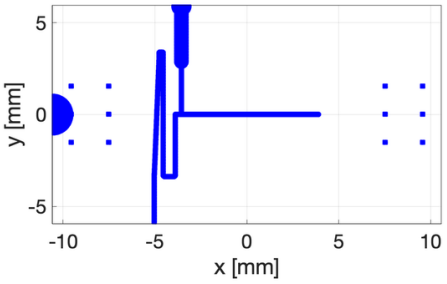

(c) x-y plane

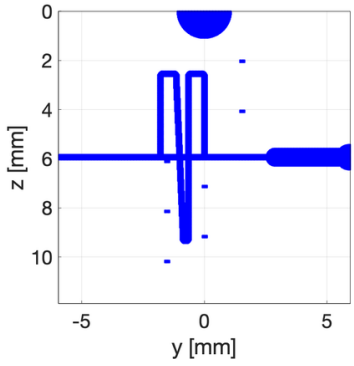

(d) y-z plane

Figure 5.4: Illustration of the inner flow channel in the 3V-phantom. The illustrations are made by Ommen (2020) and included here with permission.

CHAPTER 6

Lensed row-column arrays

This Chapter presents the concept of diverging lenses mounted on RCAs. The thin lens model, proposed by Bouzari et al. (2017a) to simplify the calculation of TOF from a lensed RCA, is described and implemented. The model is used to produce emitted fields and PSFs for a thin-lensed RCA. The Chapter is partly based on Paper 6.

Although RCAs offer a promising prospect for simplifying volumetric ultrasound imaging, the technology is limited by its usable FOV. The nature of the elongated elements in the transmit and receive arrays mean that the arrays can only steer the sound in one direction. For example, by applying a defocusing delay to the columns, the array illustrated in Fig. 6.1 can transmit sound to the red curved plane, which is limited in the y-dimension to the width of the array. Similarly, when sound is received on the rows, delay can be applied in the beamforming operation to focus sound received from image points laying on the green curved plane. This curved plane is limited in the x-direction by the width of the array. However, when the two arrays are used together to produce an image, it must be possible to both transmit sound to the image point and focus on the image point when receiving the sound. This is only attainable in the region where the two curved surfaces overlap. Therefore, the footprint of the volume that the array can image is limited to a square with sides equal to the width of the array.

Generally, two solutions have been proposed to overcome the problem of the limited FOV of RCAs: alteration to the geometry of the elements of the RCA and addition of a diverging lens to the transducer. Firstly, Démoré et al. (2009) proposed that the elements of the RCA could be curved, like the surface of a hemisphere, so that the emitted sound diverges in both directions. They simulated radiation patters from the double-curved transducer to show that its usable FOV was increased. A method for producing such an RCA was demonstrated by Ferin et al. (2018). They produced a double-curved RCA by bending a slab of partially deiced piezocomposite and bonding on flexible printed circuits. The characterization of the acoustic properties of the transducer showed promising results, but the production process was long and complex, and the authors questioned if the process was viable for commercialization. The second proposed solution is the addition of a diverging lens in front of the RCA, which was first introduced by Bouzari et al. (2016).

Adding a defocusing acoustic lens in front of a 2D array will spread out the sound and thus increase the FOV of the transducer. The spreading occurs because the sound is refracted as it travels across the boundary between the lens and the imaged medium, since the two have different sound speeds (Kinsler et al. 1982). When the sound travels from material A to material B, the amount of refraction which occurs is determined by Snell's law:

$$\frac{\sin\theta_i}{c_A} = \frac{\sin\theta_r}{c_B}. \tag{6.1}$$

Here, c_A and c_B are the speeds of sound in material A and B, respectively. θ_i is the incident angle at which the sound ray hits the interface, and θ_r is the refracted angle at which the sound leaves the interface. Both angles are taken in relation to the normal on the interface (Kinsler et al. 1982). As seen in Fig. 6.2, when a ray crosses a spherical boundary, the angles extend from the sound ray to a line at the intersection point which is collinear with the radius of the sphere.

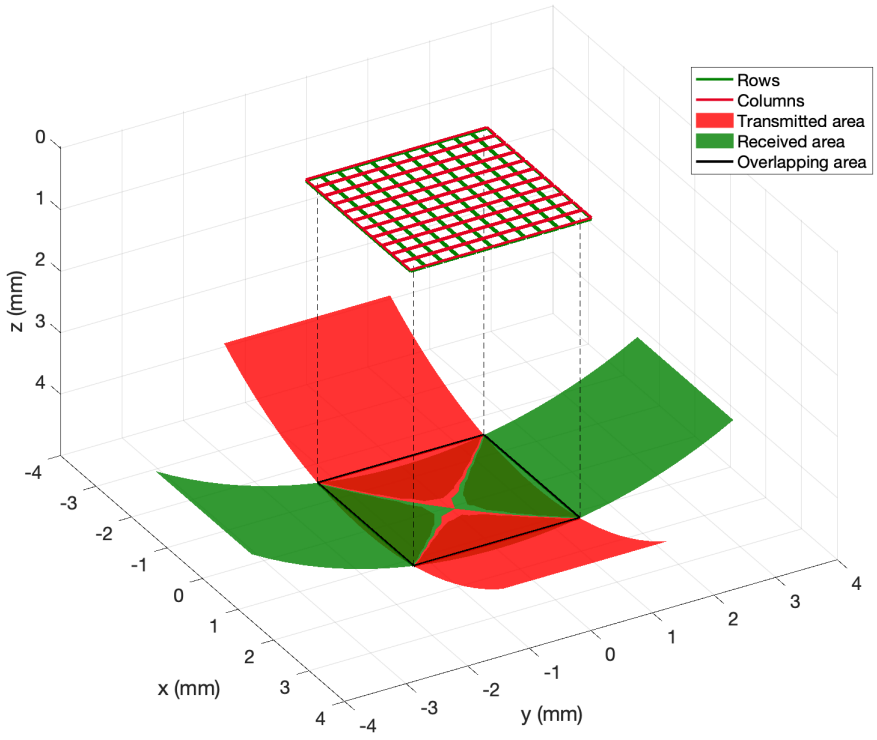

Figure 6.1: An illustration of the areas over which the two arrays in an RCA can steer the sound, and the limiting effect this has on the usable FOV.

The curved surface in acoustic lenses can be either concave or convex. To ensure that the emitted sound field is refracted outwards, rather than focused, the material of the lens should be chosen so that $c_A < c_B$ for a concave lens and $c_A > c_B$ for a convex lens. Bouzari et al. (2018) produced two concave lenses by casting a stainless steel ball partly submerged in RTV664 silicone. The larger of the two is henceforth referred to as *the concave RTV664 lens*, and will be used both in physical measurements and as a reference geometry in simulations throughout this study. The geometry of the lens is illustrated in Fig. 6.3 and its dimensions are given in Table 6.1.

A compound lens, described by Engholm et al. (2018) was also available for study. This lens is made of two materials, RTV664 silicone and Hapflex 541, and has thus a flat outer surface. It is thereby more suited for *in vivo* measurement on human skin, because it is easier to make good contact with the transducer on the surface than with a concave lens. However, the choice was made to study the concave lens, since refraction through two materials is more complex than refraction through just one. In the future, the theory presented in this thesis can be further expanded to also function for compound lenses.

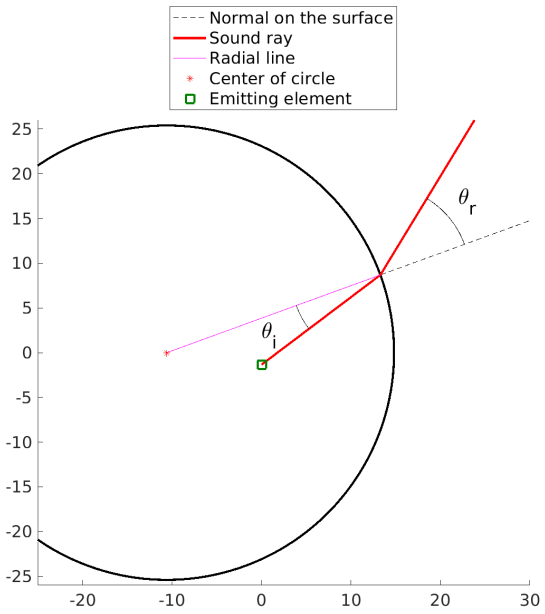

Figure 6.2: A drawing of a sound ray being refracted by a circular boundary. The angle of incidence and angle of refraction are in relation to the normal on the surface, which is collinear with the radial line of the circle.

Lens geometry	
Radius of curvature (R_L)	25.4 mm
Height (L_H)	5.57 mm
Thickness (L_T)	0.75 mm
Origo (x_0, y_0, z_0)	(0, 0, 26.15) mm
Chord radius (r_c)	15.87 mm

Table 6.1: The dimensions of the concave RTV664 lens (Bouzari et al. 2018).

As discussed in Section 1.2, to make beamformed images from data collected using a ultrasound transducer, one must first predict the TOF. This is complicated by the addition of a lens in front an RCA, because the sound paths are no longer straight lines. To overcome this issue, Bouzari et al. (2016 and 2017b) proposed a simplification of the sound path refraction, here referred to as the thin lens model. Bouzari et al. (2017b) assumes that the lens is infinitely thin and that the wavefronts are circular. Details on the theory and its implementation are given in Section 6.1. Theory on how the prediction of TOF using the thin lens model can be validated quantitatively is given in Section 6.1.1. Finally, thin lens model is applied by simulating a thin-lensed RCA and its implementation is validated by comparing the resulting emitted sound fields and PSFs with those of a flat RCA.

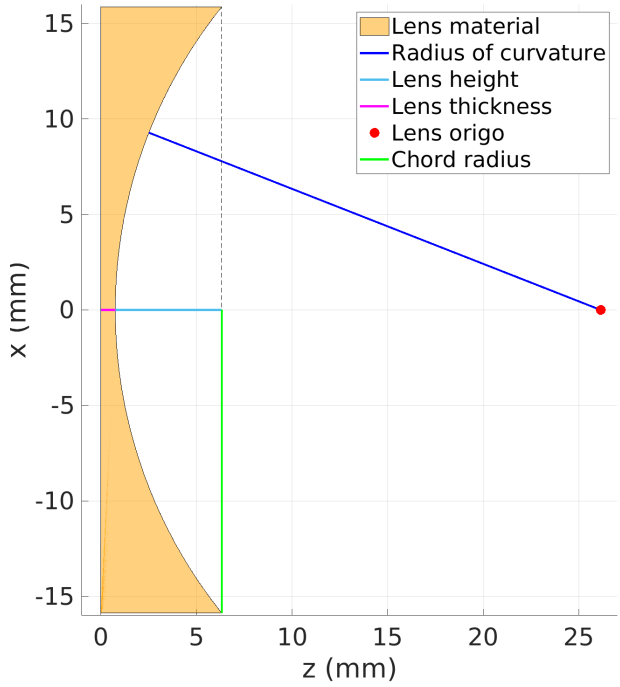

Figure 6.3: Illustration of the geometry of the concave RTV664 lens.

6.1 Theory: The thin lens model

The concept of infinitely thin lenses originates from optics and the use of this theory for ultrasound propagation through acoustic lenses was first explored by Ernst (1947). The thin lens model is based on the paraxial approximation, meaning that the incident and refracted angles are assumed to be small, so that

$$\theta_i \approx \sin\theta_i \tag{6.2}$$

holds true. This simplification makes it possible to define a single focal point for the lens, which is taken to be the center of the curved wavefronts emitted from the lens. For a concave lens, the focal point is given by

$$F_L = \frac{R_L}{1 - \frac{c_m}{c_L}}, \tag{6.3}$$

where R_L is the radius of curvature of the lens, c_m is the speed of sound in the image medium, and c_L is the speed of sound in the lens (Bouzari et al. 2018)[§]. In reality, when sound is emitted from elements laying on a straight line behind the lens, the refracted wavefront is curved, but, not circular (Carpena and Coronado 2006). Moreover, by assuming that the lens does not have any thickness, and error is introduced to the prediction of the TOF, since the speed of sound in the lens material is not taken into account.

[§] Bouzari et al. (2017a) and Bouzari et al. (2018) actually gives the bottom fraction in eq. (6.3) as $\frac{c_L}{c_m}$. However, for a concave lens with $c_L < c_m$, as is the case for the concave RTV664 lens used in the articles, this would produce a focusing wave, rather than defocusing. This is therefore taken to be a misprint, and eq. (6.3) is applied throughout this thesis.

Bouzari et al. (2017b) presents theory for predicting the TOF for an RCA with a diverging lens, according to the thin lens model. The theory is repeated in Section II B of Paper 6 and here, to ease the comprehension of the reader. According to the thin lens model, the elements of an RCA can be thought of as curved lines from point **a** to **b**, in this case laying parallel to the y-axis, according to Definition 4.1. The center of the curve is $\mathbf{C_{el}}$ and, although not explicitly stated by Bouzari et al. (2017b), the radius of curvature of the element is taken to be

$$r_{el} = \sqrt{{F_L}^2 - {x_{el}}^2}, \tag{6.4}$$

so that the curved element lays on a hemisphere with radius of curvature F_L. Notably, this hemisphere is not the same as the surface of the concave lens. When modeling a concave lens with the thin lens model, the center of curvature of the lens surface lays in front of the transducer, while the focal point of the thin lens lays behind the transducer. The resulting emitted wave-front arcs are circular, and according to Bouzari et al. (2017b) , the usable FOV is

$$\Omega = 2\cot^{-1}\left(\frac{F_L}{r_c}\right), \tag{6.5}$$

where r_c is the chord radius of the lens.

To find the TOF from one such element to an image point at $\mathbf{P} = (x_p,\, y_p,\, z_p)$, the image point is first projected onto the plane parallel to the emitting element, giving $\mathbf{P}' = (x',\, y_p,\, z_p)$. If the vector $\mathbf{P}' - \mathbf{C_{el}}$ passes between the points **a** and **b**, the TOF between the element and the image point is

$$\tau = \frac{1}{c_m}\sqrt{\|\mathbf{P}' - \mathbf{P}\|^2 + \left(\|\mathbf{P}' - \mathbf{C_{el}}\| - r_{el}\right)^2}. \tag{6.6}$$

If not, the TOF is calculated from the distance from the image point to the closest end-point of the curved element. Thus, if the closest end point is **a**,

$$\tau = \frac{1}{c_m}\|\mathbf{a} - \mathbf{P}\|. \tag{6.7}$$

Moreover, in Section II B of Paper 6, the thin lens model is elaborated on to explain how the position of a wavefront arc is found given its TOF. This will be used when calculating the position of wavefront arcs with constant TOF in Chapter 7.

6.1.1 Evaluation of the predicted TOF

When the TOF the emitted sound field has been predicted, the accuracy of the prediction can be quantified by delaying the sound field using the TOF and calculating the phase difference along the field. The phase difference is calculated by first calculating the cross-correlation of the signal at each point along the sound field with the signal at some reference position:

$$r\,(l,\, d) = P\,(t,\, d) \star P\,(t,\, d^*)\,. \tag{6.8}$$

Here, $\star$ denotes cross-correlation, r is the cross-correlation coefficient, l is the lag, d is some distance parameter, equal to either x_p or y_p, depending on the orientation, and d^* is the reference position. Then, the phase difference is taken as the lag giving the maximum cross-correlation at each value of d. Theoretically, if the TOF prediction is exact, the delayed sound field should have no phase variation across the investigated positions. In some sound fields, artefacts such as edge-waves can disturb the calculation of cross-correlation. Therefore, the calculation is limited to the positions where the amplitude of the sound field is no more than 3 dB lower than the amplitude at the reference position.

6.2 Methods and results: Simulating a thin-lensed RCA

To validate that the thin lens model by Bouzari et al. (2017b) has been correctly interpreted and implemented, the emitted and received sound field for an RCA with curved elements was simulated using Field II (Jensen 1996). The geometry of the 62 + 62 RCA given in Table 4.1 in Chapter 4 was used and delay was applied to the emitting and receiving elements. The delays corresponded to the position of curved elements positioned across a hemisphere, given by

$$\Delta = \frac{\sqrt{{F_L}^2 - x_{el}^2 - y_{el}^2} + z_0}{c_l}. \tag{6.9}$$

The radius of curvature of the thin lens was F_L, calculated using eq. (6.3), taking $R_L = 25.4\,\mathrm{mm}$, according to the dimensions of the concave RTV664 lens (Bouzari et al. 2018). The resulting delays applied to the transmitting columns and receiving rows are shown in Fig. 6.4. Notably, Fig. 6.4 shows that the active apertures are rectangular, rather than square, due to the integrated apodization regions of the 62 + 62 PZT transducer. The simulation assumes that the simulated apex of the lens sits at $z = 0\,\mathrm{mm}$, meaning that emission from any element laying off-center starts at $t < 0$.

6.2.1 Prediction of time of flight using the thin lens model

The Field II model of the thin-lensed RCA was used to simulate the transmitted sound field to two straight lines under the emitting transducer. The outermost element, number 62, transmitted a two-cycle sinusoid at 3 MHz. The two observation lines were placed at

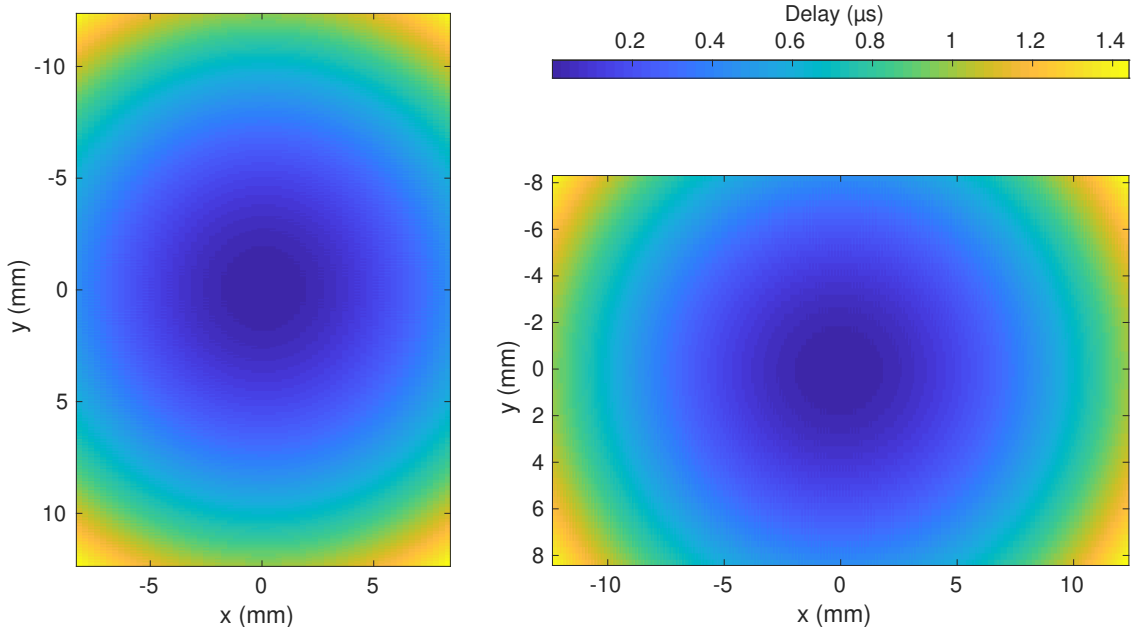

(a) Transmit delays (b) Receive delays

Figure 6.4: The delays applied to the apertures to simulate a thin-lensed RCA.

$$\begin{bmatrix} x \\ y \\ z \end{bmatrix} = \begin{bmatrix} [-30:0.5:30] \\ 0 \\ 20 \end{bmatrix} \text{mm}, \tag{6.10}$$

$$\begin{bmatrix} x \\ y \\ z \end{bmatrix} = \begin{bmatrix} x_{el} \\ [-30:0.5:30] \\ 20 \end{bmatrix} \text{mm}. \tag{6.11}$$

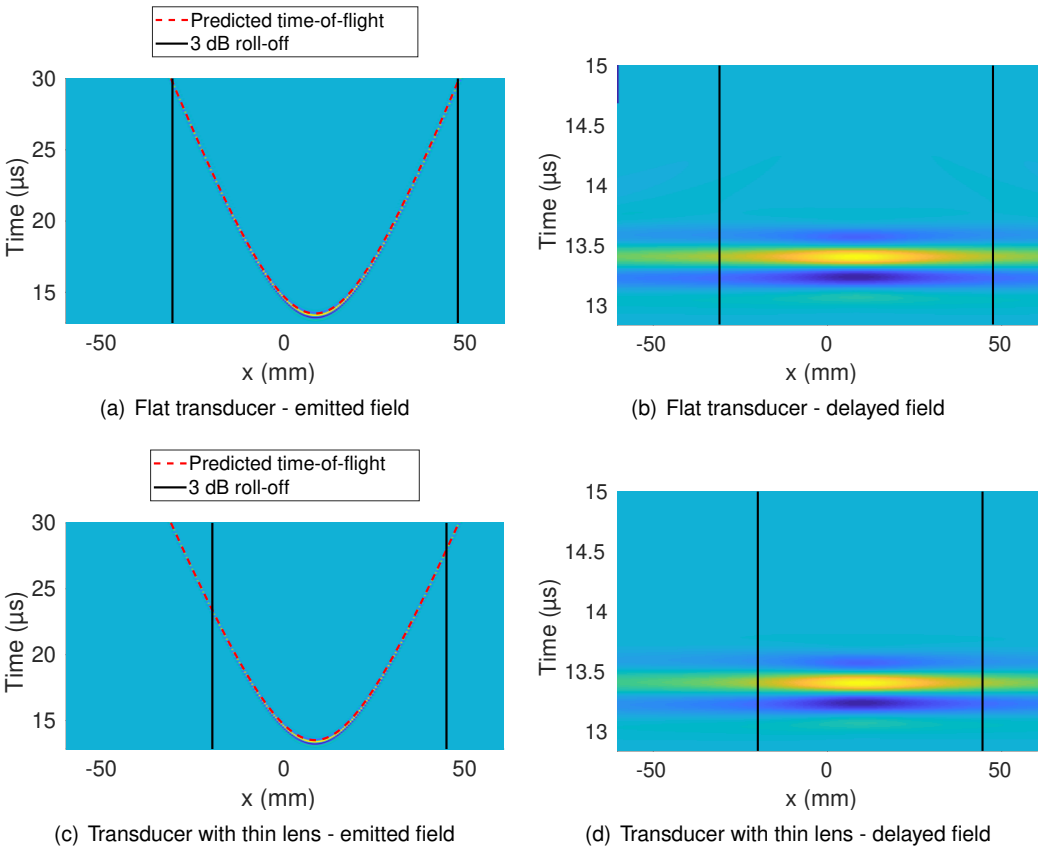

(a) Flat transducer - emitted field

(b) Flat transducer - delayed field

(c) Transducer with thin lens - emitted field

(d) Transducer with thin lens - delayed field

Figure 6.5: The emitted field at the observation line eq. (6.10), orthogonal to the emitting element. The emitted field from flat and lensed transducers are plotted in (a) and (c), respectively, and the delayed sound fields are shown in (b) and (d).

The line given by eq. (6.10) lays orthogonal to the emitting element and the line given by eq. (6.11) lays beneath the emitting element, parallel to its length. The resulting sound fields, emitted to eq. (6.10) and eq. (6.11), are shown in Fig. 6.5(c) and Fig. 6.6(c), respectively. Moreover, for comparison, the same simulations were also made using a 62 + 62 RCA without a lens. The resulting emitted sound fields are shown in Fig. 6.5(a) and Fig. 6.6(a).

To validate the implementation of the thin lens model, eq. (6.6) and eq. (6.7) were used to find the TOF from the emitting element to each position on the two observation lines. In addition, eq. (4.1) and eq. (4.2)

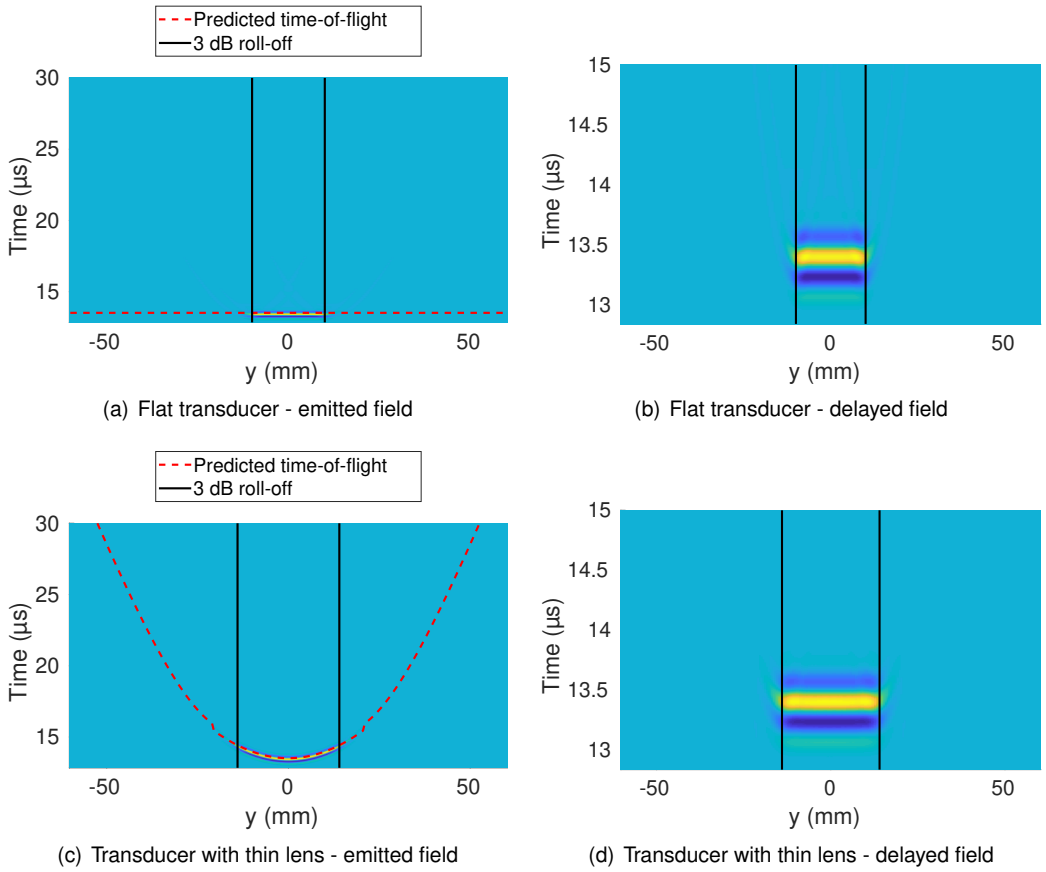

Figure 6.6: The emitted field at the observation line eq. (6.11), parallel to the emitting element. The emitted field from flat and lensed transducers are plotted in (a) and (c), respectively, and the delayed sound fields are shown in (b) and (d).

were applied to calculate the TOF for the unlensed RCA. The resulting TOFs are plotted on top of the sound fields in Fig. 6.5(a) and (c) and Fig. 6.6(a) and (c). Furthermore, to inspect how precisely the TOFs were calculated, the TOFs were used to delay the simulated sound fields and the phase variation across the delayed sound field were calculated according to Section 6.1.1. In theory, the resulting delayed sound field should look like a perfect plane wave, where the signal is in phase along x or y. The resulting delayed sound fields are shown in Fig. 6.5(b) and (d) and Fig. 6.6(b) and (d). For the observation line given by eq. (6.10), the reference point for the cross-correlation calculation was taken to be $d^* = x_{el}$, and for the observation line given by eq. (6.11) the reference point was taken to be $d^* = 0\,\mathrm{mm}$. The position of 3 dB decline in amplitude was found for each of the delayed sound fields. The positions are plotted in Fig. 6.5 and Fig. 6.6. Then, at each position along $d = x$ or y, the cross-correlation of the signal with the signal at the reference position was found. As expected, the resulting phase difference was $\Delta\phi = 0$ for all positions within the 3 dB amplitude span, for all four simulated sound fields.

6.2.2 Beamforming a PSF

The simulated thin-lensed 62 + 62 RCA was also used to make PSFs , using the single-element SA sequence described in 4.2.1. The same image set-ups and data-processing as used in Section 4.2 were

used, apart from the application of delays to the transmitting and receiving elements, making it emulate a thin-lensed RCA. The theory presented in Section 6.1 was used to calculate the TOF. Then eq. (1.1) was used to calculate the pixel intensity in all image grid points for each emission. The resulting images are shown in Fig. 6.7(c) and (d). For comparison, the images of the PSF produced with the unlensed RCA, previously presented in Fig. 4.3 are also repeated here. The FWHM of the PSF of the thin-lensed RCA were calculated according to Definition 2.1 and are shown in Table 6.2. For reference, the FWHM of the PSF of the unlensed RCA, discussed in Section 4.2.3, are also given in Table 6.2. Visually, the PSF of the lensed and unlensed PSF appear indistinguishable, indicating that the calculation of TOF for a thin lensed RCA has been correctly implemented. The FWHM of the PSF for the lensed RCA are slightly higher than for the unlensed RCA, but since the difference is minor, this can be attributed to the fact that the incorporation of delays along the transducer elements will alter its spatial impulse response, which will affect the FWHM.

Plane	**x-z**	**y-z**
Flat transducer	0.86 mm 1.75 λ	1.35 mm 2.73 λ
Lensed transducer	0.88 mm 1.78 λ	1.38 mm 2.81 λ

Table 6.2: The calculated and theoretical FWHM of the simulated PSFs for the flat RCA (shown in Fig. 4.3(a) and (b)) and the thin-lensed RCA (shown in Fig. 6.7).

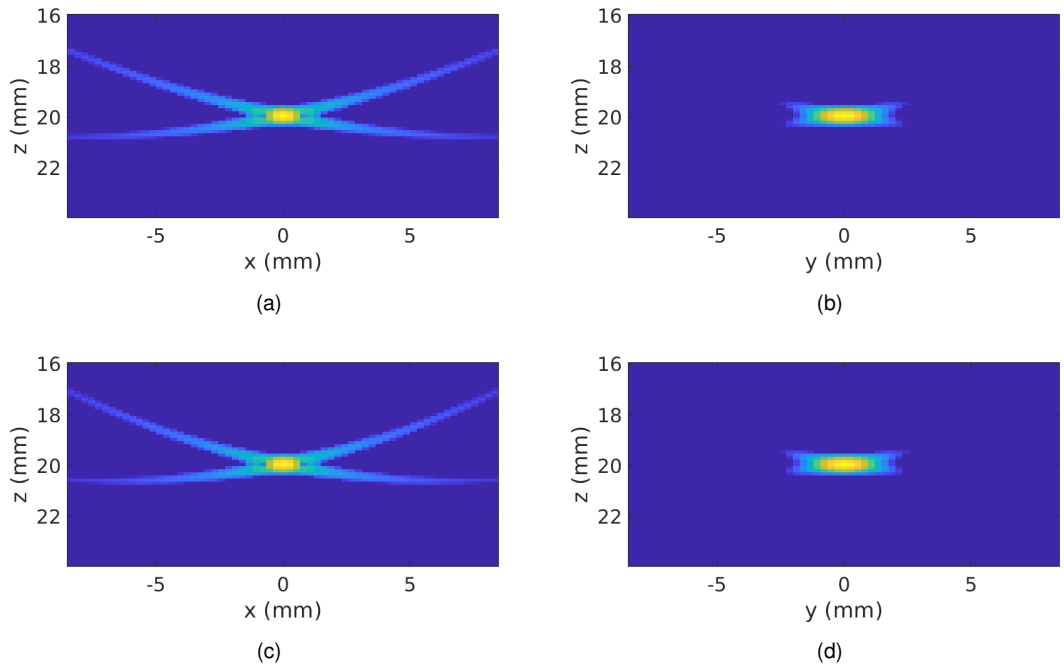

Figure 6.7: Simulated PSFs for a flat (a)-(b) and a curved (c)-(d) version of the 62 + 62 PZT RCA. Subfigures (a) and (b) are also presented in Fig. 4.3.

6.3 Discussion

The simulated and delayed emitted fields shown in Fig. 6.5 and Fig. 6.6 and the simulated PSF of the lensed RCA shown in Fig. 6.7 validate that the thin lens model by Bouzari et al. (2017a) has been interpreted and implemented successfully. This is an important step towards assessing the applicability of the model to DAS beamforming of data from RCA with physical lenses. Modeling the lensed RCA as having curved elements is convenient, because it can be done without accounting for different sound speeds, and thus be simulated using Field II (Jensen 1996), but it does not necessarily represent the true performance of a lensed array. The thin lens model describe the outwards spread of energy, but it is only an accurate representation of an actual lens if the lens is infinitely thin. According to Carpena and Coronado (2006), this approximation is only appropriate if the sound rays enter the lens close to its center, which is not the case for physical lenses mounted in front of RCAs. Thus, the theory presented by Bouzari et al. (2017b) is appropriate for RCAs with an infinitely thin lens or curved elements, but not necessarily for RCAs with a physical lens with a relevant thickness. Notably, when simulating the PSF of a thin-lensed RCA, the elements are treated as being curved, not physically lensed. Therefore, when using eq. (6.6) or eq. (6.7) to calculate the TOF for beamforming, the potential fallacy of the thin lens model is not revealed. In fact, all the results presented in Section 6.2, and in the seminal studies by Bouzari et al. (2016, 2017b) on the thin lens model, are based on simulations of an array with curved elements and should therefore not be taken as proof that the theory can be applied to predict the TOF through a physical lens. Therefore, a more accurate model for predicting the transmission through a lensed RCA is presented in Chapter 7. The accuracy of the TOF predicted by this model will be compared with the accuracy of the TOF predicted by the thin lens model in Section 7.5.1.

CHAPTER 7

Ray tracing through concave lenses

This chapter introduces the ray tracing model, and demonstrates that it can be used to accurately predict how sound emitted from a RCA is refracted by a concave lens. The theory of the model is introduced, and a backwards implementation method is suggested for its implementation. The model is then validated by comparison with simulations and measurements.

When using a lensed RCA to image a human organ, both the image quality and the size of the image is limited by how accurately one is able to predict the TOF. The refraction through the lens adds a significant complexity to this problem, and in the thin lens model this is simplified using the paraxial assumption. To improve the accuracy of predicting the TOF and the position of the sound emitted through a lensed RCA, a model based on ray tracing has been developed. The model describes the refraction through the lens by tracing the emitted sound rays through the lens and applying Snell's law of refraction, shown in eq. (6.1), at each point where the ray intersects the boundary between the lens and the imaged medium. The theory of the ray tracing model is given in Section 7.1, which describes both an analytic relationship for predicting the position of an emitted wave, given its TOF, and a backwards interpolation method used to predict the TOF given the position of the emitted wave. The theory on quantifying the usable FOV of the lensed RCA is presented in Section 7.2.1. The method used to simulate the emitted field through a lensed RCA is discussed in Section 7.3, before some examples of the application of the proposed approaches are shown. Section 7.4 presents calculations of the TOF to known image pixel positions using backwards interpolation, while Section 7.5 presents direct calculations of the positions of an emitted wave, given its TOF, as well as quantification of the usable FOV of a lensed RCA.

7.1 Theory: The ray tracing model

The ray tracing model predicts the time and place of the propagation of an emitted wave through a lens without making simplifying assumptions about the geometry. The theory of the ray tracing model is presented in Section II of Paper 6, and the reader is referred here for derivations and thorough explanations of the relationships in the model. Some of the equations from the model will be applied in Section 7.4 and 7.5, and these are summarized in Section 7.1.1. The analytic expression of the ray tracing model will be discussed in Section 7.1.2, and a backwards interpolation algorithm for implementing the model is presented in 7.1.3. Finally, Section 7.1.4 comments on the angular refraction limit posed by total internal reflection.

7.1.1 Summary of the ray tracing equations

7.1.1.1 Lens surface

The surface of a concave lens is a hemisphere, and any point on the surface is given by $(x_s,\, y_s,\, z_s)$. The radius of the hemisphere is R_L. The origo of the lens is given by $(x_0,\, y_0,\, z_0)$, and the position of the origo and the radius for the RTV664 concave lens are given in Table 6.1. At any plane which intersects the lens at either $x = x_{pl}$ or $y = y_{pl}$, perpendicular to either the y or x-axis, the intersection between the lens surface and the plane is a circular arc, which is given by

$$z_s = \begin{cases} \sqrt{{r_p}^2 - (x_s - x_0)^2} + z_0, & \text{for an } x\text{-}z \text{ plane,} \\ \sqrt{{r_p}^2 - (y_s - y_0)^2} + z_0, & \text{for a } y\text{-}z \text{ plane.} \end{cases} \tag{7.1}$$

Here, r_p is the radius of the arc, which is given by

$$r_p = \begin{cases} \sqrt{{R_L}^2 - {y_{pl}}^2}, & \text{for an } x\text{-}z \text{ plane,} \\ \sqrt{{R_L}^2 - {x_{pl}}^2}, & \text{for a } y\text{-}z \text{ plane.} \end{cases} \tag{7.2}$$

Moreover, the chord radius of the lens in a given intersection plane given by

$$r_c = \sqrt{{r_p}^2 - (R_L - L_H)^2}. \tag{7.3}$$

Here, L_H is the height of the lens in the $(x_{pl},\, y_{pl}) = (0,\, 0)$ plane, previously illustrated in Fig. 6.3.

7.1.1.2 Emitting and propagating angles

The direction at which a sound ray travels is defined by two angles: the emitting angle, α, and the propagation angle χ. When emitted, the ray first travels in the direction given by α. After refraction at the lens boundary, the ray travels in the direction given by χ. Both angles are in relation to a horizontal line, which is parallel to the normal on the emitting element. Both angles can be decomposed into their respective x and y components. The emission of a ray from a column element is illustrated in Fig. 7.1. Here, the initial direction of the ray is given by α_x. Since the element is emitting a cylindrical wave, the emitting angle in the y-z plane is

$$\alpha_y = 0. \tag{7.4}$$

The change in direction due to refraction is determined by Snell's law, shown in eq. (6.1). Both the angle of incidence, θ_i, and the angle of refraction, θ_r, can be decomposed into the x-z and y-z planes, given as subscripts in Fig. 7.1. The propagation direction after refraction is determined by χ_x and χ_y. Paper 6 concludes that these angles are given by

$$\chi_y = \theta_{r,\,y} - \theta_{i,\,y}, \tag{7.5}$$

$$\chi_x = \theta_{r,\,x} - \sin^{-1}\left(\frac{x_s}{r_p}\right). \tag{7.6}$$

7.1.1.3 Intersection points

The start position of a ray can be described by a sub-element on the transmitting element, given by its coordinates $(x_{el},\, y_{el,\,j},\, 0)$, where the subscript j refers to some position along the length of the element. When a sound ray is emitted from this position, the point at which it intersects the lens surface is $(x_s,\, y_s,\, z_s)$. The x-coordinate of the intersection point is given by

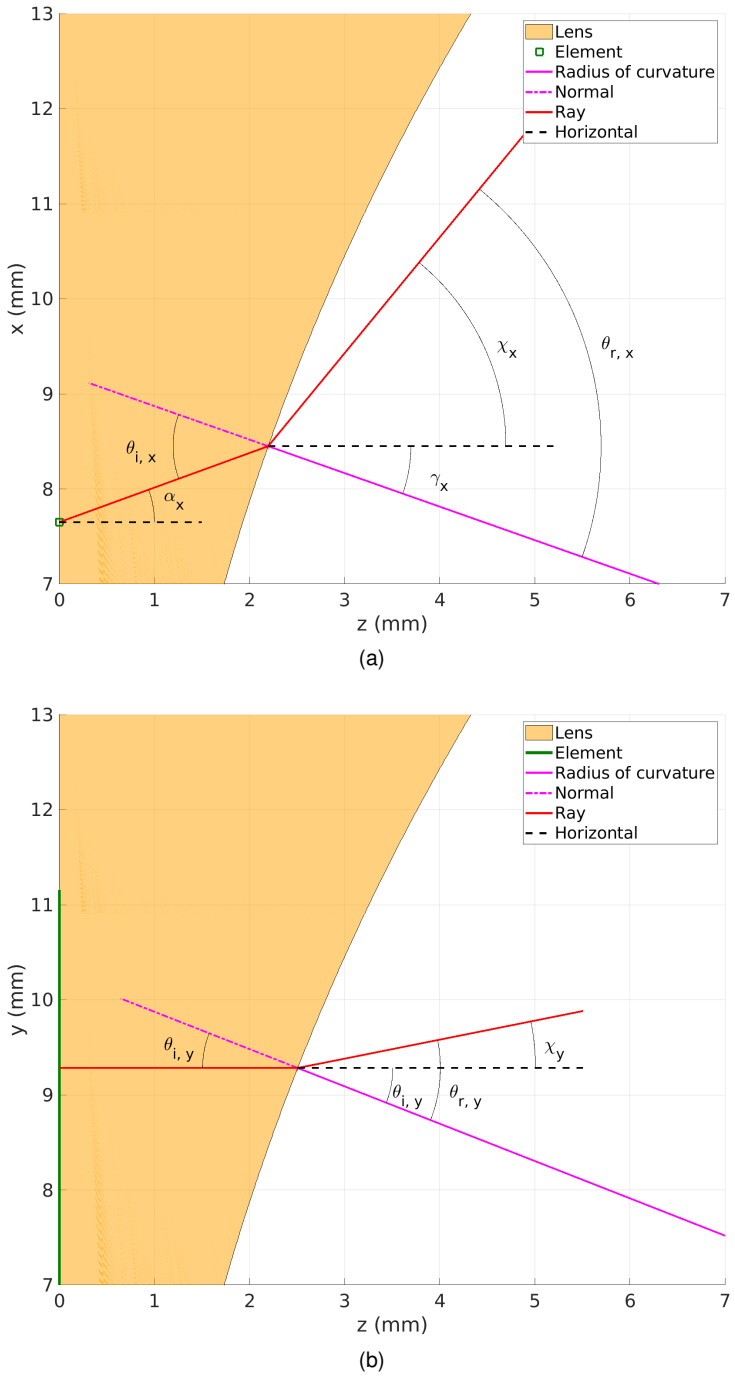

Figure 7.1: Illustrations of the emission of a sound ray from an element in the plane (a) orthogonal to the element and (b) parallel to the element. The figure is reprinted from Paper 6.

$$
\begin{aligned}
x_s = \frac{1}{2\left(\tan^2(\alpha_x)+1\right)}\Bigg(& 2x_0\tan^2(\alpha_x) + 2z_0\tan(\alpha_x) + 2x_{el} \\
& \pm \Big[\left(-2x_0\tan^2(\alpha_x) - 2z_0\tan(\alpha_x) - 2x_{el}\right)^2 \\
& - 4\left(\tan^2(\alpha_x)+1\right)\left(-{r_p}^2\tan^2(\alpha_x) + {x_0}^2\tan^2(\alpha_x)\right. \\
& \left. +2x_{el}z_0\tan(\alpha_x) + {z_0}^2\tan^2(\alpha_x) + {x_{el}}^2\right)\Big]^{0.5}\Bigg).
\end{aligned} \tag{7.7}
$$

Derivation of this rather complex relationship is given in Paper 6. The y-coordinate is

$$
y_s = y_{el,\,j}, \tag{7.8}
$$

due to eq. (7.4). Finally, the z-coordinate of the intersection point can be found by substituting eq. (7.7) into eq. (7.1).

7.1.1.4 Position of transmitted wavefront

The position of a wavefront can be calculated by first finding the intersection point of the corresponding sound ray with the lens, and adding the distance traveled from the lens, as

$$
\begin{bmatrix} x_w \\ y_w \\ z_w \end{bmatrix} = \begin{bmatrix} x_s \\ y_s \\ z_s \end{bmatrix} + \begin{bmatrix} \Delta x(t) \\ \Delta y(t) \\ \Delta z(t) \end{bmatrix}. \tag{7.9}
$$

Similarly, the transmit TOF can be divided into two: the time it takes to travel to the lens boundary and the time traveled after the intersection. Thus, expressed in terms of the distances traveled, the transmit TOF is

$$
\tau_{\mathrm{TX}} = \frac{DOF_1}{c_l} + \frac{DOF_2}{c_m}. \tag{7.10}
$$

The distance traveled by the ray after the intersection is governed by its start position and the refraction the ray experiences when intersecting the lens surface. In Paper 6, derivation of the expressions for these changes in position are found to be

$$
\begin{bmatrix} \Delta x(t) \\ \Delta y(t) \\ \Delta z(t) \end{bmatrix} = \begin{bmatrix} \dfrac{DOF_2(t)}{\sqrt{\left(1+\cot^2\chi_x + \cot^2\chi_x\cdot\tan^2\chi_y\right)}} \\ \dfrac{DOF_2(t)}{\sqrt{\left(1+\cot^2\chi_y + \cot^2\chi_y\cdot\tan^2\chi_x\right)}} \\ \dfrac{\Delta x}{\tan\chi_x} \end{bmatrix}. \tag{7.11}
$$

7.1.2 Analytic formulation of the ray tracing model

The ray tracing model has been formulated with the primary intention of using it to predict the TOF from an emitting element to an image pixel, so that DAS beamforming can be used for lensed RCAs. This requires that the TOF can be calculated given the position of the image pixel and the position of the emitting element. This can be expressed as

$$\tau\left(x_p,\, y_p,\, z_p\right) = g\left(\begin{bmatrix} x_p \\ y_p \\ z_p \end{bmatrix},\, \begin{bmatrix} x_{el} \\ y_{el} \end{bmatrix}\right). \tag{7.12}$$

Here, $(x_p,\, y_p,\, z_p)$ is position of the image pixel and g is some function which describes the refraction through the lens. However, the complex nature of the lens refraction makes deriving an analytic expression for g unfeasible.

Instead, in Paper 6, the ray tracing theory is formulated inversely, with the aim to predict the position of an emitted wave, given its TOF. Although this is two sides of the same story, the implementation becomes much less complex when the TOF is known. The position of a wavefront is given by

$$\mathbf{W}\left(\tau_{\text{TX}}\right) = f\left(\begin{bmatrix} x_{el} \\ y_{el} \end{bmatrix},\, \alpha_x,\, \tau_{\text{TX}}\right). \tag{7.13}$$

Here, τ_{TX}, is the time taken to transmit the sound to the wavefront position, and f is some other function which takes the geometry of the lens into account. The derivation of f is presented in Section II of Paper 6. This formulation makes it possible to calculate the position of an emitted wavefront given τ_{TX}, $(x_{el},\, y_{el})$, and $(\alpha_x,\, \alpha_y)$. Yet, the aim of calculating the TOF to a given image pixel is not achieved by eq. (7.13). Therefore, in Section 7.1.3, a backwards interpolation method is proposed, which makes it possible to calculate τ_{TX} to a specified image pixel by repeatedly calculating eq. (7.13) for a set of input values and then interpolating to find the desired value for τ_{TX}.

Notably, the theory presented in Paper 6 only describes calculation of the transmitted TOF. Therefore, at this stage, when using the backwards interpolation method, only τ_{TX} can be found, and not the full pulse-echo TOF. Calculating the full TOF requires formulation of the function f for received sound. In the case of a refracting lens, the principle of acoustic reciprocity is not necessarily applicable, because the assumption taken in eq. (7.4) cannot be applied when receiving the sound, as the received wave is not likely to be a cylindrical wave. Formulating the function f for received sound requires further investigation, and this has not been accomplished in this thesis.

7.1.3 Ray tracing with backwards interpolation

The aim of ray tracing with backwards interpolation is to find τ given any image point $\mathbf{P}$, without knowledge of the function g. To achieve this, the problem is inverted, and instead of finding an analytic relationship for g, the theory presented in Section II of Paper 6 is applied to evaluate eq. (7.13) for a number of values of τ_{TX}, $(x_{el},\, y_{el,\,j})$, and α_x. By repeatedly implementing eq. (7.13), a 3D matrix of wavefront positions is created. Fig. 7.2 shows an illustration of an algorithm which can be used to make the 3D matrix. Finally, 3D interpolation over the resulting matrix is used to find the value of τ_{TX} corresponding to the desired image point.

To implement the algorithm shown in Fig. 7.2, appropriate choices for the input parameters to eq. (7.13) must be made. Here follows some considerations and recommendations on these choices, which are applied to produce the results presented in Section 7.4.2. However, it is speculated that more conservative choices, leading to fewer calculations of eq. (7.13), would improve the computation time of the backwards interpolation. Computational optimization of the implementation of the backwards interpolation method has not been explored in this thesis.

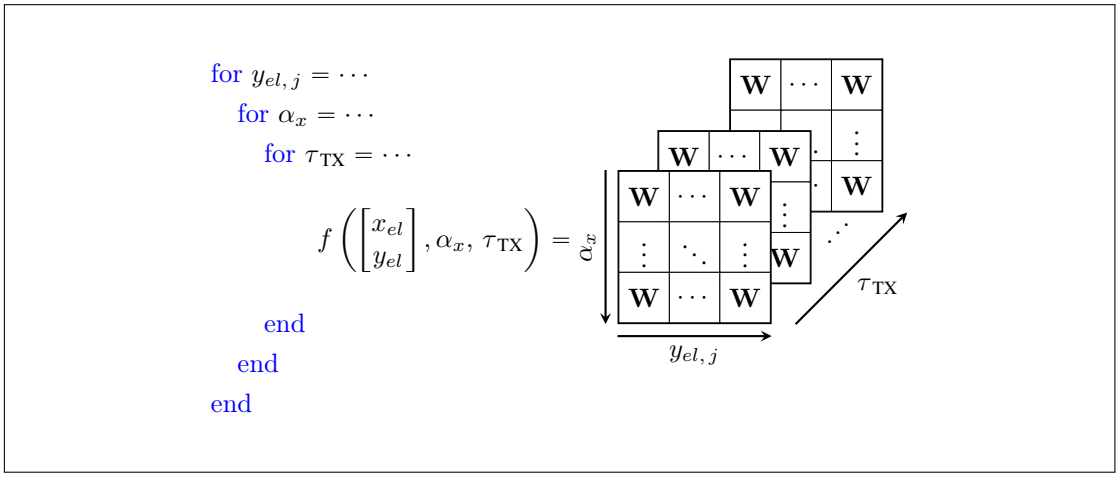

Figure 7.2: An illustration of the algorithm used to calculate the 3D matrix of wavefront positions for the ray tracing method with backwards interpolation. The annotated arrows running along the dimensions of the matrix show variation in the input variables.

7.1.3.1 Position of element

The position of the emitting element is given by the transducer geometry; for a chosen transmitting element x_{el} is constant, while $y_{el,\,j}$ varies along the length of the element. Due to the symmetry across the x-axis, only half of the emitting element needs to be included in the calculations of eq. (7.13), so $y_{el,\,j}$ is varied fro 0 mm to $\dfrac{p \cdot E}{2}$.

7.1.3.2 Emitting angle

The emitting angle in the x-z plane is normally defined by the directivity of the emitting element. However, when emitting into a lens, two factors limit the effective directivity of the element, that is, the emitting angles which produce rays which are transmitted through the lens. Both these limiting cases are illustrated in Fig. 7.3. Firstly, α_x is limited by the ray hitting the end of the curvature of the lens. For any emitting element, this occurs when

$$\alpha_e = \arctan\left(\frac{\|\mathbf{P_1} - \mathbf{P_2}\|}{L_T + L_H}\right), \tag{7.14}$$

where L_T is the thickness of the lens at $(x_p,\, y_p) = (0,\, 0)$ plane, previously illustrated in Fig. 6.3. Although the values of L_T and L_H depend on the choice of x_{pl} or y_{pl}, together, the sum of $L_T + L_H$ is constant, independent of the plane. The distance between the two points, $\mathbf{P_1}$ and $\mathbf{P_2}$ is given by

$$\|\mathbf{P_1} - \mathbf{P_2}\| = r_c - x_{el}, \tag{7.15}$$

where the chord radius, r_c, should be taken in the observed plane, as given by eq. (7.3).

The other limiting case to α_x occurs when the emitted ray no longer intersects the curvature of the lens. The largest value of α_x which does intersect the curvature occurs when the ray grazes the curvature, making a right-angle with the radius of curvature. This limiting angle, α_g, is given by the sum of two angles illustrated in Fig. 7.3:

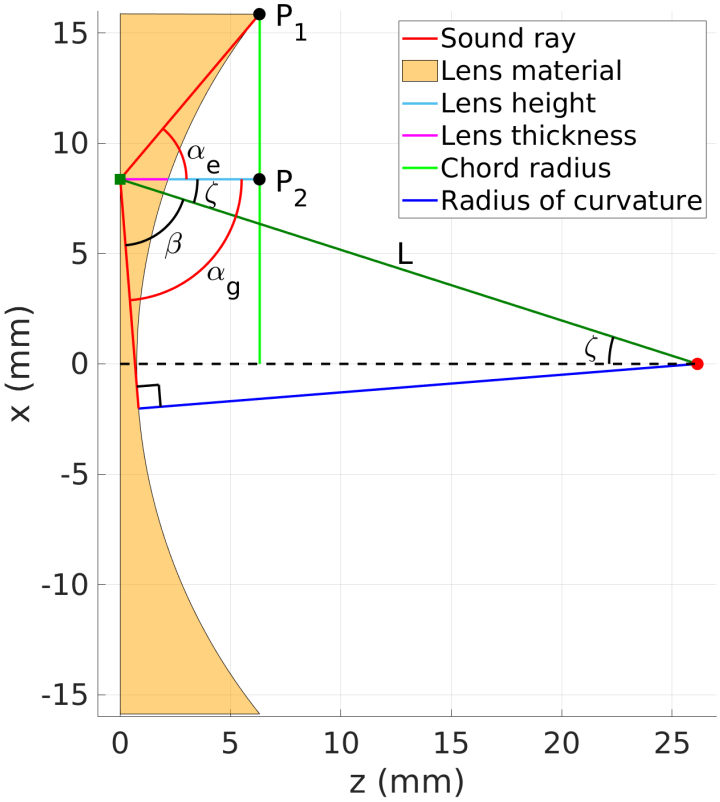

Figure 7.3: Illustration of the two cases which limit the maximum value of α_x: when the sound ray hits the edge of the lens, giving α_e, and when the sound ray no longer intersects the curvature of the lens, giving α_g. Both limiting values of α_x are drawn as red angles.

$$\alpha_g = \beta \pm \zeta. \tag{7.16}$$

Both these angles are given by trigonometric relations to the line between the emitting element and the lens origo, which has the length L:

$$\beta = \arcsin\left(\frac{r_p}{L}\right), \tag{7.17}$$

$$\zeta = \arccos\left(\frac{z_0}{L}\right). \tag{7.18}$$

Finally, the intersection point between the ray and the lens surface corresponding to α_e and α_g can be found using eq. (7.7) and eq. (7.1). For emission in the positive x-direction, the value of α_e or α_g which results in the lowest z_s gives the limit of α_x.

7.1.4 Avoiding total internal reflection

When a ray intersects the boundary between the lens and the image medium, its energy is both transmitted through the lens and reflected off of the boundary (Kinsler et al. 1982). The proportion of how much

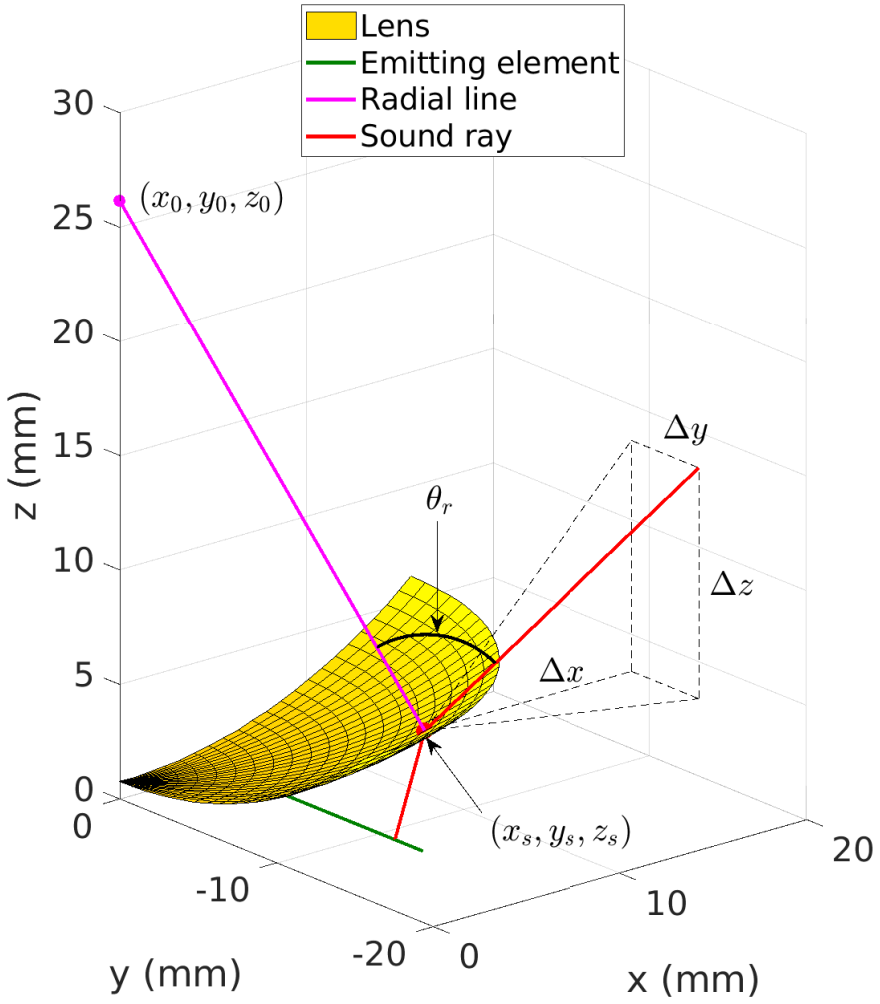

Figure 7.4: An illustration of the refraction angle. The illustration includes a quarter of the concave lens.

energy is reflected and how much is transmitted is determined by the refraction angle, θ_r. All of the energy is reflected when total internal reflection occurs. This happens when

$$\theta_r \geqslant 90°. \tag{7.19}$$

When this occurs, the calculation of the position of the emitted wave using the ray tracing model breaks down due to imaginary values. Therefore, for each ray tracing calculation, one should evaluate if the ray will be transmitted or not by checking the criterion in eq. (7.19). The value of θ_r is the angle between the transmitted ray and the radial line of the lens at the point of intersection between the lens and the ray. This angle is visualized in Fig. 7.4. The two lines can be expressed as

$$\text{Radius:} \quad l_1 = \begin{bmatrix} x_s \\ y_s \\ z_s \end{bmatrix} + \begin{bmatrix} -x_s \\ -y_s \\ z_0 - z_s \end{bmatrix} k, \qquad \text{for } 0 \leqslant k \leqslant 1, \tag{7.20}$$

$$\text{Ray:} \quad l_2 = \begin{bmatrix} x_s \\ y_s \\ z_s \end{bmatrix} + \begin{bmatrix} \Delta x \\ \Delta y \\ \Delta z \end{bmatrix} k, \qquad \text{for } 0 \leqslant k \leqslant 1, \tag{7.21}$$

where k is some parameterization variable, $(x_s,\, y_s,\, z_s)$ are given by eq. (7.7), eq. (7.8) and eq. (7.1), respectively, and $(\Delta x,\, \Delta y,\, \Delta z)$ are given by eq. (7.11). The refraction angle can be quantified by taking the dot product of the direction vectors of the two lines, as

$$\theta_r = \arccos\left(\frac{\begin{bmatrix} -x_s \\ -y_s \\ z_0 - z_s \end{bmatrix} \cdot \begin{bmatrix} \Delta x \\ \Delta y \\ \Delta z \end{bmatrix}}{\left\| \begin{bmatrix} -x_s \\ -y_s \\ z_0 - z_s \end{bmatrix} \right\| \cdot \left\| \begin{bmatrix} \Delta x \\ \Delta y \\ \Delta z \end{bmatrix} \right\|} \right). \tag{7.22}$$

7.2 Theory: Quantifying FOV

To study the clinical value of a lensed RCA, it is prudent to quantify its usable FOV. When using a lensed RCA to make beamformed images, the usable FOV is limited both by how far out the lens is able to spread the emitted energy, but also by how accurately the TOF can be predicted. Several authors (Bouzari et al. 2018; Démoré et al. 2009; Engholm et al. 2018) have previously quantified the usable FOV of a lensed RCA based only on the drop in energy across the insonified image region. However, this method fails to take into account that inaccurate prediction of the TOF can also limit the usable size of the image volume. If the prediction of the TOF is inaccurate, the summation over the received signals in eq. (1.1) will be out of phase, which will degrade the contrast of the resulting image. Contrarily, the cross-correlation method presented in Section 6.1.1 quantifies the phase error introduced by inaccurate prediction of the TOF, but does not take into account the drop in amplitude across the emitted wave. Instead, the usable transmitted FOV should be quantified based on both the spread of the emitted power and the accuracy of the prediction of the TOF. A method for making this quantification has been developed based on an SNR criterion proposed by Oddershede and Jensen (2007), and is applied in Paper 6. The method consists of quantifying the variation in power and phase in a sound field positioned on an arc which is predicted to have constant TOF. An elaboration on the Oddershede and Jensen (2007) SNR criterion and its application to TOF prediction is given in Sections 7.2.1 and 7.2.2.

7.2.1 The Oddershede-Jensen SNR criterion

Oddershede and Jensen (2007) presents a formal criterion for finding the angular extent at which the emission from a VS contributes productively to a HRI. This is based on the notion that a VS is assumed to emit a perfect spherical wave, while in fact, the emitted wave deviates from a spherical profile when the angular extent becomes large. Moreover, because the emitting aperture is of finite size, the amplitude of the emitted wave will drastically reduce at certain propagation angles. Therefore, at a certain angular extent, the emission from the VS will no longer contribute coherently to the HRI, but rather be added up out of phase or with too high noise. To determine if the signal from a certain VS should be included in the

HRI, Oddershede and Jensen (2007) compares SNR of the LRI produced by the VS with the SNR of the full HRI, and states that

$$\mathrm{SNR}_1 \leqslant \mathrm{SNR}_{1+2}, \tag{7.23}$$

where the subscripts indicate the virtual source indexes. If this inequality is true, the addition of VS number two contributes positively to the HRI and should be included. Oddershede and Jensen elaborates on this idea and conclude that the SNR criterion is fulfilled if

$$\mathrm{SNR}\,(a) \leqslant \mathrm{SNR}\,(\Delta\phi)\,. \tag{7.24}$$

Here, a is the ratio of the signal amplitude of emission number one and two, and $\Delta\phi$ is the phase difference between the two signals. For a continuous wave the two parts of the criterion are

$$\mathrm{SNR}\,(a) = \frac{1-a^2}{2a}, \tag{7.25}$$

$$\mathrm{SNR}\,(\Delta\phi) = \cos\left(\Delta\phi\right). \tag{7.26}$$

Furthermore, for a pulsed emission of b cycles, this expands to

$$\mathrm{SNR}\,(a) = \frac{1-a^2}{2a}, \tag{7.27}$$

$$\mathrm{SNR}\,(\Delta\phi) = \left(1 - \frac{\Delta\phi}{2\pi b}\right)\cos\left(\Delta\phi\right) - \frac{1}{2\pi b}\sin\left(\Delta\phi\right). \tag{7.28}$$

In Fig. 7.5, the SNR inequality is visualized. Here, it is clear that when the emission from two VSs are added together to form a HRI, the criterion only holds if two conditions are met. Firstly, the amplitude of the second VS must be large enough, so that the addition of its signal strength and noise does not contribute negatively to the SNR of the resulting HRI. Secondly, the phase difference between the two added VSs must be small, so that the addition of the two emitted signals is constructive. Commonly, the limit of when two signals can be added constructively, is taken to be when the phase difference is less than a quarter wavelength (Kinsler et al. 1982), and indeed, in the continuous case, if the amplitude ratio is one, the phase difference giving the limit of the inequality in eq. (7.24) is $\frac{\lambda}{4}$. For the pulsed wave, the limit is at lower phase difference, and the acceptable phase difference falls with decreasing amplitude ratio.

7.2.2 Applying the SNR criterion

Although Oddershede and Jensen (2007) formulated their SNR criterion for the addition of VSs to HRIs, this approach can also be used when assessing the usable FOV of lensed RCAs. In this case, the criterion in eq. (7.24) is applied to the sound field at arcs which have a constant TOF. Along these arcs, the sound field will theoretically be perfectly in phase, if the prediction of the position of these arcs is completely accurate. And, at the extremities of the arc, the sound pressure will decline due to the finite size of the emitting element. The criterion is applied along the propagation angle and both the amplitude ratio, a, and the phase difference, $\Delta\phi$, takes a point, p^*, in the middle of the arc as their reference. At the propagation angle where the criterion no long holds true, the value of $\mathrm{SNR}(a)$ exceeds $\mathrm{SNR}(\Delta\phi)$. The two propagation angles at which this occurs are referred to as intersection points, p_i. The distance between one of these points and the reference point gives the transmitted usable angular FOV so that

$$\Omega_{\pm 1/2} = \arctan\frac{p^* - p^i}{z}, \tag{7.29}$$

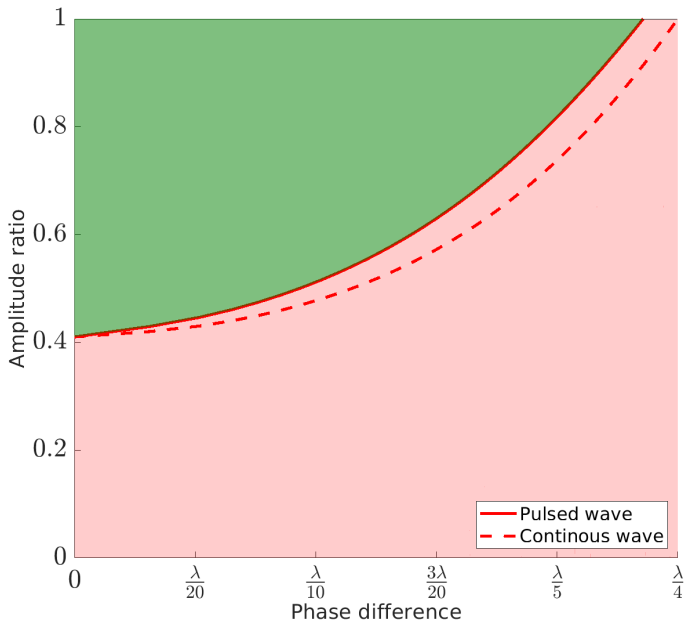

Figure 7.5: Visualization of the Oddershede and Jensen (2007) SNR criterion. In the green region, the criterion holds true. In the red region, the criterion is false, either because the amplitude ratio is too small, or because the phase difference is too large.

where Ω is the angular FOV and z is the depth of the wavefront arc at the intersection points. Here, the subscript $1/2$ on Ω indicates that this is the one-sided angular FOV, and its sign gives the direction along the arc. The subscript $\pm$ refers to either $\Omega_{+1/2}$ or $\Omega_{-1/2}$, and the total usable FOV, also known as the two-sided FOV, is given by

$$\Omega = \Omega_{+1/2} + \Omega_{-1/2}. \tag{7.30}$$

7.3 Method: Simulating the emitted field from a lensed RCA

To study the effect of a double curved lens on the transmission from an RCA, either measurement or a complex simulation is required. In the development of Paper 6, measurement of the emitted field was not feasible, due to the equipment challenges outlined in Section 4.3. Instead, a simulation of the emitted field was made. Throughout this thesis, sound field simulation has been performed in Field II (Jensen 1996). However, Field II is not capable of incorporating changes in the speed of sound, and simulating a diverging lens is therefore not possible if the material of the lens is to be taken into account. Therefore, the emitted field has been simulated with a 3D finite element method (FEM) using OnScale (OnScale LLC, Cupertino, CA, USA), as described in Section III B of Paper 6. This method takes into account the 3D propagation of the sound, the difference in speed of sound between the lens and the imaged medium, and the resulting refraction, as well as the geometry of the lens and attenuation. Throughout this thesis, the FEM simulations of the lensed RCA have been performed by Mélanie Audoin, a PhD student at DTU. The author has collaborated with Audoin in setting up the simulation domain and determining the desired outcomes, but simulations and the resulting sound fields shown or referred to in this thesis are not made by the author of the thesis.

Simulating 3D wave propagation through an inhomogeneous medium requires great computational capacity. The complexity of FEM is dependent on the simulation resolution, and when simulating a sound wave in the mega-Hertz range, the required time-resolution needed is great. Although it would be preferable to simulate emission from the RCAs at their center frequency, unfortunately, the computational capacity needed was not available during this project. Therefore, the emission frequency was reduced to obtain a functional time-resolution of 0.0281 µs, and in all FEM simulations presented in this thesis, the emitted sound wave is a two-cycle 1 MHz sinusoid.

7.4 Predicting the TOF from a lensed RCA

7.4.1 Method: Calculating the TOF to a line

To demonstrate the accuracy of ray tracing with the backwards interpolation method, it is applied to calculate the TOF from element number 86 in the 94 + 94 CMUT RCA through the concave RTV664 lens. The element lays at $x_{el} = 6.93\,\mathrm{mm}$. The dimensions of the transducer and lens are given in Table 4.1 and Table 6.1, respectively. The TOF is calculated to points on a line laying orthogonal to the emitting element, at

$$\begin{bmatrix} x \\ y \\ z \end{bmatrix} = \begin{bmatrix} [-50 : 0.5 : 50] \\ 6.93 \\ 30 \end{bmatrix} \mathrm{mm}. \tag{7.31}$$

An illustration of the geometry of the observation line and the emitting element is given in Fig. 7.6.

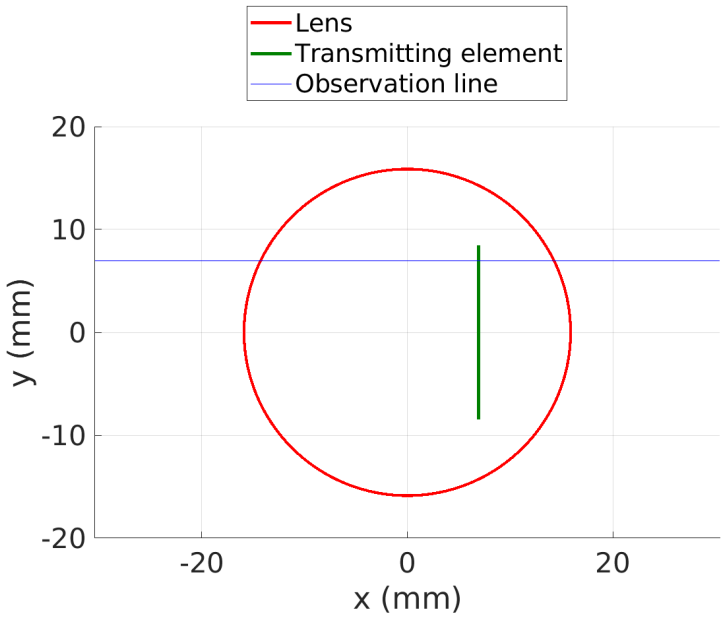

Figure 7.6: An illustration of the transmitting element and the observation line.

To investigate the accuracy of the calculated TOF, the transmitted field emitted from element number 86 to the observation line is simulated using FEM, as specified in Section 7.3, and measured using a hydrophone. The transducer was mounted in a water bath and an Onda HGL0400 Hydrophone (Onda

Corp., California, USA) was placed beneath the transducer. At first, the transducer was mounted without the lens so that an alignment measurement could be performed to establish a common coordinate system between the transducer and the hydrophone. This is important in order to place the hydrophone accurately at the observation line, and thus match the positions of the observations with the positions used to calculate the TOF. To align the transducer with the hydrophone, three focused emissions were transmitted with the columns, as proposed by Tomov et al. (2018), and the acoustic axis of the transducer was established as specified by Jensen et al. (2016). Since focused emissions with column elements produces focal lines parallel to the y-axis, finding the acoustic axis of the three focused emissions gave the relation between the position of the transducer and the position of the hydrophone in the x-z plane. Unfortunately, due to the aforementioned resistivity problems (described in Section 4.3 and by Havreland et al. (2019)) with the row elements of the 94 + 94 CMUT RCA, it was not possible to conduct the alignment procedure in the y-z plane, and the hydrophone was therefore aligned with the center of the transducer in the y-direction by holding a ruler beneath the transducer. After the alignment procedure, the transducer was removed from the water bath, and the lens was mounted in front of the transducer. The RTV664 lens was mounted in front of the RCA using a custom 3D printed holder, and ultrasound jelly was applied between the transducer and the lens to ensure adequate contact between the aperture and the lens material. The assembly was then placed back into the water bath, and care was taken to place the assembly, as accurately as possible, back into the same position as during the alignment procedure. The transducer and hydrophone were connected to SARUS (Jensen et al. 2013), and element number 86 was set to emit a two-cycle sinusoid with a center frequency of 4.5 MHz. The emitted pressure was then measured along the observation line given by eq. (7.31), from $x = -20\,\mathrm{mm}$ to $x = 20\,\mathrm{mm}$.

7.4.2 Results: The TOF to a line

The resulting simulated and measured emitted fields are plotted in Fig. 7.7(a) and 7.8(a), respectively, together with the predicted TOF. Notably, the wavelengths of the observed pulses in the two figures differ, since the measured and simulated emissions are not made using the same center frequency. The sound fields were delayed by the predicted TOF to evaluate its accuracy. The delayed sound fields are shown in 7.7(b) and 7.8(b). The cross-correlation method described in Section 6.1.1 was applied to the delayed wave fields, taking $x = 6.93\,\mathrm{mm}$ as the reference position. The resulting phase differences along the observation line are shown in Fig. 7.9.

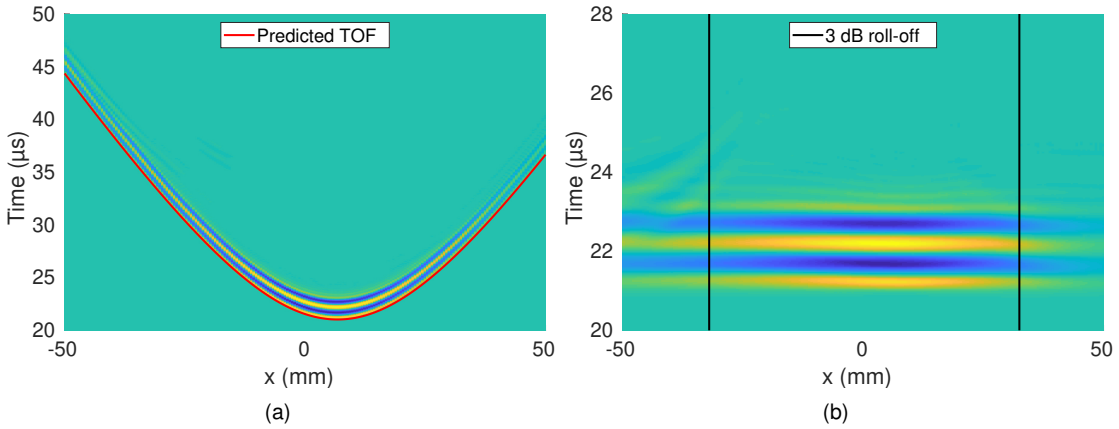

Figure 7.7: The simulated transmitted field with the predicted TOF in red. The sound field received along the observation line is shown in (a) and the sound field delayed by the TOF is shown in (b).

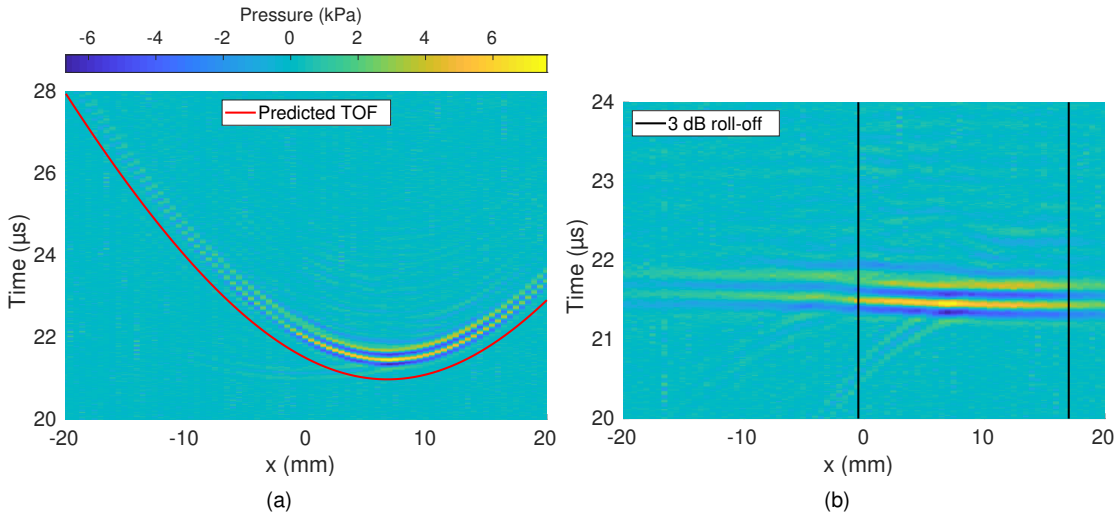

Figure 7.8: The measured transmitted field with the predicted TOF in red. The sound field received along the observation line is shown in (a) and the sound field delayed by the TOF is shown in (b).

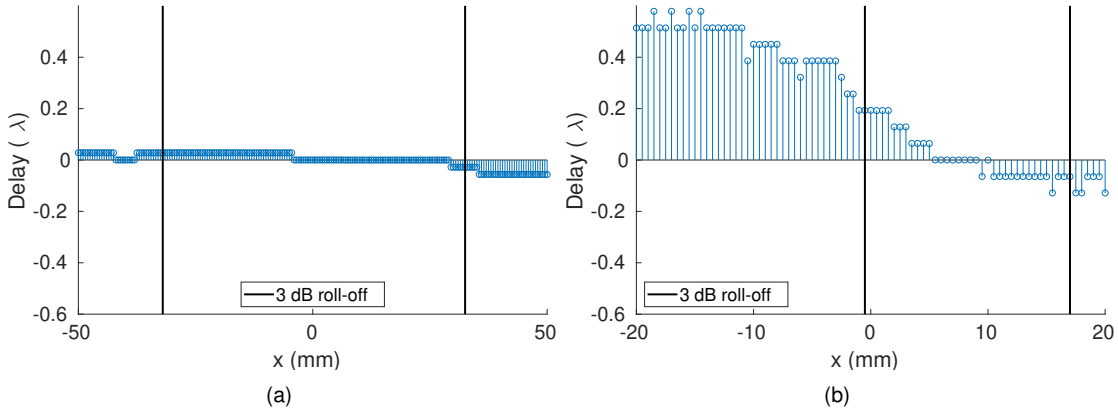

Figure 7.9: Calculated phase differences along the observation line for (a) the simulated and (b) the measured sound fields.

7.5 Predicting the position of an emitted wave

In Section II of Paper 6 the ray tracing model is formulated so that the position of an emitted wave can be predicted given its TOF. This makes it possible to predict the position of a wavefront with constant TOF, and thus to apply the Oddershede and Jensen criterion given in eq. (7.24). In Sections 7.5.1 and 7.5.2 this will be applied to find the usable FOV of a lensed RCA. Firstly, the method is used to compare the thin lens model with the ray tracing model, and secondly, the method is used to evaluate the usable FOV for a 128 + 128 element RCA. All tables and figures presented in this section are reprinted from Paper 6, and the reader is referred to the paper for details on the methods used to produce the results presented in Sections 7.5.1 and 7.5.2.

7.5.1 Results: Comparison of the thin lens model and the ray tracing model

Section 6.3 questioned how accurately the thin lens model can predict the TOF from a lensed RCA with a physical lens of finite thickness. It is hypothesized that prediction of the TOF using the ray tracing model will be more accurate than using the thin lens model, since the paraxial assumption is avoided, and that this will give a greater usable FOV. Therefore, in Section III C 1 of Paper 6, the usable FOV using the thin lens model and the ray tracing model were compared for four example cases. A table with descriptions of the four case geometries is given in Table 7.1.

Case num.	Element name	Element index	Position of element	Arc relation to element
1	Center	65	x = 0.1 mm	Orthogonal
2	Center	65	x = 0.1 mm	Along
3	Edge	128	x = 12.7 mm	Orthogonal
4	Edge	128	x = 12.7 mm	Along

Table 7.1: Description of the geometry of the simulated cases used to compare the performance of ray tracing and the thin lens model.

The sound pressure field emitted from the 128 + 128 element RCA, described in Table 4.1, was simulated along constant TOF arcs according to both the ray tracing and thin lens models for all the four example cases. The usable FOV was evaluated according to the SNR criterion presented in Section 7.2.1. The resulting two-sided usable FOV is given in Table 7.2. Generally, in Table 7.2, it can be seen that the FOV calculated using the ray tracing model arcs is comparable or higher than the FOV calculating using the arcs predicted by the thin lens model.

The largest difference between the two models is seen in case 3, where the arc runs orthogonal to the edge element. The simulated pressure field for the two prediction models, and the corresponding values for SNR($\Delta\phi$) and SNR(a) are plotted in Fig. 7.10. Here, the intersection points between the two SNR criteria curves are also indicated, giving the total usable FOV, as shown in Table 7.2. Visually, Fig. 7.10 shows the effect of inaccurately predicting the position of the emitted wave; in Fig. 7.10(a), the pressure field appears to be in phase across the propagation angles, whereas in Fig. 7.10(b), the field appears curved. The curvature indicates that the prediction of the wavefront position has introduced a phase error. This error can also be seen in Fig. 7.10(d), where the value of SNR($\Delta\phi$) deviates significantly from one.

Case number	**1**	**2**	**3**	**4**
FOV with ray tracing model	125.1°	47.6°	110.7°	39.3°
FOV with thin lens model	121.1°	44.4°	85.6°	39.9°

Table 7.2: The calculated two-sided angular FOV for the four example cases, calculated with arcs predicted by the ray tracing model and the thin lens model. This table is modified and reprinted from Paper 6.

7.5.2 Results: Evaluation of the FOV for a lensed 128 + 128 element RCA

The usable transmitted FOV for the RTV664 lens mounted on the 128 + 128 RCA has been evaluated in Paper 6. This gives an indication of how suited this lens and transducer are for imaging a human organ. The usable FOV has been evaluated from simulations of the transducer and lens for elements number 65 to 128 in steps of nine, and at depths corresponding to propagation in a homogeneous medium with $c_w = 1480\,\mathrm{m\,s^{-1}}$ through 6 mm to 21 mm in steps of 5 mm. The FOV has been evaluated using the Oddershede and Jensen (2007) SNR criterion, given in eq. (7.27) and eq. (7.28). Full details on how the

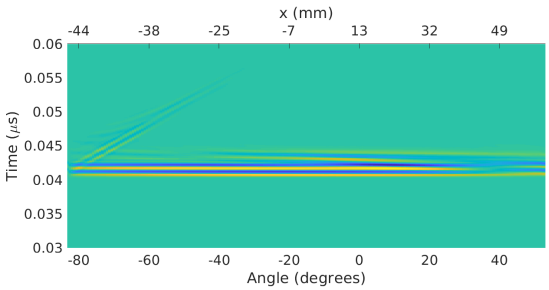

(a) Pressure field along an wave-front arc by the ray tracing model.

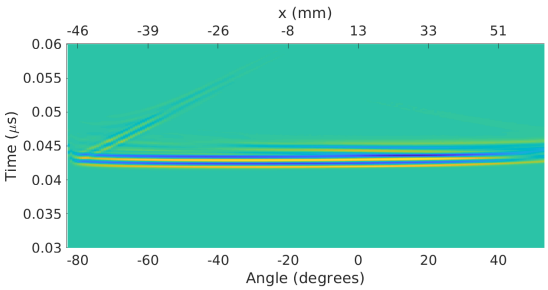

(b) Pressure field along an wavefront arc by the thin lens model.

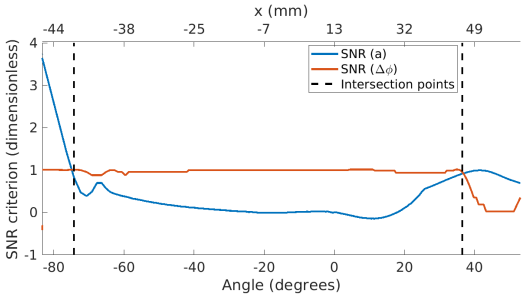

(c) SNR criterion along an wavefront arc by the ray tracing model.

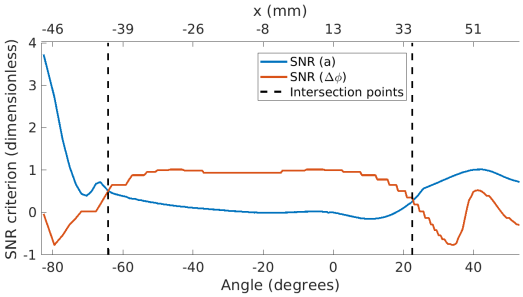

(d) SNR criterion along an wavefront arc by the thin lens model.

Figure 7.10: Examples of the simulated pressure fields for case number 3, along a constant TOF wavefront arc predicted by the ray tracing model (a) and the thin lens model (b). In the second row, the SNR criterion calculated using eq. (7.27) and eq. (7.28) from the pressure fields. The figure is reprinted from Paper 6.

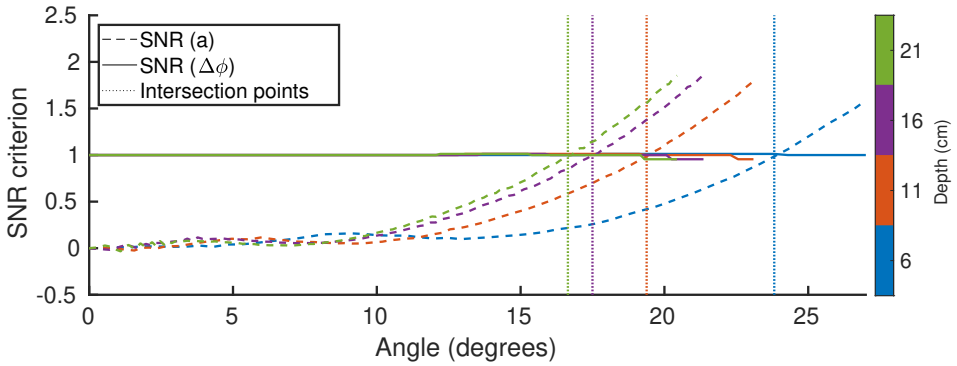

Figure 7.11: The variation in the calculated SNR criterion for the simulated sound field transmitted by the center element of the 128 + 128 element RCA, at four different depths. The figure is reprinted from Paper 6.

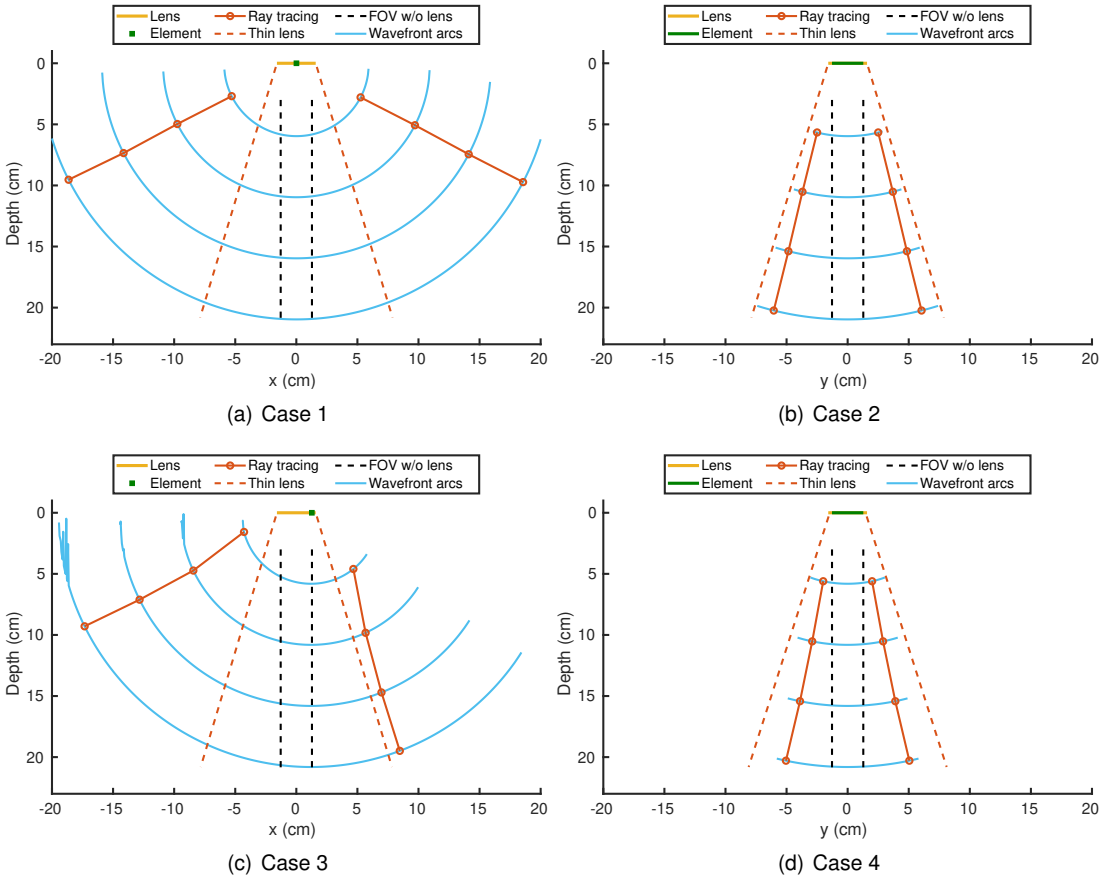

Figure 7.12: Illustrations of the positions of the wavefront arcs calculated by the ray tracing model, and the corresponding usable FOV, varying with depth. The figure is reprinted from Paper 6.

FOV was evaluated are given in Section II of Paper 6. The calculated FOV for all the simulated elements and its variation with depth are plotted in Fig. 10 of Paper 6. It shows that in the direction orthogonal to the emitting elements, the calculated usable FOVs varied with element index. This occurs because the position of the emitting element affects where the sound intersects the lens boundary, and thus how much it is refracted. Observations of the simulated emitted fields unveiled that the end of the lens curvature causes an edge wave, and this artefact degrades the usable FOV for the outermost elements in the transducer. For elements number 65 - 110, which seem to be unaffected by the edge wave artefact, the mean usable FOV was found to be $122° \pm 2°$, averaged across element number and depths. In the direction along the emitting elements, the variation in calculated FOV with elements number 65 - 110 had a maximum standard deviation of only 0.9°. The FOV averaged over element number declined with depth, from 51.2° to 28.5°. Fig. 7.11 shows the variation with propagation angle in the two parts of the SNR criterion calculated from the emission from the center element at four depths.

As example cases, in Fig. 7.12, the usable FOV evaluated for the elements and geometries outlined in Table 7.1 are illustrated as a function of depth. The illustrations also include the positions of the wavefront arcs, as calculated by the ray tracing model, the theoretical usable FOV predicted by eq. (6.5), and the FOV of the RCA without a lens.

7.6 Discussion: Lensed RCAs

Both the prediction of TOF to an observation line shown in Section 7.4 and the prediction of the position of an emitted wave shown in Section 7.5 have demonstrated that the ray tracing model can accurately predict the propagating of a transmitted wave from a lensed RCA. In Fig. 7.7(a), the simulated sound field and the predicted TOF are matched. This is supported by the calculated phase difference along the observation line, shown in Fig. 7.9(a), which is at most 0.0282 λ within the −3 dB width. Similarly, the simulated sound field to a wavefront arc predicted to have constant TOF by the ray tracing model, shown in Fig. 7.10(a), shows insignificant phase error along the arc. In Fig. 7.10(c), SNR($\Delta\phi$) is close to one within the usable FOV, indicating that the predicted position of the wavefront arc is accurate.

Paper 6 concludes that predicting the position of the emitted sound field using the thin lens model is less accurate than using the ray tracing model. As shown in Table 7.2, for the four example cases, using the ray tracing model results in higher usable FOV than using the thin lens model. Moreover, in Fig. 7.10(d), SNR($\Delta\phi$) deviates from one within the usable FOV, indicating that calculating the wavefront positions using the thin lens model has introduced phase errors to the expected plane wave. This means that if the thin lens model is used to predict τ when beamforming an image from the lensed RCA, the calculation would suffer from phase errors, leading to a degraded image contrast.

The predicted TOF using the ray tracing model appears to also match the measured sound field, shown in Fig. 7.8(a). The predicted TOF curve has the same shape as the intensity of the sound field, but with a time-shift. This is likely due to misalignment between the coordinate system of the transducer and of the hydrophone. As described in Section 7.4.1, the alignment procedure was only performed in the x-z-plane. Moreover, the transducer was removed from the water bath after the alignment procedure, to mount the lens. This might have caused a slight shift in either the x or y direction. Thus, the position of the hydrophone might have been shifted from the expected position at $y = 6.93\,\mathrm{mm}$. The TOF varies both along x and along y, and the misalignment will therefore have introduced a mismatch between the predicted TOF at $y = 6.93\,\mathrm{mm}$ and the sound field observed at some unknown y position. The misalignment issue is also observable in the delayed sound field, shown in Fig. 7.8(b). Here, the sound field appears slightly tilted, likely due to a rotation of the coordinate system used by the transducer, compared with the coordinate system used by the hydrophone. The rotation might have been introduced when mounting the lens. It is clear that a more robust alignment protocol is needed in order to validate the ray tracing model with measured data. With a fully functional RCA, alignment could also be made in the y-z plane, but even so, the removal of the transducer from the water bath before measurement is likely to introduce position errors. Running the alignment protocol after mounting the lens requires careful consideration of how to create focused emissions through a defocusing lens and of where these foci will occur. Since the lens is double-curved, it is not possible to create straight focal lines, which are used when aligning an unlensed RCA. The complexity of creating a robust alignment procedure remains to be tackled before the ray tracing model can be fully validated experimentally. Nevertheless, the predicted TOF and the measured sound field appear to have a solid resemblance, and the calculated phase difference along the observation line, shown in Fig. 7.9(b), is less than 0.19 λ within the −3 dB width. This indicates a good correspondence between the measured sound field and the predicted TOF.

The variation in the SNR criterion for four depths, shown in Fig. 7.11, shows that SNR($\Delta\phi$) is constant with propagation angle, while SNR(a) increases. The angle at which SNR(a) starts to increase and intersect SNR($\Delta\phi$) decreases with depth. This indicates that it is the amplitude of the sound field, rather than the prediction of the TOF and the corresponding phase error, that limits the usable FOV. In the simulated sound field shown in Fig. 7.7(b) the −3 dB width is 64.5 mm, while in the corresponding measured sound field, shown in Fig. 7.8(b), the −3 dB width is only 17.5 mm. This discrepancy might have been caused by poor coupling between the transducer and the lens, due to a insufficient mounting mechanism, but it also points to a more significant attenuation issue. The sound field is captured by the hydrophone in water at $z = 30\,\mathrm{mm}$, and as shown in Fig. 7.8(a) the maximum recorded pressure is

only 6 kPa. When applied to an *in vivo* measurement, where attenuation through the image medium is significantly higher than in water, this will further reduce the usable FOV and the penetration depth of the lensed RCA. Thus, further studies are required to improve the coupling between the transducer and the lens and to reduce the attenuation through the lens medium.

Generally, the study of the FOV of the 128 + 128 element RCA made in Paper 6 shows that the usable FOV can be significantly improved by introducing a lens. This is demonstrated in the visualization of the FOV for the four example cases shown in Fig. 7.12. An average FOV of $122° \pm 2°$ in the direction orthogonal to the emitting elements and a 51.2° to 28.5° in the direction along the emitting elements. Notably, these FOVs indicate the area where the position of the transmitted sound field can be predicted accurately enough, and where the amplitude of the transmitted sound field is high enough to contribute constructively to the SNR. It does not, however, indicate the FOV for received sound. This has not yet been quantified, as the ray tracing model has only been formulated for transmitted sound. Nevertheless, it is reasonable to expect that, given adequate transmitted power and not too high attenuation of the received sound, similar FOV can be achieved by the receiving aperture as by the transmitting aperture. The two are, however, likely to be orthogonal on each other, so the final pulse-echo FOV will be limited by the smallest of the two, in each direction. However, more study is needed to confirm this presumption. Generally, the quantification of the transmitted FOV of the 128 + 128 element RCA indicate that using a lens will make volumetric imaging using RCAs much more clinically applicable. For example, as previously mentioned, the median size of a left kidney in an adult human is 11.2 cm × 5.8 cm × 4.6 cm (Emamian et al. 1993), and Fig. 7.12 shows that at approximately 9 cm to 10 cm depth, the usable FOV is 37.2 cm × 12.1 cm. This indicates, given that an appropriate positioning of the transducer in relation to the kidney can be achieved, that with the lens, the 128 + 128 element RCA can be used to image the whole human kidney at once.

CHAPTER 8

Conclusion

3D SRUI using a lensed CMUT RCA has the potential to greatly improve the clinical applicability of medical ultrasound. Here, three important developmental steps have been taken towards realizing the implementation of these techniques. Firstly, it has been shown that CEUS imaging with a CMUT is attainable, despite the nonlinear emission from the transducer. Secondly, 3D ULM with a RCA has been demonstrated on a phantom. Lastly, a ray tracing model has been developed for predicting the refraction through a concave diverging lens. Together these steps move towards making it possible to make non-invasive images of the microvasculature with microscopic resolution and a macroscopic FOV.

Firstly, it has been shown that with the appropriate choice of minor sequence, CEUS imaging with a CMUT produce contrast enhancement comparable to imaging with conventional PZT arrays. CEUS imaging using CMUT is challenging because the cancellation of linearly back-scattered signals needed to achieve contrast-enhancement can be disrupted by the emission of nonlinear harmonics from the CMUT. The use of CMUTs for CEUS imaging has therefore been disputed. However, Fouan and Bouakaz (2016) suggested a three-pulse AM sequence that is unaffected by the emission of the harmonics. Here, theoretic formulation of the signals received when applying the sequence have confirmed that the sequence successfully eliminates linearly back-scattered signals, while maintaining signal at the emitted frequency, which has been nonlinearly back-scattered by the microbubble contrast agents. Moreover, measurement of the CTR of images of microbubbles flowing through a phantom have shown that the three-pulse AM sequence outperforms both the PI sequence and the two-pulse AM sequence. The amount of harmonic distortion of the signals emitted by the CMUT increase as the applied V_{AC} increases. Despite this, the contrast-enhancement achieved by the three-pulse AM sequence did not decline as V_{AC} was increased, and the sequence achieved an average increase in CTR of 35.3 dB compared with B-mode. This further reinforces that the performance of the sequence is independent of the emitted harmonics. Furthermore, the measurements of CTR revealed that the performance of the three-pulse AM sequence was comparable when emitted by a CMUT and a corresponding PZT array. However, quantification of the SNR of the two probes pointed to a difference in SNR, and it was speculated that the electrical shielding of the CMUT was not satisfactory. The measurements of CTR suggest that with improvement of the SNR of the CMUT, it can be used effectively for SRUI.

Secondly, 3D SRUI of a microflow phantom was performed using a 62 + 62 element PZT RCA. The resulting image clearly shows the 3D flow channel inside the phantom, and thus demonstrates visually that the flowing microbubbles have been localized correctly. Furthermore, quantification of the precision of the microbubble localization was performed by Jensen et al. (2020) based on the known inner dimensions of the phantom. Jensen et al. (2020) concluded that the image was super-resolved. No two objects laying closer than the diffraction limit have been imaged and resolved, and the image thus does not satisfy the super-resolution definition by Christensen-Jeffries et al. (2020). However, the localization precision was an order of magnitude smaller than the size of the PSF, and this indicates that the imaging set-up would have been able to resolve two objects laying closer than the diffraction limit, had they been imaged. Therefore, a second phantom design with three "V"-shapes with decreasing channel separation was designed. In future works, this phantom can be used to demonstrate that the diffraction limit can be overcome and to quantify the limit of how closely placed two channels lay and still be resolved. Using a 3D printed phantom has provided the possibility of quantifying the localization precision of the imaging set-up, based on the known dimensions of the phantom. This knowledge of the ground-truth of the imaged vasculature

makes it possible to validate that the structures seen in the image match the structures imaged. This is valuable when developing SRUI techniques, and difficult to achieve *in vivo*.

Lastly, in order to make beamforming of images made by lensed RCA possible, the prediction of the refraction of sound rays through a concave lens was studied. Predicting the TOF of the sound transmitted and received by the array is crucial in order to accurately delay the signals during DAS beamforming. Initially, the thin lens model suggested by (Bouzari et al. 2017) was implemented and sound fields refracted through a thin lens were simulated using Field II. It was shown that there was no phase difference along simulated emitted sound fields. Moreover, simulations of the PSF of a 62 + 62 element RCA emitting a single-element SA using both a flat transducer and a thin lensed transducer found no difference in the FWHM of the PSF. Both these findings validate that the thin lens model has been correctly implemented, and that the model suggested by (Bouzari et al. 2017) accurately describes the emission and reception of a RCA with curved elements. However, this cannot be taken as validation that the model represents refraction through a real lens, because the short-comings of the model are not revealed by simulations using curved elements. The thin lens model is based on the paraxial approximation, which greatly simplifies the geometry of the sound rays traveling through the lens. Using this simplification, it is possible to define a single focal point for the lens, which is unrealistic when a real lens of finite thickness is used.

Therefore, refraction through a concave lens was described using the ray tracing model. The model accounts for refraction through the lens by implementing Snell's law each time a sound ray intersects the lens boundary. The thin lens model and the ray tracing model were compared by delaying a sound field emitted by a lensed RCA and simulated using FEM by the positions predicted to have a constant TOF by the two models. The comparison showed that less phase difference occurred across the sound field delayed using the positions predicted by the ray tracing model. By applying the Oddershede and Jensen (2007) SNR criterion, the usable FOV of the transducer was quantified. For four example cases, prediction of the position of the emitted wavefront using the thin lens model resulted in smaller or equal FOVs than when using the ray tracing model. Thus, the ray tracing model predicts the refraction through the lens more accurately than the thin lens model. The accuracy of the ray tracing model was further validated by comparing its prediction of TOF with the time traveled by a wavefront observed at a line beneath a lensed RCA using both FEM simulations and hydrophone measurements. The comparison showed that when the simulated sound field was delayed by the predicted TOF, the largest phase difference across the sound field was at most $0.0282\,\lambda$. In the measured sound field, the phase difference was up to $0.19\,\lambda$, but this increase is likely caused by poor alignment between hydrophone and the transducer. The comparison of the predicted TOF with the simulated and measured wavefronts further support the applicability of the ray tracing model.

The drawback of the ray tracing model is its complexity. Using the ray tracing model it is not possible to define a single focal point for the lens and the model equations are intricate. The model is so complex that formulation of an analytic relationship for predicting the TOF of a sound wave, given its position, has not been achieved. Instead, a backwards interpolation method has been proposed. By repeated calculation of the position of a wavefront, given a range of TOFs, the TOF of a desired position can be found using interpolation. To beamform a 3D image, this operation has to be performed for every voxel in a 3D grid. This makes the implementation of the model computationally demanding, and considerate optimization of the efficiency of the algorithm is required before it can be implemented in a clinically useful setting. Moreover, due to the complexity of the model geometry, at the current stage it has only been implemented for transmitted sound waves. Therefore, before the ray tracing model can be used to beamform signals received on a lensed RCA the ray tracing model should also be formulated for received sound waves.

The ray tracing model was applied to evaluate the usable FOV for a lensed 128 + 128 element RCA. During the evaluation, it was also discovered that for the elements laying close to the end of the transmitting aperture, an edge wave caused by the sharp corner between the lens curvature and its baffle created a node in the emitted wavefront and thus limited the usable FOV. In future designs of lensed RCA, this should be avoided. It is proposed that the corner can be rounded, or the size of the lens in relation to the aperture can

be adjusted. However, for the elements in the transmitting aperture that were unaffected by the edge wave, the FOV was, on average, found to be $122° \pm 2°$ in the direction orthogonal to the emitting elements and 51.2° to 28.5° in the direction along the emitting elements. This indicates that the usable FOV is large enough to image a whole human kidney, and shows clearly the advantage of using a lens on a RCA to create a macroscopic FOV.

Thus, it has been demonstrated that a macroscopic FOV can be obtained using a lensed RCA, and that a microscopic resolution can be achieved using SRUI by a RCA. Further development of the prediction of the TOF through a lens when receiving sound is needed before the two techniques can be combined, but the findings indicate that this is attainable. Moreover, in the future, design of RCAs for SRUI can take advantage of the design features which are possible with CMUTs, but not with PZT arrays. The array can be designed larger, without compromising the pitch and the corresponding center frequency of the array. Together with a large bandwidth, the array can thus be designed to have high resolution, which in turn benefits the frame rate of the SRUI, and consequently the time it takes to use SRUI on a patient. Ultimately, by designing a lensed RCA using the CMUT technology, hopes are that in the future, SRUI can be made so time-efficient, and with such a large FOV and high resolution that it will be the preferred tool for diagnosing and observing microvascular diseases.

Bibliography

References from Summary

Marmottant, P., S. van der Meer, M. Emmer, M. Verskuis, N. de Jong, S. Hilgenfe, and D. Lohse (2005). "A model for large amplitude oscillations of coated bubbles accounting for buckling and rupture". In: *J. Acoust. Soc. Am.* 118, pp. 3499–3505 (cit. on p. vii).

References from Chapter 1

Ackermann, D. and G. Schmitz (Jan. 2016). "Detection and Tracking of Multiple Microbubbles in Ultrasound B-Mode Images". In: *IEEE Trans. Ultrason., Ferroelec., Freq. Contr.* 63.1, pp. 72–82 (cit. on pp. 2, 3).

Beckman, J. A., M. S. Duncan, S. M. Damrauer, Q. S. Wells, J. V. Barnett, D. H. Wasserman, R. J. Bedimo, A. A. Butt, V. C. Marconi, J. J. Sico, H. A. Tindle, and M. P. Bonaca (2019). "Microvascular Disease, Peripheral Artery Disease, and Amputation". In: *Circulation* 140, pp. 449–458 (cit. on p. 2).

Bouzari, H., M. Engholm, C. Beers, S. I. Nikolov, M. B. Stuart, E. V. Thomsen, and J. A. Jensen (2018). "Curvilinear 3-D Imaging Using Row–Column Addressed 2-D Arrays with a Diverging Lens: Phantom Study". In: *IEEE Trans. Ultrason., Ferroelec., Freq. Contr.* 65.7, pp. 1182–1192. DOI: 10.1109/TUFFC.2018.2836384 (cit. on p. 4).

Bouzari, H., M. Engholm, C. Beers, M. B. Stuart, S. I. Nikolov, E. V. Thomsen, and J. A. Jensen (2017). "Curvilinear 3-D Imaging Using Row-Column-Addressed 2-D Arrays with a Diverging Lens: Feasibility Study". In: *IEEE Trans. Ultrason., Ferroelec., Freq. Contr.* 99, pp. 978–988. DOI: 10.1109/TUFFC.2017.2687521 (cit. on pp. 3, 4, 10).

Bouzari, H., M. Engholm, T. L. Christiansen, C. Beers, A. Lei, M. B. Stuart, S. I. Nikolov, E. V. Thomsen, and J. A. Jensen (2016). "Volumetric Synthetic Aperture Imaging with a Piezoelectric 2-D Row-Column Probe". In: *Proc. SPIE Med. Imag.* Vol. 9790, pp. 1–9 (cit. on p. 3).

Bouzari, H., M. Engholm, S. I. Nikolov, M. B. Stuart, E. V. Thomsen, and J. A. Jensen (2019). "Imaging Performance for Two Row-Column Arrays". In: *IEEE Trans. Ultrason., Ferroelec., Freq. Contr.* 66.7, pp. 1209–1221. DOI: 10.1109/TUFFC.2019.2914348 (cit. on p. 1).

Christensen-Jeffries, K., R. J. Browning, M. Tang, C. Dunsby, and R. J. Eckersley (Feb. 2015). "In Vivo Acoustic Super-Resolution and Super-Resolved Velocity Mapping Using Microbubbles". In: *IEEE Trans. Med. Imag.* 34.2, pp. 433–440 (cit. on pp. 1–3).

Christensen-Jeffries, K., O. Couture, P. A. Dayton, Y. C. Eldar, K. Hynynen, F. Kiessling, M. O'Reilly, G. F. Pinton, G. Schmitz, M. Tang, et al. (2020). "Super-resolution ultrasound imaging". In: *Ultrasound Med. Biol.* 46.4, pp. 865–891 (cit. on pp. 2, 3).

Couture, O., B. Besson, G. Montaldo, M. Fink, and M. Tanter (2011). "Microbubble ultrasound super-localization imaging (MUSLI)". In: *Proc. IEEE Ultrason. Symp.* Pp. 1285–1287 (cit. on p. 2).

Davidsen, R. E., J. A. Jensen, and S. W. Smith (July 1994). "Two-Dimensional Random Arrays for Real Time Volumetric Imaging". In: *Ultrason. Imaging* 16.3, pp. 143–163 (cit. on p. 1).

de Jong, N., M. Emmer, A. van Wame, and M. Versluis (2009). "Ultrasonic characterization of ultrasound contrast agents". In: *Med. Biol. Eng. Comp.* 47.8, pp. 861–873 (cit. on p. 6).

Démoré, C. E. M., A. W. Joyce, K. Wall, and G. R. Lockwood (2009). "Real-time volume imaging using a crossed electrode array". In: *IEEE Trans. Ultrason., Ferroelec., Freq. Contr.* 56.6, pp. 1252–1261 (cit. on p. 4).

Eckersley, R. J., C. T. Chin, and P. N. Burns (2005). "Optimising phase and amplitude modulation schemes for imaging microbubble contrast agents at low acoustic power". In: *Ultrasound Med. Biol.* 31.2, pp. 213–219 (cit. on p. 4).

Edler, Inge and C. H. Hertz (1954). "The use of ultrasonic reflectoscope for the continuous recording of the movement of heart walls". In: *Kungl. Fysiogr. Sällskap. i Lund Föhandl* 24, pp. 40–58 (cit. on p. 1).

Emamian, S. A., M. B. Nielsen, J. F. Pedersen, and L. Ytte (1993). "Kidney Dimensions at Sonography: Correlation with Age, Sex, and Habitus in 665 Adult Volunteers". In: *American Journal of Roentgenology* 160, pp. 83–86 (cit. on p. 3).

Engholm, M., H. Bouzari, C. Beers, J. A. Jensen, and E. V. Thomsen (2018). "Increasing the field-of-view of row-column-addressed ultrasound transducers: implementation of a diverging compound lens". In: *Ultrasonics* 88, pp. 97–105. DOI: 10.1016/j.ultras.2018.02.001 (cit. on p. 4).

Errico, C., J. Pierre, S. Pezet, Y. Desailly, Z. Lenkei, O. Couture, and M. Tanter (Nov. 2015). "Ultrafast ultrasound localization microscopy for deep super-resolution vascular imaging". In: *Nature* 527, pp. 499–502 (cit. on pp. 1, 2).

Ferin, G., M. C. Dumoux, M. Flesch, E. Montauban, A. Lejeune, B. Rosinski, T. Mateo, J. Poree, J. Sauvage, T. Deffieux, M. Pernot, M. Tanter, and A. Nguyen-Dinh (2018). "A Novel Row-Column Addressed Stack Architecture for Enhanced Cardiac Imaging". In: *Proc. IEEE Ultrason. Symp.* Pp. 1–4 (cit. on p. 4).

Foiret, J., H. Zhang, T. Ilovitsh, L. Mahakian, S. Tam, and K. W. Ferrara (2017). "Ultrasound localization microscopy to image and assess microvasculature in a rat kidney". In: *Scientific Reports* 7.1, 13662:1–12. DOI: 10.1038/s41598-017-13676-7 (cit. on p. 3).

Fowler, M. J. (2011). "Microvascular and Macrovascular Complications of Diabetes". In: *Clinical diabetes* 29.3, pp. 116–122 (cit. on p. 2).

Grass, R. S., K. Steenberg, A. S. Havreland, M. Engholm, and E. V. Thomsen (2020). "Large Scale High Voltage 192+192 Row-Column Addressed CMUTs Made with Anodic Bonding". In: *Proc. IEEE Ultrason. Symp.* Pp. 1–4 (cit. on p. 4).

Haller, M. I. and B. T. Khuri-Yakub (1994). "A surface micromachined electrostatic ultrasonic air transducer". In: *Proc. IEEE Ultrason. Symp.* Vol. 2, pp. 1241–1244 (cit. on p. 4).

Hanahan, D. and R. A. Weinberg (2011). "Hallmarks of Cancer: The Next Generation". In: *Cell* 144, pp. 646–674 (cit. on p. 2).

Hansen, K. B., C. A. Villagomez-Hoyos, J.C. Brasen, K. Diamantis, V. Sboros, C. M. Sørensen, and J. A. Jensen (2016). "Robust Microbubble Tracking for Super Resolution Imaging in Ultrasound". In: *Proc. IEEE Ultrason. Symp.* Pp. 1–4 (cit. on p. 2).

Harput, S., K. Christensen-Jeffires, J. Brown, J. Zhu, G. Zhang, R. J. Eckersley, C. Dunsby, and Meng-Xing Tang (2018). "3-D Motion Correction for Volumetric Super-Resolution Ultrasound Imaging". In: *Proc. IEEE Ultrason. Symp.* (Cit. on p. 3).

Hingot, V., A. Chavignon, B. Heiles, and O. Couture (2021). "Measuring image resolution in Ultrasound Localization Microscopy". In: *IEEE Trans. Med. Imag.* (Cit. on pp. 2, 3).

Hingot, V., C. Errico, B. Heiles, L. Rahal, M. Tanter, and O. Couture (2019). "Microvascular flow dictates the compromise between spatial resolution and acquisition time in Ultrasound Localization Microscopy". In: *Scientific Reports* 9.1, pp. 1–10. DOI: 10.1038/s41598-018-38349-x (cit. on pp. 2, 3).

Hingot, V., C. Errico, M. Tanter, and O. Couture (2017). "Subwavelength motion-correction for ultrafast ultrasound localization microscopy". In: *Ultrasonics* 77, pp. 17–21. DOI: 10.1016/j.ultras.2017.01.008 (cit. on p. 1).

Holbek, S., T. L. Christiansen, M. F. Rasmussen, M. B. Stuart, E. V. Thomsen, and J. A. Jensen (2015). "3-D vector velocity estimation with row-column addressed arrays". In: *Proc. IEEE Ultrason. Symp.* Pp. 1–4 (cit. on pp. 1, 3).

Howry, D. H. and W. R. Bliss (1952). "Ultrasonic visualization of soft tissue structures of the body". In: *J. Lab. Clin. Med.* 40, pp. 579–592 (cit. on p. 1).

Jensen, J. A. (2002). "Ultrasound imaging and its modeling". In: *Imaging of Complex Media with Acoustic and Seismic Waves*. Berlin: Springer-Verlag, pp. 135–165 (cit. on p. 3).

Jensen, J. A., J. Kortbek, S. I. Nikolov, M. C. Hemmsen, and B. Tomov (2010). "Implementation of Synthetic Aperture Imaging in Medical Ultrasound: The Dual Stage Beamformer Approach". In: *EUSAR*, pp. 434–437 (cit. on p. 6).

Jensen, J. A., S. Nikolov, K. L. Gammelmark, and M. H. Pedersen (2006). "Synthetic Aperture Ultrasound Imaging". In: *Ultrasonics* 44, e5–e15 (cit. on p. 6).

Joyce, A. W. and G. R. Lockwood (2014). "Crossed-array transducer for real-time 3D imaging". In: *Proc. IEEE Ultrason. Symp.* Pp. 2116–2120. DOI: 10.1109/ULTSYM.2014.0527 (cit. on p. 4).

Kamaya, A., S. Machtaler, S. S. Sanjani, A. Nikoozadeh, F. G. Sommer, B. T. Khuri-Yakub, J. K. Willmann, and T. S. Desser (2013). "New Technologies in Clinical Ultrasound". In: *Seminars in Roentgenology*, pp. 214–223 (cit. on p. 4).

Lenasi, H. (2016). "Microcirculation Revisited - From Molecules to Clinical Practice". In: ed. by H. Lenasi. Books on Demand. Chap. Microcirculation in Healt and disease, pp. 1–9 (cit. on p. 2).

Lin, F., S. E. Shelton, D. Espindola, J. D. Rojas, G. Pinton, and P. A. Dayton (2017). "3-D Ultrasound Localization Microscopy for Identifying Microvascular Morphology Features of Tumor Angiogenesis at a Resolution Beyond the Diffraction Limit of Conventional Ultrasound". In: *Theranostics* 7.1, pp. 196–204. DOI: 10.7150/thno.16899 (cit. on p. 3).

Martin, K. H., B. D. Lindsey, J. Ma, M. Lee, S. Li, F. S. Foster, X. Jiang, and P. A. Dayton (2014). "Dual-Frequency Piezoelectric Transducers for Contrast Enhanced Ultrasound Imaging". In: *Sensors*, pp. 20825–20842 (cit. on p. 4).

Morton, C. E. and G. R. Lockwood (2003). "Theoretical assessment of a crossed electrode 2-D array for 3-D imaging". In: *Proc. IEEE Ultrason. Symp.* Pp. 968–971 (cit. on p. 1).

Niederhuber, J. E., J. O. Armitage, M. B. Kastan, J. H. Doroshow, and J. E. Tepper (2020). *Abeloff's Clinical Oncology*. 6th ed. Elsevier Inc. (cit. on p. 2).

O'Reilly, M. A. and K. Hynynen (2013). "A super-resolution ultrasound method for brain vascular mapping". In: *Med. Phys.* 40.11, pp. 110701–7. DOI: 10.1118/1.4823762 (cit. on p. 2).

Ommen, M. L., K. F. Pedersen, and E. V. Thomsen (2021). "Automatic optical failure detection on large ultrasonic arrays". In: *Proc. IEEE Ultrason. Symp.* Pp. 1–4 (cit. on p. 4).

Oralkan, O., A. S. Ergun, J. A. Johnson, M. Karaman, U. Demirci, K. Kaviani, T. H. Lee, and B. T. Khuri-Yakub (2002). "Capacitive micromachined ultrasonic transducers: Next-generation arrays for acoustic imaging?" In: *IEEE Trans. Ultrason., Ferroelec., Freq. Contr.* 49, pp. 1596–1610 (cit. on p. 4).

Rasmussen, M. F., T. L. Christiansen, E. V. Thomsen, and J. A. Jensen (2015). "3-D Imaging Using Row–Column-Addressed Arrays With Integrated Apodization — Part I: Apodization Design and Line Element Beamforming". In: *IEEE Trans. Ultrason., Ferroelec., Freq. Contr.* 62.5, pp. 947–958. DOI: 10.1109/TUFFC.2014.006531 (cit. on p. 1).

Rasmussen, M. F. and J. A. Jensen (2013). "3D ultrasound imaging performance of a row-column addressed 2D array transducer: a simulation study". In: *Proc. SPIE Med. Imag.* 86750C, pp. 1–11 (cit. on p. 1).

Rayleigh, J. W. S. (1945). *The theory of sound*. Vol. II. New York: Dover (cit. on p. 1).

Rindal, O. M. H., A. Austeng, and A. Fatemi (2019). "The Effect of Dynamic Range Alterations in the Estimation of Contrast". In: *IEEE Trans. Ultrason., Ferroelec., Freq. Contr.* 66.7, pp. 1198–1208 (cit. on p. 4).

Sampaleanu, A., P. Zhang, A. Kshirsagar, W. Moussa, and R. Zemp (2014). "Top-orthogonal-to-bottom-electrode (TOBE) CMUT arrays for 3-D ultrasound imaging." In: *IEEE Trans. Ultrason., Ferroelec., Freq. Contr.* 61.2, pp. 266–276 (cit. on p. 1).

Sauvage, J., M. Flesch, G. Ferin, A. Nguyen-Dinh, J. Poree, M. Tanter, M. Pernot, and T. Deffieux (2018). "A large aperture row column addressed probe for in vivo 4D ultrafast doppler ultrasound imaging". In: *Phys. Med. Biol.* 63, pp. 1–12 (cit. on pp. 1, 3).

Sauvage, J., J. Porée, C. Rabut, G. Férin, M. Flesch, B. Rosinski, A. Nguyen-Dinh, M. Tanter, M. Pernot, and T. Deffieux (June 2020). "4D Functional imaging of the rat brain using a large aperture row-column array". In: *IEEE Trans. Med. Imag.* 39.6, pp. 1884–1893. DOI: 10.1109/TMI.2019.2959833 (cit. on p. 1).

Savoia, A. S., G. Caliano, and M. Pappalardo (2012). "A CMUT Probe for Medical Ultrasonography: From Microfabrication to System Integration". In: *IEEE Trans. Ultrason., Ferroelec., Freq. Contr.* 59.6, pp. 1127–1138 (cit. on p. 4).

Schou, M., L. T. Jørgensen, C. Beers, M. S. Traberg, B. G. Tomov, M. B. Stuart, and J. A. Jensen (2020). "Fast 3-D Velocity Estimation in 4-D using a 62 + 62 Row-Column Addressed Array". In: *IEEE Trans. Ultrason., Ferroelec., Freq. Contr.* 68.3, pp. 608–623. DOI: 10.1109/TUFFC.2020.3016991 (cit. on p. 1).

Seo, C. H. and J. T. Yen (Apr. 2009). "A 256 x 256 2-D array transducer with row-column addressing for 3-D rectilinear imaging". In: *IEEE Trans. Ultrason., Ferroelec., Freq. Contr.* 56.4, pp. 837–847 (cit. on p. 1).

Siepmann, M., G. Schmitz, J. Bzyl, M. Palmowski, and F. Kiessling (2011). "Imaging tumor vascularity by tracing single microbubbles". In: *Proc. IEEE Ultrason. Symp.* Pp. 6293297, 1906–1908. DOI: 10.1109/ULTSYM.2011.0476 (cit. on p. 2).

Smith, S. W., H. G. Pavy, and O. T. von Ramm (1991). "High speed ultrasound volumetric imaging system – Part I: Transducer design and beam steering". In: *IEEE Trans. Ultrason., Ferroelec., Freq. Contr.* 38, pp. 100–108 (cit. on p. 1).

Song, P., A. Manduca, J. D. Trzasko, R. E. Daigle, and S. Chen (2018). "On the Effects of Spatial Sampling Quantization in Super-Resolution Ultrasound Microvessel Imaging". In: *IEEE Trans. Ultrason., Ferroelec., Freq. Contr.* 65.12, pp. 2264–2276 (cit. on p. 2).

Soumekh, M. (1999). *Synthetic aperture radar. Signal processing with MATLAB algorithms*. New York: John Wiley & Sons, Inc. (cit. on p. 6).

Szabo, T. L. (2004). *Diagnostic ultrasound imaging inside out*. Elsevier (cit. on p. 3).

— (2014). *Diagnostic ultrasound imaging: Inside out*. 2nd ed. Elsevier (Oxford, UK) (cit. on pp. 1, 3).

Taghavi, I., S. B. Andersen, C. A. V. Hoyos, M. B. Nielsen, C. M. Sørensen, and J. A. Jensen (2021). "In Vivo Motion Correction in Super Resolution Imaging of Rat Kidneys". In: *IEEE Trans. Ultrason., Ferroelec., Freq. Contr.* 68.10, pp. 3082–3093 (cit. on p. 1).

Taghavi, I., S. B. Andersen, C. A. V. Hoyos, M. Schou, S. H. Øygard, F. Gran, K. L. Hansen, C. M. Sørensen, M. B. Nielsen, M. B. Stuart, and J. A. Jensen (2020). "Tracking Performance in Ultrasound Super-Resolution Imaging". In: *Proc. IEEE Ultrason. Symp.* Pp. 1–4 (cit. on p. 2).

Tanter, M. and M. Fink (Jan. 2014). "Ultrafast imaging in biomedical ultrasound". In: *IEEE Trans. Ultrason., Ferroelec., Freq. Contr.* 61.1, pp. 102–119. DOI: 10.1109/TUFFC.2014.6689779 (cit. on p. 6).

von Ramm, O. T., S. W. Smith, and Henry G. Pavy (1991). "High speed ultrasound volumetric imaging system – Part II: Parallel processing and image display". In: *IEEE Trans. Ultrason., Ferroelec., Freq. Contr.* 38, pp. 109–115 (cit. on p. 1).

Wild, J. J. (1950). "The use of ultrasonic pulses for the measurement of biologic tissues and the detection of tissue density changes". In: *Surgery* 27, pp. 183–188 (cit. on p. 1).

Yeh, D. T., O. Oralkan, A. S. Ergun, X. Zhuang, I. O. Wygant, and B. T. Khuri-Yakub (2005). "High-frequency CMUT arrays for high-resolution medical imaging". In: *Proc. SPIE Med. Imag.* Pp. 87–98 (cit. on pp. 3, 4).

References from Chapter 2

Bouakaz, A., S. Frigstad, F. T. Cate, and N. de Jong (2002). "Super harmonic imaging: a new imaging technique for improved contrast detection". In: *Ultrasound Med. Biol.* 28.1, pp. 59–68 (cit. on p. 13).

Bouzari, H., M. Engholm, S. I. Nikolov, M. B. Stuart, E. V. Thomsen, and J. A. Jensen (2019). "Imaging Performance for Two Row-Column Arrays". In: *IEEE Trans. Ultrason., Ferroelec., Freq. Contr.* 66.7, pp. 1209–1221. DOI: 10.1109/TUFFC.2019.2914348 (cit. on p. 13).

Brock-Fischer, G. A., M. D. Poland, and P. G. Rafter (1996). *Means for increasing sensitivity in non linear ultrasound systems*. US Patent (5577505) (cit. on p. 13).

Brown, K. G. and K. Hoyt (2021). "Evaluation of Nonlinear Contrast Pulse Sequencing for Use in Super-Resolution Ultrasound Imaging". In: *IEEE Trans. Ultrason., Ferroelec., Freq. Contr.* 68.11, pp. 3347–3361 (cit. on pp. 12, 13).

Christensen-Jeffries, K., R. J. Browning, M. Tang, C. Dunsby, and R. J. Eckersley (Feb. 2015). "In Vivo Acoustic Super-Resolution and Super-Resolved Velocity Mapping Using Microbubbles". In: *IEEE Trans. Med. Imag.* 34.2, pp. 433–440 (cit. on p. 13).

Christensen-Jeffries, K., O. Couture, P. A. Dayton, Y. C. Eldar, K. Hynynen, F. Kiessling, M. O'Reilly, G. F. Pinton, G. Schmitz, M. Tang, et al. (2020). "Super-resolution ultrasound imaging". In: *Ultrasound Med. Biol.* 46.4, pp. 865–891 (cit. on p. 11).

Church, C. C. (1995). "The effects of an elastic solid surface layer on the radial pulsations of gas bubbles". In: *J. Acoust. Soc. Am.* 97.3, pp. 1510–1521 (cit. on p. 11).

Couture, O., M. Fink, and M. Tanter (2012). "Ultrasound Contrast Plane Wave Imaging". In: *IEEE Trans. Ultrason., Ferroelec., Freq. Contr.* 59.12, pp. 2676–2683. DOI: 10.1109/tuffc.2012.2508 (cit. on p. 13).

de Jong, N., M. Emmer, A. van Wame, and M. Versluis (2009). "Ultrasonic characterization of ultrasound contrast agents". In: *Med. Biol. Eng. Comp.* 47.8, pp. 861–873 (cit. on p. 14).

Dietrich, C. F., M. Averkiou, M. B. Nielsen, R. G. Barr, P. N. Burns, F. Calliada, V. Cantisani, B. Choi, M. C. Chammas, D. Clevert, et al. (2018). "How to perform contrast-enhanced ultrasound (CEUS)". In: *Ultrasound international open* 4.1, E2 (cit. on p. 11).

Eckersley, R. J., C. T. Chin, and P. N. Burns (2005). "Optimising phase and amplitude modulation schemes for imaging microbubble contrast agents at low acoustic power". In: *Ultrasound Med. Biol.* 31.2, pp. 213–219 (cit. on p. 13).

Foiret, J., H. Zhang, T. Ilovitsh, L. Mahakian, S. Tam, and K. W. Ferrara (2017). "Ultrasound localization microscopy to image and assess microvasculature in a rat kidney". In: *Scientific Reports* 7.1, 13662:1–12. DOI: 10.1038/s41598-017-13676-7 (cit. on p. 13).

Gorce, J.M., M.Arditi, and M. Schneider (Nov. 2000). "Influence of bubble size distribution on the echogenicity of ultrasound contrast agents: a study of SonoVue." In: *Invest. Radiol.* 35.11, pp. 661–671. URL: http://www.ncbi.nlm.nih.gov/pubmed/11110302 (cit. on p. 14).

Hansen, K. B., C. A. Villagomez-Hoyos, J.C. Brasen, K. Diamantis, V. Sboros, C. M. Sørensen, and J. A. Jensen (2016). "Robust Microbubble Tracking for Super Resolution Imaging in Ultrasound". In: *Proc. IEEE Ultrason. Symp.* Pp. 1–4 (cit. on p. 13).

Hoff, L., P. C. Sontum, and J. M. Hovem (2000). "Oscillations of polymeric microbubbles: Effect of the encapsulating shell". In: *J. Acoust. Soc. Am.* 107, pp. 2272–2280 (cit. on p. 11).

Jensen, J. A., J. Kortbek, S. I. Nikolov, M. C. Hemmsen, and B. Tomov (2010). "Implementation of Synthetic Aperture Imaging in Medical Ultrasound: The Dual Stage Beamformer Approach". In: *EUSAR*, pp. 434–437 (cit. on p. 13).

Jong, N. de, F. J. Ten Cate, C. T. Lancée, J. R. T. C. Roeland, and N. Bom (1991). "Principles and recent developments in ultrasound contrast agents". In: *Ultrasonics* 29, pp. 324–330 (cit. on p. 11).

Jong, N. de, R. Cornet, and C. T. Lancee (1994). "Higher Harmonics of Vibrating Gas-Filled Microspheres. Part Two: Measurements". In: *Ultrasonics* 1994.32, pp. 455–459 (cit. on p. 11).

Leighton, T.G. (1994). *The Acoustic Bubble*. London: Elsevier Inc. (cit. on p. 11).

Marmottant, P., S. van der Meer, M. Emmer, M. Verskuis, N. de Jong, S. Hilgenfe, and D. Lohse (2005). "A model for large amplitude oscillations of coated bubbles accounting for buckling and rupture". In: *J. Acoust. Soc. Am.* 118, pp. 3499–3505 (cit. on pp. 11, 12, 14, 15).

Morgan, K.E., J.S. Allen, P.A. Dayton, J.E. Chomas, A.L. Klibanov, and K.W. Ferrara (2000). "Experimental and Theoretical Evaluation of Microbubble Behavior: Effect of Transmitted Phase and Bubble Size". In: *IEEE Trans. Ultrason., Ferroelec., Freq. Contr.* 47.6, pp. 1494–1509 (cit. on p. 11).

Rasmussen, M. F. and J. A. Jensen (2013). "3D ultrasound imaging performance of a row-column addressed 2D array transducer: a simulation study". In: *Proc. SPIE Med. Imag.* 86750C, pp. 1–11 (cit. on p. 13).

S.p.A., Bracco Imaging (2001). *SonoVue - Summary of product characteristics*. URL: `www.ema.europa.eu/en/documents/product-information` (cit. on p. 14).

Schneider, M. (1999). "Characteristics of SonoVue". In: *Echocardiography* 16.1, pp. 743–746 (cit. on p. 16).

Tang, M. X., H. Mulvana, T. Gauthier, A. K. P. Lim, D. O. Cosgrove, R. J. Eckersley, and E. Stride (2011). "Quantitative contrast-enhanced ultrasound imaging: a review of sources of variability". In: *Interface Focus* 1.4, pp. 520–539 (cit. on p. 11).

References from Chapter 3

Certon, D., F. Teston, and F. Patat (2005). "A finite difference model for CMUT devices". In: *IEEE Trans. Ultrason., Ferroelec., Freq. Contr.* 52.12, pp. 2199–2210 (cit. on p. 19).

Chomas, J. E., P. Dayton, J. Allen, K. Morgan, and K.W. Ferrara (2001). "Mechanisms of contrast agent destruction". In: *IEEE Trans. Ultrason., Ferroelec., Freq. Contr.* 48.1, pp. 232–248 (cit. on p. 27).

Christensen-Jeffries, K., O. Couture, P. A. Dayton, Y. C. Eldar, K. Hynynen, F. Kiessling, M. O'Reilly, G. F. Pinton, G. Schmitz, M. Tang, et al. (2020). "Super-resolution ultrasound imaging". In: *Ultrasound Med. Biol.* 46.4, pp. 865–891 (cit. on p. 27).

Dayton, P.A., K. E. Morgan, A. L. Kilbanov, G. H. Brandenburger, and K. W. Ferrara (1999). "Optical and acoustical observations of the effects of ultrasound on contrast agents". In: *IEEE Trans. Ultrason., Ferroelec., Freq. Contr.* 46.1, pp. 220–232 (cit. on p. 27).

de Jong, N., M. Emmer, A. van Wame, and M. Versluis (2009). "Ultrasonic characterization of ultrasound contrast agents". In: *Med. Biol. Eng. Comp.* 47.8, pp. 861–873 (cit. on p. 27).

Diederichsen, S. E. (2020). "Micromachined Integrated Transducers for Ultrasound Imaging". PhD thesis. Denmark Technical University (cit. on pp. 23, 27).

Eckersley, R. J., C. T. Chin, and P. N. Burns (2005). "Optimising phase and amplitude modulation schemes for imaging microbubble contrast agents at low acoustic power". In: *Ultrasound Med. Biol.* 31.2, pp. 213–219 (cit. on pp. 20, 21).

Fouan, D. and A. Bouakaz (2016). "Investigation of Classical Pulse Sequences for Contrast-Enhanced Ultrasound Imaging With a CMUT Probe". In: *IEEE Trans. Ultrason., Ferroelec., Freq. Contr.* 63.10, pp. 1496–1503 (cit. on pp. 19, 20, 23).

Jin, X., Ö. Oralkan, F. L. Degertekin, and B. T. Khuri-Yakub (2001). "Characterization of One-Dimensional Capacitive Micromachined Ultrasonic Immersion Transducer Arrays". In: *IEEE Trans. Ultrason., Ferroelec., Freq. Contr.* 48.3, pp. 750–760 (cit. on p. 19).

Kinsler, L. E., A. R. Frey, A. B. Coppens, and J. V. Sanders (1982). *Fundamentals of Acoustics*. Third. New York: John Wiley & Sons (cit. on p. 19).

Lohfink, A. and P.-C. Eccardt (2005). "Linear and nonlinear equivalent circuit modeling of CMUTs". In: *IEEE Trans. Ultrason., Ferroelec., Freq. Contr.* 52.12, pp. 2163–2172 (cit. on p. 19).

Marmottant, P., S. van der Meer, M. Emmer, M. Verskuis, N. de Jong, S. Hilgenfe, and D. Lohse (2005). "A model for large amplitude oscillations of coated bubbles accounting for buckling and rupture". In: *J. Acoust. Soc. Am.* 118, pp. 3499–3505 (cit. on p. 27).

Martin, K. H., B. D. Lindsey, J. Ma, M. Lee, S. Li, F. S. Foster, X. Jiang, and P. A. Dayton (2014). "Dual-Frequency Piezoelectric Transducers for Contrast Enhanced Ultrasound Imaging". In: *Sensors*, pp. 20825–20842 (cit. on p. 19).

Meynier, C., F. Teston, and D. Certon (2010). "A multiscale model for array of capacitive micromachined ultrasonic transducers". In: *J. Acoust. Soc. Am.* 128.5, pp. 2549–2561 (cit. on p. 19).

Novell, A., A. Bouakaz, M. Legros, and N. Felix (2008). "Nonlinear contrast imaging with Capacitive Micromachined Transducers". In: *Proc. IEEE Ultrason. Symp.* (Cit. on pp. 19, 27).

— (2009). "Exploitation of capacitive micromachined transducers for nonlinear ultrasound imaging". In: *Proc. IEEE Ultrason. Symp.* Pp. 2733–2743 (cit. on pp. 19, 23).

Tang, M. X., H. Mulvana, T. Gauthier, A. K. P. Lim, D. O. Cosgrove, R. J. Eckersley, and E. Stride (2011). "Quantitative contrast-enhanced ultrasound imaging: a review of sources of variability". In: *Interface Focus* 1.4, pp. 520–539 (cit. on p. 27).

Thomas, D. H., M. Butler, T. Anderson, M. Emmer, H. Vos, M. Borden, E. Stride, N. de Jong, and V. Sboros (2012). "The quasi-stable lipid shelled microbubble in response to consecutive ultrasound pulses". In: *Appl. Phys. Lett.* 101.7 (cit. on p. 27).

References from Chapter 4

Bhuyan, A., J. W. Choe, B. C. Lee, I. O. Wygant, A. Nikoozadeh, Ö. Oralkan, and B. T. Khuri-Yakub (Dec. 2013). "Integrated Circuits for Volumetric Ultrasound Imaging With 2-D CMUT Arrays". In: *IEEE Trans. Ultrason., Ferroelec., Freq. Contr.* 7.6, pp. 796–804 (cit. on p. 34).

Bouzari, H., M. Engholm, S. I. Nikolov, M. B. Stuart, E. V. Thomsen, and J. A. Jensen (2019). "Imaging Performance for Two Row-Column Arrays". In: *IEEE Trans. Ultrason., Ferroelec., Freq. Contr.* 66.7, pp. 1209–1221. DOI: 10.1109/TUFFC.2019.2914348 (cit. on p. 31).

Christiansen, T. L. (2015). "Micromachined Ultrasonic Transducers for 3-D Imaging". PhD thesis. Technical University of Denmark (cit. on p. 35).

Christiansen, T. L., M. F. Rasmussen, J. P. Bagge, L. N. Moesner, J. A. Jensen, and E. V. Thomsen (2015). "3-D Imaging Using Row–Column-Addressed Arrays With Integrated Apodization — Part II: Transducer Fabrication and Experimental Results". In: *IEEE Trans. Ultrason., Ferroelec., Freq. Contr.* 62.5, pp. 959–971. DOI: 10.1109/tuffc.2014.006819 (cit. on pp. 29, 33).

Démoré, C. E. M., A. W. Joyce, K. Wall, and G. R. Lockwood (2009). "Real-time volume imaging using a crossed electrode array". In: *IEEE Trans. Ultrason., Ferroelec., Freq. Contr.* 56.6, pp. 1252–1261 (cit. on p. 29).

Diederichsen, S. E. (2020). "Micromachined Integrated Transducers for Ultrasound Imaging". PhD thesis. Denmark Technical University (cit. on p. 35).

Engholm, M., C. Beers, A. S. Havreland, B. G. Tomov, J. A. Jensen, and E. V. Thomsen (2018a). "A Row-Column-Addressed 2D Probe with an Integrated Compound Diverging Lens". In: *Proc. IEEE Ultrason. Symp.* (Cit. on p. 35).

Engholm, M., H. Bouzari, T. L. Christiansen, C. Beers, J. P. Bagge, L. N. Moesner, S. E. Diederichsen, M. B. Stuart, J. A. Jensen, and E. V. Thomsen (2018b). "Probe development of CMUT and PZT Row–Column-Addressed 2-D Arrays". In: *Sens. Actuators A: Phys.* 273, pp. 121–133. DOI: 10.1016/j.sna.2018.02.031 (cit. on p. 33).

Engholm, M., T. L. Christiansen, C. Beers, J. P. Bagge, L. N. Moesner, H. Bouzari, A. Lei, M. Berkheimer, M. B. Stuart, J. A. Jensen, and E. V. Thomsen (2015). "A hand-held row-column addressed CMUT

probe with integrated electronics for volumetric imaging". In: *Proc. IEEE Ultrason. Symp.* Pp. 1–4. DOI: 10.1109/ULTSYM.2015.0143 (cit. on p. 34).

Engholm, Mathias (2018). "Capacitive Micromachined Ultrasonic Transducers for 3-D Imaging". PhD thesis. Technical University of Denmark (cit. on p. 35).

Grass, R. S., A. S. Havreland, M. Engholm, J. A. Jensen, and E. V. Thomsen (2019). "188+188 Row-Column Addressed CMUT Transducer for Super Resolution Imaging". In: *Proc. IEEE Ultrason. Symp.* Pp. 1–4 (cit. on p. 33).

Grass, R. S., K. Steenberg, A. S. Havreland, M. Engholm, and E. V. Thomsen (2020). "Large Scale High Voltage 192+192 Row-Column Addressed CMUTs Made with Anodic Bonding". In: *Proc. IEEE Ultrason. Symp.* Pp. 1–4 (cit. on p. 33).

Havreland, A. S., M. Engholm, R. S. Grass, J. A. Jensen, and E. V. Thomsen (2019a). "Wafer bonded CMUT technology utilizing a Poly-Silicon-on-Insulator wafer". In: *Proc. IEEE Ultrason. Symp.* Pp. 1–4 (cit. on p. 33).

Havreland, A. S., M. Engholm, B. G. Tomov, J. A. Jensen, O. Hansen, and E. V. Thomsen (2019b). "CMUT Electrode Resistance Design: Modelling and Experimental Verification by a Row-Column Array". In: *IEEE Trans. Ultrason., Ferroelec., Freq. Contr.* Pp. 1110–1118. DOI: 10.1109/TUFFC.2019.2906795 (cit. on p. 35).

Jensen, J. A. (1996). "Field: A Program for Simulating Ultrasound Systems". In: *Med. Biol. Eng. Comp.* 10th Nordic-Baltic Conference on Biomedical Imaging, Vol. 4, Supplement 1, Part 1, pp. 351–353 (cit. on p. 30).

Jensen, J. A., H. Holten-Lund, R. T. Nilsson, M. Hansen, U. D. Larsen, R. P. Domsten, B. G. Tomov, M. B. Stuart, S. I. Nikolov, M. J. Pihl, Y. Du, J. H. Rasmussen, and M. F. Rasmussen (2013). "SARUS: A Synthetic Aperture Real-time Ultrasound System". In: *IEEE Trans. Ultrason., Ferroelec., Freq. Contr.* 60.9, pp. 1838–1852. DOI: 10.1109/TUFFC.2013.2770 (cit. on p. 33).

Jørgensen, L. T. (2019). "Synthetic aperture vector flow imaging using a row column ultrasound array". MA thesis. Denmark Technical University (cit. on p. 34).

Morton, C. E. and G. R. Lockwood (2003). "Theoretical assessment of a crossed electrode 2-D array for 3-D imaging". In: *Proc. IEEE Ultrason. Symp.* Pp. 968–971 (cit. on p. 29).

Rasmussen, M. F., T. L. Christiansen, E. V. Thomsen, and J. A. Jensen (2015). "3-D Imaging Using Row–Column-Addressed Arrays With Integrated Apodization — Part I: Apodization Design and Line Element Beamforming". In: *IEEE Trans. Ultrason., Ferroelec., Freq. Contr.* 62.5, pp. 947–958. DOI: 10.1109/TUFFC.2014.006531 (cit. on pp. 29–32, 35).

Sampaleanu, A., P. Zhang, A. Kshirsagar, W. Moussa, and R. Zemp (2014). "Top-orthogonal-to-bottom-electrode (TOBE) CMUT arrays for 3-D ultrasound imaging." In: *IEEE Trans. Ultrason., Ferroelec., Freq. Contr.* 61.2, pp. 266–276 (cit. on p. 29).

Schou, M. (2020). "Three dimensional flow and micro-flow imaging using Row-Column Arrays". PhD thesis. Denmark Technical University (cit. on p. 32).

Stuart, M. B., M. Schou, and J. A. Jensen (2019). "Row-Column Beamforming with Dynamic Apodizations on a GPU". In: *Proc. SPIE Med. Imag.* Paper number 10955-20, 109550Q. DOI: 10.1117/12.2512418 (cit. on pp. 30, 32).

Szabo, T. L. (2004). *Diagnostic ultrasound imaging inside out*. Elsevier (cit. on p. 32).

— (2014). *Diagnostic ultrasound imaging: Inside out*. 2nd ed. Elsevier (Oxford, UK) (cit. on p. 32).

Yen, J. T., C. H. Seo, S. I. Awad, and J. S. Jeong (2009). "A dual-layer transducer array for 3-D rectilinear imaging". In: *IEEE Trans. Ultrason., Ferroelec., Freq. Contr.* 56.1, pp. 204–212 (cit. on p. 29).

References from Chapter 5

Banterle, N., K. H. Bui, E. A. Lemke, and M. Beck (2013). "Fourier ring correlation as a resolution criterion for super-resolution microscopy". In: *J. Struct. Biol* 183.3, pp. 363–367 (cit. on p. 40).

Barrack, T. and E. Stride (2009). "Microbubble Destruction During Intravenous Administration: A Preliminary Study". In: *Ultrasound Med. Biol.* 35.3, pp. 515–522 (cit. on p. 38).

Chavignon, A., B. Heiles, V. Hingot, and O. Couture (2020). *3D Transcranial Ultrasound Localization Microscopy in Rat with a Multiplexed Matrix Probe*. Presentation at IEEE Ultrason. Symp. (Cit. on p. 37).

Chen, Q., J. Yu, L. Lukashova, J. D. Latoche, J. Zhu, L. Lavery, K. Verdelis, C. J. Anderson, and K. Kim (2020). "Validation of ultrasound super-resolution imaging of vasa vasorum in rabbit atherosclerotic plaques". In: *IEEE Trans. Ultrason., Ferroelec., Freq. Contr.* 67.8, pp. 1725–1729 (cit. on p. 39).

Christensen-Jeffries, K., J. Brown, P. Aljabar, M. Tang, C. Dunsby, and R. J. Eckersley (2017). "3-D In Vitro Acoustic Super-Resolution and Super-Resolved Velocity Mapping Using Microbubbles". In: *IEEE Trans. Ultrason., Ferroelec., Freq. Contr.* 64.10, pp. 1478–1486 (cit. on p. 37).

Christensen-Jeffries, K., O. Couture, P. A. Dayton, Y. C. Eldar, K. Hynynen, F. Kiessling, M. O'Reilly, G. F. Pinton, G. Schmitz, M. Tang, et al. (2020). "Super-resolution ultrasound imaging". In: *Ultrasound Med. Biol.* 46.4, pp. 865–891 (cit. on p. 40).

Descloux, A., K. S. Grußmayer, and A. Radenovic (2019). "Parameter-free image resolution estimation based on decorrelation analysis". In: *Nat. Methods* 16.9, pp. 918–924 (cit. on p. 40).

Harput, S., K. Christensen-Jeffries, A. Ramalli, J. Brown, J. Zhu, G. Zhang, C. H. Leow, M. Toulemonde, E. Boni, P. Tortoli, R. J. Eckersley, C. Dunsby, and M. Tang (Feb. 2020). "3-D Super-Resolution Ultrasound Imaging With a 2-D Sparse Array". In: *IEEE Trans. Ultrason., Ferroelec., Freq. Contr.* 67.2, pp. 269–277 (cit. on p. 37).

Heiles, B., M. Correia, V. Hingot, M. Pernot, J. Provost, M. Tanter, and O. Couture (Sept. 2019). "Ultrafast 3D Ultrasound Localization Microscopy Using a 32 x 32 Matrix Array". In: *IEEE Trans. Ultrason., Ferroelec., Freq. Contr.* 38.9, pp. 2005–2015 (cit. on p. 37).

Hingot, V., A. Chavignon, B. Heiles, and O. Couture (2021). "Measuring image resolution in Ultrasound Localization Microscopy". In: *IEEE Trans. Med. Imag.* (Cit. on p. 39).

Huang, C., M. R. Lowerison, F. Lucien, P. Gong, D. Wang, P. Song, and S Chen (2019). "Noninvasive Contrast-Free 3D Evaluation of Tumor Angiogenesis with Ultrasensitive Ultrasound Microvessel Imaging". In: *Scientific Reports* 9.1, p. 4907 (cit. on p. 37).

Jensen, J. A., M. L. Ommen, S. H. Øygard, M. Schou, T. Sams, M. B. Stuart, C. Beers, E. V. Thomsen, N. B. Larsen, and B. G. Tomov (2020). "Three-Dimensional Super Resolution Imaging using a Row-Column Array". In: *IEEE Trans. Ultrason., Ferroelec., Freq. Contr.* 67.3, pp. 538–546. DOI: 10.1109/TUFFC.2019.2948563 (cit. on pp. 39, 40).

Jensen, J. A., M. Schou, M. L. Ommen, S. H. Øygard, T. Sams, M. B. Stuart, E. V. Thomsen, N. B. Larsen, C. Beers, and B. G. Tomov (2019). "3-D Super Resolution Imaging using a 62+62 Elements Row-Column Array". In: *Proc. IEEE Ultrason. Symp.* Pp. 1–4 (cit. on p. 37).

Lin, F., S. E. Shelton, D. Espindola, J. D. Rojas, G. Pinton, and P. A. Dayton (2017). "3-D Ultrasound Localization Microscopy for Identifying Microvascular Morphology Features of Tumor Angiogenesis at a Resolution Beyond the Diffraction Limit of Conventional Ultrasound". In: *Theranostics* 7.1, pp. 196–204. DOI: 10.7150/thno.16899 (cit. on p. 37).

Lowerison, M. R., C. Huang, F. Lucien, S. Chen, and P. Song (2020). "Ultrasound localization microscopy of renal tumor xenografts in chicken embryo is correlated to hypoxia". In: *Scientific reports* 10.1, pp. 1–13 (cit. on p. 39).

Ommen, M. L. (2020). "Micromachined 2D Transducers and Phantoms for 3D Super-Resolution Ultrasound Imaging". PhD thesis. Denmark Technical University (cit. on pp. 37, 40, 42).

Ommen, M. L., M. Schou, R. Zhang, C. A. V. Hoyos, J. A. Jensen, N. B. Larsen, and E. V. Thomsen (2018). "3D Printed Flow Phantoms with Fiducial Markers for Super-Resolution Ultrasound Imaging". In: *Proc. IEEE Ultrason. Symp.* Pp. 1–4 (cit. on p. 38).

Rasmussen, M. F., T. L. Christiansen, E. V. Thomsen, and J. A. Jensen (2015). "3-D Imaging Using Row–Column-Addressed Arrays With Integrated Apodization — Part I: Apodization Design and Line

Element Beamforming". In: *IEEE Trans. Ultrason., Ferroelec., Freq. Contr.* 62.5, pp. 947–958. DOI: 10.1109/TUFFC.2014.006531 (cit. on p. 38).

Schou, M. (2020). "Three dimensional flow and micro-flow imaging using Row-Column Arrays". PhD thesis. Denmark Technical University (cit. on pp. 38, 40).

Talu, E., R. L. Powell, M. L. Longo, and P. A. Dayton (2008). "Needle Size and Injection Rate Impact Microbubble Contrast Agent Population". In: *Ultrasound Med. Biol.* 34.7, pp. 1182–1185 (cit. on p. 38).

Zhu, J., E. M. Rowland, S. Harput, K. Riemer, C. H. Leow, B. Clark, K. Cox, A. Lim, K. Christensen-Jeffries, G. Zhang, J. Brown, C. Dunsby, R. J. Eckersley, P. D. Weinberg, and M.-X. Tang (2019). "3D Super-Resolution US Imaging of Rabbit Lymph Node Vasculature in Vivo by Using Microbubbles". In: *Radiology* 291.3, pp. 642–650. DOI: 10.1148/radiol.2019182593 (cit. on p. 37).

References from Chapter 6

Bouzari, H., M. Engholm, C. Beers, S. I. Nikolov, M. B. Stuart, E. V. Thomsen, and J. A. Jensen (2018). "Curvilinear 3-D Imaging Using Row–Column Addressed 2-D Arrays with a Diverging Lens: Phantom Study". In: *IEEE Trans. Ultrason., Ferroelec., Freq. Contr.* 65.7, pp. 1182–1192. DOI: 10.1109/TUFFC.2018.2836384 (cit. on pp. 44–46, 48).

Bouzari, H., M. Engholm, C. Beers, M. B. Stuart, S. I. Nikolov, E. V. Thomsen, and J. A. Jensen (2017a). "3-D Imaging Using Row-Column Addressed 2-D Arrays with a Diverging Lens: Phantom Study". In: *Proc. IEEE Ultrason. Symp.* Pp. 1–4 (cit. on pp. 43, 46, 52).

— (2017b). "Curvilinear 3-D Imaging Using Row-Column-Addressed 2-D Arrays with a Diverging Lens: Feasibility Study". In: *IEEE Trans. Ultrason., Ferroelec., Freq. Contr.* 99, pp. 978–988. DOI: 10.1109/TUFFC.2017.2687521 (cit. on pp. 45, 47, 48, 52).

Bouzari, H., M. Engholm, M. B. Stuart, S. I. Nikolov, E. V. Thomsen, and J. A. Jensen (2016). "3-D imaging using row-column-addressed 2-D arrays with a diverging lens". In: *Proc. IEEE Ultrason. Symp.* Pp. 1–4. DOI: 10.1109/ULTSYM.2016.7728394 (cit. on pp. 43, 45, 52).

Carpena, P. and A. V. Coronado (2006). "On the focal point of a lens: beyond the paraxial approximation". In: *European Journal of Physics* 27.2, pp. 231–241 (cit. on pp. 46, 52).

Démoré, C. E. M., A. W. Joyce, K. Wall, and G. R. Lockwood (2009). "Real-time volume imaging using a crossed electrode array". In: *IEEE Trans. Ultrason., Ferroelec., Freq. Contr.* 56.6, pp. 1252–1261 (cit. on p. 43).

Engholm, M., H. Bouzari, T. L. Christiansen, C. Beers, J. P. Bagge, L. N. Moesner, S. E. Diederichsen, M. B. Stuart, J. A. Jensen, and E. V. Thomsen (2018). "Probe development of CMUT and PZT Row–Column-Addressed 2-D Arrays". In: *Sens. Actuators A: Phys.* 273, pp. 121–133. DOI: 10.1016/j.sna.2018.02.031 (cit. on p. 44).

Ernst, Paul J. (1947). "Measurement and Specification of Ultrasonic Lenses". In: *J. Acoust. Soc. Am.* 19.3, pp. 474–474 (cit. on p. 46).

Ferin, G., M. C. Dumoux, M. Flesch, E. Montauban, A. Lejeune, B. Rosinski, T. Mateo, J. Poree, J. Sauvage, T. Deffieux, M. Pernot, M. Tanter, and A. Nguyen-Dinh (2018). "A Novel Row-Column Addressed Stack Architecture for Enhanced Cardiac Imaging". In: *Proc. IEEE Ultrason. Symp.* Pp. 1–4 (cit. on p. 43).

Jensen, J. A. (1996). "Field: A Program for Simulating Ultrasound Systems". In: *Med. Biol. Eng. Comp.* 10th Nordic-Baltic Conference on Biomedical Imaging, Vol. 4, Supplement 1, Part 1, pp. 351–353 (cit. on pp. 48, 52).

Kinsler, L. E., A. R. Frey, A. B. Coppens, and J. V. Sanders (1982). *Fundamentals of Acoustics*. Third. New York: John Wiley & Sons (cit. on p. 43).

References from Chapter 7

Bouzari, H., M. Engholm, C. Beers, S. I. Nikolov, M. B. Stuart, E. V. Thomsen, and J. A. Jensen (2018). "Curvilinear 3-D Imaging Using Row–Column Addressed 2-D Arrays with a Diverging Lens: Phantom Study". In: *IEEE Trans. Ultrason., Ferroelec., Freq. Contr.* 65.7, pp. 1182–1192. DOI: 10.1109/TUFFC.2018.2836384 (cit. on p. 61).

Démoré, C. E. M., A. W. Joyce, K. Wall, and G. R. Lockwood (2009). "Real-time volume imaging using a crossed electrode array". In: *IEEE Trans. Ultrason., Ferroelec., Freq. Contr.* 56.6, pp. 1252–1261 (cit. on p. 61).

Emamian, S. A., M. B. Nielsen, J. F. Pedersen, and L. Ytte (1993). "Kidney Dimensions at Sonography: Correlation with Age, Sex, and Habitus in 665 Adult Volunteers". In: *American Journal of Roentgenology* 160, pp. 83–86 (cit. on p. 71).

Engholm, M., H. Bouzari, C. Beers, J. A. Jensen, and E. V. Thomsen (2018). "Increasing the field-of-view of row-column-addressed ultrasound transducers: implementation of a diverging compound lens". In: *Ultrasonics* 88, pp. 97–105. DOI: 10.1016/j.ultras.2018.02.001 (cit. on p. 61).

Havreland, A. S., M. Engholm, B. G. Tomov, J. A. Jensen, O. Hansen, and E. V. Thomsen (2019). "CMUT Electrode Resistance Design: Modelling and Experimental Verification by a Row-Column Array". In: *IEEE Trans. Ultrason., Ferroelec., Freq. Contr.* Pp. 1110–1118. DOI: 10.1109/TUFFC.2019.2906795 (cit. on p. 65).

Jensen, J. A. (1996). "Field: A Program for Simulating Ultrasound Systems". In: *Med. Biol. Eng. Comp.* 10th Nordic-Baltic Conference on Biomedical Imaging, Vol. 4, Supplement 1, Part 1, pp. 351–353 (cit. on p. 63).

Jensen, J. A., H. Holten-Lund, R. T. Nilsson, M. Hansen, U. D. Larsen, R. P. Domsten, B. G. Tomov, M. B. Stuart, S. I. Nikolov, M. J. Pihl, Y. Du, J. H. Rasmussen, and M. F. Rasmussen (2013). "SARUS: A Synthetic Aperture Real-time Ultrasound System". In: *IEEE Trans. Ultrason., Ferroelec., Freq. Contr.* 60.9, pp. 1838–1852. DOI: 10.1109/TUFFC.2013.2770 (cit. on p. 65).

Jensen, J. A., M. F. Rasmussen, M. J. Pihl, S. Holbek, C. A. Villagomez-Hoyos, D. P. Bradway, M. B. Stuart, and B. G. Tomov (2016). "Safety Assessment of Advanced Imaging Sequences, I: Measurements". In: *IEEE Trans. Ultrason., Ferroelec., Freq. Contr.* 63.1, pp. 110–119 (cit. on p. 65).

Kinsler, L. E., A. R. Frey, A. B. Coppens, and J. V. Sanders (1982). *Fundamentals of Acoustics*. Third. New York: John Wiley & Sons (cit. on pp. 59, 62).

Oddershede, N. and J. A. Jensen (2007). "Effects influencing focusing in synthetic aperture vector flow imaging". In: *IEEE Trans. Ultrason., Ferroelec., Freq. Contr.* 54.9, pp. 1811–1825 (cit. on pp. 61–63, 66, 67).

Tomov, B. G., S. E Diederichsen, E. V. Thomsen, and J. A. Jensen (2018). "Characterization of medical ultrasound transducers". In: *Proc. IEEE Ultrason. Symp.* Pp. 1–4 (cit. on p. 65).

Paper 1

History and Latest Advances in Flow Estimation Technology: From 1-D in 2-D to 3-D in 4-D

Jørgen Arendt Jensen, Svetoslav Ivanov Nikolov, Kristoffer Lindskov Hansen,
Matthias Bo Stuart, Carlos A. Villagomez Hoyos, Mikkel Schou, Martin Lind Ommen, **Sigrid Husebø Øygard**, Lasse Thurmann Jørgensen, Marie Sand Traberg, Tin-Quoc Nguyen, Erik Vilain Thomsen, Niels Bent Larsen, Christopher Beers,
Borislav Gueorguiev Tomov, and Michael Bachmann Nielsen

Published in:
Proceedings of the IEEE International Ultrasonic Symposium

Document Version:
Published

DOI:
10.1109/ULTSYM.2019.8926210

2019 IEEE International Ultrasonics Symposium (IUS)
Glasgow, Scotland, October 6-9, 2019

History and Latest Advances in Flow Estimation Technology: From 1-D in 2-D to 3-D in 4-D

Jørgen Arendt Jensen[1], Svetoslav Ivanov Nikolov[2], Kristoffer Lindskov Hansen[4], Matthias Bo Stuart[1], Carlos A. Villagomez Hoyos[2], Mikkel Schou[1], Martin Lind Ommen[1], Sigrid Husebø Øygard[1], Lasse Thumann Jørgensen[1], Marie Sand Traberg[1], Tin-Quoc Nguyen[4], Erik Vilain Thomsen[1], Niels Bent Larsen[1], Christopher Beers[3], Borislav Gueorguiev Tomov[1], and Michael Bachmann Nielsen[4]

[1]Department of Health Technology, Technical University of Denmark, Lyngby, Denmark
[2]BK Medical, Herlev, Denmark, [3]BK Medical, State College, PA 16803, USA,
[4]Department of Diagnostic Radiology, Rigshospitalet, Denmark

***Abstract*—Ultrasound imaging of flow has seen a tremendous development over the last sixty years from 1-D spectral displays to color flow mapping and the latest Vector Flow Imaging (VFI). The paper gives an overview of the development from current commercial vector flow systems to the latest advances in fast 4-D volumetric visualizations. It includes a description of the radical break with the current sequential data acquisition by the introduction of synthetic aperture imaging, where the whole region of interest is insonified using either spherical or plane waves also known as ultrafast imaging. This makes it possible to track flow continuously in all directions at frame rates of thousands of images per second. The latest research translates this to full volumetric imaging by employing matrix arrays and row-column arrays for full 3-D vector velocity estimation at all spatial points visualized at very high volume rates (4-D).**

I. Introduction

The measurement of blood flow has undergone a tremendous development since the first system devised by Satomura in Japan in 1957 and 1959 [1, 2] more than sixty years ago. The continuous wave system could detect heart wall movements and flow patterns in peripheral arteries. Pulsed systems developed by Baker [3] and Wells [4] could display the spectral content of the flow signals at one depth in the vessel. These early 1-D systems forms the basis for the spectral Doppler systems of today, which are used for investigating and quantifying flow everywhere in the human circulation. Even the continuous wave systems are still in use in cardiology, where the velocities can be too high to measure for a pulsed system. Both yield quantitative estimates but can only measure at a single spatial location.

This limit was lifted by the Color Flow Mapping (CFM) system developed by Kasai et al [5, 6], where an auto-correlation estimator can estimate the velocity from only 8 to 16 emissions, thereby making it possible to acquire and display axial velocity images. This introduced the second most important innovation in velocity estimation, which is implemented in all commercial scanners for flow imaging of the vessels and the heart. The estimator has been investigated and improved in numerous papers using e.g. both RF averaging [7, 8] and cross-correlation [9, 10].

Although these systems are widely used in the clinic, and a whole range of diagnostic measures are routinely used, they also have a number of drawbacks and technical problems. Most importantly, only the axial velocity component is estimated. This is often compensated for by finding the beam-to-flow angle using the B-mode image, but it is inherently unreliable as the angle can vary over the cardiac cycle, and the flow is not necessarily parallel to the vessel wall. Often the beam-to-flow angle can be difficult to keep below 60°, and even a modest error of 5° can here lead to 20-30% errors in the estimated velocities. In many cases the axial velocity is actually the smallest component for e.g. peripheral vessels, and the lateral component is more important. The problem is addressed by the 2-D Vector Flow Imaging (VFI) systems presented in Section II, which also describes how more accurate measures of flow and turbulence can be attained in Section II-B.

A second problem is that CFM systems are limited in their frame rate by the sequential data acquisition due to the speed of sound [11, 12]. Eight to sixteen emissions must be acquired in multiple directions to yield an image, and the precision of the velocity estimates is limited by the number of emissions in the same direction. It is, thus, not possible to have both a large imaging region (large depth), fast frame rates, and precise estimates at the same time. Further, it is often difficult to detect flow in both the systolic and diastolic phase. The limits number of lines making low velocity estimation difficult, if aliasing should be avoided at the same time. These problems are addressed in Section III with the introduction of Synthetic Aperture (SA) systems, which radically breaks the trade-off between frame rate and precision [12]. It opens a whole range of new possibilities for flow imaging, where both slow and fast velocities can be estimated from the same data with a very high precision.

The third problem is that current systems only show flow in a 2-D image. Recently, 3-D volumetric imaging has been introduced, and these systems can show CFM images in a volume. Even though parallel beamforming is employed, it is still difficult to attain decent frame rates for real-time

978-1-7281-4596-9/19/$31.00 ©2019 IEEE

cardiac imaging, and often the scanners have to resort to ECG gated sequences to stitch the volume together from multiple acquisitions. A further problem is the use of matrix array probes. Attaining a high resolution and contrast in ultrasound images require 64 to 128 transducer elements along the imaging plane, and for 3-D volumetric imaging matrix probes have to be used. These should ideally have at least 4,000 to 16,000 elements making them prohibitively expensive to develop and costly to use. Current state-of-the-art probes have more than 9,000 elements, which is still too low to attain a state-of-the-art image quality. Further, the velocity estimation is still only in the axial direction and not in full 3-D. These problems are addressed in Section IV, which shows how the latest research in Row-Column (RC) matrix probes potentially can be a solution to the problems of fast 4-D imaging with display of the full 3-D velocity vector in all points in the volume in real time.

II. 2-D Vector Flow Imaging

It was early realized that only estimating the axial velocity component was not sufficient to give a complete picture of the complex human blood flow. Fox [13] suggested the first system with two crossing beams to enable estimation of the lateral velocity component from triangulation. This has later been investigated and optimized by a number of authors [14, 15]. A second approach developed by Trahey et al [16] used speckle tracking, where a small search region was correlated to a larger image region. The velocity could then be found for both components.

A. Transverse oscillation

The first approach to make it into commercial scanners was the Transverse Oscillation (TO) method developed by Jensen, Munk, and Anderson [17, 18]. Axial velocity estimators rely on the sinusoidal signal emitted, and the velocity is estimated by correlating multiple emissions in the same direction. The motion between emissions is then found through either an autocorrelation using the phase shift or a cross-correlation for the time shift [19]. The idea in TO is to introduce an oscillation transverse to the ultrasound beam and then find the lateral displacement. A Fourier relationship exists between the transducer's aperture sensitivity and the lateral far-field sensitivity [17, 20, 21]. Introducing two peaks in the receive apodization therefore generates a lateral oscillation, where the frequency is determined by the separation of the two peaks. A dedicated estimator was developed for separately estimating the axial and lateral velocity components [22]. The method was implemented on BK Medical scanners (Herlev, Denmark) and FDA approved in 2012 [23]. It made it possible for the first time to visualize the complex flow in the body in real-time, and vortices in e.g. the bulbous of the carotid artery could be seen as shown in Fig. 1. The approach has been implemented on linear [17, 22], convex [24], and phased array probes [25] and can also be used for finding the spectrum of the transverse velocity [26].

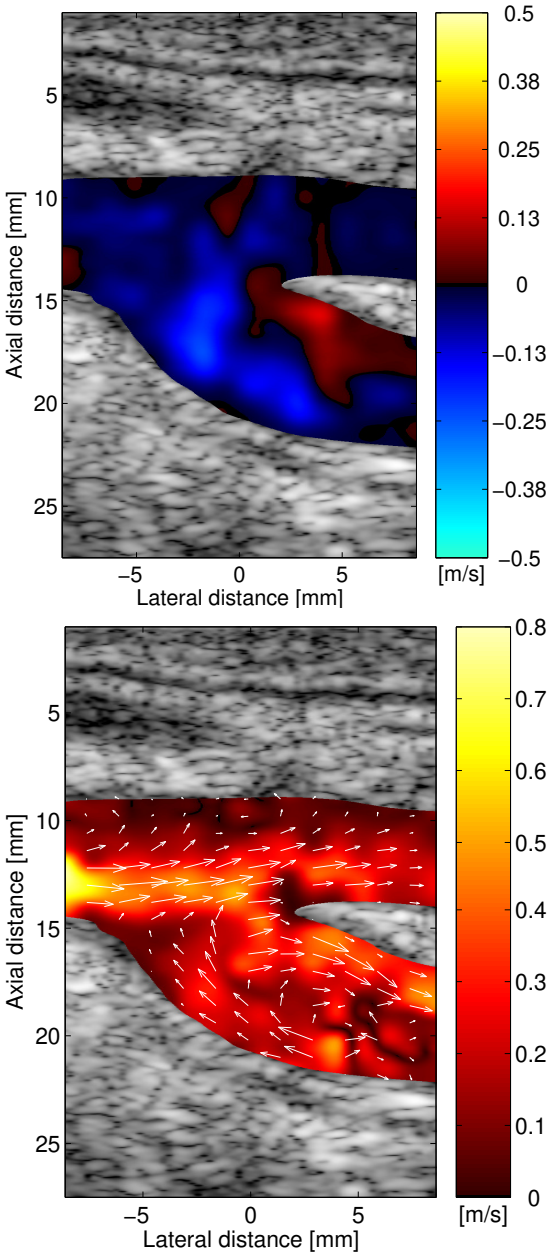

Fig. 1. In-vivo images of flow in the carotid bifurcation right before peak systole. The top images shows the CFM image for the axial velocity, and the bottom image shows the VFI using TO. A vortex is seen in the carotid bulb, and the velocity estimates are more consistent with what is found in the carotid artery (from [27]).

An example of flow in the aorta is shown in Fig. 2 for a short-axis view. The direction and velocity magnitude of the blood flow are displayed as colored pixels defined by the 2-D color bar with arrows superimposed for showing direction and magnitude. The short-axis view shows the rotation of the flow, which is nearly always found during the cardiac cycle, and the image demonstrates that the velocity can be estimated for all directions [28].

A range of studies have been conducted using the BK

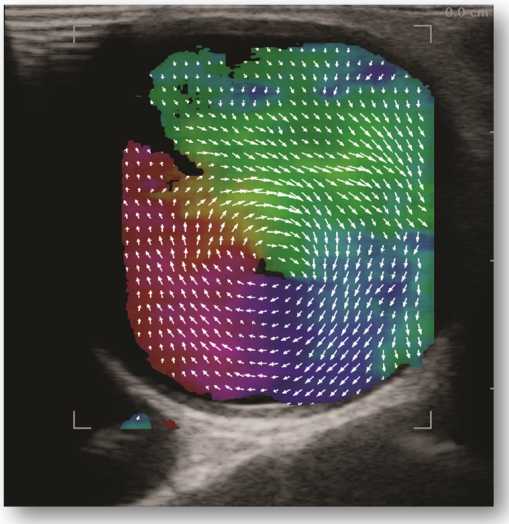

Fig. 2. Vector velocity imaging of blood flow in the ascending aorta in a short-axis view. The colors and arrows indicate velocity direction and magnitude (modified from [28]).

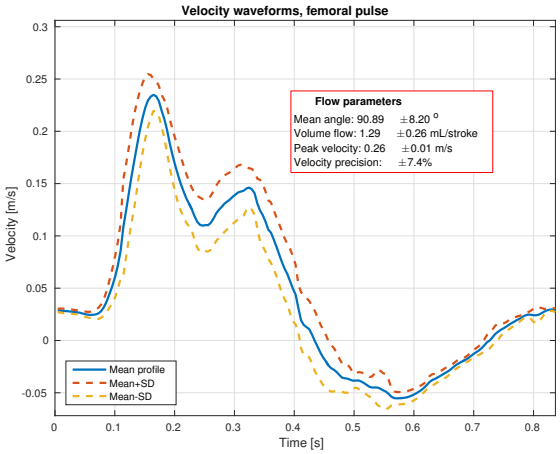

Fig. 3. Quantitative velocity measurements from a carotid phantom using a linear array probe with a directional TO velocity estimator (from [34]). Several cardiac cycles are automatically aligned and the mean value and SD are estimated from the 10 cycles for both the beam-to-flow angle and various velocity measures.

implementation. This includes investigating volume flow in arteriovenous fistulas [29], intraoperative cardiac examinations [30], flow in the aorta [28], flow in the ascending aorta for normal, stenotic and replaced aortic valves [31], and transthoracic VFI examination of newborns and infants with congenital heart defects [32]. Other groups have also investigated VFI and compared it to e.g. spectral velocity methods [33].

Vector flow is now also implemented on systems from Mindray and Toshiba, and a comprehensive review of all the developed methods can be found in [11], which also lists the comprehensive literature in the field for a range of different methods and clinical investigations.

B. Quantitative Measurements in VFI

Currently, quantification of velocities is obtained by using the axial velocity component from spectral velocity estimates, as the measurements are more precise than CFM results due to the continuous acquisition in one direction. The measurements have to be corrected for the beam-to-flow angle, and variations in this can lead to a serious bias. A 5° error at a 60° beam-to-flow angle can lead to a 20% error in the velocity. VFI can automatically compensate such errors and can also handle that the beam-to-flow angle varies over the cardiac cycle. An example of quantitative VFI measurements is shown in Fig. 3, where both the mean value and the standard deviation (SD) can be estimated by measuring over several cardiac cycles [34].

Many other quantities can be derived from VFI data including flow complexity for revealing disturbed and turbulent flow [31, 35], volume flow [36], and pressure gradients [37]. In the last example, the pressure gradients are estimated by solving a simplified version of the Navier-Stokes equation with the VFI estimates as input. An example of this is shown in Fig. 4, where the top image shows the trajectory for the pressure gradient calculation, and the lower graph shows the mean pressure gradient and its SD found from 11 cardiac cycles. The pressure gradient can be retrospectively found from the 10 seconds of data for any trajectory within the vector flow imaging region with a precision of 19% . A large improvement compared to a pressure catheter, which had a relative SD of 786% [38].

III. Synthetic Aperture Flow Imaging

A major problem in conventional flow imaging is the sequential data acquisition, which limits the frame rate and the amount of data available for velocity estimation [12, 41]. This limits the penetration depth, the maximum detectable velocity, and the precision of the estimates. A break with this paradigm is to employ SA imaging as shown in Fig. 5, where the region of interest is broadly insonified by using spherical or plane waves. The scattered signal is then received on part or all of the elements, and a full Low Resolution Image (LRI) can be generated. Combining LRIs from a number of emissions then yields a High Resolution Image (HRI) dynamically focused in both transmit and receive. The focusing is performed by summing the waves in phase, and for spherical emissions the focusing times are calculated as:

$$t_{i,j} = \frac{|\vec{r}_i - \vec{r}_p|}{c} + \frac{|\vec{r}_j - \vec{r}_p|}{c}, \tag{1}$$

where $\vec{r}_i$ is the origin of emission i, $\vec{r}_p$ is the location of the imaging point, and $\vec{r}_j$ is the position of the receiving element j. The high resolution image is then made by:

$$y(\vec{r}_p) = \sum_{i=1}^{N_i} \sum_{j=1}^{N_j} a(\vec{r}_i, \vec{r}_p, \vec{r}_j) r(t_{i,j}), \tag{2}$$

where N_i is the number of transmissions and N_j the number of receiving elements. Here $a()$ is the apodization function or relative weight between emissions and between receiving elements, which is often calculated from the F-number in transmit and receive. The same calculations are performed for

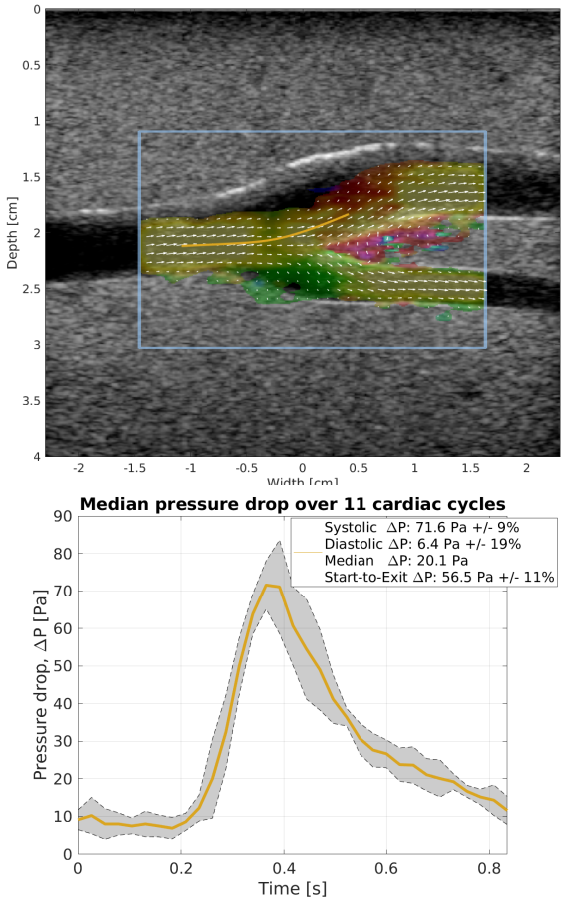

Fig. 4. Estimated pressure gradient from a carotid artery phantom. The top image shows the VFI and the trajectory for finding the pressure gradient (orange line). The lower graph shows the estimated pressure gradient from 11 cardiac cycles including the relative SD.

plane wave imaging with a replacement of the transmit delay (the first term in (1)) with the corresponding equation for a plane wave. This is often called ultrafast imaging [42], but the imaging scheme is really the same for both types of waves. The only difference is the calculation of the transmit delay in the beamforming, and we will, therefore, call both schemes for SA imaging in this paper. Creating SA images decouples frame rate from the number of lines in the image, and the frame rate is only determined by the number of emissions.

It might be counter-intuitive that such images acquired over multiple emissions can be used for velocity estimation, as the investigated object is moving between emissions and, thus, cannot be summed coherently. The initial idea for SA flow imaging is illustrated in Fig. 6, where a short sequence is used for SA imaging [43–45]. The emissions are shown on the top and the LRIs beneath. The bottom row shows the HRIs when the different LRIs are combined. A singe scatterer moving towards the probe is investigated. The LRIs are not summed in phase, and HRI $H^{(n-3)}$ is different from $H^{(n-2)}$, but equal to $H^{(n-1)}$ apart from the shift in position, where n is the emission number. The basic idea is that the HRIs are highly correlated, if their emission sequences are the same. They may not be summed fully in phase, but the defocusing from motion is the same for all HRIs, as the emission sequence is the same. They can, therefore, be correlated to find the velocity.

This might seem like a small detail, but it has major implications for flow imaging. Firstly, imaging is continuous, and data are available everywhere in the imaging region for all time. It is, thus, possible to average the correlation functions over as long time as the flow can be considered stationary [46]. Also, flow can be followed in any direction, as data is available for the whole imaging region, and beamformation can be made in all directions. Any echo canceling filter can be used without detrimental initialization effects, making it much easier to separate out flow from tissue [47–50].

An example of the benefits from SA flow imaging can be seen in Fig. 7, which shows a velocity magnitude image acquired using an 8 emissions SA sequence [51]. The data have been beamformed along the flow direction and the velocity estimated by cross-correlating these directional lines for 16 HRIs, which yields the velocity magnitude. No post processing has been employed on the image, and only the raw estimates are shown. The relative standard deviation to the peak velocity is 0.3% for very precise quantitative data, ideal for the quantification described in Section II-B. Data can be beamformed in any direction, making it also possible to estimate transverse flow [51]. Methods for estimating the correct beam-to-flow angle have also been developed [52, 53].

The current state-of-the-art in SA flow imaging is shown in Fig. 8, where the flow in the carotid bifurcation is measured on a healthy volunteer [53]. Here, a five emissions sequence was used, and it can potentially yield more than 3000 frames per second. Images at three different time points in the cardiac cycle are shown at the top. The bottom graph shows the velocity magnitude estimated in the white circle in graph c). The evolution on the vortex in the carotid bulb can be studied in detail using such ultrafast imaging.

A major issue in these images is the very large amount of data and the significant number of calculations to conduct for creating real time imaging. The current trend is to employ fast GPUs to perform the beamforming and this can often approach real time imaging [54–57]. Another approach is to reduce the amount of data and thereby the calculation load. Dual stage beamforming has been developed to reduce the sampled data to one channel, and the processing demand is thereby also reduced proportionally. It was demonstrated in [58] that very fast SA VFI could be attained by this approach using TO and dual stage beamforming, and the processing could be performed in real time on a Tablet [59].

A. Fast Flow

One problem in SA imaging has been the reduction of the detectable peak velocity. For SA flow imaging the data has to be acquired over N_e emissions, and the effective pulse repetition frequency $f_{prf,eff}$ is equal to f_{prf}/N_e. The maximum detectable velocity v_{max} in velocity estimation is generally proportional to $\lambda f_{prf,eff} = v_{max}$, which is reduced by a factor N_e compared to traditional flow imaging. There is,

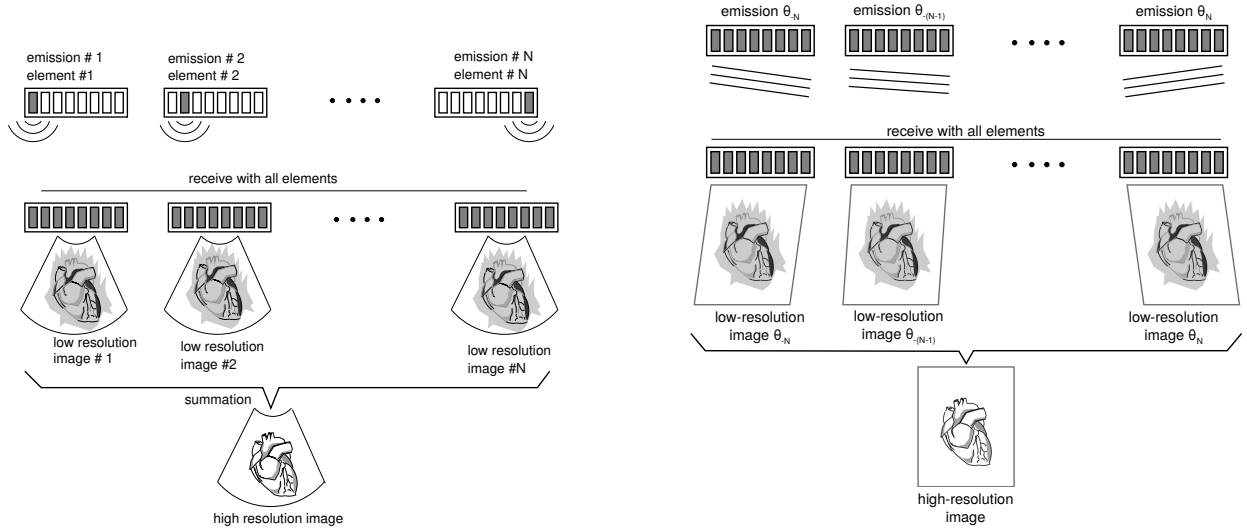

Fig. 5. Principle of SA imaging (left figure from [39]). The spherical emissions are shown on the top row with reception on all elements in the middle row. Plane wave imaging is shown in the right figure (from [40]).

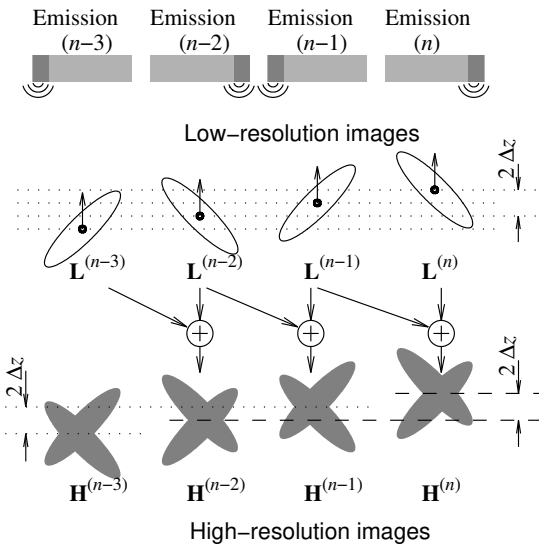

Fig. 6. Principle of SA flow imaging (from [43]).

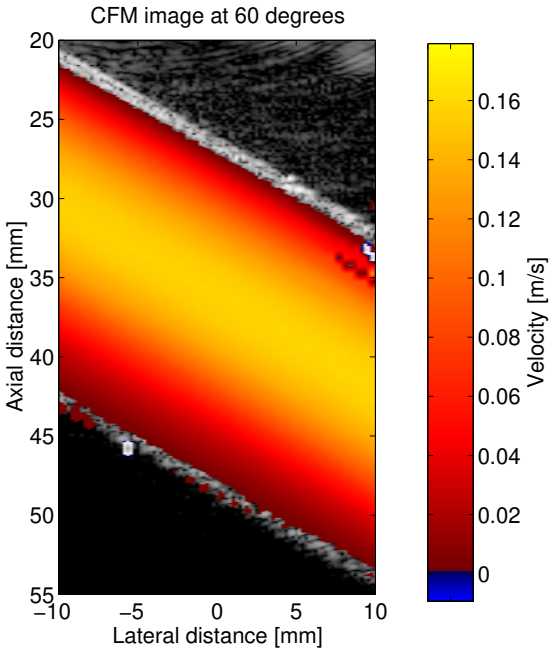

Fig. 7. Velocity magnitude velocity image acquired using SA flow imaging and directional beamforming (from [51]).

thus, a compromise between sequence length and v_{max}. Often a longer sequence is preferred to enhance contrast and this reduces v_{max}. A possible solution is to use single emissions like in [61–64], but this reduces contrast and makes it difficult to estimate flow in small vessels.

The problem has recently been solved by introducing interleaved sequences, where an emission is repeated as shown in Fig. 9. The beamformed HRIs are then only temporally separated by $1/f_{prf}$ and not $1/f_{prf,eff}$, and v_{max} is increased by a factor N_e. Combined with a cross-correlation estimator made it possible to estimate velocities above 5 m/s for imaging down to 15 cm [60, 65], and it is also possible to further increase the limit by using directional beamforming as in Fig. 7.

B. Slow Flow

A major advantage of continuous imaging is the possibility of using advanced echo canceling filters to separate flow from tissue. This is especially important for low velocities, and SA imaging has created major breakthroughs in studying slow flow in e.g. the rat brain as shown in Fig. 10 and the kidney [66, 67]. In particular the employment of Singular Value Decomposition (SVD) echo canceling methods has benefited low velocity imaging and introduced a whole new range of possibilities [47, 50, 68].

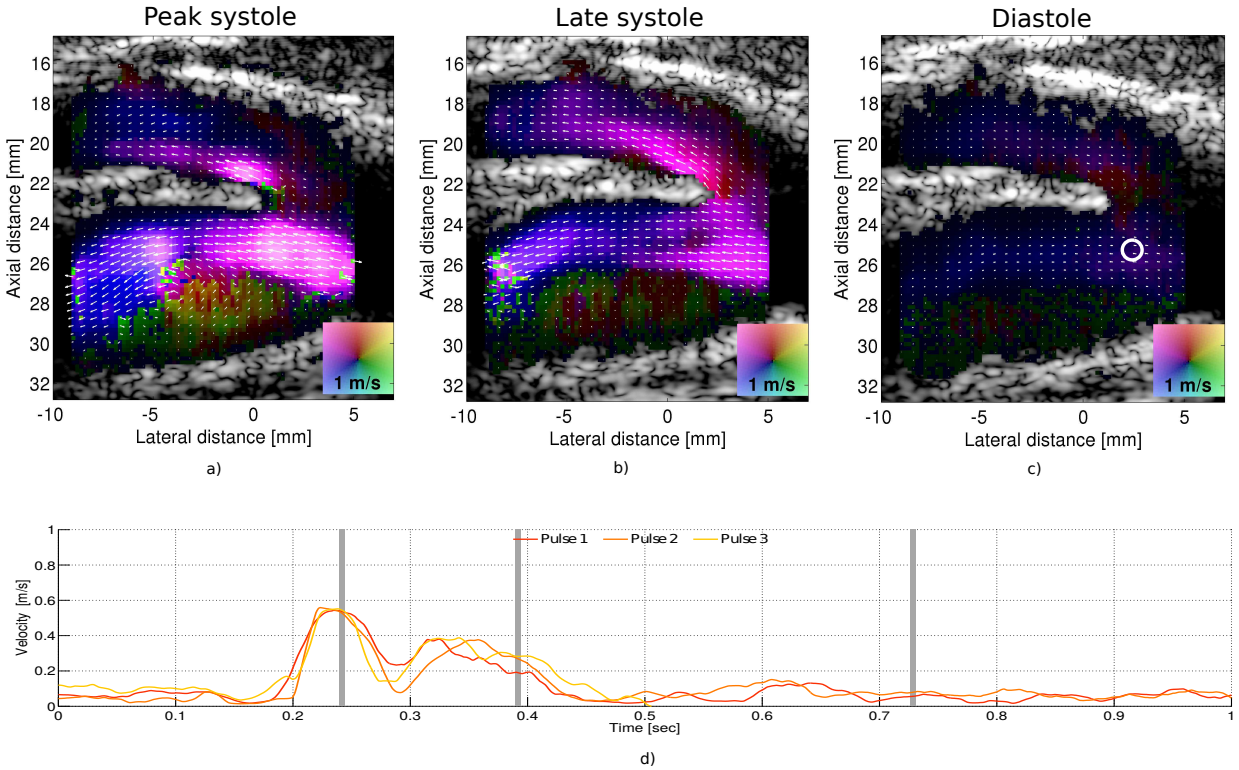

Fig. 8. VFI acquired using a SA flow sequence and directional beamforming (from [53]). Images at three different time points in the cardiac cycle is shown on the top, and the measured velocity magnitude over time for three cardiac cycles are shown in the bottom figure.

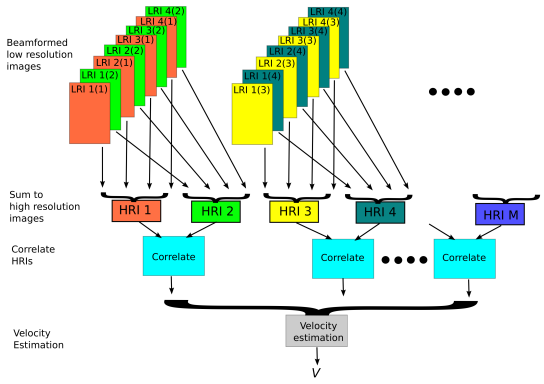

Fig. 9. Inter-leaved SA sequence where LRIs are repeated to minimize the distance between HRIs. The same colored LRIs are summed to yield one HRI. The effective $f_{prf,eff}$ is equal to the highest possible value (f_{prf}) due to the inter-leaving. Correlations in the blue boxes yield the same correlation function, which are then averaged to improve precision (from [60]).

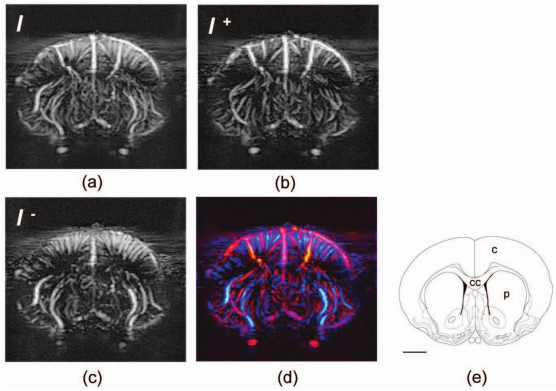

Fig. 10. Directional power Doppler. (a) Initial μDoppler image. (b) Positive part of the Doppler power spectrum I+ quantifying the volume of blood flowing up. (c) Negative part of the Doppler power spectrum I quantifying the volume of blood flowing down. (d) Color-coded μDoppler image: in each pixel, the positive part is colored on a red range of intensities and the negative part on a blue range of intensities. (e) Anatomy of the brain slice (bregma + 1.0 mm). Main structures: cortex (denoted c), corpus callosum (cc) and caudate putamen (p). Scale bar: 2 mm. (from [67]).

IV. From 2-D to 4-D

The ultimate goal for VFI is to yield a full 3-D volumetric image at a high frame rate (4-D) with the full velocity vector determined for all three velocity components (3-D). This could be called 3-D VFI in 4-D. SA imaging can be used for this using matrix probes, where the emitted waves can be steered in all directions to insonify the whole volume continuously. The TO approach has been modified to estimate all three velocity components [71, 72]. A 1024 elements Vermon matrix probe

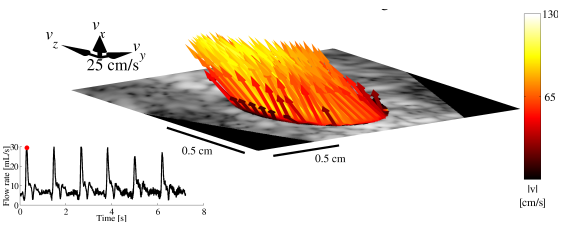

Fig. 11. Three-dimensional vector flow from the common carotid artery of a volunteer during peak systole using a 3-D TO estimator (modified from [69]).

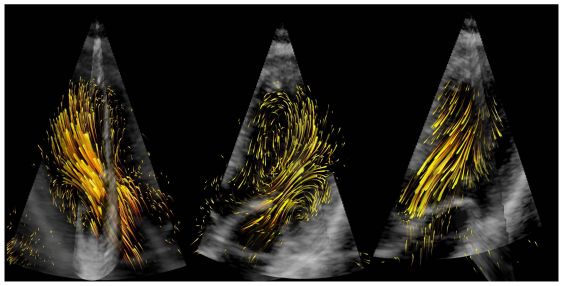

Fig. 12. Three-dimensional cardiac VFI rendering of the flow path lines at three time points in the cardiac cycle corresponding to diastole, diastasis, and systole. (from [70]).

[73] was used with the SARUS research scanner [74]. In-vivo imaging of ten volunteers was conducted on the carotid artery in [69] as shown in Fig. 11, and the volume flow could be determined with a SD of 5.7%. 3-D VFI has also been conducted in the heart using a modified GE Vivid E95 ultrasound scanner (GE Vingmed, Horten, Norway) using a GE 4V-D matrix array transducer for full volumetric coverage of the left ventricle at 50 volumes/second utilizing ECG-gating [70]. An example of these measurements is shown in Fig. 12.

One major problem is, however, the amount of elements needed. Both examples above use more than 1000 transducer elements, with probe foot-prints that are small, thus, impeding focusing. Good focusing in 2-D demands larger probes with 128 to 192 elements to maintain a low F-number for all imaging depths. Translating this to 3-D yields $192^2 = 36,864$ independent elements, which is impossible to connect through a cable to the scanner. A possible solution is to use a sparse array or electronic beamforming in the handle. This still restricts the number of elements to around 9,000 for roughly 100 elements on each side of the array. Low F-number focusing is therefore very difficult and expensive to attain in 3-D imaging, and compromises have to be made in both the imaging schemes and beamforming.

A novel solution to this problem is to employ Row-Column Arrays (RCAs), where rows and columns are independently addressed [75–78]. The number of interconnects is then transformed from N^2 to $2N$, thus reducing it by a factor of $N/2$. This makes very large arrays possible, and much lower F-numbers can be maintained for larger depths. A further advantage of the large array size is the increased penetration depth. This again can be used for increasing the center frequency of the probe and thereby resolution. Arrays with only 64+64 elements at 3 MHz have attained a decent volumetric image quality and a penetration down to 30 cm for SA imaging sequences [79].

The RCAs can be combined with all the methods presented here, and, thereby, attain the previously mentioned advantages. Three-dimensional VFI was presented for a line and a plane in [81] and for a volume [80, 81] using a 64+64 RC array, and the TO approach adapted to 3-D VFI as shown in Fig. 13.

Recently, a SA RCA imaging sequence has also been developed using an interleaved sequence for fast imaging, high detectable velocities, and continuous data available in the full

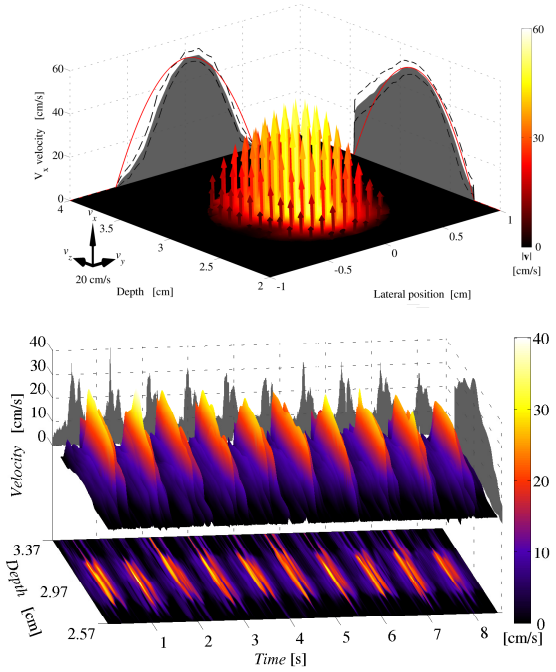

Fig. 13. Cross sectional mean 3-D vector flow averaged over 100 frames acquired using a 62+62 element RCA. The magnitude and direction of the flow is depicted by the length and the color of the arrows on the top figure. The shaded gray areas represent the projection of the flow in the respective direction with their standard deviations (dotted line). The theoretical flow profiles are illustrated by the red lines. The bottom figure shows an M-mode of the out-of-plane v_x velocity component measured for a pulsating carotid flow waveform (modified from [80]).

volume [82]. Results from simulated flow with components in all directions are shown in Fig. 14, where the vessel is rotated 45°=β compared to the probe, and the beam-to-flow angles α are 90°, 75°, and 60°. All velocity components can be estimated with a bias less than -6.2% and an SD below 4.5% for situations. An example of 3-D vector flow in 4-D is shown in Fig. 15, which was measured on pulsating flow in a bifurcation phantom using the 62+62 RCA, SARUS and the SA sequence. It is possible to obtain new VFI estimates of all components and a B-mode image after 56 emissions, which yields 275 volumes/second for imaging down to 5 cm. This demonstrates than quantitative 3-D VFI can be attained in a full volume at high volume rates (4-D) using only 62 receive channels.

The continuous data for SA RC imaging can also be employed for estimating low velocities using the methods described in Section III-B. Another example is to use super resolution imaging with RC arrays and ultrasound contrast agents. An example of this is shown in Fig. 16 for flow in a micro-phantom. The 3 MHz 62+62 array was used together with a 32+32 emission SA pulse inversion sequence. The full volume was beamformed continuously, and the envelope signal was processed in a 3-D super resolution pipeline for bubble detection and presentation. A precision of roughly 20 μm was attained in all three coordinates in the full volume [83].

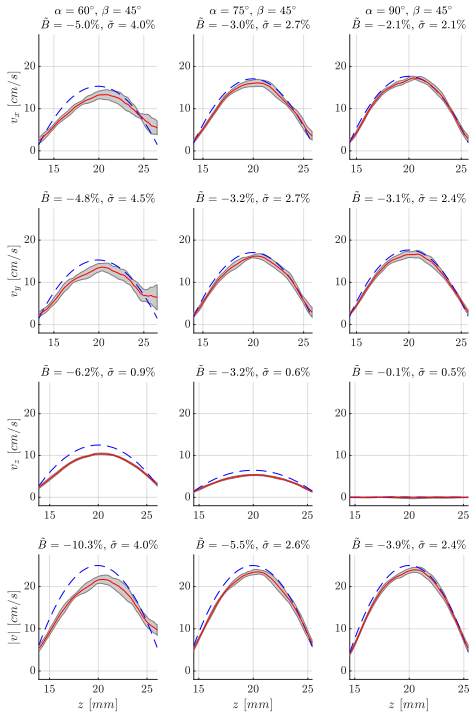

Fig. 14. Simulated velocity profiles for the SA RC flow sequence. The vessel i rotated 45°=β compared to the probe, and the beam-to-flow angles α are 90°, 75°, and 60°. The true profiles are shown as dashed blue lines, the mean profiles are red, and the gray backgrounds show ± 1 SD.

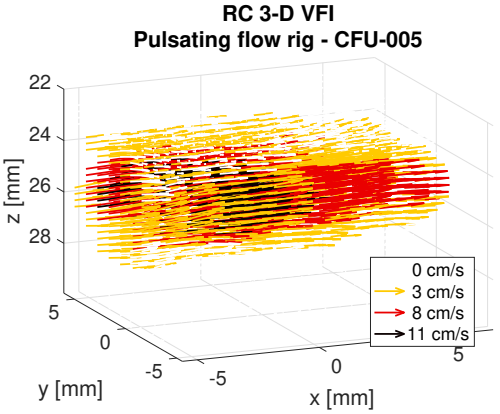

Fig. 15. Three-dimensional RC VFI from pulsating flow in a carotid artery phantom.

V. Challenges and Opportunities

Flow imaging has progressed in the last sixty years from simple 1-D measurements to the potential of revealing the full 3-D velocity vector in a full volume in real time at very high volumetric frame rates. The development has included new imaging schemes, new estimators and progress in making advanced arrays for both 2-D and 3-D imaging.

Many challenges still lie ahead. Larger 2-D probes should be developed to fully exploit the potential of RCA SA imaging. The field-of-view should also be expanded by employing e.g. lenses on the RC array as investigated in [79]. Much research is also needed for developing imaging schemes for such arrays using sparse sets of interleaved emissions to yield the fastest imaging with the fewest emissions for an optimal contrast and resolution. The years of development has also shown that new estimators can increase precision at the same time as the number of calculations is reduced by using TO estimators. This is quite a significant point, when real time flow estimation has to be conducted in a large volume at high frame rates. Echo canceling has been an object of intense research, and the new SVD based methods are very promising for separating flow from tissue, especially when employed on the new ultrafast SA sequences.

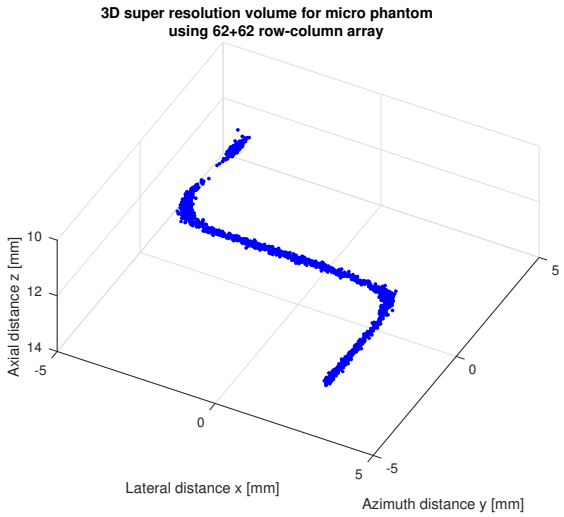

Fig. 16. Three-dimensional super resolution of of 3-D printed micro-phantom with a 200 μm diameter channel. The blue dots each indicate a single detected bubble (from [83]).

Implementation of the processing of the data from the probes is also a problem. The data rates from RC probes are comparable to the rates already processed in commercial consoles, but the output rate is higher since a full volume has to be made. Often, several volumes have to be made from the same data at a rate of f_{prf} for flow imaging, when 3-D VFI is made.

The large amount of 3-D data being made available at fast rates is a challenge to visualize and understand in the clinic, and new display methods have to be developed in collaboration with clinicians. It is especially important to keep in mind, what is usable in the clinic, and what can improve work flow and diagnostic reliability. The further development of quantitative measures can be an avenue for improving diagnostic information. Volume flow, peak velocities, and pressure gradients might be beneficial, and their precision can be directly deduced from the data for showing diagnostic reliability.

Acknowledgment

This work was financially supported by grant 82-2014-4 from the Danish National Advanced Technology Foundation, by grant 7050-00004B from Innovation Fund Denmark, and from BK Medical, Herlev, Denmark.

REFERENCES

[1] S. Satomura, "Ultrasonic Doppler method for the inspection of cardiac functions," *J. Acoust. Soc. Am.*, vol. 29, pp. 1181–1185, 1957.

[2] ——, "Study of the flow patterns in peripheral arteries by ultrasonics," *J. Acoust. Soc. Jap.*, vol. 15, pp. 151–158, 1959.

[3] D. W. Baker, "Pulsed ultrasonic Doppler blood-flow sensing," *IEEE Trans. Son. Ultrason.*, vol. SU-17, no. 3, pp. 170–185, 1970.

[4] P. N. T. Wells, "A range gated ultrasonic Doppler system," *Med. Biol. Eng.*, vol. 7, pp. 641–652, 1969.

[5] K. Namekawa, C. Kasai, M. Tsukamoto, and A. Koyano, "Realtime bloodflow imaging system utilizing autocorrelation techniques," in *Ultrasound '82*, R. Lerski and P. Morley, Eds. New York: Pergamon Press, 1982, pp. 203–208.

[6] C. Kasai, K. Namekawa, A. Koyano, and R. Omoto, "Real-Time Two-Dimensional Blood Flow Imaging using an Autocorrelation Technique," *IEEE Trans. Son. Ultrason.*, vol. 32, no. 3, pp. 458–463, 1985.

[7] T. Loupas, J. T. Powers, and R. W. Gill, "An axial velocity estimator for ultrasound blood flow imaging, based on a full evaluation of the Doppler equation by means of a two-dimensional autocorrelation approach," *IEEE Trans. Ultrason., Ferroelec., Freq. Contr.*, vol. 42, pp. 672–688, 1995.

[8] T. Loupas, R. B. Peterson, and R. W. Gill, "Experimental evaluation of velocity and power estimation for blood flow imaging, by means of a two-dimensional autocorrelation approach," *IEEE Trans. Ultrason., Ferroelec., Freq. Contr.*, vol. 42, pp. 689–699, 1995.

[9] P. M. Embree and W. D. O'Brien, "The accurate ultrasonic measurement of volume flow of blood by time-domain correlation," in *Proc. IEEE Ultrason. Symp.*, 1985, pp. 963–966.

[10] O. Bonnefous and P. Pesqué, "Time domain formulation of pulse-Doppler ultrasound and blood velocity estimation by cross correlation," *Ultrason. Imaging*, vol. 8, pp. 73–85, 1986.

[11] J. A. Jensen, S. I. Nikolov, A. Yu, and D. Garcia, "Ultrasound vector flow imaging I: Sequential systems," *IEEE Trans. Ultrason., Ferroelec., Freq. Contr.*, vol. 63, no. 11, pp. 1704–1721, 2016.

[12] ——, "Ultrasound vector flow imaging II: Parallel systems," *IEEE Trans. Ultrason., Ferroelec., Freq. Contr.*, vol. 63, no. 11, pp. 1722–1732, 2016.

[13] M. D. Fox, "Multiple crossed-beam ultrasound Doppler velocimetry," *IEEE Trans. Son. Ultrason.*, vol. SU-25, pp. 281–286, 1978.

[14] B. Dunmire, K. W. Beach, K.-H. Labs., M. Plett, and D. E. Strandness, "Cross-beam vector Doppler ultrasound for angle independent velocity measurements," *Ultrasound Med. Biol.*, vol. 26, pp. 1213–1235, 2000.

[15] B. Dunmire and K. W. Beach, "A brief history of vector doppler," in *Proc. SPIE Med. Imag.*, vol. 4325, Feb. 2001, pp. 200–214.

[16] G. E. Trahey, J. W. Allison, and O. T. von Ramm, "Angle independent ultrasonic detection of blood flow," *IEEE Trans. Biomed. Eng.*, vol. BME-34, no. 12, pp. 965–967, 1987.

[17] J. A. Jensen and P. Munk, "A new method for estimation of velocity vectors," *IEEE Trans. Ultrason., Ferroelec., Freq. Contr.*, vol. 45, no. 3, pp. 837–851, 1998.

[18] M. E. Anderson, "Multi-dimensional velocity estimation with ultrasound using spatial quadrature," *IEEE Trans. Ultrason., Ferroelec., Freq. Contr.*, vol. 45, pp. 852–861, 1998.

[19] J. A. Jensen, *Estimation of Blood Velocities Using Ultrasound: A Signal Processing Approach*. New York: Cambridge University Press, 1996.

[20] J. W. Goodman, *Introduction to Fourier optics*, 2nd ed. New York: McGraw Hill Inc., 1996.

[21] J. Udesen and J. A. Jensen, "Investigation of transverse oscillation method," *IEEE Trans. Ultrason., Ferroelec., Freq. Contr.*, vol. 53, pp. 959–971, 2006.

[22] J. A. Jensen, "A new estimator for vector velocity estimation," *IEEE Trans. Ultrason., Ferroelec., Freq. Contr.*, vol. 48, no. 4, pp. 886–894, 2001.

[23] P. M. Hansen, M. M. Pedersen, K. L. Hansen, M. B. Nielsen, and J. A. Jensen, "Demonstration of a vector velocity technique," *Ultraschall in Med.*, vol. 32, pp. 213–215, 2011.

[24] J. A. Jensen, A. H. Brandt, and M. B. Nielsen, "Convex array vector velocity imaging using transverse oscillation and its optimization," *IEEE Trans. Ultrason., Ferroelec., Freq. Contr.*, vol. 62, no. 12, pp. 2043–2053, 2015.

[25] M. J. Pihl, J. Marcher, and J. A. Jensen, "Phased-array vector velocity estimation using transverse oscillations," *IEEE Trans. Ultrason., Ferroelec., Freq. Contr.*, vol. 59, no. 12, pp. 2662–2675, 2012.

[26] J. A. Jensen, "Transverse spectral velocity estimation," *IEEE Trans. Ultrason., Ferroelec., Freq. Contr.*, vol. 61, no. 11, pp. 1815–1823, 2014.

[27] J. Udesen, M. B. Nielsen, K. R. Nielsen, and J. A. Jensen, "Examples of in-vivo blood vector velocity estimation," *Ultrasound Med. Biol.*, vol. 33, pp. 541–548, 2007.

[28] K. L. Hansen, H. Møller-Sørensen, J. Kjaergaard, J. T. Lund, M. M. Pedersen, T. Lange, J. A. Jensen, and M. B. Nielsen, "Analysis of systolic backflow and secondary helical blood flow in the ascending aorta using vector flow imaging," *Ultrasound Med. Biol.*, vol. 42, no. 4, pp. 899–908, 2016.

[29] P. M. Hansen, J. B. Olesen, M. J. Pihl, T. Lange, S. Heerwagen, M. M. Pedersen, M. Rix, L. Lönn, J. A. Jensen, and M. B. Nielsen, "Volume flow in arteriovenous fistulas using vector velocity ultrasound," *Ultrasound Med. Biol.*, vol. 40, no. 11, pp. 2707–2714, 2014.

[30] K. L. Hansen, M. M. Pedersen, H. Møller-Sørensen, J. Kjaergaard, J. C. Nilsson, J. T. Lund, J. A. Jensen, and M. B. Nielsen, "Intraoperative cardiac ultrasound examination using vector flow imaging," *Ultrason. Imaging*, vol. 35, no. 4, pp. 318–332, Oct 2013.

[31] K. L. Hansen, H. Møller-Sørensen, J. Kjaergaard, M. B. Jensen, J. T. Lund, M. M. Pedersen, T. Lange, J. A. Jensen, and M. B. Nielsen, "Intraoperative vector flow imaging using ultrasound of the ascending aorta among 40 patients with normal, stenotic and replaced aortic valves," *Ultrasound Med. Biol.*, vol. 42, no. 10, pp. 2414–2422, 2016.

[32] K. L. Hansen, K. Juul, H. Møller-Sørensen, J. C. Nilsson, J. A. Jensen, and M. B. Nielsen, "Pediatric transthoracic cardiac vector flow imaging - A preliminary pictorial study," *Ultrasound International Open*, vol. 5, no. 1, pp. E20–E26, 2019.

[33] P. Tortoli, M. Lenge, D. Righi, G. Ciuti, H. Liebgott, and S. Ricci, "Comparison of carotid artery blood velocity measurements by vector and standard Doppler approaches," *Ultrasound Med. Biol.*, vol. 41, no. 5, pp. 1354–1362, 2015.

[34] J. A. Jensen, "Directional transverse oscillation vector flow estimation," *IEEE Trans. Ultrason., Ferroelec., Freq. Contr.*, vol. 64, no. 8, pp. 1194–1204, 2017.

[35] K. L. Hansen, H. Møller-Sørensen, J. Kjaergaard, M. B. Jensen, J. A. Jensen, and M. B. Nielsen, "Aortic valve stenosis increases helical flow and flow complexity: A study of intra-operative cardiac vector flow imaging," *Ultrasound Med. Biol.*, vol. 43, no. 8, pp. 1607–1617, 2017.

[36] J. Jensen, J. B. Olesen, P. M. Hansen, M. B. Nielsen, and J. A. Jensen, "Accuracy and sources of error for an angle independent volume flow estimator," *Proc. IEEE Ultrason. Symp.*, pp. 1714–1717, 2014.

[37] J. B. Olesen, C. A. Villagómez Hoyos, N. D. Møller, C. Ewertsen, K. L. Hansen, M. B. Nielsen, B. Bech, L. Lönn, M. S. Traberg, and J. A. Jensen, "Non-invasive estimation of pressure changes using 2-D vector velocity ultrasound: An experimental study with in-vivo examples," *IEEE Trans. Ultrason., Ferroelec., Freq. Contr.*, vol. 65, no. 5, pp. 709–719, 2018.

[38] T.-Q. Nguyen, M. S. Traberg, J. B. Olesen, P. H. Møller-Sørensen, R. Moshavegh, L. Lönn, J. A. Jensen, M. B. Nielsen, and K. L. Hansen, "Pressure difference estimation in carotid bulbs using vector flow imaging - a phantom study," in *Proc. IEEE Ultrason. Symp.*, 2019, pp. 1–4.

[39] S. I. Nikolov, "Synthetic aperture tissue and flow ultrasound imaging," Ph.D. dissertation, Ørsted•DTU, Technical University of Denmark, 2800, Lyngby, Denmark, 2001.

[40] J. Jensen, "Fast plane wave imaging," Ph.D. dissertation, DTU Elektro, Technical University of Denmark, 2017.

[41] J. A. Jensen, S. Nikolov, K. L. Gammelmark, and M. H. Pedersen, "Synthetic aperture ultrasound imaging," *Ultrasonics*, vol. 44, pp. e5–e15, 2006.

[42] M. Tanter and M. Fink, "Ultrafast imaging in biomedical ultrasound," *IEEE Trans. Ultrason., Ferroelec., Freq. Contr.*, vol. 61, no. 1, pp. 102–119, January 2014.

[43] S. I. Nikolov and J. A. Jensen, "In-vivo synthetic aperture flow imaging in medical ultrasound," *IEEE Trans. Ultrason., Ferroelec., Freq. Contr.*, vol. 50, no. 7, pp. 848–856, 2003.

[44] ——, "Velocity estimation using synthetic aperture imaging," in *Proc. IEEE Ultrason. Symp.*, 2001, pp. 1409–1412.

[45] J. A. Jensen, S. I. Nikolov, T. Misaridis, and K. L. Gammelmark, "Equipment and methods for synthetic aperture anatomic and flow imaging," in *Proc. IEEE Ultrason. Symp.*, 2002, pp. 1555–1564.

[46] N. Oddershede and J. A. Jensen, "Effects influencing focusing in synthetic aperture vector flow imaging," *IEEE Trans. Ultrason., Ferroelec., Freq. Contr.*, vol. 54, no. 9, pp. 1811–1825, 2007.

[47] L. A. F. Ledoux, P. J. Brands, and A. P. G. Hoeks, "Reduction of the clutter component in Doppler ultrasound signals based on singular value

decomposition: A simulation study," *Ultrason. Imaging*, pp. 1–18, 1997.
[48] L. Løvstakken, S. Bjærum, and H. Torp, "Optimal velocity estimation in ultrasound color flow imaging in presence of clutter," *IEEE Trans. Ultrason., Ferroelec., Freq. Contr.*, vol. 54, no. 3, pp. 539–549, March 2007.
[49] A. C. H. Yu and L. Løvstakken, "Eigen-based clutter filter design for ultrasound color flow imaging: a review," *IEEE Trans. Ultrason., Ferroelec., Freq. Contr.*, vol. 57, no. 5, pp. 1096–1111, 2010.
[50] C. Demene, T. Deffieux, M. Pernot, B.-F. Osmanski, V. Biran, J.-L. Gennisson, L.-A. Sieu, A. Bergel, S. Franqui, J.-M. Correas, I. Cohen, O. Baud, and M. Tanter, "Spatiotemporal clutter filtering of ultrafast ultrasound data highly increases Doppler and fUltrasound sensitivity," *IEEE Trans. Med. Imag.*, vol. 34, no. 11, pp. 2271–2285, 2015.
[51] J. A. Jensen and S. I. Nikolov, "Directional synthetic aperture flow imaging," *IEEE Trans. Ultrason., Ferroelec., Freq. Contr.*, vol. 51, pp. 1107–1118, 2004.
[52] J. A. Jensen and N. Oddershede, "Estimation of velocity vectors in synthetic aperture ultrasound imaging," *IEEE Trans. Med. Imag.*, vol. 25, pp. 1637–1644, 2006.
[53] C. A. Villagomez-Hoyos, M. B. Stuart, K. L. Hansen, M. B. Nielsen, and J. A. Jensen, "Accurate angle estimator for high frame rate 2-D vector flow imaging," *IEEE Trans. Ultrason., Ferroelec., Freq. Contr.*, vol. 63, no. 6, pp. 842–853, 2016.
[54] B. Y. S. Yiu, I. K. H. Tsang, and A. C. H. Yu, "GPU-based beamformer: Fast realization of plane wave compounding and synthetic aperture imaging," *IEEE Trans. Ultrason., Ferroelec., Freq. Contr.*, vol. 58, no. 7, pp. 1698–1705, 2011.
[55] J. M. Hansen, D. Schaa, and J. A. Jensen, "Synthetic aperture beamformation using the GPU," in *Proc. IEEE Ultrason. Symp.*, 2011, pp. 373–376.
[56] M. Lewandowski, M. Walczak, B. Witek, P. Kulesza, and K. Sielewicz, "Modular & scalable ultrasound platform with GPU processing," *Proc. IEEE Ultrason. Symp.*, pp. 1–4, 2012.
[57] M. B. Stuart, M. Schou, and J. A. Jensen, "Row-column beamforming with dynamic apodizations on a GPU," in *Proc. SPIE Med. Imag.*, 2019, pp. 1–7, paper number 10955-20.
[58] T. di Ianni, K. L. Hansen, C. A. V. Hoyos, R. Moshavegh, M. B. Nielsen, and J. A. Jensen, "Portable vector flow imaging compared with spectral doppler ultrasonography," *IEEE Trans. Ultrason., Ferroelec., Freq. Contr.*, vol. 66, no. 3, pp. 453–462, 2018.
[59] T. Di Ianni, T. Kjeldsen, C. Villagomez-Hoyos, J. Mosegaard, and J. A. Jensen, "Real-time implementation of synthetic aperture vector flow imaging in a consumer-level tablet," in *Proc. IEEE Ultrason. Symp.*, 2017, pp. 1–4.
[60] J. A. Jensen, "Estimation of high velocities in synthetic aperture imaging: I: Theory," *IEEE Trans. Ultrason., Ferroelec., Freq. Contr.*, vol. 66, no. 6, pp. 1024–1031, 2019.
[61] M. Tanter, J. Bercoff, L. Sandrin, and M. Fink, "Ultrafast compound imaging for 2-D motion vector estimation: application to transient elastography," *IEEE Trans. Ultrason., Ferroelec., Freq. Contr.*, vol. 49, pp. 1363–1374, 2002.
[62] J. Udesen, F. Gran, K. L. Hansen, J. A. Jensen, C. Thomsen, and M. B. Nielsen, "High frame-rate blood vector velocity imaging using plane waves: Simulations and preliminary experiments," *IEEE Trans. Ultrason., Ferroelec., Freq. Contr.*, vol. 55, no. 8, pp. 1729–1743, 2008.
[63] K. L. Hansen, J. Udesen, F. Gran, J. A. Jensen, and M. B. Nielsen, "In-vivo examples of flow patterns with the fast vector velocity ultrasound method," *Ultraschall in Med.*, vol. 30, pp. 471–476, 2009.
[64] S. Fadnes, S. A. Nyrnes, H. Torp, and L. Lovstakken, "Shunt flow evaluation in congenital heart disease based on two-dimensional speckle tracking," *Ultrasound Med. Biol.*, vol. 40, no. 10, pp. 2379–2391, 2014.
[65] J. A. Jensen, "Estimation of high velocities in synthetic aperture imaging: II: Experimental investigation," *IEEE Trans. Ultrason., Ferroelec., Freq. Contr.*, vol. 66, no. 6, pp. 1032–1038, 2019.
[66] E. Mace, G. Montaldo, I. Cohen, M. Baulac, M. Fink, and M. Tanter, "Functional ultrasound imaging of the brain," *Nature methods*, vol. 8, no. 8, pp. 662–664, 2011.
[67] E. Mace, G. Montaldo, B. Osmanski, I. Cohen, M. Fink, and M. Tanter, "Functional ultrasound imaging of the brain: Theory and basic principles," *IEEE Trans. Ultrason., Ferroelec., Freq. Contr.*, vol. 60, no. 3, pp. 492–506, 2013.
[68] J. Baranger, B. Arnal, F. Perren, O. Baud, M. Tanter, and C. Demene, "Adaptive spatiotemporal SVD clutter filtering for ultrafast Doppler imaging using similarity of spatial singular vectors," *IEEE Trans. Med. Imag.*, vol. 37, no. 7, pp. 1574–1586, July 2018.
[69] S. Holbek, K. H. Lindskov, H. Bouzari, C. Ewertsen, M. B. Stuart, C. Thomsen, M. B. Nielsen, and J. A. Jensen, "Common carotid artery flow measured by 3-D ultrasonic VFI and validated with MRI," *Ultrasound Med. Biol.*, vol. 43, no. 10, pp. 2213–2220, 2017.
[70] M. S. Wigen, S. Fadnes, A. Rodriguez-Molares, T. Bjåstad, M. Eriksen, K. H. Stensæth, A. Støylen, and L. Løvstakken, "4-D intracardiac ultrasound vector flow imaging-reasibility and comparison to phase-contrast MRI," *IEEE Trans. Med. Imag.*, vol. 37, no. 12, pp. 2619–2629, December 2018.
[71] M. J. Pihl and J. A. Jensen, "A transverse oscillation approach for estimation of three-dimensional velocity vectors. Part I: Concept and simulation study," *IEEE Trans. Ultrason., Ferroelec., Freq. Contr.*, vol. 61, pp. 1599–1607, 2014.
[72] M. J. Pihl, M. B. Stuart, B. G. Tomov, M. F. Rasmussen, and J. A. Jensen, "A transverse oscillation approach for estimation of three-dimensional velocity vectors. Part II: Experimental validation," *IEEE Trans. Ultrason., Ferroelec., Freq. Contr.*, vol. 51, no. 10, pp. 1608–1618, 2014.
[73] L. Ratsimandresy, P. Mauchamp, D. Dinet, N. Felix, and R. Dufait, "A 3 MHz two dimensional array based on piezocomposite for medical imaging," in *Proc. IEEE Ultrason. Symp.*, 2002, pp. 1265–1268.
[74] J. A. Jensen, H. Holten-Lund, R. T. Nilsson, M. Hansen, U. D. Larsen, R. P. Domsten, B. G. Tomov, M. B. Stuart, S. I. Nikolov, M. J. Pihl, Y. Du, J. H. Rasmussen, and M. F. Rasmussen, "SARUS: A synthetic aperture real-time ultrasound system," *IEEE Trans. Ultrason., Ferroelec., Freq. Contr.*, vol. 60, no. 9, pp. 1838–1852, 2013.
[75] C. E. Morton and G. R. Lockwood, "Theoretical assessment of a crossed electrode 2-D array for 3-D imaging," in *Proc. IEEE Ultrason. Symp.*, 2003, pp. 968–971.
[76] N. M. Daher and J. T. Yen, "2-D array for 3-D ultrasound imaging using synthetic aperture techniques," *IEEE Trans. Ultrason., Ferroelec., Freq. Contr.*, vol. 53, no. 5, pp. 912–924, 2006.
[77] M. F. Rasmussen, T. L. Christiansen, E. V. Thomsen, and J. A. Jensen, "3-D imaging using row–column-addressed arrays with integrated apodization — Part I: Apodization design and line element beamforming," *IEEE Trans. Ultrason., Ferroelec., Freq. Contr.*, vol. 62, no. 5, pp. 947–958, 2015.
[78] T. L. Christiansen, M. F. Rasmussen, J. P. Bagge, L. N. Moesner, J. A. Jensen, and E. V. Thomsen, "3-D imaging using row–column-addressed arrays with integrated apodization — part II: Transducer fabrication and experimental results," *IEEE Trans. Ultrason., Ferroelec., Freq. Contr.*, vol. 62, no. 5, pp. 959–971, 2015.
[79] H. Bouzari, M. Engholm, S. I. Nikolov, M. B. Stuart, E. V. Thomsen, and J. A. Jensen, "Imaging performance for two row-column arrays," *IEEE Trans. Ultrason., Ferroelec., Freq. Contr.*, vol. 66, no. 7, pp. 1209–1221, 2019.
[80] S. Holbek, T. L. Christiansen, M. B. Stuart, C. Beers, E. V. Thomsen, and J. A. Jensen, "3-D vector flow estimation with row-column addressed arrays," *IEEE Trans. Ultrason., Ferroelec., Freq. Contr.*, vol. 63, no. 11, pp. 1799–1814, 2016.
[81] S. Holbek, T. L. Christiansen, M. F. Rasmussen, M. B. Stuart, E. V. Thomsen, and J. A. Jensen, "3-D vector velocity estimation with row-column addressed arrays," in *Proc. IEEE Ultrason. Symp.*, 2015, pp. 1–4.
[82] M. Schou, L. T. Jørgensen, M. B. Stuart, M. S. Traberg, B. G. Tomov, and J. A. Jensen, "Full volumetric 3-D vector flow imaging using a 62+62 row-column array," in *Proc. IEEE Ultrason. Symp.*, 2019, pp. 1–4.
[83] J. A. Jensen, M. L. Ommen, S. H. Øygard, M. Schou, T. Sams, M. B. Stuart, C. Beers, E. V. Thomsen, N. B. Larsen, , and B. G. Tomov, "Three-dimensional super resolution imaging using a row-column array," *IEEE Trans. Ultrason., Ferroelec., Freq. Contr.*, p. Submitted, 2019.

Paper 2

3-D Super-Resolution Imaging using a 62+62 Elements Row-Column Array

Jørgen Arendt Jensen, Mikkel Schou, Martin Lind Ommen, **Sigrid Husebø Øygard**, Thomas Sams, Matthias Bo Stuart, Erik Vilain Thomsen, Niels Bent Larsen, Christopher Beers, and Borislav Gueorguiev Tomov

Published in:
Proceedings of the IEEE International Ultrasonic Symposium

Document Version:
Published

DOI:
10.1109/ULTSYM.2019.8926092

2019 IEEE International Ultrasonics Symposium (IUS)
Glasgow, Scotland, October 6-9, 2019

3-D Super Resolution Imaging using a 62+62 Elements Row-Column Array

Jørgen Arendt Jensen[1], Mikkel Schou[1], Martin Lind Ommen[1], Sigrid Husebø Øygard[1],
Thomas Sams[1], Matthias Bo Stuart[1], Erik Vilain Thomsen[1],
Niels Bent Larsen[1], Christopher Beers[2] and Borislav Gueorguiev Tomov[1]

[1]Department of Health Technology,
Technical University of Denmark, DK-2800 Lyngby, Denmark
[2] BK Medical, 401 Science Park Road, State College, PA 16803, USA

***Abstract*—Current 2-D Super Resolution (SR) imaging is limited by the slice thickness determined by the elevation focus. The fixed, geometric elevation focus is often poor due to its high F-number. SR images are, thus, a summation of vessels across the elevation plane without the possibility to track scatterers in 3-D for full visualization. 3-D SR imaging has been obtained by translating the probe, but this does not remove the elevation summation. Full 3-D can be acquired using 2-D matrix probes, but the equipment is expensive, and the amount of data is excessive, when channel data are acquired over thousands of elements for minutes. This paper demonstrates that full volumetric SRI can be attained using a 62+62 channels Row-Column (RC) probe with a high frame rate and with μm precision. Data were acquired by a 3 MHz 62+62 PZT RC probe with $\lambda/2$ pitch connected to the SARUS scanner. A synthetic aperture scan sequence with 32 positive and 32 negative emissions was employed for pulse inversion (PI) imaging with an MI of 0.3. The pulse repetition frequency was 10 kHz for a 156 Hz volume rate. A PEGDA 700 g/mol based hydrogel flow-microphantom was 3-D printed by stereo-lithography. It contains a single cylindrical 200 μm diameter channel placed 3 mm from the top surface of the phantom. After a 5.8 mm long inlet, the channel bends 90° into a 7 mm long central region before bending 90° again into the 5.8 mm outlet. The flow channel was infused at 1.61 μL/s with Sonovue (Bracco) in a 1:10 dilution. The received RF signals from the 62 row elements were beamformed with PI to yield a full volume of 15 x 15 x 15 mm^3. The interpolated 3-D positions of the bubbles were estimated after local maximum detection. The reconstructed 3-D SR volume clearly shows the 200 μm channel shape with a high resolution in all three dimensions. The center line for the channel was found by fitting a line to all bubble positions, and their radial position calculated. The observed fraction of bubbles falling outside the channel was used for estimating the location precision. The precision was 16.5 μm in the $y-z$ plane and 23.0 μm in the $x-z$ plane. The point spread function had a size of 0.58 x 1.05 x 0.31 mm^3, so the interrogated volume was 15,700 times smaller than for normal volumetric B-mode imaging. This demonstrates that full 3-D SRI can be attained with just 62 receive channels. The SA sequence has a low MI, but attains a large measured penetration depth of 14 cm in a tissue mimicking phantom, due to the large RC probe size. The 156 Hz volume rate also makes it possible to track high velocities in 3-D in the volume.**

I. Introduction

Super resolution (SR) imaging has recently been introduced in ultrasound. The method is based on tracking the centroid of contrast agent bubbles and thereby paint an image of the micro-vasculature [1–6]. Very high resolutions can be attained from the non-linear estimation of the target's centroid positions, and reports of image resolution in the 10 μm range have been given [7]. The results presented are predominantly in 2-D, and the high resolution is only attained in the image plane. The out-of-plane resolution is determined by the elevation focus, which often is poor due to the fixed-focus lens. The F-number (imaging depth divided by the probe width) is usually 2 to 5 giving an ideal resolution of $2\lambda - 5\lambda$ at the focal depth and worse away from it (λ is the wavelength given by c/f_0, where c is the speed of sound and f_0 is transducer center frequency). The images are acquired over several seconds to minutes generating Gbytes of data. Currently, most SRI is conducted using 1-D array probes due to the large amount of data generated, and that few scanners are capable of full 3-D imaging.

Visualization of 3-D SR volumes has been performed by several groups using mechanically translated linear array probes [6, 8, 9], but such a setup does not make it possible to estimate the out-of-plane location. SR has also been made using two orthogonal probes for 3-D localization in a line [10], and mechanical scanning is needed to cover a full volume. A matrix probe is, thus, needed for avoiding mechanical scanning.

Currently, the largest research scanners have 1024 channels [11, 12], and they generate around 20-50 Gbytes/s of data for 3 MHz probes, only making short acquisitions possible and precluding the use of high-frequency probes. They can handle 2-D arrays with $32 \times 32 = 1024 = N^2$ elements, which have been fabricated with $\lambda/2$ pitch . This makes them suitable for phased array imaging, but severely limits their focusing ability due to their small size and hence high F-numbers.

The problem can be somewhat alleviated by using sparse arrays, and Harput et al. [13] recently used a 512 elements sparse 2-D array based on a spiral pattern to acquire full 3-D SR imaging. Two 256 channels research scanners [14] were used for scanning of 200 μm cellulose tubes with a final localization precision of 18 μm. The main drawback of this approach is the many transducer channels needed to avoid grating lobes and the corresponding large amounts of data generated per second. Further, the probe is quite small

978-1-7281-4596-9/19/$31.00 ©2019 IEEE

($\varnothing$ 10.4 mm), as it has to be nearly fully populated to avoid side and grating lobes, limiting the possible F-numbers.

This paper describes a 3-D SR method based on a Row-Column (RC) array with only 62+62 elements. The approach is implemented using a prototype RC array, and the imaging is conducted using the SARUS research scanner [11]. Its precision is investigated using a 3-D printed micro-phantom and is estimated from the located bubbles in the phantom.

II. Methods

A. Data acquisition and beamforming

A prototype 3 MHz PZT RC array with 62 rows and 62 columns was used for the data acquisition [15]. It contains amplifiers in the handle and was fabricated with edge apodization to reduce ghost echoes after the main point spread function (PSF) [16]. The probe has $\lambda/2$ pitch to avoid grating lobes. It was connected to the SARUS scanner [11], which acquired full RF data for all the receiving channels.

A synthetic aperture, pulse inversion sequence was used for imaging. Transmissions were conducted using the rows, and data were received on all 62 columns. The virtual line sources emitted cylindrical waves [17] in a sequence with 32 positive emissions and 32 negative emission to make pulse inversion imaging possible. The transmit F-number was -1 using 32 Hanning apodized active elements, with the virtual source placed behind the array.

B. 3-D micro-phantom

A flow micro-phantom is fabricated for validating the approach by 3-D printing of a PEGDA 700 g/mol hydrogel using stereo-lithography, as described in [18]. The phantom measures $21.1 \times 8.16 \times 11.9$ mm^3, and the voxel size of the printer is $(\Delta x, \Delta y, \Delta z) = 10.8 \times 10.8 \times 20 \mu$m^3. The flow micro-phantom contains a single cylindrical 100 μm radius channel placed 3 mm from the top surface of the phantom. After a 5.8 mm long inlet, the channel bends 90° into a 7 mm long central region before bending 90° again into the 5.8 mm outlet. The flow channel is infused at 1.61 μL/s with SonoVue (Bracco, Milano, Italy) in a 1:10 dilution, giving a peak velocity of 102.4 mm/s.

C. Processing pipeline

The beamformed volumes are processed in Matlab using our 3-D SR processing pipeline consisting of three steps. The first is to beamform the stored RF data from the SARUS scanner using the beamforming strategy described by Rasmussen et al. [16, 17] implemented in Matlab and running on an Nvidia GeForce GTX 1050 Ti (Nvidia, Santa Clara, CA, USA) GPU [19]. For the flow micro-phantom the second harmonic signal is employed, and a filter matched to the second harmonic is employed on all the received signals. The GPU beamformer was used for making the focusing of the full volumes for all emissions with an F-number of 1.5 in transmit and 1 in receive with a dynamic Hanning apodization weighting the elements. The volumes with a size of $\pm 15\lambda$ in both the x and y directions were beamformed with a line density of $\lambda/2$ covering the full depth of the phantom. The sampling density in the z direction is $\lambda/16$. All emissions are added to generate the high resolution volume (HRV), and the positive and negative emissions HRVs are added to enhance the bubble signals.

The second step is to subtract the stationary background signal. The mean value of twenty volumes is found and subtracted from all the 400 volumes acquired. The envelope of the HRV is then found using a Hilbert transform and log compressed to a 40 dB dynamic range in relation to the data in the volume for finding locations.

The bubble locations can either be found from calculation of the centroid of local maxima, or the peak locations can be interpolated to increase the location accuracy. Experimentation with the data showed that the interpolation scheme is the most stable and accurate method, and this is the one used in this paper.

The third stage finds bubble locations by interpolating the peak position by fitting a second order polynomial to the data and then finding its interpolated maximum position x_i, as:

$$x_i = i - \frac{0.5(d(i+1,j,k) - d(i-1,j,k))}{d(i+1,j,k) - 2d(i,j,k) + d(i-1,j,k)}, \quad (1)$$

where i, j, k are the indices of the maximum and d is the envelope data for the volume. This is conducted in all three coordinates x_i, y_j, z_k with similar equations for an increased resolution in all three directions.

D. Statistical evaluation

The detected bubble locations are randomly distributed in the flow micro-phantom tube due to noise in the localization estimation, and some of them will appear to be located outside the phantom wall. The distribution of positions found can therefore yield an estimate of the localization precision. An estimate of the $y-z$ and $x-z$ precision can be obtained from the two straight segments of the 200μm channel phantom. In the straight segments a line is fitted to the data and considered an estimate of the center of the channel, and the distance from each bubble to the center is calculated. Assuming the measurement uncertainty in each dimension is normal distributed, the radial distribution of all bubbles in the segment will follow the distribution

$$f(r) = 2\pi r \int_{|\vec{r}_t|<R} \frac{1}{\pi R^2} \frac{1}{2\pi\sigma^2} \exp\left(\frac{-|\vec{r}-\vec{r}_t|^2}{2\sigma^2}\right) d^2 r_t, \quad (2)$$

where r is radial position, R is the radius of the tube, and σ is the standard deviation of the uncertainty. The integral is a convolution of a constant density $(1/(\pi R^2))$ with a two-dimensional Gaussian. The non-analytical integral (2) is estimated in a Monte-Carlo calculation and is a Rayleigh distribution convolved with a uniform disk distribution of radius $R = 100$ μm. The fraction of bubbles estimated to fall outside the tube can then be translated into an estimate for the standard deviation σ (localization precision).

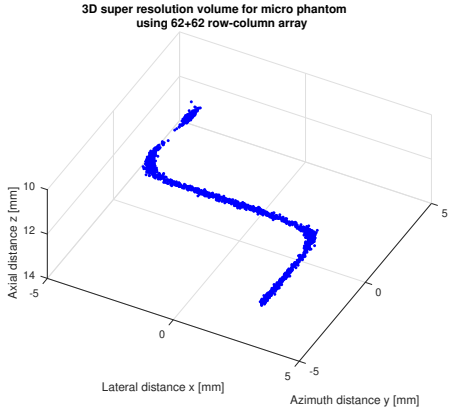

Fig. 1. Visualization of the 3-D phantom after detection of bubble locations each indicated by a blue dot.

III. Results

Initially the penetration depth for the scheme is measured. It gives a penetration depth of 14 cm (0 dB signal-to-noise ratio) when using a tissue mimicking phantom with an attenuation of 0.5 dB/[MHz cm]. The SA imaging sequence and array were also simulated in Field II [20, 21] and yielded a PSF with a size of $(1.17\lambda \times 2.12\lambda \times 0.63\lambda)$ at 15 mm.

The resulting 3-D SR image is shown in Fig. 1, where each blue dot indicates the identification of a bubble. The full geometry of the phantom can be seen with the inlet and outlet and the detected bubbles seem confined to the tube.

The localization in the $y-z$ has been investigated by selecting the bubble only moving in the x direction as is shown in the top graph in Fig. 2, where blue crosses are the selected bubbles and red dots indicates all localized bubbles. Lines have then been fitted to the center of all the locations as shown in Fig. 3, so the distance from the tube center to the bubble locations can be found. The radial positions are then found and shown in Fig. 4. Bubbles inside the tube are marked by a cross and bubbles outside are marked by a red circle with a blue cross.

The fraction of bubbles outside the tube, as shown in Fig. 5, is then an indication of the precision of the bubble localization as described in Section II-D. The fraction is in this case 13.0%, which translates to a precision of 16.5 μm. The fraction is 18.2% in the $x-z$ plane translating to a precision of 23.0 μm. The simulated point spread function of the imaging setup at this depth is $0.58 \times 1.05 \times 0.31$ mm^3 (x,y,z), which corresponds to an interrogated volume of 0.189 mm^3 . Assuming the precision in all three coordinates is 23.0 μm gives a volume of 12,167 μm^3, which is 15,700 times smaller than for the PSF limited system.

IV. Discussion and Conclusion

A 3-D SR measurement scheme and processing pipeline have been presented. The approach uses a 62+62 elements RC probe, where only rows are used for emission and columns for reception. The scheme employs two times 32 emissions for pulse inversion imaging attaining a volume rate of 240 Hz down to 5 cm or 85 Hz down to 14 cm, which is the penetration depth of the imaging scheme.

The major advantage is that the volume is focused in all three directions including the elevation direction, which yields a resolution of $(1.17\lambda \times 2.12\lambda \times 0.63\lambda)$ at a depth of 15 mm. This was attained for a modest 62 elements, which both reduces the amount of data from the probe by a factor of 8 compared to previous 3-D SRI [13] as well as the beamforming time for a probe with 4 times the area of a 1024 elements 2-D matrix probe.

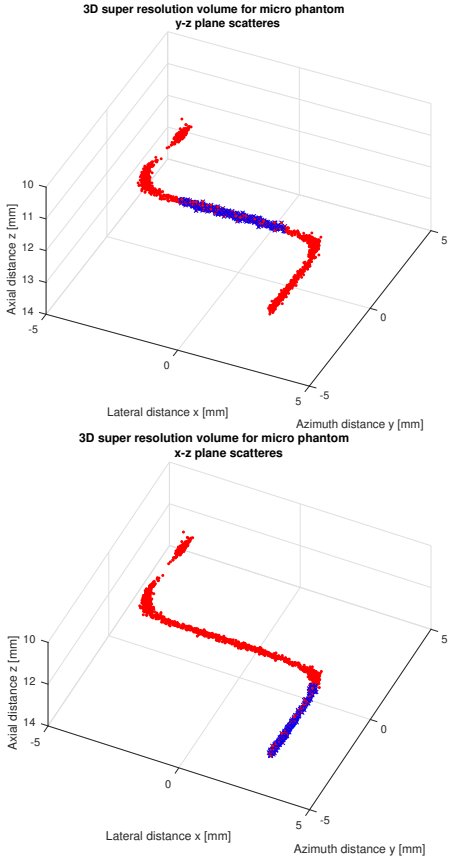

Fig. 2. Identification of bubbles only flowing in the x direction (top) and only in the y direction in the outlet (bottom). Red dots show all the bubble locations and blue crosses are the selected bubbles.

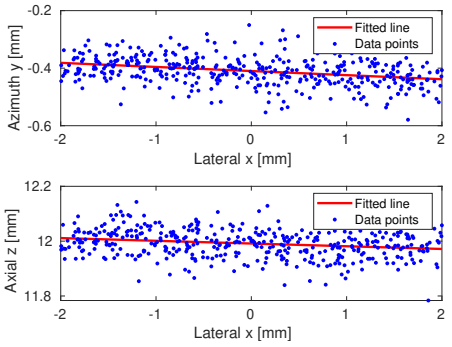

Fig. 3. Fitted center line for the bubble locations with movement in the x direction.

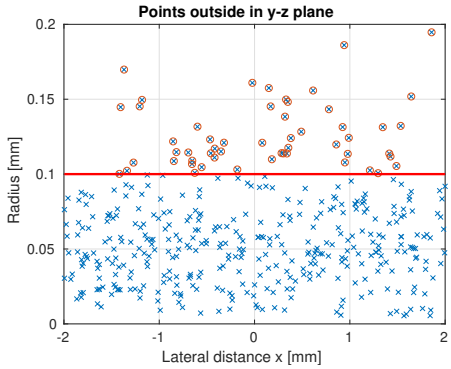

Fig. 4. Radius of the bubble position relative to the fitted center line in the $y-z$ plane. Blue crosses marks the locations of all bubbles and red circles mark bubbles outside the vessel boundary.

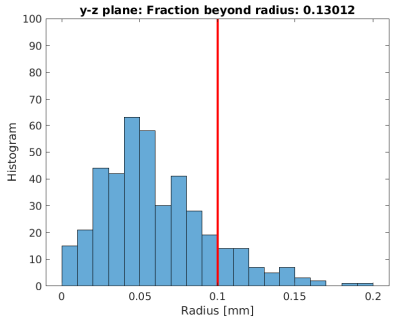

Fig. 5. Histogram for the bubble radius. The red line indicates the 100 μm radius of the tube and the fraction of bubbles outside is 13.0%.

The processing pipeline yielded a precision of 16.5 μm in the $y-z$ plane and 23.0 μm in the $x-z$ plane, which is 15,700 times smaller in volume than for the PSF limited RC system. The number of active elements is three times less than what is available in commercial ultrasound consoles, and the beamforming can be attained in near real-time, when employing a state-of-the-art GPU card [22].

Acknowledgement

This work was financially supported by grant 7050-00004B from Innovation Fund Denmark, and from BK Medical, Herlev, Denmark.

References

[1] O. Couture, B. Besson, G. Montaldo, M. Fink, and M. Tanter, "Microbubble ultrasound super-localization imaging (MUSLI)," in *Proc. IEEE Ultrason. Symp.*, 2011, pp. 1285–1287.

[2] O. M. Viessmann, R. J. Eckersley, K. C. Jeffries, M. X. Tang, and C. Dunsby, "Acoustic super-resolution with ultrasound and microbubbles," *Phys. Med. Biol.*, vol. 58, pp. 6447–6458, 2013.

[3] M. Siepmann, G. Schmitz, J. Bzyl, M. Palmowski, and F. Kiessling, "Imaging tumor vascularity by tracing single microbubbles," *Proc. IEEE Ultrason. Symp.*, pp. 6 293 297, 1906–1908, 2011.

[4] M. A. O'Reilly and K. Hynynen, "A super-resolution ultrasound method for brain vascular mapping," *Med. Phys.*, vol. 40, no. 11, pp. 110 701–7, 2013.

[5] K. Christensen-Jeffries, R. J. Browning, M. Tang, C. Dunsby, and R. J. Eckersley, "In vivo acoustic super-resolution and super-resolved velocity mapping using microbubbles," *IEEE Trans. Med. Imag.*, vol. 34, no. 2, pp. 433–440, February 2015.

[6] C. Errico, J. Pierre, S. Pezet, Y. Desailly, Z. Lenkei, O. Couture, and M. Tanter, "Ultrafast ultrasound localization microscopy for deep super-resolution vascular imaging," *Nature*, vol. 527, pp. 499–502, November 2015.

[7] O. Couture, V. Hingot, B. Heiles, P. Muleki-Seya, and M. Tanter, "Ultrasound localization microscopy and super-resolution: A state of the art," *IEEE Trans. Ultrason., Ferroelec., Freq. Contr.*, vol. 65, no. 8, pp. 1304–1320, 2018.

[8] J. Zhu, E. M. Rowland, S. Harput, K. Riemer, C. H. Leow, B. Clark, K. Cox, A. Lim, K. Christensen-Jeffries, G. Zhang, J. Brown, C. Dunsby, R. J. Eckersley, P. D. Weinberg, and M.-X. Tang, "3D super-resolution US imaging of rabbit lymph node vasculature in vivo by using microbubbles," *Radiology*, vol. 291, no. 3, pp. 642–650, 2019.

[9] F. Lin, S. E. Shelton, D. Espindola, J. D. Rojas, G. Pinton, and P. A. Dayton, "3-D ultrasound localization microscopy for identifying microvascular morphology features of tumor angiogenesis at a resolution beyond the diffraction limit of conventional ultrasound," *Theranostics*, vol. 7, no. 1, pp. 196–204, 2017.

[10] K. Christensen-Jeffries, S. Harput, J. Brown, P. N. T. Wells, P. Aljabar, C. Dunsby, M. Tang, and R. J. Eckersley, "Microbubble axial localization errors in ultrasound super-resolution imaging," *IEEE Trans. Ultrason., Ferroelec., Freq. Contr.*, vol. 64, no. 11, pp. 1644–1654, 2017.

[11] J. A. Jensen, H. Holten-Lund, R. T. Nilsson, M. Hansen, U. D. Larsen, R. P. Domsten, B. G. Tomov, M. B. Stuart, S. I. Nikolov, M. J. Pihl, Y. Du, J. H. Rasmussen, and M. F. Rasmussen, "SARUS: A synthetic aperture real-time ultrasound system," *IEEE Trans. Ultrason., Ferroelec., Freq. Contr.*, vol. 60, no. 9, pp. 1838–1852, 2013.

[12] L. Petrusca, F. Varray, R. Souchon, A. Bernard, J. Y. Chapelon, H. Liebgott, W. A. N'Djin, and M. Viallon, "Fast volumetric ultrasound B-mode and Doppler imaging with a new high-channels density platform for advanced 4D cardiac imaging/therapy," *Applied Sciences (Switzerland)*, vol. 8, no. 2, pp. 200:1–15, 2018.

[13] S. Harput, K. Christensen-Jeffries, A. Ramalli, J. Brown, J. Zhu, G. Zhang, C. H. Leow, M. Toulemonde, E. Boni, P. Tortoli, R. J. Eckersley, C. Dunsby, and M. Tang, "3-D super-resolution ultrasound (SR-US) imaging with a 2-D sparse array," *arXiv preprint*, p. 1902.01608v1, 2019.

[14] E. Boni, L. Bassi, A. Dallai, F. Guidi, V. Meacci, A. Ramalli, S. Ricci, and P. Tortoli, "ULA-OP 256: A 256-channel open scanner for development and real-time implementation of new ultrasound methods," *IEEE Trans. Ultrason., Ferroelec., Freq. Contr.*, vol. 63, no. 10, pp. 1488–1495, 2016.

[15] M. Engholm, H. Bouzari, T. L. Christiansen, C. Beers, J. P. Bagge, L. N. Moesner, S. E. Diederichsen, M. B. Stuart, J. A. Jensen, and E. V. Thomsen, "Probe development of CMUT and PZT row–column-addressed 2-D arrays," *Sens. Actuators A: Phys.*, vol. 273, pp. 121–133, 2018.

[16] M. F. Rasmussen, T. L. Christiansen, E. V. Thomsen, and J. A. Jensen, "3-D imaging using row–column-addressed arrays with integrated apodization — Part I: Apodization design and line element beamforming," *IEEE Trans. Ultrason., Ferroelec., Freq. Contr.*, vol. 62, no. 5, pp. 947–958, 2015.

[17] H. Bouzari, M. Engholm, S. I. Nikolov, M. B. Stuart, E. V. Thomsen, and J. A. Jensen, "Imaging performance for two row-column arrays," *IEEE Trans. Ultrason., Ferroelec., Freq. Contr.*, vol. 66, no. 7, pp. 1209–1221, 2019.

[18] M. L. Ommen, M. Schou, R. Zhang, C. A. V. Hoyos, J. A. Jensen, N. B. Larsen, and E. V. Thomsen, "3D printed flow phantoms with fiducial markers for super-resolution ultrasound imaging," in *Proc. IEEE Ultrason. Symp.*, 2018, pp. 1–4.

[19] M. B. Stuart, M. Schou, and J. A. Jensen, "Row-column beamforming with dynamic apodizations on a GPU," in *Proc. SPIE Med. Imag.*, 2019, pp. 1–7, paper number 10955-20.

[20] J. A. Jensen and N. B. Svendsen, "Calculation of pressure fields from arbitrarily shaped, apodized, and excited ultrasound transducers," *IEEE Trans. Ultrason., Ferroelec., Freq. Contr.*, vol. 39, no. 2, pp. 262–267, 1992.

[21] J. A. Jensen, "Field: A program for simulating ultrasound systems," *Med. Biol. Eng. Comp.*, vol. 10th Nordic-Baltic Conference on Biomedical Imaging, Vol. 4, Supplement 1, Part 1, pp. 351–353, 1996.

[22] M. B. Stuart, P. M. Jensen, J. T. R. Olsen, A. B. Kristensen, M. Schou, B. Dammann, H. H. B. Sørensen, and J. A. Jensen, "Fast GPU-beamforming of row-column addressed probe data," in *Proc. IEEE Ultrason. Symp.*, 2019, pp. 1–4.

Paper 3

Three-Dimensional Super-Resolution Imaging using a Row-Column Array

Jørgen Arendt Jensen, Martin Lind Ommen, Mikkel Schou, **Sigrid Husebø Øygard**, Thomas Sams, Matthias Bo Stuart, Christopher Beers, Erik Vilain Thomsen, Niels Bent Larsen,, and Borislav Gueorguiev Tomov

Name of journal:
IEEE Transactions on Ultrasonics, Ferroelectrics, and Frequency Control

Document Version:
Published

DOI:
10.1109/TUFFC.2019.2948563

Three-Dimensional Super-Resolution Imaging Using a Row–Column Array

Jørgen Arendt Jensen, *Fellow, IEEE*, Martin Lind Ommen, Sigrid Husebø Øygard, Mikkel Schou, Thomas Sams, Matthias Bo Stuart, Christopher Beers, Erik Vilain Thomsen, Niels Bent Larsen, and Borislav Gueorguiev Tomov

***Abstract*— A 3-D super-resolution (SR) pipeline based on data from a row–column (RC) array is presented. The 3-MHz RC array contains 62 rows and 62 columns with a half wavelength pitch. A synthetic aperture (SA) pulse inversion sequence with 32 positive and 32 negative row emissions is used for acquiring volumetric data using the SARUS research ultrasound scanner. Data received on the 62 columns are beamformed on a GPU for a maximum volume rate of 156 Hz when the pulse repetition frequency is 10 kHz. Simulated and 3-D printed point and flow microphantoms are used for investigating the approach. The flow microphantom contains a 100-μm radius tube injected with the contrast agent SonoVue. The 3-D processing pipeline uses the volumetric envelope data to find the bubble's positions from their interpolated maximum signal and yields a high resolution in all three coordinates. For the point microphantom, the standard deviation on the position is (20.7, 19.8, 9.1) μm (x, y, z). The precision estimated for the flow phantom is below 23 μm in all three coordinates, making it possible to locate structures on the order of a capillary in all three dimensions. The RC imaging sequence's point spread function has a size of 0.58 × 1.05 × 0.31 mm^3 (1.17λ × 2.12λ × 0.63λ), so the possible volume resolution is 28 900 times smaller than for SA RC B-mode imaging.**

***Index Terms*— Matrix arrays, row–column (RC), super-resolution (SR), ultrasound.**

I. Introduction

ULTRASOUND super-resolution imaging (SRI) was introduced by a number of groups for increasing the resolution of ultrasound imaging beyond the diffraction limit [1]–[6]. The approach is based on the injection of a diluted ultrasound contrast agent to enable tracking of individual bubbles. The centroids of the bubble signals are calculated, and their tracks are determined and displayed to show an image of the vasculature. This can reveal the microvasculature down to vessel sizes of 10 μm [7]. The images are acquired over several seconds to minutes, generating gigabytes of data. Currently, most SRIs are conducted using 1-D array probes due to the large amount of data, and that few scanners are capable of full 3-D imaging. The 2-D SR images, therefore, have a high resolution in the imaging plane, but localization in the elevation direction is not possible. Two-dimensional SRI, therefore, displays a summation of vessels in the elevation plane.

Visualization of 3-D SR volumes has been performed by several groups using mechanically translated linear array probes [6], [8], [9], but such a setup does not make it possible to estimate the out-of-plane location. SR has also been made using two orthogonal probes for 3-D localization in a line [10], and mechanical scanning is needed to cover a full volume. A matrix probe is thus needed for avoiding mechanical scanning.

Currently, the largest research scanners have 1024 channels [11], [12], and they generate around 20–50 GB/s of data for 3-MHz probes, only making short acquisitions possible and precluding the use of high-frequency probes. They can handle 2-D arrays with $32 \times 32 = 1024 = N^2$ elements that have been fabricated with $\lambda/2$ pitch (λ is the wavelength given by c/f_0, where c is the speed of sound and f_0 is the transducer center frequency). This makes them suitable for phased array imaging but severely limits their focusing ability due to their small size and, hence, high F-numbers (imaging depth divided by the probe width).

The problem can be somewhat alleviated by using sparse arrays, and Harput *et al.* [13] recently used a 512-element sparse 2-D array based on a spiral pattern to acquire full 3-D SR imaging. Two 256 channels research scanners [14] were used for scanning of 200-μm cellulose tubes with a final localization precision of 18 μm. The main drawback of this approach is the many transducer channels needed to avoid grating lobes and the corresponding large amounts of data generated per second. Furthermore, the probe is quite small ($\varnothing$10.4 mm), as it has to be nearly fully populated to avoid the sidelobe and grating lobe, limiting the possible F-numbers.

A new approach is, therefore, needed for 3-D SR volumetric imaging. One possibility for reducing the number of elements by a factor of $N/2$ is the employment of row–column (RC) arrays as introduced by Morton and Lockwood [15] and later investigated by a number of groups [16]–[20]. Here, the array is addressed by either its rows or columns, and imaging can be conducted using synthetic aperture (SA) imaging schemes [21] for high resolution, deep penetration depth, and high volume

Manuscript received August 13, 2019; accepted October 17, 2019. Date of publication October 21, 2019; date of current version February 25, 2020. This work was supported in part by the Danish National Advanced Technology Foundation under Grant 82-2014-4, in part by Innovation Fund Denmark under Grant 7050-00004B, and in part by BK Medical, Herlev, Denmark. *(Corresponding author: Jørgen Arendt Jensen.)*

J. A. Jensen, M. L. Ommen, S. H. Øygard, M. Schou, T. Sams, M. B. Stuart, E. V. Thomsen, N. B. Larsen, and B. G. Tomov are with the Department of Health Technology, Technical University of Denmark, 2800 Lyngby, Denmark (e-mail: jaje@dtu.dk).

C. Beers is with BK Medical, State College, PA 16803 USA.

This article has supplementary downloadable material available at http://ieeexplore.ieee.org, provided by the author.

Digital Object Identifier 10.1109/TUFFC.2019.2948563

TABLE I
RC 62 + 62 PZT PROBE DIMENSIONS

Parameters	62+62 RC
Number of elements	62+62
Center frequency f_0	3 MHz
Wavelength λ	513 μm
Kerf	25 μm
Pitch	270 μm ($\approx \lambda/2$)
Apodization region length	4.05 mm
Element length	24.84 mm
Total Active Surface area	282.2 mm^2

rate. Furthermore, RC SA imaging schemes can have a low mechanical index (MI) due to the emission of cylindrical waves, making them ideally suited for contrast agent imaging. The RC arrays can be made large without having an excessive amount of elements, making it possible to both have low F-numbers for high resolutions and still have modest data rates from the arrays.

This article presents a 3-D SR imaging method using a prototype 62 + 62 RC array [22] connected to the SARUS research scanner [11]. Two 3-D printed microphantoms are used for validating the approach along with a simulation of a point phantom. The precision of the pipeline is revealed from these simulations and measurements.

II. METHODS

This section describes the various methods used in the 3-D SR pipeline, including the imaging scheme, processing pipeline, and statistical evaluation.

A. Imaging Sequence and Processing

The imaging sequence was optimized for a 62 + 62 RC PZT 3-MHz experimental probe with dimensions given in Table I. The probe includes a mechanical apodization at each end of the elements to reduce edge element artifacts, as described in previous publications on the probe [19]–[22]. The volumetric RC SA imaging scheme consists of 32 virtual focus lines using 32 active elements per emissions. An F-number of −1 was used for emitting defocused line sources with the focal point placed behind the probe surface and with a Hanning weighting to reduce sidelobes. The 32 different virtual lines were placed to generate a sliding aperture imaging sequence across the rows. The transmission was only made with the rows, and reception was made with the column elements, resulting in 62 signals to be stored per emission. Pulse-inversion imaging was conducted by emitting two two-cycle sinusoidal 3-MHz waves, one positive and one negative, for each virtual line source. The imaging sequence was implemented on the SARUS experimental scanner [11], with a transmit sampling frequency of 70 MHz. The receive sampling frequency was 23.7 MHz to preserve the second-harmonic component in the signal.

Each emission was beamformed using a MATLAB-based GPU beamformer [23] to generate a low-resolution volume (LRV). The 32 different LRVs were summed to reveal a high-resolution volume (HRV). A simplified schematic of the sequence can be seen in Fig. 1. The positive + LRV (1:32) and negative − LRV (1:32) beamformed emissions were summed to reveal a second-harmonic HRV using pulse inversion. These data were then passed to the SRI processing pipeline described in Section II-B. The pulse repetition frequency (f_{prf}) was 10 kHz, and a pause of 10 ms was inserted between volumes to reduce the memory usage and extend the duration of the acquisition. The MI of the sequence was determined to be 0.2 at 12 mm from the probe surface, which is the location of the microphantom flow channel. The actual MI in the phantom is probably slightly lower due to the attenuation in the phantom.

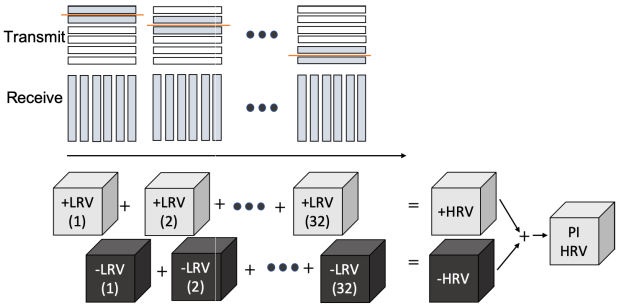

Fig. 1. Transmitting row elements and their translation across the aperture is shown in the top figure along with the receiving column elements. The time sequence of the positive and negative emissions and their combination is shown in the bottom figure.

Three sets of measurements were performed using a precision translation stage. The RC probe was mounted on a Newport PG Series floating optical table, Irvine, CA, USA, for stability with the microphantoms mounted on an 8MR190-2-28 rotation stage combined with an 8MTF-75LS05 xy translation stage (Standa, Vilnius, Lithuania). These were used to align both microphantoms with the imaging axis and to generate translation in the xy-plane used for the validation described in Section III-B.

B. Processing Pipeline

The processing pipeline consists of several stages. The first step is to beamform the stored RF data from the SARUS scanner using the beamforming strategy described by Rasmussen *et al.* [19] and Bouzari *et al.* [21] implemented in MATLAB and running on an Nvidia GeForce GTX 1050 Ti (Nvidia, Santa Clara, CA, USA) [23]. A volume with a size of $\pm 15\lambda$ in both the x- and y-directions is beamformed with a line density of $\lambda/2$ and covering the depth of the phantom. The sampling density in the z-direction is $\lambda/16$. A matched filter is applied on the received signals. It is designed using the measured impulse response of the probe to match the first-harmonic signal found in the linearly simulated data. The same filter is also used for the point spread function (PSF) phantom. The positive and negative emissions are then subtracted to increase the signal-to-noise ratio (SNR). For the flow microphantom, the second-harmonic signal is employed, the filter is matched to this, and the two emissions are added. The full LRV is beamformed for all emissions with an F-number of 1.5 in transmit and 1 in receive with a dynamic

Hanning apodization weighting the elements, and all emissions are added to generate the HRV. The mean value of the first 20 HRVs is averaged and subtracted from the processed HRVs to remove stationary objects in the processing. The envelope of the HRV is then found using a Hilbert transform and log compressed to a 40-dB dynamic range in relation to the data in the volume for finding locations.

The peak location can either be found from the calculation of the centroid of a global maximum, or the peak location can be interpolated to increase the location accuracy. Experimentation with the data has shown that the interpolation scheme is the most stable and accurate method, and this is the one used in this article.

The second stage finds bubble locations by interpolating the peak position by fitting a second-order polynomial to the data and then finding its interpolated maximum position x_i, as

$$x_i = i - \frac{0.5(d(i+1, j, k) - d(i-1, j, k))}{d(i+1, j, k) - 2d(i, j, k) + d(i-1, j, k)} \quad (1)$$

where i, j, and k are the indices of the maximum and d is the envelope data for the volume. This is conducted in all three coordinates x_i, y_j, and z_k with similar equations for an increased resolution in all three directions.

The third step used only on the point microphantom finds contiguous tracks of target locations. A target in a first HRV is used as a reference point, and the adjacent HRV is searched to find a detected target location lying within a radius of $r = v_s/f_r$ from the reference, where f_r is the volume rate and v_s is the maximum search velocity, where $v_s = 10$ mm/s was used. The track is terminated, if no target is found, and the whole track is discarded, if it does not contain more than 200 contiguous locations. No tracks were formed for the microflow phantom due to the high velocity employed, and all bubble locations in all images are shown in Section III-C.

C. Simulations and Measurement Phantoms

The method is evaluated using both simulations and measurements from two 3-D printed microphantoms that are all described in this section. The penetration depth is also determined from measurements on a tissue-mimicking phantom with a 0.5-dB/[MHz cm] attenuation.

1) Simulation of 3-D SRI System: The SA RC sequence has been simulated using Field IIpro [24]–[26] to generate reference data, where the positions of the scatterers are known in the volume. The phantom contains a number of point targets located at a depth of 5, 15, and 25 mm at the center axis of the probe. It is used for determining the PSF of the imaging method.

2) Fabrication of Microphantoms: Two microphantoms have been made and used for validating the approach. Both have been fabricated by 3-D printing of a PEGDA 700-g/mol hydrogel using stereolithography. The phantoms measure 21.1 × 8.16 × 11.9 mm^3, and the voxel size of the printer is $(\Delta x, \Delta y, \Delta z) = 10.8 \times 10.8 \times 20$ μm^3. More information about the fabrication process can be found in [27].

The first point phantom contains eight markers with a size of $10.8 \times 10.8 \times 20 = 233$ μm^3. The marker sizes are in all dimensions smaller than the imaging wavelength of 500 μm for the RC probe used, resulting in markers appearing as single targets in the B-mode volume. The markers are positioned with a minimum distance of 3 mm to ensure a clear separation of the reflected signals. The phantom is moved relative to the ultrasound probe using the xy translation stage in two experiments: one along x and one along y. An intervolume movement of 12.5 μm is used to emulate a constant velocity of 1.95 mm/s at 156 Hz. After each movement, the positions of the markers are determined and tracks for the targets are made.

The second flow microphantom contains a single cylindrical 100-μm radius channel placed 3 mm from the top surface of the phantom. After a 5.8-mm-long inlet, the channel bends 90° into a 7-mm-long central region before bending 90° again into the 5.8-mm outlet. The flow channel was infused at 1.61 μL/s with SonoVue (Bracco, Milan, Italy) in a 1:10 dilution, giving a peak velocity of 102.4 mm/s.

D. Statistical Evaluation

The bubble locations are randomly distributed in the flow microphantom tube due to noise in the localization estimation, and some of them will appear to be located outside the phantom wall. The distribution of positions found can then yield an estimate of the localization precision. An estimate of the yz- and xz-precision can be obtained from the two straight segments of the 200-μm channel phantom. In the straight segments, a line is fit to the data and considered as an estimate of the center of the channel, and the distance from each bubble to the center is calculated. Assuming that the measurement uncertainty in each dimension is normal distributed, the radial distribution of all bubbles in the segment will follow the distribution:

$$f(r) = 2\pi r \int_{|\vec{r}_t|<R} \frac{1}{\pi R^2} \frac{1}{2\pi\sigma^2} \exp\left(\frac{-|\vec{r} - \vec{r}_t|^2}{2\sigma^2}\right) d^2 r_t \quad (2)$$

where r is radial position, R is the radius of the tube, and σ is the standard deviation of the uncertainty. The integral is a convolution of a constant density $[1/(\pi R^2)]$ with a 2-D Gaussian. The nonanalytical integral (2) is estimated in a Monte Carlo calculation and is a Rayleigh distribution convolved with a uniform disk distribution of radius $R = 100$ μm. The factor $2\pi r$ is the Jacobian needed to convert from Cartesian to cylindrical coordinates. The fraction of bubbles estimated to fall outside the tube can then be translated into an estimate for the standard deviation σ (localization precision), as is performed in Section III-C1.

III. Result

A. Imaging Performance

The performance of the imaging scheme has been both simulated and measured. The responses from several point scatterers were simulated using Field II, and the FWHM was determined for the first-harmonic signal to be (FWHM$_x$, FWHM$_y$, FWHM$_z$, $= 0.58 \times 1.05 \times 0.31$ mm $= (1.17\lambda \times 2.12\lambda \times 0.63\lambda)$ at a depth of 15 mm. The receive F-number is 1, so the PSF is close to the theoretical limit of λ.

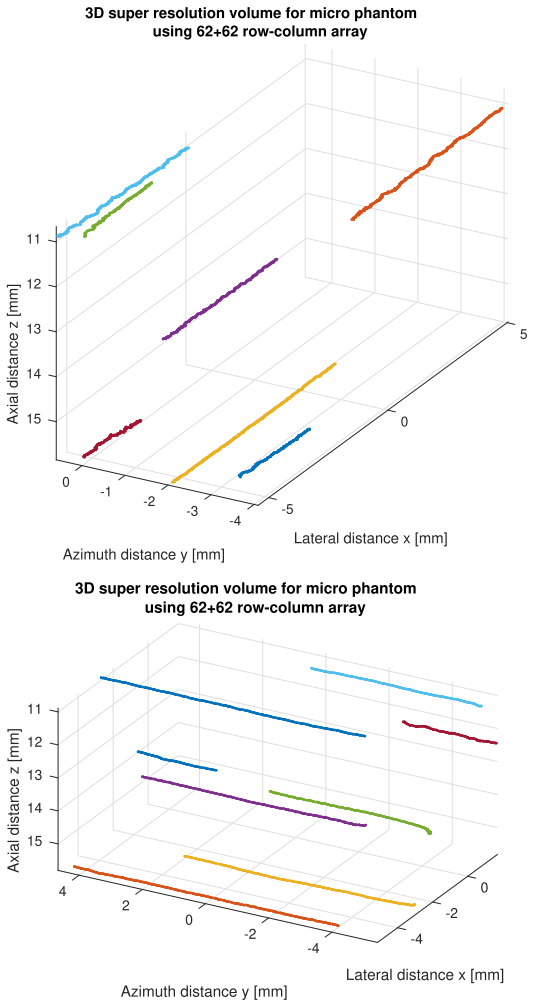

Fig. 2. Tracks estimated from mechanical translation of the PSF microphantom, where the colors indicate the detected positions. The top graph is for translation in the x-direction and bottom for translation in the y-direction.

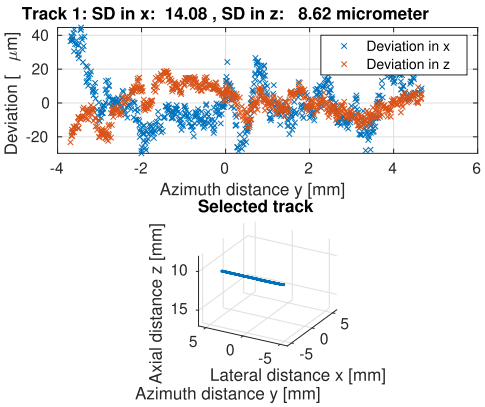

Fig. 3. Deviations calculated for one of the tracks when a line has been fit to the data. The bottom graph shows the estimated target locations, and the top graph shows the deviations in x and z when the line has been subtracted from the target position.

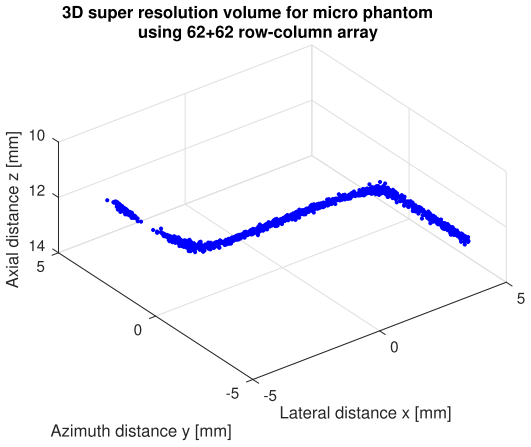

Fig. 4. View of the 200-μm channel phantom. Each blue dot represents a detected contrast agent bubble. See accompanying video for a 3-D view of the phantom.

The transmit F-number is 1.5 and, thus, gives a slightly wider PSF in the y-direction along emissions.

The penetration depth of the scheme was determined using a uniformly scattering phantom model 571 (Danish Phantom Service, Frederikssund, Denmark) with the speed of sound of 1540 m/s and a uniform attenuation of 0.5 dB/[MHz cm]. Determining the SNR from ten independent measurements gave a penetration depth of 14 cm (SNR $=$ 0 dB).

B. Validation in Point Microphantom

Fig. 2 shows the cumulative localized positions of 3-D printed markers within the microphantom acquired over 640 beamformed volumes at the emulated speed of 1.95 mm/s. The top figure shows movement in the x-direction and in the y-direction at the bottom. Seven markers have been detected and are shown as colored points. The eighth marker was too weak to be detected. Lines are fit to the positions using a least squares fit, as shown in Fig. 3 for one of the tracks. The deviations from the fit line are calculated, and the standard deviations are estimated to $(\sigma_x, \sigma_y, \sigma_z) = (20.7, 19.8, 9.1)$ μm when taking the average across all tracks.

C. 3-D SRI Imaging

The measured data from the flow microphantom acquired from 400 frames of the SA imaging sequence have been processed by the SR pipeline, including beamforming and detection of bubble locations, using the interpolation scheme in (1). A 3-D view of the detected bubbles is shown in Fig. 4, where each blue dot is a detected bubble. The geometry of the phantom can clearly be seen.

1) Precision of Bubble Locations: Bubbles in the central part of the phantom (-2 mm $< x <$ 2 mm) have been selected for estimating the localization precision in the yz-plane as shown Fig. 5 (top), where blue crosses indicate bubbles used for this estimation. Center lines for all selected bubbles are estimated with a least square fit, as shown in Fig. 6. The channel's center depth is at 12.0 mm from the probe, and the channel is slightly rotated in the xy-plane (57-μm tilt of the xy line in the top graph). These lines are used for calculating the radial positions

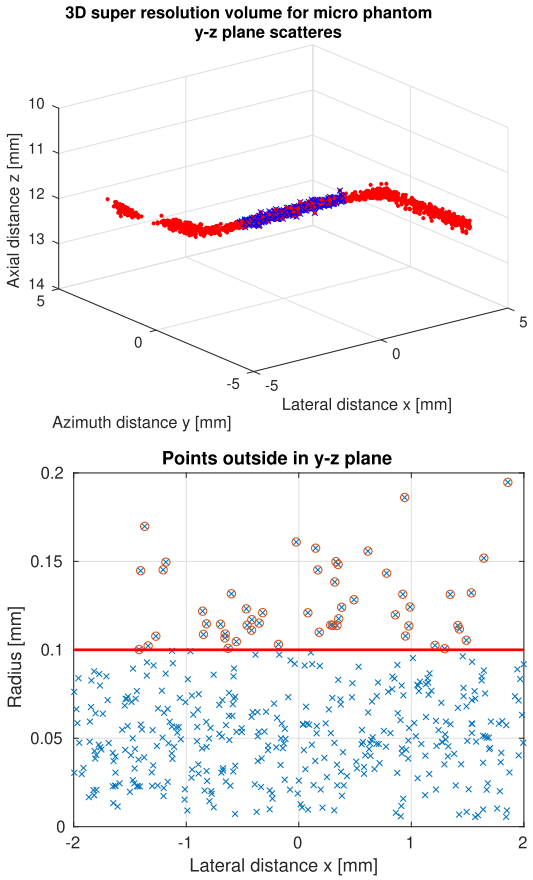

Fig. 5. Selected bubbles in the *yz*-plane (blue crosses) for estimating precision (top graph), and the calculated radial position of the bubbles in the vessel (bottom graph). Blue crosses indicate bubbles inside the vessel and red circles indicate outside.

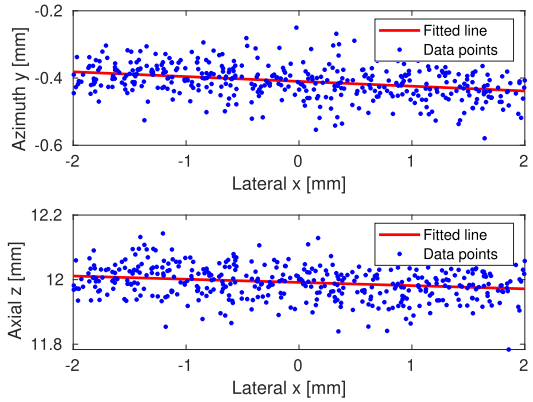

Fig. 6. Fit line for calculating the center position of the vessel in the phantom in the *yz*-plane.

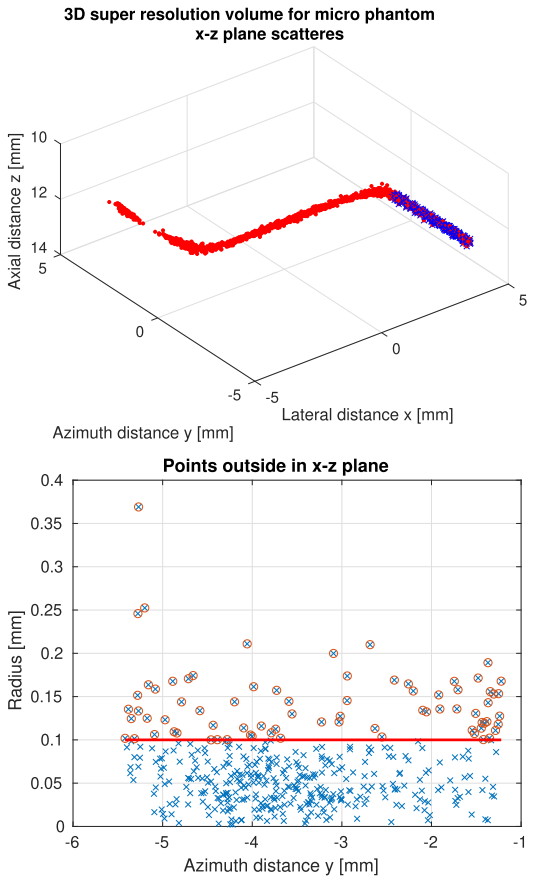

Fig. 7. Selected bubbles in the *xz*-plane (blue dots) for estimating precision.

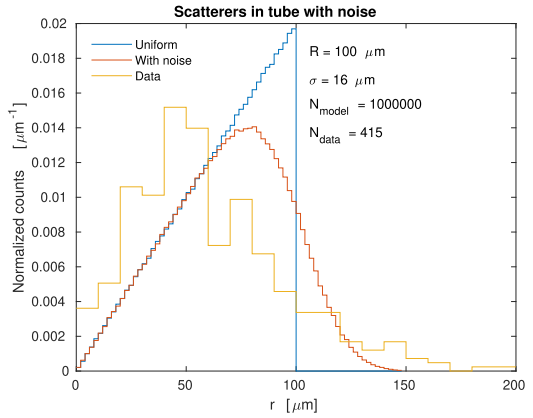

Fig. 8. Fit distribution for the bubble locations in the *yz*-plane.

of the bubbles in the vessel, as shown in Fig. 5 (bottom). Here, a blue cross indicates bubbles inside the vessel, and a red circle indicates bubbles outside of the vessel boundary, shown as the red solid line ($r = 100$ μm). The same graph for the xz-plane is shown in Fig. 7, where the outlet part of the vessel has been employed for finding the precision (-5.5 mm $< y <$ -1 mm).

The fraction of bubbles estimated to fall outside the tube can then be translated into an estimate for the standard deviation, as described in Section II-D. The fit distribution for the bubble locations in the yz-plane is shown in Fig. 8. For the yz-plane, 13% of the bubbles fall outside the tube, which leads to a position uncertainty of 16.5 μm. Similarly, for the xz-plane, 18% of the bubbles are estimated to fall outside the tube, which leads to a position uncertainty of 23 μm.

IV. Discussion

A method for 3-D super-resolution (SR) imaging has been developed based on an RC array and a pulse inversion SA imaging sequence using 32 positive and negative emissions.

A full volume is, thus, created in 64 emissions for a possible volume rate of 156 Hz at $f_{\text{prf}} = 10$ kHz, and the modest number of emissions makes it possible to have a 100-Hz volume rate down to a depth of 12 cm. The 3-MHz array's penetration depth is 14 cm due to its low frequency and fairly large size ($31\lambda \times 31\lambda$). Only 62 elements were employed during receive, making it possible to implement the approach on a standard ultrasound console with the advantage that a limited amount of data are generated. A $\lambda/8$ sampling density on the receiving elements can be employed and will continuously generate 2.9 GB/s, which is well within the reach of modern ultrasound research scanners [11], [14], [28]–[30]. This is significantly less for a fully populated array, where a 32×32 array yields 49 GB/s for an array with one-fourth the area of the RC probe used here.

The attained precision of the schemes was investigated using both a point microphantom and a flow microphantom with a 200-μm-diameter tube. The point phantom yielded a localization precision of (20.7, 19.8, 9.1) μm in the x, y, and z coordinates. The flow microphantom yielded an estimated radial precision of 16.5 μm in the yz-plane and 23 μm in the xz-plane. Assuming that the coordinate precisions are independent, the radial precision would be 15.4 μm in the yz-plane and 16.0 μm in the xz-plane when using the estimated precisions from the point phantoms. The $10.8 \times 10.8 \times 20$ μm^3 voxel size of the printer will give rise to tube-wall fluctuations, with an increase in precision, so the estimated precisions for the two phantoms are, therefore, similar.

The precision should be compared with the emitted wavelength of 500 μm, and improved localization of a factor of at least 20 times is attained in all three coordinates. The measured PSF has a size of $0.58 \times 1.05 \times 0.31$ mm^3, making it, in theory, possible to interrogate a volume 28 900 times smaller than a PSF limited system.

The main advantage of a 3-D system compared to the current 2-D systems is the increased resolution in the elevation plane. Current 2-D SR displays images averaged across the elevation plane thickness, which can often be 5λ–15λ away from the elevation focus. The resolution is, thus, improved by a factor of 100–300 times compared to a 1-D probe even though the number of elements is three times lower than a 192-element 1-D probe.

Several factors can be improved in the current setup and should be incorporated into a clinically useful 3-D SR imaging scheme. Currently, no motion correction is conducted, but the SA imaging scheme makes it possible to beamform a full volume at more than 100 Hz. This is sufficient to employ speckle tracking [31] in 3-D to yield and compensate for the motion, as described for SA flow imaging [32], [33]. Although many schemes use very high frame rates with 1000 images/s [6], [9], it has been shown that a conventional linear array scan with frame rates at 54 Hz can yield excellent SR images with both motion estimation [34] and quantification of flow [35]. The 154-Hz volume rate should, thus, be sufficient for *in vivo* imaging.

The fairly high velocity of 102.4 mm/s in the flow microphantom is used to prevent clogging of the phantom. This currently prevents the formation of tracks in the SR pipeline as is done for the PSF microphantom, but further experiments should be conducted to lower the velocity and maybe introduce a phantom with less sharp bends to prevent clogging. No efforts have been made to reduce false detections in the SR pipeline. Forming long tracks can significantly reduce the number of false detections, and this could potentially improve the precision of the location estimates.

The number of bubbles used here was sparse to make isolation easier. The acquisition length could be reduced if more number of detections could be made per second. Methods for increasing the number of bubble detections have been the topic of a number of articles [36]–[38]. Such approaches can also be employed here, as full RF data are acquired and can be processed using more advanced schemes.

The RC array can also be improved. The current array is a five-year-old prototype PZT array with only 62 elements. The array has eight nonfunctioning row elements and is slightly curved with a deviation around 0.1λ from a flat surface. This introduces phase errors and impedes image contrast. Other more advanced focusing schemes, such as matched filter focusing, could also be used for increasing contrast [21], [39]. It is also possible to optimize the emission sequence for contrast agent enhancement, where amplitude modulation potentially could be used [40]–[42], and it could also be possible to optimize the imaging sequence with fewer emissions for yielding less data and higher volume rates [43]. Adding more elements to the probe can also increase resolution and, thereby, reduce acquisition time, as more bubbles can be separated. Early investigations have been made for a $192 + 192$ RC array and showed an increased resolution proportional to the F-number and wavelength [44]. Such arrays can directly be used on modern ultrasound consoles with few modifications in the beamforming.

The approach can fairly easily be translated to clinical use by modifying our current 2-D SR pipeline to include searches and localizations in 3-D [34], [35]. The motion correction schemes developed for 2-D imaging and needed for *in vivo* imaging can then also be applied [34]. The main clinical applications could be superficial structures, where the F-number in beamforming can be kept low. The penetration depth is 14 cm for this array and imaging scheme, which is beneficial for larger organs, such as the liver. The bubble density would have to be reduced for reliable detection, and the imaging region will only be within the rectilinear area of the probe. This can potentially be alleviated by using a lens in front of the array [45].

A first *in vivo* target would be to scan a rat kidney, as performed in [34] and [35]. The acquisition time was between 1 and 10 min for a 2-D image, with 1 min giving an overall rough view of the vasculature and 10 min giving precise quantitative data for the blood flow. We predict that the same scan times can be kept with the method presented here for a full volume and maybe with a shorter time when employing more advanced SRI [36]–[38].

The high resolution will also give some future challenges. The RC array can image a volume of $31\lambda \times 31\lambda \times 280\lambda$, which, with a voxel size of $(10\ \mu\text{m})^3$, would yield 33 GVoxels. This might give some challenges in the display of such data.

V. Conclusion

A method for 3-D SRI has been investigated, where a $62 + 62$ RC array was employed. A detection precision better than 23 μm was attained in all three coordinates for both the SonoVue contrast agent flowing in a microphantom and the point microphantom. The precision was obtained using 1/8 of the elements employed in previous 3-D SRI, which reduces both the storage and processing demands by a factor of eight. The approach yielded an increase in volumetric resolution by a factor of more than 28 900 with a possible penetration depth down to 14 cm and the corresponding increase in the amount of volumetric data to 10–40 GVoxels. Potentially, a volume of $16 \times 16 \times 140$ mm^3 can be resolved with a voxel size of $(10\ \mu\text{m})^3$.

References

[1] O. Couture, B. Besson, G. Montaldo, M. Fink, and M. Tanter, "Microbubble ultrasound super-localization imaging (MUSLI)," in *Proc. IEEE Ultrason. Symp.*, Oct. 2011, pp. 1285–1287.

[2] O. M. Viessmann, R. J. Eckersley, K. Christensen-Jeffries, M. X. Tang, and C. Dunsby, "Acoustic super-resolution with ultrasound and microbubbles," *Phys. Med. Biol.*, vol. 58, no. 18, pp. 6447–6458, Sep. 2013.

[3] M. Siepmann, G. Schmitz, J. Bzyl, M. Palmowski, and F. Kiessling, "Imaging tumor vascularity by tracing single microbubbles," in *Proc. IEEE Ultrason. Symp.*, Oct. 2011, pp. 1906–1908.

[4] M. A. O'Reilly and K. Hynynen, "A super-resolution ultrasound method for brain vascular mapping," *Med. Phys.*, vol. 40, no. 11, 2013, Art. no. 110701.

[5] K. Christensen-Jeffries, R. J. Browning, M. X. Tang, C. Dunsby, and R. J. Eckersley, "*In vivo* acoustic super-resolution and super-resolved velocity mapping using microbubbles," *IEEE Trans. Med. Imag.*, vol. 34, no. 2, pp. 433–440, Feb. 2015.

[6] C. Errico *et al.*, "Ultrafast ultrasound localization microscopy for deep super-resolution vascular imaging," *Nature*, vol. 527, no. 7579, pp. 499–502, Nov. 2015.

[7] O. Couture, V. Hingot, B. Heiles, P. Muleki-Seya, and M. Tanter, "Ultrasound localization microscopy and super-resolution: A state of the art," *IEEE Trans. Ultrason., Ferroelectr., Freq. Control*, vol. 65, no. 8, pp. 1304–1320, Aug. 2018.

[8] J. Zhu *et al.*, "3D super-resolution US imaging of rabbit lymph node vasculature *in vivo* by using microbubbles," *Radiology*, vol. 291, no. 3, pp. 642–650, 2019.

[9] F. Lin, S. E. Shelton, D. Espíndola, J. D. Rojas, G. Pinton, and P. A. Dayton, "3-D ultrasound localization microscopy for identifying microvascular morphology features of tumor angiogenesis at a resolution beyond the diffraction limit of conventional ultrasound," *Theranostics*, vol. 7, no. 1, pp. 196–204, 2017.

[10] K. Christensen-Jeffries *et al.*, "Microbubble axial localization errors in ultrasound super-resolution imaging," *IEEE Trans. Ultrason., Ferroelectr., Freq. Control*, vol. 64, no. 11, pp. 1644–1654, Nov. 2017.

[11] J. A. Jensen *et al.*, "SARUS: A synthetic aperture real-time ultrasound system," *IEEE Trans. Ultrason., Ferroelectr., Freq. Control*, vol. 60, no. 9, pp. 1838–1852, Sep. 2013.

[12] L. Petrusca *et al.*, "Fast volumetric ultrasound B-mode and Doppler imaging with a new high-channels density platform for advanced 4D cardiac imaging/therapy," *Appl. Sci.*, vol. 8, no. 2, p. 200, 2018.

[13] S. Harput *et al.*, "3-D super-resolution ultrasound (SR-US) imaging with a 2-D sparse array," 2019, *arXiv:1902.01608*. [Online]. Available: https://arxiv.org/abs/1902.01608

[14] E. Boni *et al.*, "ULA-OP 256: A 256-channel open scanner for development and real-time implementation of new ultrasound methods," *IEEE Trans. Ultrason., Ferroelectr., Freq. Control*, vol. 63, no. 10, pp. 1488–1495, Oct. 2016.

[15] C. E. Morton and G. R. Lockwood, "Theoretical assessment of a crossed electrode 2-D array for 3-D imaging," in *Proc. IEEE Symp. Ultrason.*, Oct. 2003, pp. 968–971.

[16] C. E. M. Demore, A. W. Joyce, K. Wall, and G. R. Lockwood, "Real-time volume imaging using a crossed electrode array," *IEEE Trans. Ultrason., Ferroelectr., Freq. Control*, vol. 56, no. 6, pp. 1252–1261, Jun. 2009.

[17] J. T. Yen, C. H. Seo, S. I. Awad, and J. S. Jeong, "A dual-layer transducer array for 3-D rectilinear imaging," *IEEE Trans. Ultrason., Ferroelectr., Freq. Control*, vol. 56, no. 1, pp. 204–212, Jan. 2009.

[18] A. Sampaleanu, P. Zhang, A. Kshirsagar, W. Moussa, and R. J. Zemp, "Top-orthogonal-to-bottom-electrode (TOBE) CMUT arrays for 3-D ultrasound imaging," *IEEE Trans. Ultrason., Ferroelectr., Freq. Control*, vol. 61, no. 2, pp. 266–276, Feb. 2014.

[19] M. F. Rasmussen, T. L. Christiansen, E. V. Thomsen, and J. A. Jensen, "3-D imaging using row-column-addressed arrays with integrated apodization—Part I: Apodization design and line element beamforming," *IEEE Trans. Ultrason., Ferroelectr., Freq. Control*, vol. 62, no. 5, pp. 947–958, May 2015.

[20] T. L. Christiansen, M. F. Rasmussen, J. P. Bagge, L. N. Moesner, J. A. Jensen, and E. V. Thomsen, "3-D imaging using row–column-addressed arrays with integrated apodization—Part II: Transducer fabrication and experimental results," *IEEE Trans. Ultrason., Ferroelectr., Freq. Control*, vol. 62, no. 5, pp. 959–971, May 2015.

[21] H. Bouzari, M. Engholm, S. I. Nikolov, M. B. Stuart, E. V. Thomsen, and J. A. Jensen, "Imaging performance for two row–column arrays," *IEEE Trans. Ultrason., Ferroelectr., Freq. Control*, vol. 66, no. 7, pp. 1209–1221, Jul. 2019.

[22] M. Engholm *et al.*, "Probe development of CMUT and PZT row–column-addressed 2-D arrays," *Sens. Actuators A, Phys.*, vol. 273, pp. 121–133, Apr. 2018.

[23] M. B. Stuart, M. Schou, and J. A. Jensen, "Row-column beamforming with dynamic apodizations on a GPU," *Proc. SPIE*, vol. 10955, Mar. 2019, Art. no. 109550Q.

[24] J. A. Jensen and N. B. Svendsen, "Calculation of pressure fields from arbitrarily shaped, apodized, and excited ultrasound transducers," *IEEE Trans. Ultrason., Ferroelectr., Freq. Control*, vol. 39, no. 2, pp. 262–267, Mar. 1992.

[25] J. A. Jensen, "FIELD: A program for simulating ultrasound systems," *Med. Biol. Eng. Comp.*, vol. 4, no. 1, pp. 351–353, 1996.

[26] J. A. Jensen, "A multi-threaded version of field II," in *Proc. IEEE Ultrason. Symp.*, Sep. 2014, pp. 2229–2232.

[27] M. L. Ommen *et al.*, "3D printed flow phantoms with fiducial markers for super-resolution ultrasound imaging," in *Proc. IEEE Ultrason. Symp.*, Oct. 2018, pp. 1–4.

[28] J. A. Jensen *et al.*, "Ultrasound research scanner for real-time synthetic aperture data acquisition," *IEEE Trans. Ultrason., Ferroelectr., Freq. Control*, vol. 52, no. 5, pp. 881–891, May 2005.

[29] P. Tortoli and J. A. Jensen, "Introduction to the special issue on novel equipment for ultrasound research," *IEEE Trans. Ultrason., Ferroelectr., Freq. Control*, vol. 53, no. 10, pp. 1705–1706, Oct. 2006.

[30] E. Boni, A. C. H. Yu, S. Freear, J. A. Jensen, and P. Tortoli, "Ultrasound open platforms for next-generation imaging technique development," *IEEE Trans. Ultrason., Ferroelectr., Freq. Control*, vol. 65, no. 7, pp. 1078–1092, Jul. 2018.

[31] G. E. Trahey, J. W. Allison, and O. T. von Ramm, "Angle independent ultrasonic detection of blood flow," *IEEE Trans. Biomed. Eng.*, vol. BME-34, no. 12, pp. 965–967, Dec. 1987.

[32] S. I. Nikolov and J. A. Jensen, "*In-vivo* synthetic aperture flow imaging in medical ultrasound," *IEEE Trans. Ultrason., Ferroelectr., Freq. Control*, vol. 50, no. 7, pp. 848–856, Jul. 2003.

[33] K. L. Gammelmark and J. A. Jensen, "2-D tissue motion compensation of synthetic transmit aperture images," *IEEE Trans. Ultrason., Ferroelectr., Freq. Control*, vol. 61, no. 4, pp. 594–610, Apr. 2014.

[34] J. A. Jensen *et al.*, "History and latest advances in flow estimation technology: From 1-D in 2-D to 3-D in 4-D," in *Proc. IEEE Ultrason. Symp.*, Jun. 2019, pp. 1–4.

[35] S. B. Andersen *et al.*, "Super-resolution ultrasound imaging of rat kidneys before and after ischemia-reperfusion," in *Proc. IEEE Ultrason. Symp.*, Jun. 2019, pp. 1–4.

[36] E. Kanoulas *et al.*, "Super-resolution contrast-enhanced ultrasound methodology for the identification of *in vivo* vascular dynamics in 2D," *Investigative Radiol.*, vol. 54, no. 8, pp. 500–516, 2019.

[37] A. Bar-Zion, O. Solomon, C. Tremblay-Darveau, D. Adam, and Y. C. Eldar, "SUSHI: Sparsity-based ultrasound super-resolution hemodynamic imaging," *IEEE Trans. Ultrason., Ferroelectr., Freq. Control*, vol. 65, no. 12, pp. 2365–2380, Dec. 2018.

[38] O. Solomon, R. J. G. van Sloun, H. Wijkstra, M. Mischi, and Y. C. Eldar, "Exploiting flow dynamics for superresolution in contrast-enhanced ultrasound," *IEEE Trans. Ultrason., Ferroelectr., Freq. Control*, vol. 66, no. 10, pp. 1573–1586, Oct. 2019.

[39] J. T. Yen, "Beamforming of sound from two-dimensional arrays using spatial matched filters," *J. Acoust. Soc. Amer.*, vol. 134, no. 5, pp. 3697–3704, 2013.
[40] V. Mor-Avi, E. G. Caiani, K. A. Collins, C. E. Korcarz, J. E. Bednarz, and R. M. Lang, "Combined assessment of myocardial perfusion and regional left ventricular function by analysis of contrast-enhanced power modulation images," *Circulation*, vol. 104, no. 3, pp. 352–357, 2001.
[41] R. J. Eckersley, C. T. Chin, and P. N. Burns, "Optimising phase and amplitude modulation schemes for imaging microbubble contrast agents at low acoustic power," *Ultrasound Med. Biol.*, vol. 31, no. 2, pp. 213–219, Feb. 2005.
[42] C. Tremblay-Darveau, R. Williams, L. Milot, M. Bruce, and P. N. Burns, "Visualizing the tumor microvasculature with a nonlinear plane-wave Doppler imaging scheme based on amplitude modulation," *IEEE Trans. Med. Imag.*, vol. 35, no. 2, pp. 699–709, Feb. 2016.
[43] R. Moshavegh, J. Jensen, C. A. Villagomez-Hoyos, M. B. Stuart, M. C. Hemmsen, and J. A. Jensen, "Optimization of synthetic aperture image quality," *Proc. SPIE*, vol. 9790, Apr. 2016, Art. no. 97900Z.
[44] M. Schou, A. S. Havreland, M. Engholm, M. B. Stuart, E. V. Thomsen, and J. A. Jensen, "Design of a novel zig-zag 192+192 row column addressed array transducer: A simulation study," in *Proc. IEEE Ultrason. Symp.*, Oct. 2018, pp. 1–4.
[45] H. Bouzari *et al.*, "Curvilinear 3-D imaging using row–column-addressed 2-D arrays with a diverging lens: Phantom study," *IEEE Trans. Ultrason., Ferroelectr., Freq. Control*, vol. 65, no. 7, pp. 1182–1192, Jul. 2018.

Jørgen Arendt Jensen (M'93–SM'02–F'12) received the M.Sc., Ph.D., and the Dr.Techn. degrees from the Technical University of Denmark (DTU), Lyngby, Denmark, in 1985, 1989, and 1996, respectively.

Since 1993, he has been a Full Professor of biomedical signal processing with the Department of Health Technology, DTU. He has been the Founder and the Head of the Center for Fast Ultrasound Imaging, DTU, since its inauguration in 1998; this center has contributed with innovations in transverse oscillation vector flow imaging, synthetic aperture flow imaging in 2-D and 3-D, ultrasound simulation, research scanners, and row–column probes, and beamforming. He is also the developer and maintainer of the Field II Simulation Program. He has been a Visiting Scientist with Duke University, Durham, NC, USA, Stanford University, Stanford, CA, USA, and the University of Illinois at Urbana–Champaign, Champaign, IL, USA. He was the Founder and Head of the Biomedical Engineering Group, DTU, from 2007 to 2010. In 2003, he was one of the founders of the Biomedical Engineering Program in Medicine and Technology, which is a joint degree program between the DTU and the Faculty of Health and Medical Sciences, University of Copenhagen, Copenhagen, Denmark; the degree is one of the most sought-after engineering degrees in Denmark. He was Chairman of the Study Board from 2003 to 2010 and an Adjunct Professor with the University of Copenhagen from 2005 to 2010. He has published more than 500 journal and conference articles on signal processing and medical ultrasound and the book *Estimation of Blood Velocities Using Ultrasound* (Cambridge University Press, 1996). He has given a number of short courses on simulation, synthetic aperture imaging, and flow estimation at international scientific conferences and teaches biomedical signal processing and medical imaging at the DTU. He has educated 41 Ph.D. students and currently advises 17 Ph.D. students. He has given more than 60 invited talks at international meetings and received several awards for his research. His research is centered around the simulation of ultrasound imaging, synthetic aperture imaging, vector blood flow estimation, 3-D and super-resolution imaging, row–column probes, and construction of ultrasound research systems.

Dr. Jensen received the Grand Solutions Prize from the Danish Minister of Science, the Order of the Dannebrog by her Majesty the Queen of Denmark, and the Rayleigh Award from the UFFC Society in the field of Ultrasonics in 2019.

Martin Lind Ommen received the M.Sc. degree in physics and nanotechnology from the Technical University of Denmark, Lyngby, Denmark, in 2017, where he is currently pursuing the Ph.D. degree with the Biomedical Engineering Section, Department of Health Technology.

His current research interests include microfabrication and nanofabrication in general, in particular the fabrication of capacitive micromachined ultrasonic transducers (CMUTs), as well as phantom fabrication, with a current focus on stereolithographic fabrication of microflow and scatter phantoms.

Sigrid Husebø Øygard received the B.Eng. degree in acoustical engineering with a focus on bubble acoustics from the Institute of Sound and Vibration, University of Southampton, Southampton, U.K., in 2016, and the M.Sc. degree in physics with a focus on theoretical acoustics from the University of Bergen, Bergen, Norway, in 2018. She is currently pursuing the Ph.D. degree with the DTU Health Tech, Center for Fast Ultrasound Imaging, Technical University of Denmark.

Her research interests include 3-D ultrasound imaging, super-resolution imaging, and bubble acoustics.

Mikkel Schou was born in 1990. He received the M.Sc. degree in biomedical engineering from the Technical University of Denmark, Lyngby, Denmark, and the University of Copenhagen, Copenhagen, Denmark, in 2017. He is currently pursuing the Ph.D. degree in biomedical engineering with the Center for Fast Ultrasound Imaging, Technical University of Denmark. His Ph.D. research is on 3-D ultrasound perfusion and flow imaging using row–column arrays.

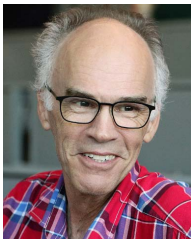

Thomas Sams received the M.Sc. degree in physics and the Ph.D. degree in collective vibrations in nuclei from the Niels Bohr Institute, University of Copenhagen, Copenhagen, Denmark, in 1986 and 1991, respectively.

He has worked for ten years on patterns in natural backgrounds at the Danish Defence Research Establishment. He was a Postdoctoral Researcher at Saclay, France, and the Niels Bohr Institute, Copenhagen, Denmark, and a Visiting Researcher at Los Alamos, NM, USA, and the University of Cambridge, Cambridge, U.K. Since 2005, he has been an Associate Professor of biomedical engineering with the Technical University of Denmark, Lyngby, Denmark, where he heads a research group in Cellular Signaling and Bioransport and the Biomedical Engineering Section. The common theme in his research is on the understanding of collective behavior in systems composed of smaller building blocks, including bacterial cell communities, patterns in yeast, patterns in sand ripples, and neural networks.

Matthias Bo Stuart received the M.Sc. and Ph.D. degrees in computer engineering from the Technical University of Denmark, Lyngby, Denmark, in 2006 and 2010, respectively.

He is currently an Associate Professor with the Biomedical Engineering Section, Department of Health Technology, Technical University of Denmark. His research interests include synthetic aperture methods for both anatomical and flow imaging in both 2-D and 3-D, ultrasound systems, and real-time implementations of ultrasound processing algorithms.

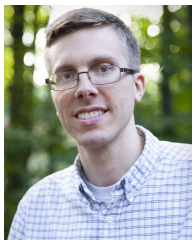

Christopher Beers received the M.S. degree in acoustics from Pennsylvania State University, State College, PA, USA, in 2007. His M.S. thesis research explored end-element anomalies in medical ultrasound transducer arrays.

He has been with BK Medical (formerly Sound Technology), State College, since 2007, where he has been developing transducer technology and designs commercial medical ultrasound probes.

Erik Vilain Thomsen was born in Aarhus, Denmark, in 1964. He received the M.Sc. degree in physics from the University of Southern Denmark, Odense, Denmark, in 1992, and the Ph.D. degree in electrical engineering from the Technical University of Denmark (DTU), Lyngby, Denmark, in 1998.

He is currently Professor with the Department of Health Technology, DTU, where he is also the Head of the MEMS Applied Sensors Group and Head of Division with responsibility for the educations in healthcare engineering. He teaches classes in solid-state electronics, microtechnology, and nanofabrication and microfabrication. His current research interests include all aspects of capacitive micromachined ultrasonic transducers (CMUTs), general MEMS technology, and piezoelectric MEMS.

Dr. Thomsen received the Danish National Advanced Technology Foundation's Grand Solution Prize in 2017, the AEG Electron Prize in 1995, and several teaching awards at DTU.

Niels Bent Larsen received the M.Sc. and Ph.D. degrees in chemistry from the University of Copenhagen, Copenhagen, Denmark, in 1993 and 1997, respectively.

He is currently a Professor and the Section Head of the Department of Health Technology, Technical University of Denmark, Lyngby, Denmark. His current research interests are in high-resolution 3-D printing of compliant hydrogel materials to recreate the vascular network of body organs to enable advanced *in vitro* organ models.

Borislav Gueorguiev Tomov received the M.Sc. degree in electronics engineering from the Technical University of Sofia, Sofia, Bulgaria, in 1996, and the Ph.D. degree in medical electronics from the Technical University of Denmark, Lyngby, Denmark, in 2003.

He is currently a Senior Researcher with the Center for Fast Ultrasound Imaging, Department of Health Technology, Technical University of Denmark. His research interests include medical ultrasound signal processing and ultrasound scanner architectures and implementations.

Paper 4

Investigating a CMUT's Ability to Achieve Non-linear Contrast Enhancement

Sigrid Husebø Øygard, Martin L. Ommen,Mathias Engholm, Mikkel Schou, Søren E. Diederichsen, Erik V. Thomsen, Matthias Bo Stuart, and Jørgen Arendt Jensen

Published in:
Proceedings of the IEEE International Ultrasonic Symposium

Document Version:
Published

DOI:
10.1109/IUS46767.2020.9251326

Investigating a CMUT's Ability to Achieve Non-linear Contrast Enhancement

Sigrid H. Øygard[1], Martin L. Ommen[2],Mathias Engholm[2], Mikkel Schou[1],
Søren E. Diederichsen[2], Erik V. Thomsen[2], Matthias Bo Stuart[1], and Jørgen Arendt Jensen[1]

[1] Center for Fast Ultrasound Imaging,
[2] MEMS Applied Sensors Group
Department of Health Technology, Technical University of Denmark, DK-2800 Lyngby, Denmark

***Abstract*—Capacitive micromachined ultrasonic transducers (CMUTs) are inherently non-linear and often believed to be unsuitable for non-linear contrast-enhanced ultrasound (CEUS) imaging. The ability of CMUTs to perform contrast-enhanced ultrasound imaging has been investigated by experimentally evaluating the contrast-to-noise ratio (CTR) and its variation with emitted pressure. This has been evaluated using amplitude modulation, pulse inversion and B-mode imaging sequences. The study shows that the CTR of the AM-mode was 7.5 dB higher than the B-mode on average, while the PI-mode is 5.9 dB lower than the B-mode. This indicates that contrast-enhancement can be achieved with a CMUT when a suitable image sequence is chosen.**

***Index Terms*—Contrast-enhanced ultrasound, CEUS, capacitive micromachined ultrasound transducers, pulse inversion, amplitude modulation**

I. Introduction

CAPACITIVE micromachined ultrasonic transducers (CMUTs) offer sensitivity features that are especially suitable for contrast-enhanced ultrasound imaging (CEUS) [1]. A high recieve sensitivity combined with a relatively low emitted pressure are suitable for generating and receiving the non-linear back-scattering from microbubble contrast agents. However, the excitation from CMUTs are inherently non-linear [2, 3] and this limits the potential contrast-to-noise ratio attainable when using a CMUT for CEUS imaging.

Contrast-enhanced ultrasound is a common imaging technique used clinically for dynamic visualization of vasculature [4], contrast enhancement of lesions [5], and most recently, super resolution imaging [6]. Contrast enhancement is achieved by utilizing the high echogenicity of microbubble contrast agents, which are injected into the blood-stream of the patient. The non-linear components of the signal scattered by the microbubbles are utilized to filter out the linear components of the signal reflected off of the surrounding tissue. This way, the vasculature of the patient can be visualized, often at high resolution [7]. The non-linear contrast enhancement is commonly achieved using sequence techniques with varying phase and amplitude, such as pulse inversion (PI) [8, 9, 10] and amplitude modulation (AM) [11, 12].

The contrast of the CEUS images will be high if the power of the signal scattered by the microbubbles is high compared with that scattered by the surrounding tissue. Several studies [13, 14, 15, 16] have found that increasing the emitted pressure amplitude, up to the limit where the microbubbles are destroyed, increases the power of the signal scattered by the microbubbles. Moreover, several studies [13, 14, 17] have suggested that the non-linear component of the back-scattered signal increases more rapidly than the fundamental. This implies that too low insonification pressure will hamper the tissue-removal when performing CEUS imaging.

On the other hand, using low voltages on a CMUT to produce low insonification pressure makes the CMUT more viable for CEUS imaging. CMUTs are inherently non-linear, as they emit harmonics of the fundamental frequency component of the desired emission [18]. The harmonic content of the emitted signal is dependent on both the amplitude and the sign of the applied voltage, which in turn determines the sign and amplitude of the emitted pressure. Thus, a low emission pressure will reduce the degrading effects of using a CMUT to perform CEUS. In this case, only the advantages of CMUTs remain; CMUTs may have a wide frequency response, fit to receive non-linear scattering by the microbubbles, a low transmission sensitivity, and a high receive sensitivity [19]. There therefore exist a trade-off between detrimental non-linear behaviour of the CMUT and the power of the back-scattering from the microbubbles, which are both dependent on the emitted pressure of the probe. Combined, these effects dictate the contrast-to-noise ratio of the resulting images and thus the viability of using a CMUT for CEUS imaging.

To investigate the impact of CMUT non-linearity on CEUS imaging, this study will therefore compare the contrast-to-noise ratio achieved by PI, AM, and B-mode imaging on using 4.8 MHz linear CMUT. Moreover, to study the trade-off between non-linearity in the back-scattering of the microbubbles and the destructive harmonic content of the CMUT emission the CTR was quantified at 30% - 100% of the maximal safe operational voltage of the transducer.

II. Method

The attainable contrast-to-noise ratio was assessed for a linear CMUT array with a center frequency of 4.8 MHz [20]. The specifications of the probe are given in Table I. All frame types were recorded using a synthetic aperture sequence [21] with 10 virtual sources (VS) placed behind the transducer

978-1-7281-5448-0/20/$31.00 ©2020 IEEE

surface with an F# of -1 to produce a diverging wave with a low pressure amplitude. Each virtual source emitted a minor sequence with 3 emissions, which accommodates a combination of amplitude modulation and pulse inversion. The minor sequence consisted of a *positive*, a *half*, and a *negative* amplitude emission. These emissions were combined to form 3 image modes, as

$$\text{B-mode} = \text{Positive} \tag{1}$$

$$\text{Amplitude modulation} = \text{Positive} - 2 \cdot \text{Half} \tag{2}$$

$$\text{Pulse inversion} = \text{Positive} + \text{Negative} \tag{3}$$

The polarity of the *positive* and *negative* emissions were set using the AC voltage supply to the probe. Since the harmonic content of the emitted signal depends on the applied voltage, scaling the amplitude for the *half* emission with the voltage supply would make the harmonic content of the *positive* emission different from that of the *half* emission, thus degrading the contrast enhancement of the AM-mode. Therefore, the halving of the amplitude was achieved by emitting with only every second element in each active aperture, as suggested by [2].

TABLE I
SPECIFICATIONS OF THE CMUT PROBE AND THE IMAGING SEQUENCE

Total number of elements	192
Center frequency	4.8 MHz
Pitch (p)	0.2 mm
Kerf	0.025 mm
Pulse repetition frequency	3000 Hz
Number of elements in sub-aperture	63
Emission frequency	3.2 MHz
Transmit F-number	-1
Receive F-number	1
Number of virtual sources (N)	10
Number of cycles in emission	2
Virtual source pitch (s)	14
Apodization	von Hann

An experimental set-up was designed, which enabled comparison of the power scattered by a small volume of microbubbles with the power scattered by a tissue-mimicking material. An illustration of the set-up is seen in Fig. 1. The microbubbles were allowed to flow through a 200 µm diameter tube in a 3D printed hydrogel phantom, which was fixated on top of a tissue-mimicking material. The fabrication process and material properties of the phantom have been described in [22]. The phantom was held on top of a block of polyvinyl alcohol (PVA) cryogel [23] by a brace. The scattering properties of the cryogel are similar to that of human tissue. A low pressure flow pump (neMESYS 290N, Cetoni) fitted with a syringe of SonoVue (diluted 1:10) was connected to the phantom and used to pump microbubbles into the phantom at $1\,\mu\text{L}\,\text{s}^{-1}$.

To investigate how the pressure amplitude affects the CTR the periodic voltage supply to the transducer was varied from 100% to 30% of its maximal safe operational voltage, in steps of 10%. The maximal applied voltage for the probe

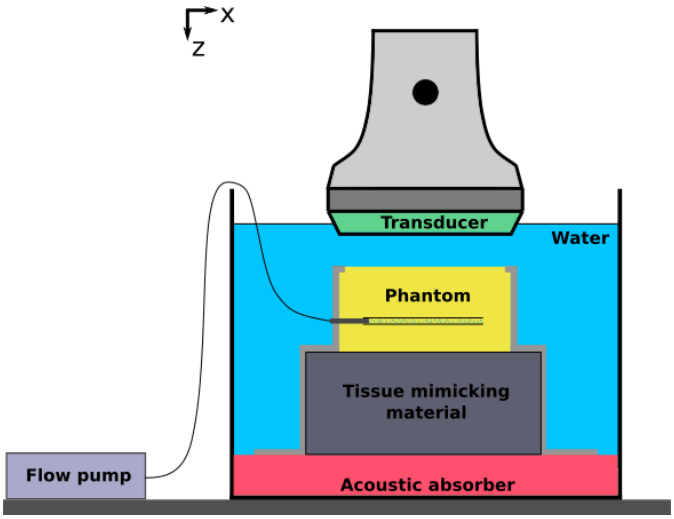

Fig. 1. An illustration of the experimental set-up showing the phantom, tissue-mimicking material and acoustic absorber stacked on top of each other in a water bath and held in place by a brace. The transducer sits directly above the phantom, in contact with the water.

was 190 V DC and 60 V AC. For each pressure amplitude value, 10 consecutive frames were collected, while the flow of microbubbles was running through the phantom. To avoid capturing effects of microbubble degradation due to repeated ultrasound exposure, a 15 second pause was added between each frame, enough to allow a fresh volume of microbubbles into the phantom. In addition, the transducer was placed in an empty water bath and a hydrophone was used to measure the emitted peak negative for each voltage level. The hydrophone was placed directly beneath the transducer, at 12 mm from the transducer surface. The attenuation in the phantom, the water, and the tissue-mimicking material has not been accounted for.

After capturing 10 frames at each of the pressure amplitude levels, all the frames were beamformed using a delay-and-sum beamformer and the different image modes were composed according to (1) - (3). For each composed image, the CTR was calculated as

$$CTR = \frac{P_B}{P_{TMM}}, \tag{4}$$

where P_B is the average power of the signal scattered by the microbubbles and P_{TMM} is the average power scattered by the tissue-mimicking material. The average power was calculated as

$$P = \frac{1}{L_2 - L_1 + 1} \frac{1}{n_2 - n_1 + 1} \sum_{l=L_1}^{L_2} \sum_{m=n_1}^{n_2} \sqrt{y_{l,m}^2}, \tag{5}$$

where y is the signal in a single beamformed line of data, m is the sample number, n_1 and n_2 are sample numbers determining the axial position for the signal, and L_1 and L_2 are line numbers. The sample numbers and line numbers were chosen so that they formed a small rectangle around the tube in the phantom when calculating P_B, and so that they formed

a rectangle of equal size inside the tissue-mimicking material when calculating P_{TMM}.

III. Results

The CTR calculated for each emitted pressure level and averaged over the repeated frames is shown in Fig. 2. It is apparent that the AM-mode provides greater contrast enhancement than conventional B-mode. On average, the AM CTR is 7.5 dB higher than B-mode. On the other hand, the CTR of the PI-mode is on average 5.9 dB lower than the B-mode CTR. Moreover, the CTR of the PI-mode is negative for all the emitted pressure levels. This indicates that even though PI has been used to try to remove the signal from the tissue-mimicking material, the power in this region is still higher than the non-linear scattering of the microbubbles. This is a clear indication that the PI sequence has failed to enhance the contrast. This failure is expected, since the PI sequence contains emissions of opposing polarity which will induce different harmonic content in the received signal. Thus, the measured CTR indicates that CEUS imaging can be achieved with a CMUT, if the appropriate contrast enhancing sequence is chosen.

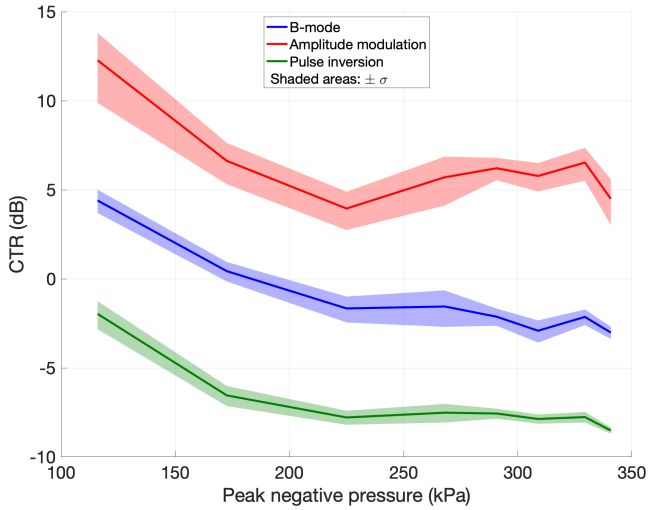

Fig. 2. The calculated CTR with varied emitted pressure for 3 different image modes. The shaded areas indicate the standard deviation of the 10 repetitions.

Varying the emitted pressure shows that the CTR is highest at low peak negative pressures. Examination of the individual image frames revealed that this effect is likely caused by reverberation in the water bath, and does not necessarily reflect the true relationship between pressure and CTR. Further studies should refine the experimental set-up or data processing to resolve this issue in order to further study how the trade-off between bubble non-linearity and CMUT harmonics depend on pressure.

IV. Conclusion

The ability of a CMUT to perform contrast-enhanced ultrasound was studied by comparing the contrast enhancement of 2 CEUS modes with conventional B-mode. An experimental set-up designed for comparing the power scattered by a small volume of SonoVue and the power scattered by a tissue-mimicking material was used to quantify contrast-to-noise ratio. Due to the relationship between emitted pressure and the detrimental non-linear content of CMUT emissions, the effect of varying the emitted pressure on CTR was also studied. This preliminary study found that the CTR was highest for the AM-mode, yet lowest for the PI-mode. The contrast enhancement achieved with the AM-mode, as compared with B-mode, indicates that CMUTs can be used for CEUS imaging.

References

[1] Ö. Oralkan, A. S. Ergun, J. A. Johnson, M. Karaman, U. Demirci, K. Kaviani, T. H. Lee, and B. T. Kuri-Yakub, "Capacitive micromachined ultrasonic transducers: Next-generation arrays for acoustic imaging?" *IEEE Trans. Ultrason., Ferroelec., Freq. Contr.*, vol. 49, pp. 1596–1610, 2002.

[2] D. Fouan and A. Bouakaz, "Investigation of classical pulse sequences for contrast-enhanced ultrasound imaging with a CMUT probe," *IEEE Trans. Ultrason., Ferroelec., Freq. Contr.*, vol. 63, no. 10, pp. 1496–1503, 2016.

[3] A. Novell, A. Bouakaz, M. Legros, and N. Felix, "Non-linear contrast imaging with capacitive micromachined transducers," *Proc. IEEE Ultrason. Symp.*, 2008.

[4] N. Lassau, L. Chami, B. Benatsou, P. Peronneau, and A. Roche, "Dynamic contrast-enhanced ultrasonography (dce-us) with quantification of tumor perfusion: a new diagnostic tool to evaluate the early effects of antiangiogenic treatment," *European Radiology Supplements*, vol. 17, no. 6, pp. 89–98, 2007.

[5] C. F. Dietrich, M. Averkiou, M. B. Nielsen, R. G. Barr, P. N. Burns, F. Calliada, V. Cantisani, B. Choi, M. C. Chammas, D. Clevert *et al.*, "How to perform contrast-enhanced ultrasound (ceus)," *Ultrasound international open*, vol. 4, no. 1, p. E2, 2018.

[6] C. Errico, J. Pierre, S. Pezet, Y. Desailly, Z. Lenkei, O. Couture, and M. Tanter, "Ultrafast ultrasound localization microscopy for deep super-resolution vascular imaging," *Nature*, vol. 527, pp. 499–502, November 2015.

[7] J. Brown, K. Christensen-Jeffries, S. Harput, G. Zhang, J. Zhu, C. Dunsby, M.-X. Tang, and R. J. Eckersley, "Investigation of microbubbles detection methods for super-resolution imaging of microvasculature," *IEEE Trans. Ultrason., Ferroelec., Freq. Contr.*, vol. 66, no. 4, pp. 676–691, 2019.

[8] D. H. Simpson, C. T. Chin, and P. N. Burns, "Pulse inversion Doppler: a new method for detecting nonlinear echoes from microbubble contrast agents," *IEEE Trans. Ultrason., Ferroelec., Freq. Contr.*, vol. 46, no. 2, pp. 372–382, 1999.

[9] R. J. Eckersley, C. T. Chin, and P. N. Burns, "Optimising phase and amplitude modulation schemes for imaging

microbubble contrast agents at low acoustic power," *Ultrasound Med. Biol.*, vol. 31, no. 2, pp. 213–219, 2005.
[10] J. A. Jensen, M. L. Ommen, S. H. Øygard, M. Schou, T. Sams, M. B. Stuart, C. Beers, E. V. Thomsen, N. B. Larsen, and B. G. Tomov, "Three-dimensional super resolution imaging using a row-column array," *IEEE Trans. Ultrason., Ferroelec., Freq. Contr.*, vol. 67, no. 3, pp. 538–546, 2020.
[11] G. A. Brock-Fischer, M. D. Poland, and P. G. Rafter, "Means for increasing sensitivity in non linear ultrasound systems us patent(5577505)," US Patent, 1996.
[12] K. Christensen-Jeffries, S. Harput, J. Brown, P. N. T. Wells, P. Aljabar, C. Dunsby, M. Tang, and R. J. Eckersley, "Microbubble axial localization errors in ultrasound super-resolution imaging," *IEEE Trans. Ultrason., Ferroelec., Freq. Contr.*, vol. 64, no. 11, pp. 1644–1654, 2017.
[13] M. X. Tang, H. Mulvana, T. Gauthier, A. K. P. Lim, D. O. Cosgrove, R. J. Eckersley, and E. Stride, "Quantitative contrast-enhanced ultrasound imaging: a review of sources of variability," *Interface Focus*, vol. 1, no. 4, pp. 520–539, 2011.
[14] W. T. Shi, F. Forsberg, J. S. Raichlen, and L. Needleman, "Pressure dependence of subharmonic signals from contrast microbubbles," *Ultrasound Med. Biol.*, vol. 25, pp. 275–283, 1999.
[15] V. Sboros, "The dependence of ultrasound contrast agents backscatter on acoustic pressure: theory versus experiment," *Ultrasonics*, vol. 40, no. 11, pp. 579–583, 2002.
[16] K. E. Morgan, P. A. Dayton, D. Kruse, A. L. Kilbanov, G. H. Branden, and K. W. Ferrara, "Changes in the echoes from ultrasonic contrast agents with imaging parameters," *IEEE Trans. Ultrason., Ferroelec., Freq. Contr.*, vol. 45, no. 6, pp. 1537–1548, 1998.
[17] M. Emmer, A. van Wamel, D. E. Goertz, and N. de Jong, "The onset of microbubble vibration," *Ultrasound Med. Biol.*, vol. 33, pp. 941–949, 2007.
[18] A. Lohfink and P. C. Eccardt, "Investigation of nonlinear CMUT behavior," in *Proc. IEEE Ultrason. Symp.*, 2005, pp. 585–588.
[19] A. S. Savoia, G. Caliano, and M. Pappalardo, "A CMUT probe for medical ultrasonography: From microfabrication to system integration," *IEEE Trans. Ultrason., Ferroelec., Freq. Contr.*, vol. 59, no. 6, pp. 1127–1138, 2012.
[20] S. E. Diederichsen, "Micromachined integrated transducers for ultrasound imaging," Ph.D. dissertation, Denmark Technical University, 2020.
[21] J. A. Jensen, S. Nikolov, K. L. Gammelmark, and M. H. Pedersen, "Synthetic aperture ultrasound imaging," *Ultrasonics*, vol. 44, pp. e5–e15, 2006.
[22] M. L. Ommen, M. Schou, R. Zhang, C. A. V. Hoyos, J. A. Jensen, N. B. Larsen, and E. V. Thomsen, "3D printed flow phantoms with fiducial markers for super-resolution ultrasound imaging," in *Proc. IEEE Ultrason. Symp.*, 2018, pp. 1–4.
[23] J. B. Olesen, C. A. Villagómez Hoyos, N. D. Møller, C. Ewertsen, K. L. Hansen, M. B. Nielsen, B. Bech, L. Lönn, M. S. Traberg, and J. A. Jensen, "Non-invasive estimation of pressure changes using 2-D vector velocity ultrasound: An experimental study with in-vivo examples," *IEEE Trans. Ultrason., Ferroelec., Freq. Contr.*, vol. 65, no. 5, pp. 709–719, 2018.

Paper 5

Contrast-enhanced ultrasound imaging using capacitive micromachined ultrasonic transducers

Sigrid H. Øygard, Martin L. Ommen, Borislav G. Tomov, Søren E. Diederichsen, Erik V. Thomsen, Niels B. Larsen, Matthias B. Stuart and Jørgen A. Jensen

Name of journal:
BMC Medical Imaging

Document Version:
In review

RESEARCH

Contrast-enhanced ultrasound imaging using capacitive micromachined ultrasonic transducers

Sigrid H. Øygard[1*], Martin L. Ommen[3], Borislav G. Tomov[1], Søren E. Diederichsen[3], Erik V. Thomsen[3], Niels B. Larsen[2], Matthias B. Stuart[1] and Jørgen A. Jensen[1]

Abstract

Capacitive micromachined ultrasonic transducers (CMUTs) have a nonlinear relationship between the applied voltage and the emitted signal, which is detrimental to conventional contrast enhanced ultrasound (CEUS) techniques. Instead, a three-pulse amplitude modulation (AM) sequence has been proposed, which is not adversely affected by the emitted harmonics. In this paper, this is shown theoretically, and the performance of the sequence is verified using a 4.8 MHz linear CMUT array, and a comparable lead zirconate titanate (PZT) array, across 6 V to 60 V applied AC voltage. CEUS images of the contrast agent SonoVue flowing through a 3D printed hydrogel phantom showed an average enhancement in contrast-to-tissue ratio (CTR) between B-mode and CEUS images of 49.9 dB and 37.4 dB for the PZT array and CMUT, respectively. Furthermore, hydrophone recordings of the emitted signals showed that the nonlinear emissions from the CMUT did not significantly degrade the cancellation in the compounded AM signal, leaving an average of 2 % of the emitted power between 26 V and 60 V AC. Thus, it is demonstrated that CMUTs are capable of CEUS imaging independent of the applied excitation voltage when using a three-pulse AM sequence.

Keywords: Contrast-enhanced ultrasound imaging, capacitive micromachined ultrasonic transducers, amplitude modulation

*Correspondence: shoy@dtu.dk

[1] Center for Fast Ultrasound Imaging, Department of Health Technology, Technical University of Denmark, Kgs. Lyngby, Denmark

Full list of author information is available at the end of the article

1 Introduction

Recently, capacitive micromachined ultrasonic transducers (CMUTs) have become available as an alternative to the more conventional piezoelectric transducers [1, 2]. CMUTs offer sensitivity features that are particularly suitable for microbubble contrast-enhancement imaging, with low transmit pressure, yet high receive sensitivity [1]. Contrast enhanced ultrasound (CEUS) imaging with microbubble contrast agents is used clinically to study the blood's wash-in and wash-out time in organs [3], to quantify the blood-flow velocity using time-intensity curves [4], and, most recently, to image blood-flow through capillaries beyond the diffraction limit, through super-resolution ultrasound imaging (SRI) [5, 6]. CEUS imaging with a CMUT is a combination of two nonlinear processes; the spectral content of the emission from a CMUT is nonlinearly related to its excitation voltage [7], and the spectral content of the scattering of the excitation by the microbubble contrast agents is nonlinearly related to the acoustic pressure [8]. This combination poses some challenges to the conventional CEUS techniques, and the viability of CEUS imaging using CMUTs has been questioned [9].

CMUTs emit ultrasound by applying an AC voltage potential across thin plates suspended on top of nanometer to micrometer sized cavities. The technology offers great design flexibility [10], making it possible to produce transducers with several advantageous features for CEUS imaging. Firstly, the transducer can achieve wide bandwidth, resulting in high axial resolution [10]. For SRI, where separation of the microbubbles within each image frame is essential, this could enable SRI with a higher number of resolved microbubbles within each frame, and thus a lower acquisition time. The wide bandwidth would also facilitate detection of higher harmonics scattered by the microbubbles, often utilized in the pulse inversion (PI) technique. Secondly, CMUTs can produce a low emitted pressure, suitable for exciting microbubbles without destroying them [11], whilst maintaining a high receive sensitivity [12]. However, the drawback of CMUT technology is that the electrostatic force driving the

excitation causes the emitted signal to contain considerable harmonic components [13]. The amount of harmonic content produced by the transducer is dependent on the ratio of the applied AC voltage to the applied DC voltage [7], which renders the transducer incapable of removing of tissue-generated signals using conventional CEUS techniques.

CEUS imaging achieves high contrast by removing the signal scattered by the tissue from that scattered by the microbubbles. The most common techniques used to remove the tissue signal are PI, amplitude modulation (AM), and singular value decomposition (SVD). The first two utilize the fact that when a bubble is insonified, it will scatter the sound nonlinearly [14]. SVD is a spatiotemporal filtering technique, which utilizes the bubble's high scattered intensity and temporally transient behavior to separate the bubbles from the tissue [5]. These techniques are thus capable of removing the linearly scattered signals caused by the tissue surrounding the contrast agents. PI combines the responses from two excitations with opposite signs [15]. Conventionally, AM is achieved by combining the response from two excitations, one with half the amplitude of the next [16]. Both the difference in amplitude and difference in polarity will cause the CMUT to emit harmonics that differ between the emissions, which conventional AM and PI will not be able to remove. Using such sequences with CMUTs will therefore result in poor contrast in the CEUS images [17, 18]. Several attempts have been made to overcome this issue by altering the frequency content of the emitted pulse [19, 20], but such approaches are not necessarily compatible with the bipolar pulsers often found in commercial scanners. Moreover, these methods rely on all elements in the probe behaving identically, which is often not the case. However, Fouan and Bouakaz [18] have proposed that CEUS imaging can be obtained using simple sinusoidal excitations by implementing a three-pulse AM sequence. In this sequence, the difference in amplitude between emissions, which is needed to preserve the nonlinear back-scattering from the microbubbles, is achieved by emitting once with the full active aperture, once with the odd-numbered elements, and once with the even-numbered elements. Fouan and Bouakaz [18] shows that for a single transmit voltage of 20 V applied to a CMUT, a 15 dB improvement in contrast-to-tissue ratio (CTR) was achieved, compared with an AM sequence with scaled voltage. A similar approach has been studied in [17], where it was shown that a two-pulse AM sequence with halving of the active elements resulted in better contrast than conventional PI imaging. The contrast of CEUS images is influenced by the power of the AM signal compared with the power of any remaining signal scattered by tissue, often quantified by CTR [21]. Since the applied voltage and polarity to each emitting element is constant for all emissions in these modified AM sequences, the theory predicts that the emitted signals therefore contain the same harmonics. This indicates that the increasing harmonic content resulting from increased applied AC voltage does not affect the performance of the imaging technique.

This paper investigates the two-pulse and three-pulse AM sequence at a wide range of transmit voltages, corresponding to varying nonlinear components in the emissions. It is hypothesized that the amount of nonlinear harmonics in the emitted signal does not affect the efficiency of these modified AM techniques. This is demonstrated theoretically, and verified with measurements. The method's ability to cancel linear components is measured using hydrophone recordings, and its contrast enhancement is assessed using CEUS imaging of a microflow phantom with SonoVue contrast agents. The measurements are made using a linear CMUT array produced in house, and, for reference, using a corresponding commercial lead zirconate titanate (PZT) array.

2 Theory

2.1 Emission from a CMUT

The propagation of sound waves from a CMUT array is induced by applying an AC voltage, V_{AC}, across the CMUT cells. This causes a time-varying deflection, driven by electrostatic force on the cell plates. [22]. The acoustic pressure radiated from a circular cell plate is proportional to the resulting displacement of the plate [23], and the relationship between the applied voltage and the displacement is governed by a nonlinear differential equation [24]. Analytic evaluation of this equation is not straight forward, but several authors have studied the relationship numerically [22, 24, 25]. It has been shown that the emitted sound pressure from CMUTs contain harmonics to the applied excitation frequency [24, 26]. Thus, when the applied V_{AC} is a simple sinusoid at some excitation frequency, ω_0, the resulting emitted pressure, $p(t)$, can be expressed as

$$p(t) = \alpha_0 \sin(\omega_0 t) + \sum_{h=2}^{\infty} \alpha_h \sin(h\omega_0 t + \phi_h), \quad \begin{cases} h \in \mathbb{Z}, \\ \alpha_h \in \mathbb{R}, \end{cases} \tag{1}$$

$$= p_L(t) + \sum_{h=2}^{\infty} p_H(t) \tag{2}$$

Here, t is time, α is some amplitude, h is a harmonic index, ϕ is a phase difference. Since α_h can be any real number, including zero, this notation is applicable

even when only certain harmonics are present in the emitted signal. A compact form of (1) is given in (2), where $p_L(t)$ is the linear part, i.e. the component of the signal which has the same frequency content as the applied ω_0, and $\sum p_H(t)$ is the harmonics. The amplitude and phase of the harmonics are determined by the complex dynamics of the CMUT array, and are not further described here. Notably, it has been shown that the amount of harmonic content in the emitted pressure wave depends on the ratio of the amplitude of the applied V_{AC} to the applied DC voltage [26], and CMUTs are therefore said to be inherently nonlinear. However, it will here be shown that the nature of the harmonics does not affect the effectiveness of the three-pulse AM sequence.

In the three-pulse AM sequence proposed by Fouan and Bouakaz [18], a pulse of full amplitude, p_A, is emitted, followed by two pulses of halved amplitude, p_B and p_C. The applied voltage is constant across all three emissions, and the two half amplitudes are made by halving the number of active elements compared with the full emission, spread across the same active aperture width. Thus, the three emitted pulses are

$$p_A(t) = \alpha_0 \sin(\omega_0 t) + \sum_{h=2}^{\infty} \alpha_h \sin(h\omega_0 t + \phi_h), \quad (3)$$

$$p_B(t) = 0.5\Big[\alpha_0 \sin(\omega_0 t) + \sum_{h=2}^{\infty} \alpha_h \sin(h\omega_0 t + \phi_h)\Big], \quad (4)$$

$$p_C(t) = 0.5\Big[\alpha_0 \sin(\omega_0 t) + \sum_{h=2}^{\infty} \alpha_h \sin(h\omega_0 t + \phi_h)\Big]. \quad (5)$$

2.2 The amplitude modulation technique

When the microbubbles are insonified with an ultrasound pulse, the reflections contain harmonics of the incident frequency. Eckersley et al. [11] show that the nonlinear reflections can be modeled as a polynomial expansion of the incident wave, as

$$y(t) = a_1 p_i(t) + a_2 {p_i}^2(t) + a_3 {p_i}^3(t) + ... + a_\infty {p_i}^\infty(t). \quad (6)$$

Here, $y(t)$ is the reflected signal, $p_i(t)$ is the incident pressure wave on the bubble, and a_i are reflection coefficients determining the different nonlinear contributions, where a_1 represents the linear reflection and $a_{i>1}$ represents the nonlinear reflections. To suppress the linear component of the emitted signal, while preserving the nonlinear components at the fundamental, the reflected signals are combined as

$$y_{AM}(t) = y_A(t) - y_B(t) - y_C(t), \quad (7)$$

where y_{AM} is the remaining three-pulse amplitude modulation signal, and y_A, y_B, y_C are the scattered signals caused by the three emissions. If instead, only 2 emissions are used the combination is made as

$$y_{AM}(t) = y_A(t) - 2 \cdot y_B(t). \quad (8)$$

2.3 Amplitude modulation with a CMUT

By assuming that no distortion of the signal occurs between the emission and the bubble position, we can apply (6) to the tree emissions given in (3) - (5) before applying (7). By expressing the pressure waves in their compact form and limiting the polynomial expansion to third order for simplicity, this gives

$$\begin{aligned} y_{AM}(t) =& a_1 p_A + a_2 {p_A}^2 + a_3 {p_A}^3 - a_1 p_B - a_2 {p_B}^2 \\ & - a_3 {p_B}^3 - a_1 p_C - a_2 {p_C}^2 - a_3 {p_C}^3. \end{aligned} \quad (9)$$

Then, by expanding to the long form of (3) - (5), setting $\alpha_0 = 1$, working through the algebra (shown in more detail in the appendix) gives

$$\begin{aligned} y_{AM}(t) =& 0.5\, a_2 \sin(\omega_0 t)^2 \\ & + 0.5\, a_2 \left(\sum_{h=2}^{\infty} \alpha_h \sin(h\omega_0 t + \phi_h)\right)^2 \\ & + a_2 \sin(\omega_0 t) \left(\sum_{h=2}^{\infty} \alpha_h \sin(h\omega_0 t + \phi_h)\right) \\ & + 2.25\, a_3 \sin(\omega_0 t) \left(\sum_{h=2}^{\infty} \alpha_h \sin(h\omega_0 t + \phi_h)\right)^2 \\ & + 2.25\, a_3 \sin(\omega_0 t)^2 \left(\sum_{h=2}^{\infty} \alpha_h \sin(h\omega_0 t + \phi_h)\right) \\ & + 0.75\, a_3 \left(\sum_{h=2}^{\infty} \alpha_h \sin(h\omega_0 t + \phi_h)\right)^3 \\ & - 0.1875\, a_3 \sin(3\omega_0 t) \\ & + 1.5\, a_3 \sin(\omega_0 t). \end{aligned} \quad (10)$$

Two important observations can be made about (10). Firstly, it reveals a subtle, but, essential property of AM imaging; the remaining signal lacks any linearly scattered components, yet, the last term of (10) contains energy at the fundamental frequency. The reflection coefficient a_3 indicates that this component

is caused by the nonlinear scattering properties of the microbubbles. Secondly, it is observed that this cancellation of the linearly scattered signal was attained despite the nonlinear nature of the CMUT. Although harmonics to the fundamental frequency are emitted, as seen in (3) - (5), (10) does not contain any emitted harmonics with the linear reflection coefficient a_1. This shows that when the emitted signals are reflected only linearly, the AM compounding cancels all of these terms. Some emitted harmonics remain in the y_{AM} signal, but, these terms all carry the reflection coefficients a_2 or a_3, meaning that the signals have been nonlinearly scattered by the microbubble. Notably, the fact that these emitted harmonics remain in the y_{AM} signal has not impaired the efficiency of the AM theory. Moreover, although the amplitude and phase of the emitted harmonics will be affected by the amplitude of V_{AC}, this does not affect the cancellation of linearly scattered signals. Because of this, when using the AM modality to image *in vivo* with a CMUT, it is possible to filter out linear scattering from tissue whilst attaining reflections from the microbubbles at the emitted frequency. Thus, it is shown theoretically that CEUS imaging with a CMUT using the three-pulse AM sequence is achievable.

3 Methods

To verify the outcome of the theoretical evaluation shown in Section 2, the ability of a linear CMUT array to cancel received linear components while preserving nonlinearly scattered signal was assessed using three measurement set-ups. Firstly, an experimental set-up was designed to quantify CTR. Section 3.1 outlines the design of the set-up. Contrast enhanced AM images were collected using a synthetic aperture imaging sequence on a CMUT and a PZT probe, further described in Section 3.2. Subsequently, the CTR was calculated for all the collected images, as detailed in Section 3.3. Secondly, Section 3.4 describes how the emitted signal from the transducers were recorded using a hydrophone, and used to determine the peak-negative-pressure (PNP) and the power annihilation ratio. Lastly, Section 3.5 describes how the signal-to-noise ratio of the two probes were evaluated to fairly compare the CMUT's and PZT arrays's performance.

3.1 CEUS imaging set-up

The experimental set-up used to quantify CTR consisted of a microflow phantom and a block of tissue-mimicking material. An illustration of the measurement set-up can be seen in Fig. 1. The microflow phantom was 3D printed in a PEGDA 700 g mol^{-1} hydrogel block using stereo-lithography. A hollow channel of 200 µm in diameter was printed inside the phantom, as

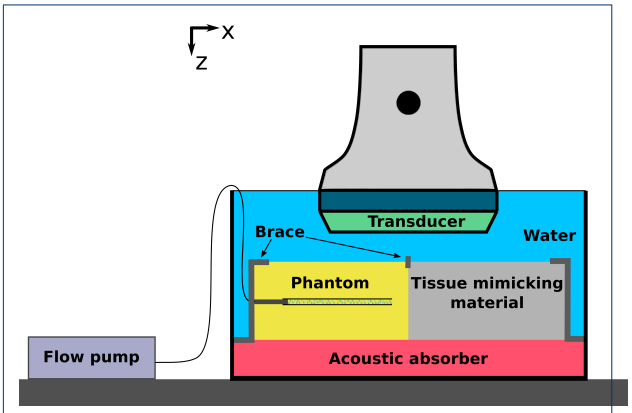

Figure 1: An illustration of the experimental set-up showing how the phantom and tissue-mimicking material are positioned under the transducer and held in place by a brace. The transducer sits directly above the phantom and tissue-mimicking material, in contact with the water.

Table 1: Specifications of the transducers.

	CMUT	PZT
Total number of elements	192	192
Center frequency	4.8 MHz	5.2 MHz
Pitch (p)	0.2 mm	0.2 mm
Kerf	0.02 mm	0.02 mm
Maximum tolerable AC voltage	60 V	100 V
Applied DC voltage	190 V	N/A

shown in Fig. 2. The fabrication process of the phantom has been described in [27]. The phantom was held in place by a brace next to a block of tissue-mimicking material made of polyvinyl alcohol cryogel [28, 29], resulting in scattering properties similar to that of human tissue. The ensemble was placed in a water bath, which was lined with an acoustic absorber. The phantom was positioned so that the center of the flow channel was 25 mm below the surface of the transducer. A low pressure flow pump (neMESYS 290N, Cetoni) fitted with a syringe of SonoVue microbubble contrast agents, diluted 1:10 with saline, was connected to the phantom and used to pump microbubbles through the phantom.

3.2 Image acquisition

The phantom and tissue-mimicking material was imaged using a linear CMUT [30] and, as a reference, a commercial linear PZT array of equivalent design dimensions, using a Verasonics research scanner (Verasonics Vantage 256). The specifications of the probes are given in Table 1. The set-up was imaged using a synthetic aperture sequence [31] with low intensity di-

Table 2: Parameters of the synthetic aperture sequence.

Pulse repetition frequency	1000 Hz
Number of active elements	32
Emission frequency	4.8 MHz
Focal distance	-16 mm
Receive F-number	1
Number of emissions (n)	13
Number of cycles in emission	2
Number of elements separating emissions (s)	13

verging wave propagation. A summary of the sequence parameters are given in Table 2. The transducers emitted a 2 cycle sine wave at 4.8 MHz, with 32 active elements in each full amplitude emission, and with a pulse repetition frequency of 1000 Hz. The sequence consisted of emissions from $n = 13$ virtual sources placed 16 mm behind the transducer surface. The lateral positions of the virtual sources were given by

$$x_i = s \cdot i \cdot p, \forall\, i \in \mathbb{Z} : i \in [-\frac{(n-1)}{2}, \frac{(n-1)}{2}], \tag{11}$$

where s denotes the number of elements separating the lateral positions of two virtual sources, i is emission index, p is the transducer pitch, and $x_i = 0$ lays in the middle of the transducer. The three emissions described in (3) - (5) are referred to as the minor sequence. The minor sequence was emitted once by each virtual source at each x_i to make a full image frame.

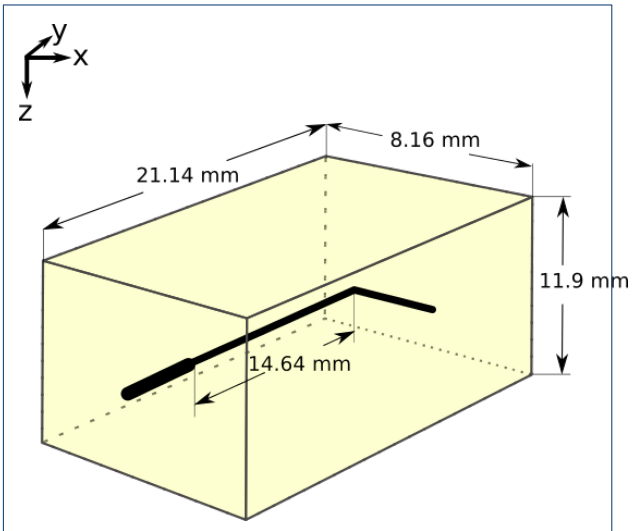

Figure 2: An illustration of the phantom, where the bold black line illustrates the internal channel.

The sequence was used to quantify how the CTR in the resulting images vary with the applied AC voltage. The lowest V_{AC} was 6 V, at which the imaging system approaches its noise floor. For the CMUT, V_{AC} was then increased in steps of 10 V until the maximum tolerable AC voltage of the probe, as given in Table 1, was reached. Additionally, a constant DC voltage of 190 V was applied to the CMUT, as specified in [30]. For the PZT array, the same voltage range was used, from 6 V to the probe's maximum tolerable voltage. But, the step size was reduced to 3 V between 6 V and 15 V. This was done to ensure a good population of data-points within the overlapping range of PNP for the two probes, since the relationship between applied voltage and PNP is not linear.

The SonoVue solution was allowed to flow continuously through the phantom channel at 0.6 µL s^{-1}, while 10 image frames were collected at each V_{AC}. To avoid degradation of the microbubbles during the collection of the 10 frames, a pause of 15 s was inserted between each frame to allow a fresh batch of microbubbles to flow into the phantom. A fresh syringe of diluted contrast agents were prepared directly prior to each data-set acquisition. Due to the higher number of AC voltages, the acquisition using the PZT probe was divided into two data-sets to make the time each syringe spent in the infusion pump comparable for each data-set. Thus, 3 data-sets were acquired; 6 V to 60 V with the CMUT, and 6 V to 26 V as well as 26 V to 90 V with the PZT array.

3.3 Calculation of CTR

The collected data from both probes were matched filtered and beamformed using delay-and-sum beamforming. CEUS images were composed using both (7) and (8). The two-pulse AM sequence, which was also studied by the authors in [32], is included for comparison with the three-pulse AM proposed by Fouan and Bouakaz [18], to study how an additional emission in the minor sequence affects the image quality. In addition, the data from every full amplitude emission in the minor sequence was used to compose B-mode images, for comparison. For each composed image, the CTR was calculated as

$$CTR = \frac{P_B}{P_{TMM}}, \tag{12}$$

where P_B is the average power of the signal scattered by the bubbles and P_{TMM} is the average power scattered by the tissue-mimicking material. The average power was calculated as

$$P = \frac{1}{L_2 - L_1} \frac{1}{k_2 - k_1} \sum_{l=L_1}^{L_2} \sum_{m=k_1}^{k_2} y_{l,m}^2, \tag{13}$$

where y is the signal in a single beamformed line of data, m is the sample number, k_1 and k_2 are sample numbers determining the axial position for the signal, and L_1 and L_2 are line numbers. Thus, the power was calculated in two rectangular regions-of-interest (ROIs). After beamforming the collected data, the ROIs used to calculate power in (13) were drawn around the channel in the phantom. The ROI in the tissue-mimicking phantom was taken to be the same size as the channel ROI, and placed at the same depth, in the middle of the tissue-mimicking phantom.

3.4 Hydrophone recordings

The derivation of (10) assumes that the same signal is produced by the full emission as the two half emissions combined. Array effects could arguably make the assumption fail if emission from one CMUT cell affects the emission from a neighbouring cell. It has been shown that the emission from an array of CMUTs is dependent on the distance between adjacent cells [25]. This distance varies between the emissions in the proposed sequences; in the full amplitude emissions the distance is one pitch, while in the half amplitude emissions it is $2 \cdot$ pitch. To evaluate if this effect adversely affects the similarity of the emitted pulses, and thus the cancellation of received linear terms, the signals emitted by each virtual source were recorded using a hydrophone. The hydrophone was placed in a water tank directly beneath the transducer, at $(y, z) = (0, 25)$ mm and moved to the x-positions corresponding to each virtual source, given by (11). The hydrophone recorded the minor sequence using all the applied AC voltages, from each virtual source. Then, the sequence's ability to cancel linear terms was quantified by defining an annihilated power ratio as

$$\text{Annihilated power ratio} = \frac{\Sigma p_A^2 - \Sigma p_{AM}^2}{\Sigma p_A^2}. \quad (14)$$

Here, the numerator contains the remaining AM signal subtracted from the full emitted signal and thus gives the power of the annihilated signal. For each x-position and applied V_{AC}, the recordings of the minor sequence were used to compose the compounded emitted AM signal, p_{AM}, according to (7), and the annihilated power ratio. This evaluation will be affected by nonlinear propagation in the water. The evaluation was therefore performed using both the PZT array and CMUT for comparison, to distinguish effects caused by nonlinear propagation from the effects caused by nonlinear excitation.

In addition, the measured hydrophone signals were used to quantify the PNP caused by each applied V_{AC} for both transducers. The minimum of the recording of the full emission was found from the recording beneath each virtual source and averaged to give the PNP.

3.5 Quantifying signal-to-noise ratio

Because the imaging performance of a CMUT and a PZT transducer are to be compared, it is prevalent to also quantify and compare the signal-to-noise ratio (SNR) of the two transducers. The three-pulse AM imaging sequence was used to acquire $N = 10$ frames of a speckle phantom with $0.5\,\text{dB}\,\text{cm}^{-1}\,\text{MHz}^{-1}$ attenuation. Only the full emission was used to beamform B-mode images of the phantom, using the same axial sampling and depths as the images acquired of the microflow phantom in Section 3.2. The acquisition was repeated using both the PZT transducer and the CMUT for the range of applied AC voltages specified in Section 3.2, with a step-size of 10 V. After beamforming, the power of an image line located at $x = 0$ was extracted from the images, and the SNR was quantified as

$$\text{SNR} = \frac{1}{N}\sum_{N=1}^{10} \frac{\sum_{m=k_1}^{k_2} \overline{y}^2}{\sum_{m=k_1}^{k_2} (y - \overline{y})^2}, \quad (15)$$

where y is the image line and $\overline{y}$ represents the average of the image line across the 10 acquisitions.

4 Results

Fig. 3 shows examples of a B-mode image and both a two-pulse and a three-pulse AM image of the microflow phantom and tissue-mimicking material, where the chosen ROIs are drawn on top of the images. In the images, it is clear that both the AM sequences with both probes have succeeded in removing most of the speckle pattern from the tissue-mimicking phantom, whereas the signal from the microbubbles remain. More speckle pattern remains in the AM images composed with two pulses, indicating that the three-pulse sequence outperforms the two-pulse sequence. The similarity of the images collected with the CMUT, in the left column of Fig. 3, and the PZT transducer, in the right column, gives a clear indication that CEUS with a CMUT is possible, despite the nonlinear nature of the probe.

Equations (12) and (13) were applied to all the collected images, both in three-pulse AM, two-pulse AM, and B-mode to calculate their CTR. The mean and standard deviation of the CTR was calculated for each set of 10 frames collected with constant V_{AC}. Fig. 4 shows the resulting mean CTR values with standard deviations as a function of V_{AC} applied to the CMUT for the three-pulse AM and B-mode, in addition to the difference between the two in decibels. Comparing the two modes shows that the CMUT has achieved a significant contrast enhancement across all the applied AC voltages, with 30 - 38 dB higher CTR in the CEUS images than in the B-mode.

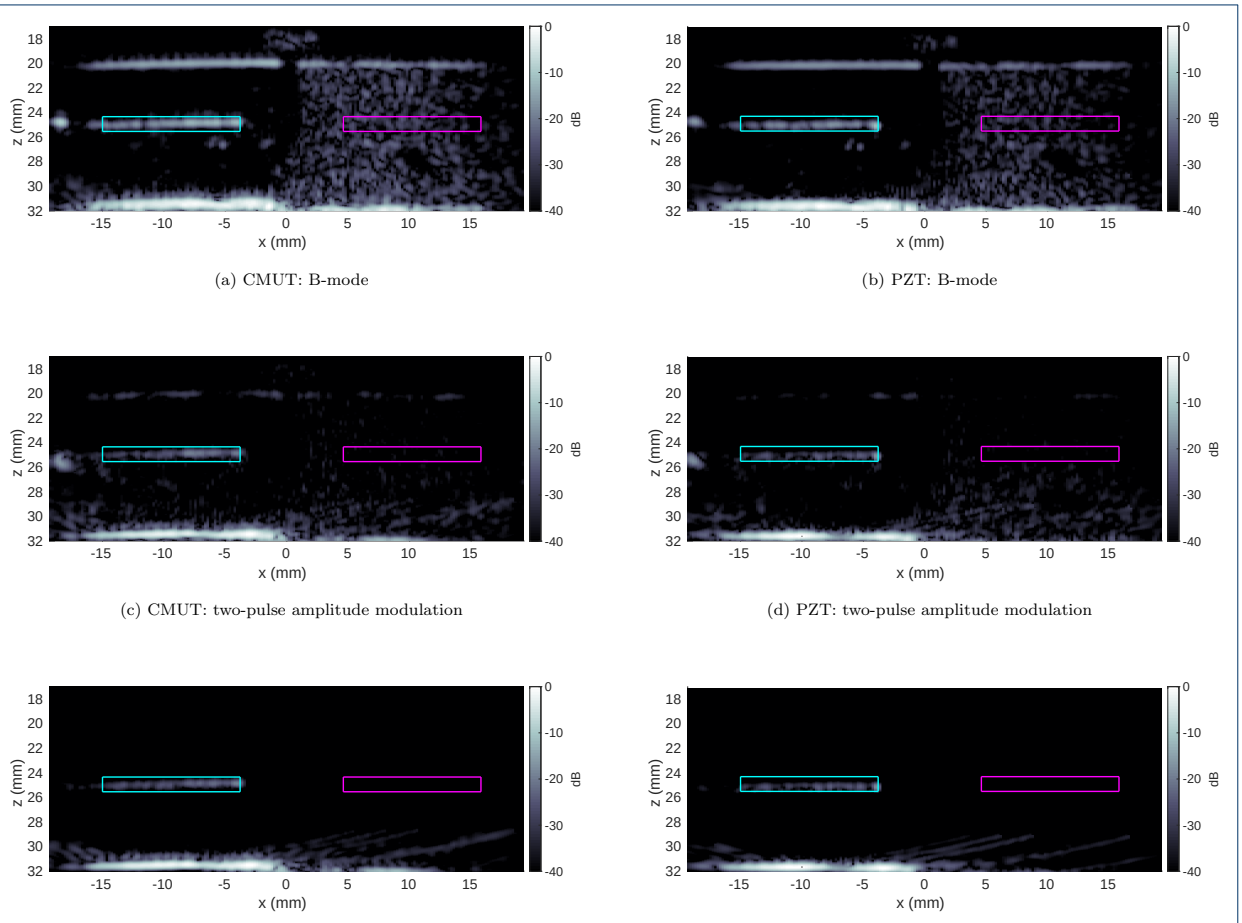

(a) CMUT: B-mode

(b) PZT: B-mode

(c) CMUT: two-pulse amplitude modulation

(d) PZT: two-pulse amplitude modulation

(e) CMUT: three-pulse amplitude modulation

(f) PZT: three-pulse amplitude modulation

Figure 3: Example images of the experimental set-up collected with the CMUT probe (left column) and PZT transducer (right column). Comparing the B-mode (a and b) with the two-pulse AM images (c and d) and the three-pulse AM image (e and f) show that the three-pulse sequence has successfully removed the speckle pattern inside the tissue-mimicking material (on the right of the image), while retaining the signal from the microbubbles (on the left of the image). The magenta and cyan boxes show the regions of interest used to calculate the CTR.

Although the theory of the three-pulse AM sequence, presented in Section 2, predicts that CTR should not degrade as the amount nonlinearity in the emitted signal rises with the applied AC voltage, it is expected that the CTR varies with AC voltage due to the nature of the microbubble contrast agents. As the applied voltage increases, so does the PNP of the emitted signal, which affects both the power and the spectral content of the scattered signal from the microbubbles [33]. Therefore, to fully understand the observed variation in CTR seen in Fig. 4, in Fig. 5, the CTR values are also plotted as a function of the emitted PNP, as recorded by the hydrophone measurements. In addition, the CTR of the B-mode and CEUS images collected using the PZT probe are plotted, to provide a reference of how the CTR varies with PNP when the emission from the probe is linear. The CTR for the PZT array is divided into two data-sets, representing the images collected with separate syringes of SonoVue.

The compounded AM signals were computed from the collected hydrophone recordings, using (7), and the annihilated power ratio was calculated as in (14). Fig. 6 shows how the power ratio varies with PNP. Had the cancellation of the signals been completely successful, all power would be removed and the power ratio would be 100 %. That is not the case, and it can be seen that the power ratio declines as PNP increases above approximately 455 kPa. In the region where the two probes' PNP overlap, the power ratios of both the

Table 3: The measured SNR of the CMUT and PZT arrays across all of the applied AC voltages. The SNR is calculated according to (15) and displayed with ± one standard deviation, σ.

AC voltage (V)	**6**	**16**	**26**	**36**	**46**	**56**	**60**	**66**	**76**	**86**	**90**
CMUT SNR $\pm\sigma$ (dB)	37 ± 4	50 ± 6	61 ± 7	65 ± 6	71 ± 6	72 ± 6	72 ± 6	N/A	N/A	N/A	N/A
PZT SNR $\pm\sigma$ (dB)	71 ± 5	64 ± 4	75 ± 5	80 ± 6	81 ± 7	84 ± 5	N/A	87 ± 5	92 ± 5	92 ± 5	85 ± 5

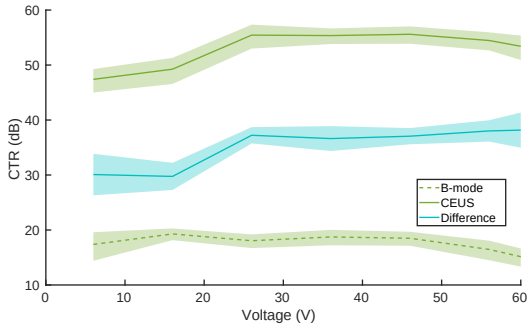

Figure 4: The calculated CTR values of the images collected with the CMUT using the three-pulse AM sequence, as a function of the applied AC voltage. The shaded areas indicated ± one standard deviation, calculated from the repeated acquisitions at each applied AC voltage. The green lines give the CTR of the CEUS and B-mode images, while the blue line gives the difference between the two.

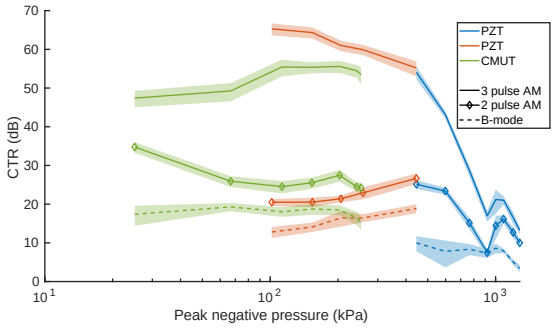

Figure 5: The calculated CTR values of the images collected with the CMUT and PZT transducer, as a function of the emitted peak-negative-pressure. The CTR of three-pulse AM images are plotted with solid lines, of the two-pulse AM images with solid lines with diamonds, and the CTR of the B-mode images are plotted with dotted lines. The shaded areas indicated ± one standard deviation, calculated from the repeated acquisitions at each applied AC voltage.

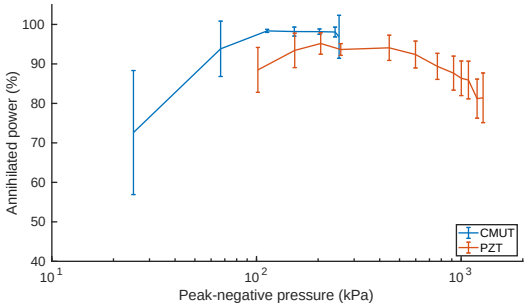

Figure 6: The average percentage ratio of power annihilated in the AM signal, normalized to the emitted power. A power ratio of 100 % indicates that all of the power in the AM signal was removed. Error bars indicate ± one standard deviation of variation along virtual source (VS) positions.

PZT transducer and the CMUT are high, indicating that the emitted signals are suitable for CEUS imaging, and that the efficiency of the three-pulse sequence is not affected by the increase in nonlinearity in the emitted signal from the CMUT, as the AC voltage is increased.

Finally, the SNR of the image acquisition using the two probes at varying AC voltages were calculated according to (15). The measured SNR is given in Table 3. Generally, it is seen that the SNR of the CMUT probe is lower than the PZT transducer, with a mean difference of 16 dB across 6 V to 56 V applied AC voltage. Further discussion of the data will be given in Section 5.

5 Discussion

As predicted by the theory laid out in Section 2, Fig. 4 shows that the CTR of the CEUS images collected with the CMUT using the three-pulse AM sequence is not affected by the increase in nonlinear emission caused by an increasing AC voltage. There is a significant enhancement of contrast between the CEUS images and the B-mode images, with an av-

erage of 35.3 dB enhancement across the applied voltages. Moreover, although the CTR of the CEUS images shown in Fig. 4 declines above 46 V, the difference between the logarithm of the CTR of the CEUS images and the B-mode images increases from 26 V to 60 V, demonstrating that the enhancement of the contrast caused by the three-pulse AM sequence is not affected by the applied AC voltage. On the other hand, it can bee seen in Fig. 5 that the two-pulse AM sequence has not accomplished the same enhancement. Clearly, reducing the number of emissions in the minor sequence, would benefit the frame rate. However, the average difference in CTR between the CEUS images and the B-mode images for the two-pulse AM sequence is only 9.1 dB. Thus, CEUS imaging using a CMUT should use the three-pulse AM sequence, despite the decrease in frame rate this will lead to.

The CTR of the CEUS images follows the expected trend; it increases initially, before starting to decrease at higher voltages. This progression is caused by the back-scattering properties of microbubbles. At low pressures, the nonlinear component of the back-scattering from microbubbles is proportional to the incident acoustic pressure [33, 34], and Emmer et al. [35] showed that SonoVue exhibits a low pressure threshold, under which the bubbles do not scatter nonlinearly. On the other hand, at high pressures, the CTR is expected to drop because the microbubbles start to degrade, through processes such as rupture of the lipid shell, diffusion of the gas core, or fragmentation [36–38]. A decline in CTR of the CEUS images collected with the CMUT is observed in Fig. 4 starting at 46 V, and correspondingly in Fig. 5 at 203 kPa. However, this decline in CTR does not point to a failure of the three-pulse AM sequence, but rather a natural consequence of the properties of the microbubbels. According to de Jong et al. [33], SonoVue can withstand up to 150 kPa before it starts to deform, and it is destroyed with a few repeated ultrasound exposures above approximately 300 kPa. This corresponds to the range at which the CTR in Fig. 5 starts to decline, taking into account the attenuation the emitted signal will experience before reaching the microbubbles inside the phantom. Thus, it has been shown that the ideal pressure range to perform CEUS imaging with a CMUT lies approximately between 100 kPa to 200 kPa.

Moreover, the same downwards trend in CTR of the CEUS images above approximately 100 kPa is observed for the images collected using the PZT transducer as for the images collected using the CMUT, further reinforcing that the decline is not caused by a deterioration of the three-pulse AM sequence. The PZT transducer displays a rapid decline in CTR above 455 kPa, likely caused by both the microbubble disruption discussed above, but also by nonlinear propagation in the image medium. The ratio of annihilated power shown in Fig. 6 also declines above 455 kPa, pointing to a discrepancy in the emitted pulses. Observation of the recorded hydrophone signals reveal sawtooth like pulse shapes, indicative of nonlinear propagation [39]. This distortion of the emitted pulses will differ between the full amplitude and half amplitude emissions, and thus cause the cancellation in (7) to fail.

Although the same AC voltage was applied to the CMUT and the PZT transducer, up to the maximum tolerable AC voltage of the CMUT, the PZT transducer emits higher PNP than the CMUT. The two probes have some overlap in their area of operation between 101 kPa to 258 kPa. In this region, both probes exhibit a significant contrast enhancement, with an average difference in CTR between the CEUS images and the B-mode images of 49.9 dB and 37.4 dB for the PZT transducer and CMUT, respectively. The fact that the PZT transducer overall performs better contrast enhancement than the CMUT is likely caused by the PZT transducer's superior SNR. At a constant emitted pressure, the back-scattering from the microbubbles will generally be the same for the PZT transducer and CMUT. Yet, the CTR can differ, if the amount of received noise is higher for the CMUT. As shown in Table 3 the CMUT has a lower SNR than the PZT transducer at all applied voltages. This is expected, since the probe is built in-house, whereas the PZT transducer is a commercial probe and has superior shielding from electromagnetic interference noise.

Yet, the quantification of the annihilated power shown in Fig. 6 shows that the CMUT generally outperforms the PZT transducer. The power annihilation ratio quantifies how much power that remains in the compounded emission and thus gives an indication of how well the transducers are able to perform contrast enhancement imaging. The cancellation of the emitted pulses is more effective for the CMUT than the PZT transducer, indicating that array effects in the CMUT is not causing significant degradation of the contrast enhancement. In the region where the two probes' PNPs overlap, the compounding of the AM signal from the CMUT leaves an average of 2 % of the emitted power, while for the PZT transducer the average remaining power is 7 %. When using the emissions for imaging, the amount of remaining power will transfer to the scattered signals and impair the ability to cancel linear signal from the tissue, thus lowering the CTR. Moreover, both probes exhibit an increase in the annihilated power with applied AC voltage, as well as an increased standard deviation of the annihilated power at low applied AC voltages. This further

supports that the nonlinear emission from the CMUT does not negatively impact the creation of CEUS images using the proposed three-pulse AM sequence.

6 Conclusion

Investigation of the creation of CEUS images with a CMUT has shown that the probe's inherent nonlinearity does not affect its performance, and that high contrast CEUS images can be created using a three-pulse AM sequence. The fact that the performance of the CMUT probe is not dependent on the harmonics of its emissions has been demonstrated theoretically, using quantification of CTR of CEUS images of microbubbles, and using hydrophone measurements of the emitted signals. Theoretically, it has been shown that there is no reason why the emitted harmonics will affect the CEUS images. This was confirmed by the acquired CEUS images, where an average of 37.4 dB contrast enhancement was achieved, using the three-pulse AM sequence. Comparison of the CTR of the images obtained using the proposed three-pulse AM sequence with the CTR of images obtained using only 2 emissions showed a significant advantage of the three-pulse AM, as the two-pulse AM sequence gave only an average of 9.07 dB contrast enhancement. Thus, a higher number of emissions in the minor sequence must be used, despite its negative impact on the frame rate. Further, comparison of the performance of the CMUT with a PZT transducer of similar design showed a comparable amount of contrast enhancement, as the images produced with the PZT transducer achieved an average of 49.9 dB contrast enhancement. The PZT transducer achieved higher CTR, but also higher SNR, and improvement of the design of the CMUT, especially focused on noise shielding, will likely improve its contrast enhancement abilities. Finally, hydrophone recordings and quantification of the annihilated power in the minor sequence showed that in the region of overlapping PNPs, the CMUT annihilated 98 % of the power, whereas the PZT transducer only annihilated 93 %. Thus, more power was cancelled in the CMUT's minor sequence than in the PZT transducer's, further reinforcing that the difference between the CTR produced by the CMUT and the PZT transducer is caused by the probes respective receive capabilities, rather than the emitted harmonics. Thus, future use of CMUT technology for CEUS images show great potential, and it will be possible to take advantage of the wide bandwidth, low emission pressure, and favorable sensitivity features of CMUTs for CEUS imaging.

7 Declarations

7.1 Abbreviations

AM Amplitude modulation.
CEUS Contrast enhanced ultrasound.
CMUT Capacitive micromachined ultrasonic transducer.
CTR Contrast-to-tissue ratio.
PI Pulse inversion.
PNP Peak-negative-pressure.
PZT Lead zirconate titanate.
ROI Region-of-interest.
SNR Signal-to-noise ratio.
SRI Super-resolution ultrasound imaging.
SVD singular value decomposition.
VS Virtual source.

7.2 Ethics approval and consent to participate

Not applicable.

7.3 Consent for publication

Not applicable.

7.4 Availability of data and material

The datasets used and/or analysed during the current study are available from the corresponding author on reasonable request.

7.5 Competing interests

The authors declare that they have no competing interests.

7.6 Funding

This work was financially supported by grant 82-2014-4 from the Danish National Advanced Technology Foundation, by grant 7050-00004B from Innovation Fund Denmark, and by BK Medical, Herlev, Denmark.

7.7 Authors' contributions

S.H. Øygard wrote the main manuscript text and prepared the figures. M. L. Ommen manufactured the phantom and designed part of the experimental set-up. B. G. Tomov assisted with technical measurements. S. E. Diederichsen manufactured the CMUT probe. E. V. Thomsen, N. B. Larsen, M. B. Stuart, and J. A. Jensen contributed to designing the study and discussed the results. All authors reviewed the manuscript.

7.8 Acknowledgments

Not applicable.

8 Appendix

The tree emissions given in (3) - (5) can be written on the compact form seen in (2) as

$$p_A(t) = p_L + \sum_{h=2}^{\infty} p_H, \tag{16}$$

$$p_B(t) = 0.5\,p_L + 0.5\sum_{h=2}^{\infty} p_H, \tag{17}$$

$$p_C(t) = 0.5\,p_L + 0.5\sum_{h=2}^{\infty} p_H. \tag{18}$$

The emissions in this form are inserted into (9);

$$\begin{aligned} y_{AM}(t) = {} & a_1 p_A + a_2 {p_A}^2 + a_3 {p_A}^3 \\ & - a_1 p_B - a_2 {p_B}^2 - a_3 {p_B}^3 \\ & - a_1 p_C - a_2 {p_C}^2 - a_3 {p_B}^3 \end{aligned} \tag{19}$$

$$
\begin{aligned}
&= a_1 \left(p_L + \sum_{h=2}^{\infty} p_H \right) + a_2 \left(p_L + \sum_{h=2}^{\infty} p_H \right)^2 \\
&+ a_3 \left(p_L + \sum_{h=2}^{\infty} p_H \right)^3 - a_1 \left(0.5 p_L + 0.5 \sum_{h=2}^{\infty} p_H \right) \\
&- a_2 \left(0.5 p_L + 0.5 \sum_{h=2}^{\infty} p_H \right)^2 - a_3 \left(p_L + \sum_{h=2}^{\infty} p_H \right)^3 \\
&- a_1 \left(0.5 p_L + 0.5 \sum_{h=2}^{\infty} p_H \right) \\
&- a_2 \left(0.5 p_L + 0.5 \sum_{h=2}^{\infty} p_H \right)^2 - a_3 \left(p_L + \sum_{h=2}^{\infty} p_H \right)^3 .
\end{aligned} \tag{20}
$$

Canceling terms and expanding the parenthesis gives

$$
\begin{aligned}
y_{AM}(t) = &\, 0.5\, a_2\, {p_L}^2 + 0.5\, a_2 \left(\sum_{h=2}^{\infty} p_H \right)^2 \\
&+ a_2\, p_L \left(\sum_{h=2}^{\infty} p_H \right) + 2.25\, a_3\, p_L \left(\sum_{h=2}^{\infty} p_H \right)^2 \\
&+ 2.25\, a_3\, {p_L}^2 \left(\sum_{h=2}^{\infty} p_H \right) \\
&+ 0.75\, a_3 \left(\sum_{h=2}^{\infty} p_H \right)^3 + 0.75\, a_3\, {p_L}^3 .
\end{aligned} \tag{21}
$$

The long form of (3) - (5) are then reintroduced;

$$
\begin{aligned}
y_{AM}(t) = &\, 0.5\, a_2 \sin(\omega_0 t)^2 \\
&+ 0.5\, a_2 \left(\sum_{h=2}^{\infty} \alpha_h \sin(h\omega_0 t + \phi_h) \right)^2 \\
&+ a_2\, \sin(\omega_0 t) \left(\sum_{h=2}^{\infty} \alpha_h \sin(h\omega_0 t + \phi_h) \right) \\
&+ 2.25\, a_3\, \sin(\omega_0 t) \left(\sum_{h=2}^{\infty} \alpha_h \sin(h\omega_0 t + \phi_h) \right)^2 \\
&+ 2.25\, a_3 \sin(\omega_0 t)^2 \left(\sum_{h=2}^{\infty} \alpha_h \sin(h\omega_0 t + \phi_h) \right) \\
&+ 0.75\, a_3 \left(\sum_{h=2}^{\infty} \alpha_h \sin(h\omega_0 t + \phi_h) \right)^3 \\
&+ 0.75\, a_3 \sin(\omega_0 t)^3 .
\end{aligned} \tag{22}
$$

Finally, the last term of (22) is expanded to give

$$
\begin{aligned}
y_{AM}(t) = &\, 0.5\, a_2 \sin(\omega_0 t)^2 \\
&+ 0.5\, a_2 \left(\sum_{h=2}^{\infty} \alpha_h \sin(h\omega_0 t + \phi_h) \right)^2 \\
&+ a_2\, \sin(\omega_0 t) \left(\sum_{h=2}^{\infty} \alpha_h \sin(h\omega_0 t + \phi_h) \right) \\
&+ 2.25\, a_3\, \sin(\omega_0 t) \left(\sum_{h=2}^{\infty} \alpha_h \sin(h\omega_0 t + \phi_h) \right)^2 \\
&+ 2.25\, a_3 \sin(\omega_0 t)^2 \left(\sum_{h=2}^{\infty} \alpha_h \sin(h\omega_0 t + \phi_h) \right) \\
&+ 0.75\, a_3 \left(\sum_{h=2}^{\infty} \alpha_h \sin(h\omega_0 t + \phi_h) \right)^3 \\
&- 0.1875\, a_3\, \sin(3\omega_0 t)) + 1.5\, a_3\, \sin(\omega_0 t).
\end{aligned} \tag{23}
$$

Author details

[1] Center for Fast Ultrasound Imaging, Department of Health Technology, Technical University of Denmark, Kgs. Lyngby, Denmark. [2] Biomimetics, Department of Health Technology, Technical University of Denmark, Kgs. Lyngby, Denmark. [3] MEMS - Applied Sensors, Department of Health Technology, Technical University of Denmark, Kgs. Lyngby, Denmark.

References

1. Oralkan, O., Ergun, A.S., Johnson, J.A., Karaman, M., Demirci, U., Kaviani, K., Lee, T.H., Khuri-Yakub, B.T.: Capacitive micromachined ultrasonic transducers: Next-generation arrays for acoustic imaging? IEEE Trans. Ultrason., Ferroelec., Freq. Contr. **49**, 1596–1610 (2002)
2. Haller, M.I., Khuri-Yakub, B.T.: A surface micromachined electrostatic ultrasonic air transducer. In: Proc. IEEE Ultrason. Symp., vol. 2, pp. 1241–1244 (1994)
3. Dietrich, C.F., Averkiou, M., Nielsen, M.B., Barr, R.G., Burns, P.N., Calliada, F., Cantisani, V., Choi, B., Chammas, M.C., Clevert, D., *et al.*: How to perform contrast-enhanced ultrasound (CEUS). Ultrasound international open **4**(1), 2 (2018)
4. Tang, M.X., Mulvana, H., Gauthier, T., Lim, A.K.P., Cosgrove, D.O., Eckersley, R.J., Stride, E.: Quantitative contrast-enhanced ultrasound imaging: a review of sources of variability. Interface Focus **1**(4), 520–539 (2011)
5. Errico, C., Pierre, J., Pezet, S., Desailly, Y., Lenkei, Z., Couture, O., Tanter, M.: Ultrafast ultrasound localization microscopy for deep super-resolution vascular imaging. Nature **527**, 499–502 (2015)
6. Christensen-Jeffries, K., Browning, R.J., Tang, M., Dunsby, C., Eckersley, R.J.: In vivo acoustic super-resolution and super-resolved velocity mapping using microbubbles. IEEE Trans. Med. Imag. **34**(2), 433–440 (2015)
7. Novell, A., Bouakaz, A., Legros, M., Felix, N.: Nonlinear contrast imaging with capacitive micromachined transducers. Proc. IEEE Ultrason. Symp. (2008)
8. Leighton, T.G.: The Acoustic Bubble. Elsevier Inc., London (1994)
9. Martin, K.H., Lindsey, B.D., Ma, J., Lee, M., Li, S., Foster, F.S., Jiang, X., Dayton, P.A.: Dual-frequency piezoelectric transducers for contrast enhanced ultrasound imaging. Sensors, 20825–20842 (2014)
10. Kamaya, A., Machtaler, S., Sanjani, S.S., Nikoozadeh, A., Sommer, F.G., Khuri-Yakub, B.T., Willmann, J.K., Desser, T.S.: New technologies in clinical ultrasound. Seminars in Roentgenology, 214–223 (2013)
11. Eckersley, R.J., Chin, C.T., Burns, P.N.: Optimising phase and amplitude modulation schemes for imaging microbubble contrast agents at low acoustic power. Ultrasound Med. Biol. **31**(2), 213–219 (2005)
12. Savoia, A.S., Caliano, G., Pappalardo, M.: A CMUT probe for medical ultrasonography: From microfabrication to system integration. IEEE Trans. Ultrason., Ferroelec., Freq. Contr. **59**(6), 1127–1138 (2012)
13. Lohfink, A., Eccardt, P.C.: Investigation of nonlinear CMUT behavior. In: Proc. IEEE Ultrason. Symp., pp. 585–588 (2005)
14. Miller, D.L.: Ultrasonic detection of resonant cavitation bubbles in a flow tube by their second-harmonic emissions. Ultrasonics **19**, 217–224 (1981)
15. Simpson, D.H., Chin, C.T., Burns, P.N.: Pulse inversion Doppler: A new method for detecting nonlinear echoes from microbubble contrast agents. IEEE Trans. Ultrason., Ferroelec., Freq. Contr. **46**(2), 372–382 (1999)
16. Brock-Fischer, G.A., Poland, M.D., Rafter, P.G.: Means for increasing sensitivity in non linear ultrasound systems. US Patent (5577505) (1996)
17. Oygard, S.H., Ommen, M.L., Engholm, M., Schou, M., Diederichsen, S.E., Thomsen, E.V., Stuart, M.B., Jensen, J.A.: Investigating a CMUT's ability to achieve non-linear contrast enhancement. In: Proc. IEEE Ultrason. Symp., pp. 1–4 (2020)
18. Fouan, D., Bouakaz, A.: Investigation of classical pulse sequences for contrast-enhanced ultrasound imaging with a CMUT probe. IEEE Trans. Ultrason., Ferroelec., Freq. Contr. **63**(10), 1496–1503 (2016)
19. Zhou, S., Reynolds, P., Hossack, J.: Pre-compensated excitation waveform to suppress second harmonic generation in MEMS electrostatic transducers. In: Proc. IEEE Ultrason. Symp., pp. 477–480 (2003)

20. Lei, A., E.Diederichsen, S., Hansen, S.M., Stuart, M.B., Bagge, J.P., Jensen, J.A., Thomsen, E.V.: Elimination of second-harmonics in CMUTs using square pulse excitation. In: Proc. IEEE Ultrason. Symp., pp. 1–4 (2016)
21. Bouakaz, A., Frigstad, S., Cate, F.T., de Jong, N.: Super harmonic imaging: a new imaging technique for improved contrast detection. Ultrasound Med. Biol. **28**(1), 59–68 (2002)
22. Certon, D., Teston, F., Patat, F.: A finite difference model for CMUT devices. IEEE Trans. Ultrason., Ferroelec., Freq. Contr. **52**(12), 2199–2210 (2005)
23. Kinsler, L.E., Frey, A.R., Coppens, A.B., Sanders, J.V.: Fundamentals of Acoustics, 3rd edn. John Wiley & Sons, New York (1982)
24. Lohfink, A., Eccardt, P.-C.: Linear and nonlinear equivalent circuit modeling of CMUTs. IEEE Trans. Ultrason., Ferroelec., Freq. Contr. **52**(12), 2163–2172 (2005)
25. Meynier, C., Teston, F., Certon, D.: A multiscale model for array of capacitive micromachined ultrasonic transducers. J. Acoust. Soc. Am. **128**(5), 2549–2561 (2010)
26. Novell, A., Bouakaz, A., Legros, M., Felix, N.: Exploitation of capacitive micromachined transducers for nonlinear ultrasound imaging. Proc. IEEE Ultrason. Symp., 2733–2743 (2009)
27. Ommen, M.L., Schou, M., Zhang, R., Hoyos, C.A.V., Jensen, J.A., Larsen, N.B., Thomsen, E.V.: 3D printed flow phantoms with fiducial markers for super-resolution ultrasound imaging. In: Proc. IEEE Ultrason. Symp., pp. 1–4 (2018)
28. Lai, S.S.M., Yiu, B.Y.S., Poon, A.K.K., Yu, A.C.H.: Design of anthropomorphic flow phantoms based on rapid prototyping of compliant vessel geometries. Ultrasound Med. Biol. **39**(9), 1654–1664 (2013)
29. Olesen, J.B., Villagómez Hoyos, C.A., Møller, N.D., Ewertsen, C., Hansen, K.L., Nielsen, M.B., Bech, B., Lönn, L., Traberg, M.S., Jensen, J.A.: Non-invasive estimation of pressure changes using 2-D vector velocity ultrasound: An experimental study with in-vivo examples. IEEE Trans. Ultrason., Ferroelec., Freq. Contr. **65**(5), 709–719 (2018). doi:10.1109/TUFFC.2018.2808328
30. Diederichsen, S.E.: Micromachined integrated transducers for ultrasound imaging. PhD thesis, Denmark Technical University (2020)
31. Jensen, J.A., Nikolov, S., Gammelmark, K.L., Pedersen, M.H.: Synthetic aperture ultrasound imaging. Ultrasonics **44**, 5–15 (2006)
32. Oygard, S.H., Ommen, M.L., Engholm, M., Schou, M., Diederichsen, S.E., Thomsen, E.V., Stuart, M.B., Jensen, J.A.: Investigating a CMUT's ability to achieve non-linear contrast enhancement. In: Proc. IEEE Ultrason. Symp., pp. 1–4 (2020)
33. de Jong, N., Emmer, M., van Wame, A., Versluis, M.: Ultrasonic characterization of ultrasound contrast agents. Med. Biol. Eng. Comp. **47**(8), 861–873 (2009)
34. Marmottant, P., van der Meer, S., Emmer, M., Verskuis, M., de Jong, N., Hilgenfe, S., Lohse, D.: A model for large amplitude oscillations of coated bubbles accounting for buckling and rupture. J. Acoust. Soc. Am. **118**, 3499–3505 (2005)
35. Emmer, M., van Wamel, A., Goertz, D.E., de Jong, N.: The onset of microbubble vibration. Ultrasound Med. Biol. **33**, 941–949 (2007)
36. Dayton, P.A., Morgan, K.E., Kilbanov, A.L., Brandenburger, G.H., Ferrara, K.W.: Optical and acoustical observations of the effects of ultrasound on contrast agents. IEEE Trans. Ultrason., Ferroelec., Freq. Contr. **46**(1), 220–232 (1999)
37. Thomas, D.H., Butler, M., Anderson, T., Emmer, M., Vos, H., Borden, M., Stride, E., de Jong, N., Sboros, V.: The quasi-stable lipid shelled microbubble in response to consecutive ultrasound pulses. Appl. Phys. Lett. **101**(7) (2012)
38. Chomas, J.E., Dayton, P., Allen, J., Morgan, K., Ferrara, K.W.: Mechanisms of contrast agent destruction. IEEE Trans. Ultrason., Ferroelec., Freq. Contr. **48**(1), 232–248 (2001)
39. Hamilton, M.F., Blackstock, D.T.: Nonlinear Acoustics. Academic Press, San Diego (1998)

Paper 6

Prediction of transmission through a lensed row-column addressed array

Sigrid H. Øygard, Mélanie Audoin, Andreas Austeng, Erik V. Thomsen, Matthias B. Stuart, and Jørgen A. Jensen

Name of journal:
The Journal of the Acoustical Society of America

Document Version:
In review

Prediction of transmission through a lensed row-column addressed array

Sigrid H. Øygard,[1, a] Mélanie Audoin,[1] Andreas Austeng,[2] Erik V. Thomsen,[1] Matthias B. Stuart,[1] and Jørgen A. Jensen[1]

[1] *Department of Health Technology, Technical University of Denmark, DK-2800 Lyngby, Denmark*

[2] *Department of Informatics, University of Oslo, Gaustadalléen 23B, 0373 Oslo, Norway*

Using a diverging lens on a row-column array (RCA) can increase the size of its volumetric image and thus significantly improve its clinical value. Here, a ray tracing method is presented to predict the position of the transmitted wave, so that it can be used to make beamformed images. The usable transmitted field-of-view (FOV) is evaluated for a lensed 128 + 128 element RCA by comparing the theoretic prediction of the emitted wave-front position with 3D finite element simulation of the emitted field. The FOV of the array is found to be $122^\circ \pm 2^\circ$ in the direction orthogonal to the emitting elements and 28.5° to 51.2°, depending on depth and element position, for the direction laying along the element. Moreover, the proposed ray tracing method is compared with a simpler thin lens model and it is shown that the improved accuracy of the proposed method can increase the usable transmitted FOV up to 25.1°.

[https://doi.org(DOI number)]

[XYZ] Pages: 1–12

I. INTRODUCTION

Row-column arrays (RCAs) offer medical volumetric imaging without being limited by the high channel count needed with more conventional matrix arrays (Morton and Lockwood, 2003; Rasmussen *et al.*, 2015; Sampaleanu *et al.*, 2014; Seo and Yen, 2009). Whereas fully populated matrix arrays with N elements along one dimension need a total of $N \times N$ channels, a RCA only requires $N + N$ connections (Yen, 2013). Sparsely populated arrays can be used to reduce the channel count, but at the expense of higher side-lobe levels (Davidsen *et al.*, 1994). Yet, RCAs often suffer from small foot-prints, as they can only image the volume directly in front of the aperture. The clinical value of RCAs can be increased by making alterations to its design so that the emitted sound is spread geometrically. This would enable the transducer to keep a small foot-print, while increasing the imaged volume, a feature which is useful for instance in cardiac imaging through the ribs. Such a transducer design was first proposed by Démoré *et al.* (2009), who simulated the radiation pattern from a RCA where the elements were curved onto the surface of a hemi-sphere. A manufacturing technique for such arrays has been proposed (Ferin *et al.*, 2018), but a simpler way of achieving diverging sound fields is the addition of a double-curved lens in front of a flat transducer, as proposed by Joyce and Lockwood (2014). The lens increased the field-of-view (FOV), but the authors also recognized that its addition introduced a non-trivial complexity when determining the propagation paths for beamforming images produced by the transducer.

Bouzari *et al.* (2017) studied the feasibility of beamforming images using a defocusing lens on a RCA. To make beamformed images, the time-of-flight to and from each element, through the lens, must be predicted. Bouzari *et al.* (2017) suggested determining this by assuming that the lens is infinitely thin and that the emitted wave-fronts are spherical. An expression for the focal point of these wave-fronts was given in terms of the geometrical and material properties of the physical lens. Although not explicitly stated by Bouzari *et al.* (2017), this theory is based on the paraxial assumption, and takes any refraction angles to be small. This lens model, originating from the field of optics, was first proposed used on ultrasound transducer lenses by Ernst (1947). The model is only exact when the lens is infinitely thin, and only an appropriate approximation for rays entering the lens close to its center (Carpena and Coronado, 2006). It does not account for the speed of sound of the material within the lens, although inaccuracy in the speed of sound during beamforming is known to negatively impact both resolution and contrast (Anderson *et al.*, 2000).

In this paper, we propose a model for predicting the time-of-flight (TOF) of transmission from a RCA through a diverging concave lens, without making the paraxial assumption. We hypothesize that rigorous prediction of the TOF will increase the width of the usable FOV wherein the predicted TOF is exact, as compared with the thin lens model. Further, the size and shape of the potential image volume that can be achieved using a 128 + 128 element RCA with a concave diverging lens is explored. The size of the image volume determines the applicability of RCAs to volumetric imaging in the clinic, and

[a] shoy@dtu.dk

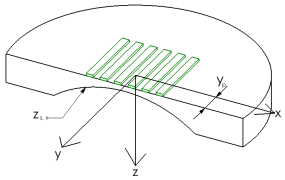

FIG. 1. An illustration of a concave lens with a cross-section cut through the lens to reveal its curvature. Six emitting elements are illustrated on top of the lens, to demonstrate the orientation of the elements in relation to the defined co-ordinate system.

the usable FOV for the lensed 128 + 128 element RCA is compared with the FOV of standard commercial convex arrays, which often achieve a FOV of 60° to 70° (GE Healthcare, 2021; Phillips, 2021; Siemens Healthineers, 2021).

II. THEORY

When sound emerges from an acoustic lens, the sound is refracted. The direction of the sound is changed due to the difference in speed of sound between the lens material and the imaged domain. The new direction of the sound is governed by Snell's law;

$$\frac{\sin\theta_i}{c_l} = \frac{\sin\theta_r}{c_w}, \tag{1}$$

where c_l is the speed of sound in the lens material, c_w is the speed of sound in the image material, here taken to be water, θ_i is the angle of incidence, and θ_r is the angle of refraction. To make a diverging lens, the shape of the lens must be concave if $c_l < c_w$ and convex if $c_l > c_w$. It is also possible to make a composite lens, with two materials, so that the surface of the lens is flat (Engholm *et al.*, 2018). As a first step, a single material will be studied here. The chosen design is the same as the lens used by Bouzari *et al.* (2018, 2017), and since the RCA is 2D, the lens is double-curved. The manufacturing of the lens and its material and geometrical properties are presented in Bouzari *et al.* (2018).

The concave lens consists of a single material cast with a carved hole in the shape of the cap of a sphere. Thus, the lens is double-curved and will refract the transmitted sound both in x- and y-directions. The sphere's origo is at $\begin{bmatrix} x_0 \\ y_0 \\ z_0 \end{bmatrix}$, where $(x_0, y_0) = (0, 0)$ when the lens is centered on the emitting array. The surface of the lens is described by the co-ordinates $\begin{bmatrix} x_s \\ y_s \\ z_s \end{bmatrix}$. An illustration of a concave lens and a set of column elements are shown in Fig. 1. The elements are not drawn to scale. Only 6 elements are drawn to make the illustration clearer. As shown, the origo of the co-ordinate system is taken to be in the middle of the emitting elements, and the length of the emitting columns are taken to run along the y-axis. This orientation is adopted throughout the paper. Fig. 1 also shows a cross-section cutting through the lens, parallel to the x-axis at the distance $y = y_p$ from the origo, revealing the curvature of the carved hole. Similarly, for a cross-section through the lens parallel to the y-axis, the distance from the origo to the plane is $x = x_p$. At each cross-section plane, the lens's surface makes a circular arc on the plane, which is given by

$$z_s = \begin{cases} \sqrt{R^2 - (x_s - x_0)^2} + z_0, & \text{for a } x\text{-}z \\ & \text{plane at } y_p, \\ \sqrt{R^2 - (y_s - y_0)^2} + z_0, & \text{for a } y\text{-}z \\ & \text{plane at } x_p. \end{cases} \tag{2}$$

Here, R is the radius of the circle in the particular plane. This radius is given by

$$R = \begin{cases} \sqrt{R_S^2 - y_p^2}, & \text{for a } x\text{-}z \text{ plane at } y_p, \\ \sqrt{R_S^2 - x_p^2}, & \text{for a } y\text{-}z \text{ plane at } x_p, \end{cases} \tag{3}$$

where R_S is the radius of the sphere.

To beamform images made using a lensed RCA, one must be able to predict the position of the emitted wave-front as a function of time. The position of the wave-front is governed by the position of the emitting element, the angles at which the ray is emitted, the geometry of the lens, and time, so that

$$\begin{bmatrix} x_W \\ y_W \\ z_W \end{bmatrix}(t) = f\left(\begin{bmatrix} x_{el} \\ y_{el} \end{bmatrix}, \begin{bmatrix} \alpha_x \\ \alpha_y \end{bmatrix}, t \right). \tag{4}$$

Here, (x_W, y_W, z_W) is the position of the emitted wave-front, (x_{el}, y_{el}) is the center position of the emitting element, (α_x, α_y) are the angles at which the sound is emitted, with respect to the normal on the emitting element, and f is some function which takes the geometry of the lens into account. To predict the position of the wave-front, this function f must be described. Previous works on lensed RCAs (Bouzari *et al.*, 2018, 2017; Engholm *et al.*, 2018) have solved this by implementing a thin lens model, which will be further described in Section II B. Here, we present the theory of a new model which does not carry the same assumptions as the thin lens model, but describes the function f through an accurate implementation of ray tracing. This task can be divided into two parts; determining the positions at which the emitted ray intersects the lens boundary, and determining the propagation direction after the ray is refracted by the lens.

A. The ray tracing method

1. Surface interception

The elongated elements can be assumed to emit cylindrical waves (Rasmussen *et al.*, 2015). Thus, when first emitted, the ray travels merely in the positive z-direction in the y-z plane. This means that $\alpha_y = 0$. The element can be divided into N virtual sub-elements

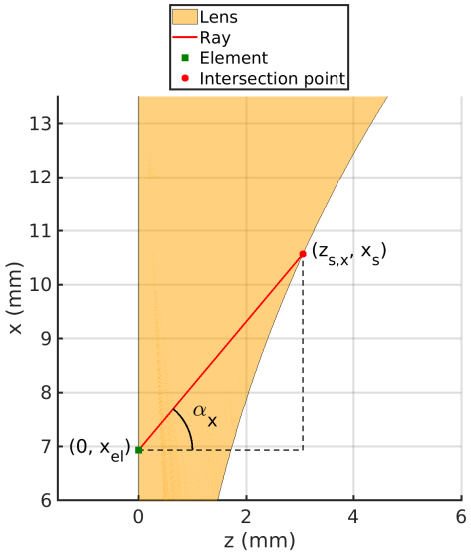

FIG. 2. Illustration of a ray intersecting the lens boundary at α_x emitted angle.

along its length. The subscript j refers to the sub-element number, and $y_{el,j}$ thus indicates a unique position in the y-direction. Since $\alpha_y = 0$, $y_{el,j}$, is also the y-coordinate of the intersection of the ray with the lens surface. The depth of the intersection is thus

$$z_{s,y} = \sqrt{R^2 - (y_{el,j} - y_0)^2} + z_0. \tag{5}$$

In the x-z planes, the sound spreads out in 180°. To determine the relationship between the emission direction, α_x, and the intersection point at the surface, $(z_{s,\,x},\, x_s)$, recognize that the emitted ray forms a triangle with a horizontal line, as shown in Fig. 2, which gives

$$\tan\alpha_x = \left(\frac{x_s - x_{el}}{z_{s,\,x}}\right). \tag{6}$$

The point at which the ray intersects the surface can be found by combining (6) with (2), and solving for x_s, giving

$$\begin{aligned} x_s = \frac{1}{2\left(\tan^2(\alpha_x)+1\right)}\Bigg(& 2x_0\tan^2(\alpha_x) + 2z_0\tan(\alpha_x) \\ &+ 2x_e \pm \Big[\left(-2x_0\tan^2(\alpha_x) - 2z_0\tan(\alpha_x) - 2x_{el}\right)^2 \\ &- 4\left(\tan^2(\alpha_x)+1\right)\left(-R^2\tan^2(\alpha_x) + x_0^2\tan^2(\alpha_x)\right. \\ &\left. +2x_{el}z_0\tan(\alpha_x) + z_0^2\tan^2(\alpha_x) + x_{el}^2\right)\Big]^{\frac{1}{2}}\Bigg). \end{aligned} \tag{7}$$

This relationship can in turn be used to find $z_{s,x}$ using (2).

2. Emitted directions in medium

Having established where the emitted ray intersects the lens, one must then determine which direction the ray will travel after having been refracted. The refraction itself is governed by (1), where both angles are in relation to the normal on the surface. In the case of the spherical surface, the normal is at all times collinear with the line between the point of incidence and the center of the circle given by (2). The length of this line is the radius of the circle.

3. Angle of incidence

In the y-z planes, the angle of incidence, $\theta_{i,y}$, can be found by recognizing that it is equal to the angle made by the radius of the surface and the horizontal, γ, as shown in Fig. 3. This angle is given by

$$\theta_{i,y} = \gamma_y = \sin^{-1}\left(\frac{y_{el,j}}{R}\right). \tag{8}$$

In the x-z planes, γ_x is given by the same geometry;

$$\gamma_x = \sin^{-1}\left(\frac{x_s}{R}\right). \tag{9}$$

Here, the incident ray is not necessarily horizontal, and thus the angle of the emitted ray must be added to γ_x, so that the incident angle is

$$\theta_{i,x} = \gamma_x + \alpha_x. \tag{10}$$

4. Emitted direction

Having calculated the incident angle, (1) can be used to calculate the refracted angle. This gives the direction of the ray emerging from the lens with reference to the normal to the surface, which is not a constant reference direction. Therefore, the propagation direction of the ray in relation to the horizontal, χ, must be found.

As shown in Fig. 4, the geometry gives

$$\chi_y = \theta_{r,\,y} - \theta_{i,\,y}, \tag{11}$$

$$\chi_x = \theta_{r,\,x} - \gamma_x. \tag{12}$$

The components of χ determine the propagation directions of the ray, as illustrated in Fig. 5.

The two direction angles can be used to determine the position of the emitted angle at time t. The ray travels along two distinct, straight lines; from the point of emission to the lens boundary, and from the lens boundary to the wave-front position $(x_W,\, y_W,\, z_W)$. The time it takes to reach the array boundary is taken to be t_1 and is given by

$$t_1 = \frac{z_{s,\,x}}{\cos(\alpha_x)\cdot c_l}. \tag{13}$$

The distance travelled by a ray outside the lens corresponds to the magnitude of the hypotenuse in the red

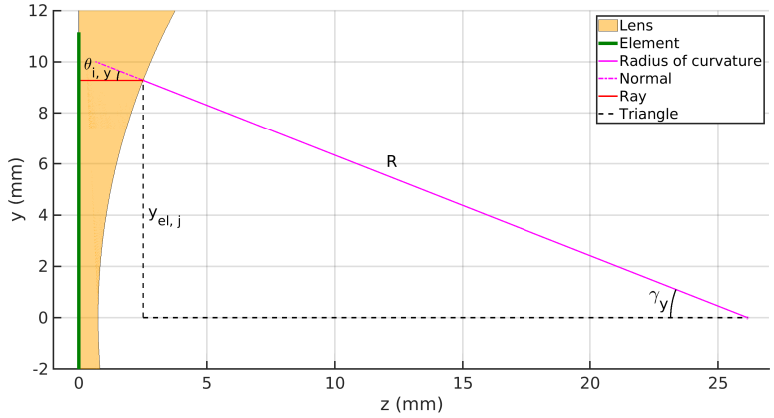

FIG. 3. The triangle made by the radius of curvature and the horizontal, giving the incident angle in the y-z planes.

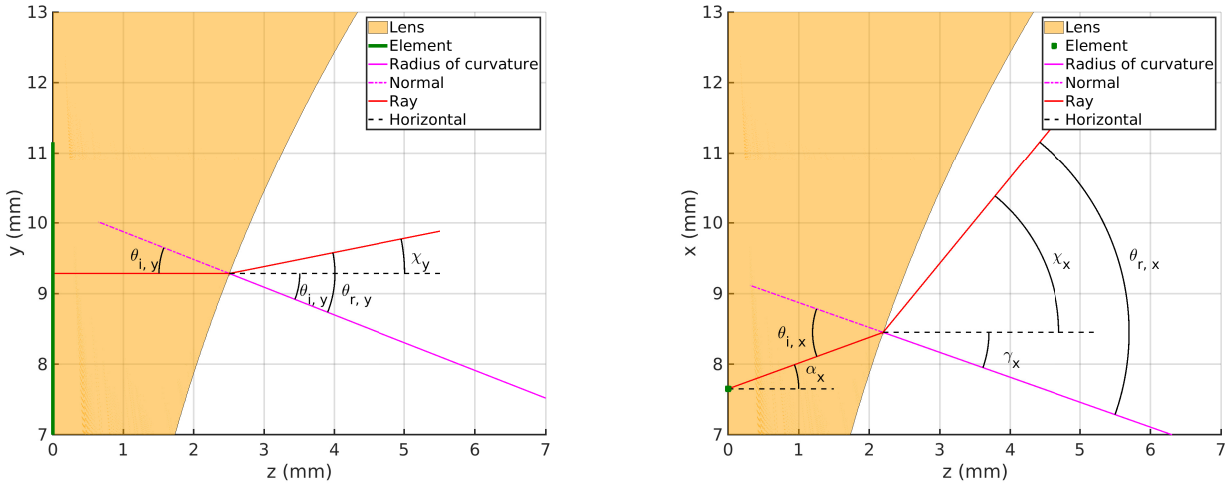

(a) (b)

FIG. 4. Illustrations of how χ is found in the y-z planes (a) and the x-z planes (b).

triangle in Fig. 5. This second distance of flight, DOF_2, is

$$DOF_2 = c_w \cdot (t - t_1). \tag{14}$$

The final position of the ray is

$$\begin{bmatrix} x_W \\ y_W \\ z_W \end{bmatrix} = \begin{bmatrix} x_s \\ y_s \\ z_s \end{bmatrix} + \begin{bmatrix} \Delta x(t) \\ \Delta y(t) \\ \Delta z(t) \end{bmatrix}, \tag{15}$$

where the the changes in position are given by

$$\begin{bmatrix} \Delta x(t) \\ \Delta y(t) \\ \Delta z(t) \end{bmatrix} = \begin{bmatrix} \dfrac{DOF_2(t)}{\sqrt{\left(1 + \cot^2\chi_x + \cot^2\chi_x \cdot \tan^2\chi_y\right)}} \\ \dfrac{DOF_2(t)}{\sqrt{\left(1 + \cot^2\chi_y + \cot^2\chi_y \cdot \tan^2\chi_x\right)}} \\ \dfrac{\Delta x}{\tan\chi_x} \end{bmatrix}. \tag{16}$$

Thus, by specifying the position of the emitting element, the initial emission angle α_x and the time of flight, it is possible to determine the corresponding position of

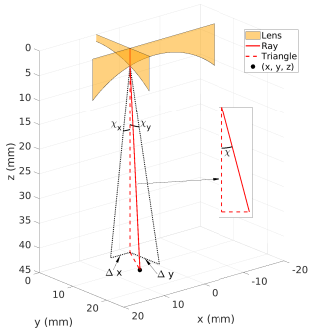

FIG. 5. Two crossing cross-sections of the lens, showing how the distance traveled by the ray outside the lens, the hypotenuse of the red triangle, is related to the two propagation angles χ_x and χ_y.

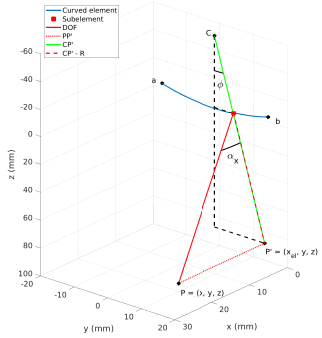

FIG. 6. An illustration of the curved element geometry proposed by Bouzari *et al.* (2017). The position of the subelement and α_x can be used to calculate the wave-front position, $\mathbf{P}$.

the emitted wave-front after refraction through a double curved lens.

B. The thin lens model

This method has been formulated by Bouzari *et al.* (2018, 2017), and is repeated here to ease the comprehension of the reader. According to the thin lens model, the acoustic lens has a single focal point, which is given by

$$F = \frac{R}{1 - \dfrac{c_w}{c_l}}. \tag{17}$$

For a diverging lens, the focal point lays behind the lens and the focal distance, F, should thus be negative. Note that in Bouzari *et al.* (2018), the fraction in the denominator of (17) is given as $\dfrac{c_l}{c_w}$, which results in a focusing wave when $c_l < c_w$. This is taken to be a misprint, and (17) is applied throughout this paper. Each element laying at $x = x_{el}$ is assumed to take on the shape of a spherical arc from point $\mathbf{a}$ to $\mathbf{b}$, with origo at $\mathbf{C} = (0,\, x_{el},\, F)$, and with a radius of curvature, R, given by (3). According to Bouzari *et al.* (2018) the two-sided angular FOV, Ω, is given by

$$\Omega = 2\cot^{-1}\left(\frac{F}{r_c}\right), \tag{18}$$

where r_c is the chord radius of the lens.

Bouzari *et al.* (2017) writes that to find the TOF to an arbitrary image-point, $\mathbf{P} = (x, y, z)$, it is first projected onto the x-z plane collinear with the emitting element to find the point $\mathbf{P}' = (x', y, z)$. If the vector $\mathbf{CP}'$ passes between the points $\mathbf{a}$ and $\mathbf{b}$, the distance traveled by the emitted ray is

$$\mathrm{DOF} = \sqrt{\|\mathbf{PP}'\|^2 + (\|\mathbf{CP}'\| - R)^2}, \tag{19}$$

where $\|\cdot\|$ is taken to be the norm of the vector. This geometry is illustrated in Fig. 6. To use this to calculate the position of a wave-front, given a constant TOF, recognize that if a ray is emitted from an element at some position $(x_{el},\, y_{el\,j})$ in the direction α_x, the two distances in (19) are given by

$$\|\mathbf{CP}'\| - R = \frac{x_W - x_{el}}{\tan\alpha_x}, \tag{20}$$

$$\|\mathbf{PP}'\| = x_w - x_{el}. \tag{21}$$

Equation (19) can thus be solved for the x-position of the wave-front for a certain TOF, given that the image medium is homogeneous, so that

$$\mathrm{TOF} = \frac{\mathrm{DOF}}{c_w}. \tag{22}$$

Furthermore, to find the y and z-positions of the wave-front, calculate the angle ϕ made by the vertical and the distance between $\mathbf{C}$ and the sub-element position $y_{el,j}$. This is used to find the vertical and horizontal distances between $\mathbf{C}$ and $\mathbf{P}'$, so that

$$y_W = \sin(\phi)\cdot(|F| + \|\mathbf{CP}'\| - R), \tag{23}$$

$$z_W = \frac{y_W}{\tan(\phi) - |F|}, \tag{24}$$

where $|\cdot|$ denotes the absolute value.

Bouzari *et al.* (2017) further states that if the vector $\mathbf{CP}'$ passes outside the arc, the distance is simply taken to be the distance from the point $\mathbf{P}$ to the closest endpoint on the arc, $\mathbf{a}$ or $\mathbf{b}$.

C. Evaluation of field-of-view

For a single element emitting through a lens, the wave-front will have a constant TOF in a double-curved surface beneath the lens. Any arc which lays on this surface is henceforth referred to as a wave-front arc. For simplicity, all wave-front arcs used in this study lay parallel to either the x or the y-axis. The clinical value of

a lensed RCA is defined by the extent of these arcs, and the extent at which it is possible to accurately determine the position of these arcs. Several authors (Bouzari *et al.*, 2018; Démoré *et al.*, 2009; Engholm *et al.*, 2018) have previously studied the extent of the arcs by looking at how wide the pressure field is, purely based on the sound's intensity level along the arc, and taken this to be the usable FOV of the RCA. However, this approach fails to recognize that it is necessary to predict the position of the emitted wave in order to successfully use it to beamform an image. Therefore, the usable FOV might be smaller than the field containing energy.

Instead, the usable FOV should be assessed by studying both the amplitude of the pressure wave and the potential phase error introduced by the prediction of its position. Given a sound pressure field along a wave-front arc that has been predicted to have a constant TOF, the extent of the usable FOV in this pressure field can be evaluated using a formal signal-to-noise (SNR) criterion proposed by Oddershede *et al.* (2007);

$$\mathrm{SNR}\,(a) \leq \mathrm{SNR}\,(\Delta\phi)\,. \tag{25}$$

Here, a is the amplitude of the pressure wave normalized to its amplitude at some reference point, p^*, on the arc, and $\Delta\phi$ is the phase difference in relation to the reference point. The two SNR functions evaluated for amplitude and phase difference are

$$\mathrm{SNR}\,(a) = \frac{1-a^2}{2a}, \tag{26}$$

$$\mathrm{SNR}\,(\Delta\phi) = \left(1 - \frac{\Delta\phi}{2\pi b}\right)\cos\Delta\phi - \frac{1}{2\pi b}\sin\Delta\phi, \tag{27}$$

where b is the number of cycles in the emitted wave. For arcs parallel with the emitting element, the reference point, p^*, is taken to be the center point on the element, and for arcs orthogonal on the emitting element, the reference point is taken to be the lateral position of the element. The usable FOV is taken to be the region of the arc where the criterion is true. The SNR criterion fails if the amplitude of the signal is too low, or, if the phase difference is too high. Several factors will determine the width of the usable FOV, including the accuracy of the prediction of the position of the wave-front and the lens' ability to spread the energy.

After evaluating (26) and (27) along a wave-front arc, the two equations will be equal at two points. The two corresponding positions are named the intersection points, p^i, and give the one-sided width of the FOV as

$$W_{\pm 1/2} = p^* - p^i. \tag{28}$$

The intersection points can also be used to calculate the one-side angular FOV as;

$$\Omega_{\pm 1/2} = \arctan\frac{p^* - p^i}{z}, \tag{29}$$

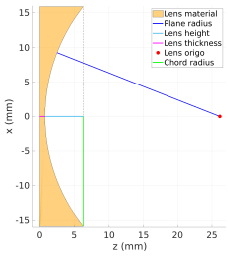

FIG. 7. Illustration of the geometry of the lens, at a cross-section through $y = 0\,\mathrm{mm}$.

Transducer features	
Number of elements	128 + 128
Center frequency	6 MHz
Emitted frequency	1 MHz
Pitch	0.2 mm
Kerf	0.02 mm
Element length	25.6 mm
Lens geometry	
Radius of curvature (R_S)	25.4 mm
Lens height	5.57 mm
Lens thickness	0.75 mm
Lens origo (x_0, y_0, z_0)	(0, 0, 26.15) mm
Chord radius	15.87 mm
Lens material properties	
Speed of sound (c_l)	$1000\,\mathrm{m\,s^{-1}}$
Attenuation (A_l)	$14\,\mathrm{dB\,cm^{-1}}$
Density (ρ_l)	$1050\,\mathrm{kg\,m^{-3}}$

TABLE I. A summary of the transducer and lens geometry and features.

where z is depth of the arc at the intersection point. For both $W_{\pm 1/2}$ and $\Omega_{\pm 1/2}$, the subscript + denotes the FOV in the positive direction, the subscript − denotes the FOV in the negative direction, and the subscript ± refers to one or the other. The FOV on each side of the reference point are found independently, as it is not assumed that the emitted pressure field is symmetrical. The total FOV is found by adding the two one-sided FOVs.

III. METHODS

The lens is modelled with the geometry of the $R_S = 25.4\,\mathrm{mm}$ RTV664 silicone lens described by Bouzari *et al.* (2018). The geometry of a cross-section of the lens is illustrated in Fig. 7. The physical dimensions of the lens and the transducer are given in Table I.

The width and angular extent of the usable FOV have been assessed for a number of example cases, which will be specified further in Sections III C 1 and III C 2. For all the studied cases, the extent of the FOV was determined using the following method. Firstly, the position of a wave-front with constant TOF was determined

using the appropriate geometrical relationships, as given in either Section II A or II B. Then, finite element modeling (FEM) was used to simulate the sound pressure field at the positions of this wave-front, as described in Section III B. Finally, the simulated pressure field was used to determine its usable width and angular extent of the FOV, according to the SNR criterion (25). This evaluation method is further described in Section III C.

A. Calculating wave-front arcs

For a given TOF, (5) to (16) was used to calculate the position of constant TOF surface for the ray tracing model and (19) to (24) for the thin lens model. In both cases, α_x was varied as $-90°{:}0.1°{:}90°$, and $y_{el,j}$ was set equal to positions along the element in increments of 0.04 mm. From this surface, interpolation was used to calculate a 2D wave-front arc laying in a plane parallel to the x or the y-axis, giving $(y_A,\, z_A)$ or $(x_A,\, z_A)$, respectively. The position of the plane is given by x_p or y_p, and the resulting 2D wave-front arcs are thus given by

$$\text{Position of arc} = \begin{cases} (x_A,\, y_p,\, z_A), & \text{orthogonal to the element,} \\ (x_p,\, y_A,\, z_A), & \text{along the element,} \end{cases} \tag{30}$$

Throughout this paper, this method is used when calculating the position of wave-front arcs.

B. Finite element method simulations

3D FEM simulations of the transmit pressure field were done with OnScale (OnScale LLC, Cupertino, CA, USA). The lens was modeled as a 3D domain whose boundaries correspond to the lens geometry described in Table I and Fig. 7. The lens domain was assigned the material properties specified in Table I. The rest of the simulated domain had the properties of water (speed of sound $c_w = 1480\,\mathrm{m\,s^{-1}}$, density $\rho_w = 997\,\mathrm{kg\,m^{-3}}$, attenuation $\mathrm{A}_w = 0.0022\,\mathrm{dB\,cm^{-1}}$). Each emitting element was identified by a rectangular area having the width and the length of the transducer's column element. This rectangular area is positioned on top of the lens at $z = 0$, with its length along y-direction and its width centered around x_{el}, the coordinate of the emitting element. A pressure wave was applied from this area and through the lens to mimic the firing of an emitting element. The excitation signal was a normalized two-cycled sinusoid at 1 MHz. The applied signal has a discontinuous derivative at the end of the pulse, causing the emitted signal to have a ringing tail. This will not affect the evaluation of the FOV. The simulation used symmetry boundary condition in the middle of the emitting element due to the (x-z) symmetry plane, impedance boundary at the bottom of the lens (x-y plane at $z = 0$) and an absorbing boundary everywhere else. The pressure field was calculated with FEM up to 1 mm above the lens. Kirchoff extrapolation (Margrave and Daley, 2001) was used in the homogeneous water domain to calculate the pressure field beyond the lens. Thus, the time-varying pressure was calculated at the positions of the desired wave-front arc, as given by (30).

C. Assessing the width of the FOV

Initially, FEM was used to simulate the acoustic pressure field, as described in Section III B, at wave-front arcs with constant TOF. For each position along the arc, the time-varying pressure field was correlated with the pressure-field at p^* to find the phase difference, $\Delta\phi$. Also, the the maximum of the time-varying pressure field was used to calculate a at each position. Then, a and $\Delta\phi$ were used to calculate how the two parts of the SNR criterion (25) varied with position along the arc, using (26) and (27). Finally, the two intersection points, p^i, were found and each used to calculate the one-sided width and angular FOV using (28) and (29).

1. Comparison of ray tracing and the thin lens model

In order to compare how accurately ray tracing and the thin lens model are able to predict the position of wave-front arcs, the FOV was evaluated for four example cases; along the center element of the transducer, orthogonal to the center element, along the edge element of the transducer, and orthogonal to the edge element. A summary of the properties of the four cases are given in Table II. For all cases, the TOF was chosen to be 40.54 µs, corresponding to 6 cm propagation in a homogeneous media at $c_w = 1480\,\mathrm{m\,s^{-1}}$. For all cases, the wave-front arc was evaluated according to Section III A, the pressure field was simulated according to Section III B, and the FOV was evaluated according to Section II C.

2. Evaluation of the lensed RCAs usable FOV

The clinical value of a lensed RCA lays in its ability to spread the sound outwards as it propagates into the image domain and thus extend the usable FOV with depth. Therefore, the usable FOV was evaluated at different depths, at the constant TOFs corresponding to propagation in a homogeneous medium with $c_w = 1480\,\mathrm{m\,s^{-1}}$ through 6 cm to 21 cm in steps of 5 cm. The TOFs were used to calculate the wave-front arcs using the ray tracing model, and the simulation and evaluation procedure previously described in Sections III A to III C was applied to find the usable FOV at each depth, for each of the four example cases given in Table II.

The same evaluation was also made for a set of elements across the RCA. The FOV was evaluated at the aforementioned constant TOFs at arcs laying along each element and orthogonal to each element at $y = 0$. The studied elements were chosen from element number 65, which lays closest to the center of the array, to element number 128, which is the outermost element, in steps of 9.

Case number	Element name	Element index	Position of element	Arc relation to element	Arc parallel to axis
1	Center	65	$x = 0.1\,\text{mm}$	Orthogonal	x
2	Center	65	$x = 0.1\,\text{mm}$	Along	y
3	Edge	128	$x = 12.7\,\text{mm}$	Orthogonal	x
4	Edge	128	$x = 12.7\,\text{mm}$	Along	y

TABLE II. Description of the geometry of the simulated cases used to compare the performance of ray tracing and the thin lensed model.

IV. RESULTS

A. Comparison of ray tracing and the thin lens model

The extent of the FOV was evaluated for the four simulated cases given in Table II for wave-front arcs predicted by both the thin lens model and the ray tracing model. The resulting two-sided angular FOVs are given in Table III. The ray tracing model gives comparable or higher FOV than the FOVs calculated using the arcs predicted by the thin lens model.

Case number	1	2	3	4
FOV with RT	125.1°	47.6°	110.7°	39.3°
FOV with TL	121.1°	44.4°	85.6°	39.9°

TABLE III. The calculated two-sided angular FOV for the four example cases, calculated with arcs predicted by the ray tracing (RT) model and the thin lens (TL) model.

The largest difference between the thin lens and ray tracing models can be observed in case 3. The simulated pressure field for the two arcs used in case 3 are presented in Fig. 8a and b. The pressure fields are plotted both as a function of the angle made between the emitting element and the (x, z) position of the arc, and of the x-position of their respective arcs, which is not the same for the two cases. The two parts of the SNR criterion calculated with (26) and (27) along the extent of the arcs are plotted in Fig 8c and d, and the points of intersection between the curves is marked. These give the two one-sided angular FOVs, calculated by (29), and summed the resulting angular FOV is 110.7° and 85.6° for the ray tracing model and the thin lens model, respectively.

B. The lensed RCAs' usable FOV

The wave-front arcs calculated using the ray tracing model at varying depth, and the resulting usable FOV width are illustrated in Fig. 9. Here, the usable FOV is presented as a width to give a visual indicator of the effect of the lens, compared with the size of the emitting array. For comparison, the figures also show the width of the FOV for the RCA without a lens, and width corresponding to the theoretical FOV predicted by the thin lens model in (18). Notably, (18), gives a FOV where the origo of the emitted circular wave-front arc is at some position (0, 0, F), behind the lens. Therefore, the width of the usable FOV is symmetrical across the z-axis, even when the position of the element position is not at $x = 0$.

The variation in the angular FOV with depth, evaluated for several element indexes are shown in Fig. 10. The angular FOV evaluated along each element is shown in Fig. 10b. Here, the two-sided angular FOV is given, since symmetry gives $\Omega = 2 \cdot \Omega_{+1/2}$ along the y-axis. On the other hand, Fig. 10a, shows the angular FOV orthogonal to the emitting elements, and here Ω is divided into its two one-sided parts. The variation in angular FOV with depth is plotted for a sub-set of elements laying between the the center element (element index = 65) and the edge element (element index = 128). And since the lensed RCA is symmetrical, the $\Omega_{+1/2}$ for element number $65 + n$ is equal to $\Omega_{-1/2}$ for element number $65 - n$. In both subfigures, the theoretical FOV predicted by the thin lens model in (18) is plotted for comparison. In the orthogonal case, in Fig. 10a, this results in the same value for all emitting elements, since the thin lens model theory does not account for variation in the element position in the plane orthogonal to the emitting element. Here, the calculation of Ω made using (18) takes the origo of the opening angle to be the same as when using (29), namely the position of the element, so that the theoretical value can be directly compared with the simulated results.

For the ray tracing model, it is observed that the angular FOV for element number 128 is significantly smaller than for the lower element indexes, both along and orthogonal to the emitting element. In the y-direction, which runs along the element, this is expected, because the extent of the element is longer than the chord of the lens at this x-position. Thus, the sound emitted from the outermost part of the edge element is not refracted by the lens. Furthermore, as seen in Fig. 10a, the angular FOV for element number 128 is also lower than for the rest of the elements in the x-direction, running orthogonal to the element. A possible explanation for this could be that the wave emitted from this element is negatively impacted by the edge of the lens. Fig. 11 shows the simulated pressure wave emitted from element number 128 at time = 8.83 µs, just as the pressure wave passes the edge of the lens. Here, an apparent node in the interference pattern, indicated by an arrow, is observed, just below the corner of the lens curvature. The same node

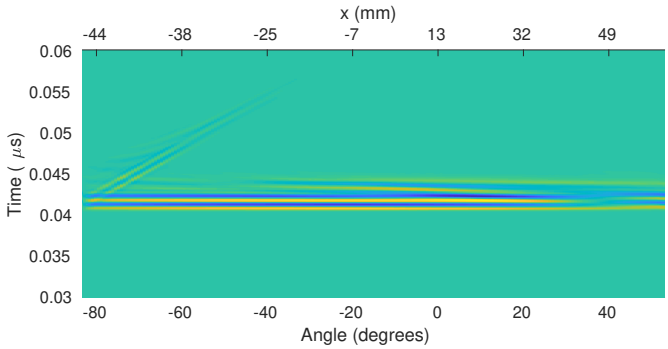

(a) Pressure field along an wave-front arc predicted by the ray tracing model.

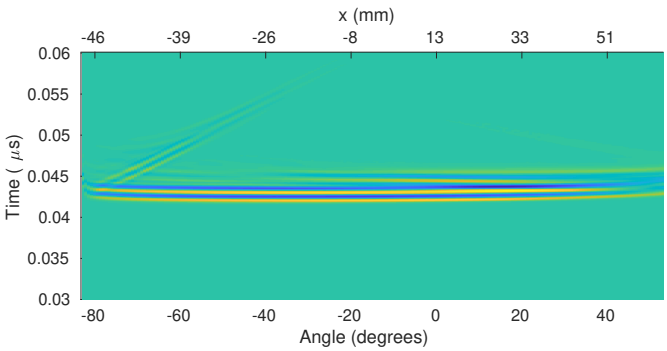

(b) Pressure field along an wave-front arc predicted by the thin lens model.

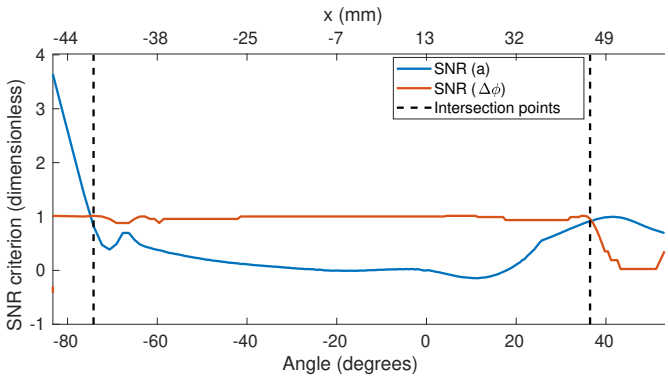

(c) SNR criterion along an wave-front arc by the RT model.

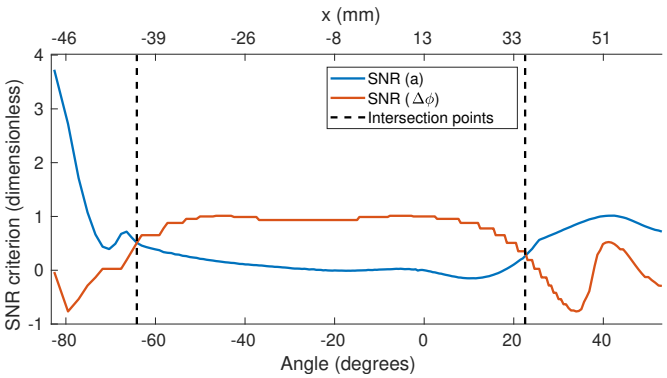

(d) SNR criterion along an wave-front arc by the TL model.

FIG. 8. Examples of the simulated pressure fields for case number 3, along a constant TOF wave-front arc predicted by the ray tracing model (a) and the thin lens model (b). In (c) and (d), the SNR criterion calculated using (26) and (27) from the pressure fields.

can be observed in Fig. 8a, at approximately 36°, where the SNR criterion breaks down. The node is caused by an edge-wave emerging as the propagating wave transverses the sharp edge between the curvature of the lens and its baffle. Since the lens edge is cylindrically symmetric around the z-axis, while the emitting element is off-set from the z-axis, the edge-wave occurs at different times along the edge. Therefore, the edge-wave can also be seen in Fig. 8a and b, at an angle to the main wave-front, between $-80°$ to $-40°$. The interference between the edge-wave and the emitted wave could also explain the rapid increase in $\Omega_{+1/2}$ with depth for element number 119, seen in Fig. 10a.

In Fig. 10b it is observed that both the Ω predicted from the simulated pressure fields and the Ω predicted by (18) show a similar declining trend with depth. To investigate the cause of this decline, the variation in the SNR criterion with position along the constant TOF arc predicted along y for the center element is plotted in Fig. 12 for the four simulated depths.

V. DISCUSSION

As observed in Table III and Fig. 8, generally, higher usable FOV is attained when predicting the position of the wave-front arcs with the ray tracing model than with the thin lens model. This indicates that the ray tracing model is more accurate in predicting the true position of the propagating wave. Moreover, the shape of the SNR($\Delta\phi$) is more curved in Fig. 8d than in Fig. 8c, and this curvature indicates that the prediction of the position of the wave-front arc has introduced some phase error. If the prediction of the wave-front arc position was to be used to beamform images, this phase error would affect the contrast of the beamformed image. The SNR($\Delta\phi$) deviates from 1 even in the range 0° to 20°, before the SNR criterion fails, and this curvature indicates a phase error. Thus, the use of the thin lens model would degrade the contrast of the beamformed image, even if the acceptance angle of the transmitted field was limited to the predicted Ω.

The thin lens model's theoretical value for angular FOV is presented in Fig. 9 and Fig 10. Here, it can be seen that using (18), Ω is underestimated along x and

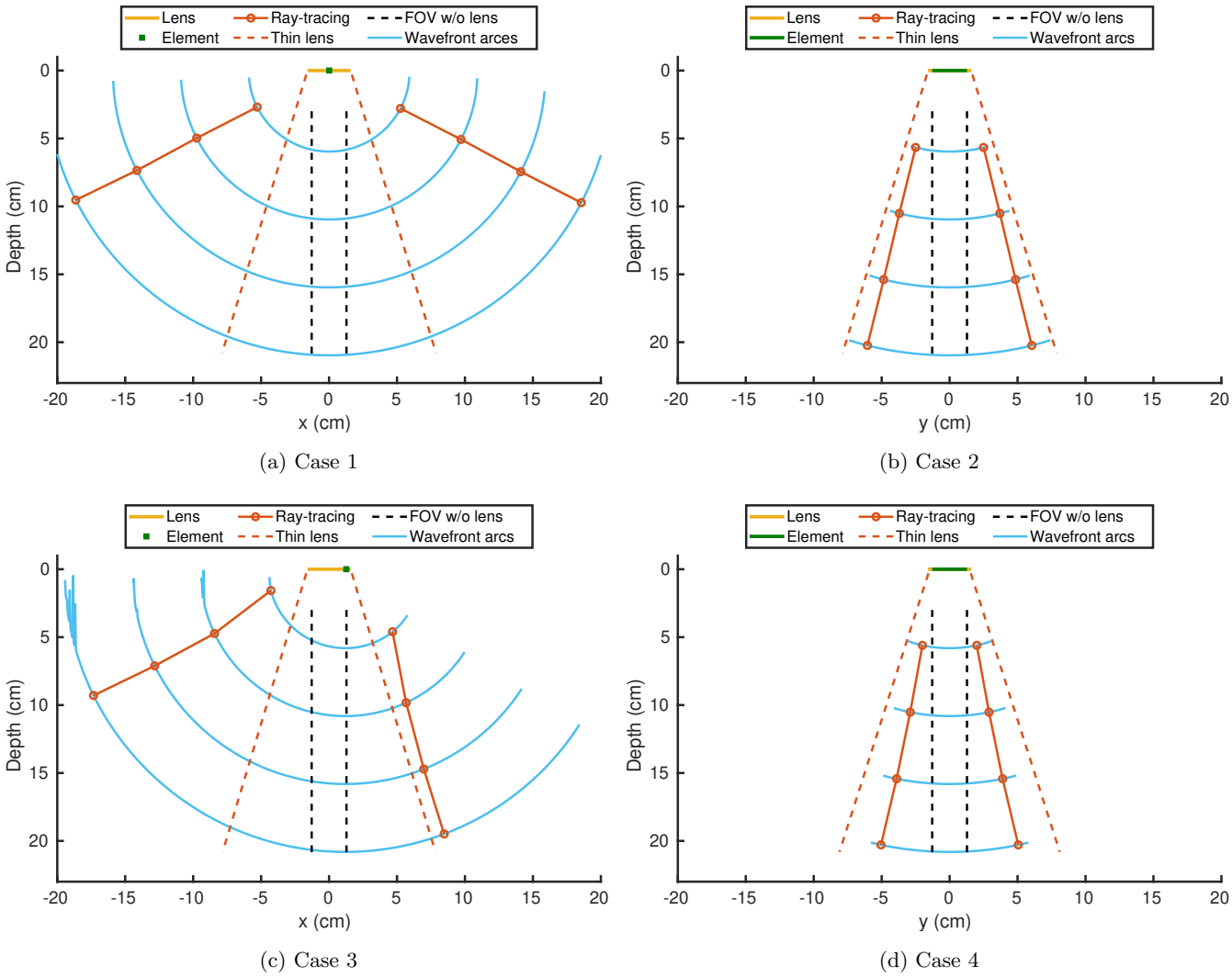

(a) Case 1

(b) Case 2

(c) Case 3

(d) Case 4

FIG. 9. Results on the evaluation of variation of the usable FOV with depth for the four example cases. The wave-front arcs are calculated using the ray tracing model, and the extent of the FOV shown as circled lines are evaluated from FEM simulations of the pressure field. The theoretical FOV according to the thin lens model is also shown.

overestimated along y. In the x-direction, the thin lens model theory severely underestimates the usable FOV, and fails to recognize that the usable FOV varies with element index. This variation occurs because the variation in element position causes the emitted ray to intersect the curve of the lens in the x-z plane at different positions, which in turn determines the angle of incidence, $\theta_{i,x}$, and thus the refraction. This is likely the reason why Ω is underestimated. In the case of Ω calculated along y, the overestimation likely occurs because the theoretical values from the thin lens model does not take into account the attenuation of the emitted wave, both due to attenuation from the lens material, geometric spreading, and absorption in the image medium.

In the x-direction, running orthogonal to the emitting elements, a significant usable FOV has been predicted using the ray tracing model. For the element indexes 65 - 110, which as seen in Fig. 10 seem to be unaffected by the edge wave from the lens corner, the mean of the predicted total Ω, averaged over depth and element index, is $122^\circ \pm 2^\circ$. Firstly, this is indicative of the accuracy of the arc positions, thus supporting that the ray tracing method is suitable for predicting the position of the propagating wave when beamforming images from a lensed RCA. Secondly, the large usable FOV suggests that the lensed RCA can be used to image a volume with a width nearly twice as large as the typical FOV of commercial convex arrays (GE Healthcare, 2021; Phillips, 2021; Siemens Healthineers, 2021).

However, the calculated FOV in the y-direction, along the emitting elements, is smaller than in the x-direction. The usable FOV for the center element is visu-

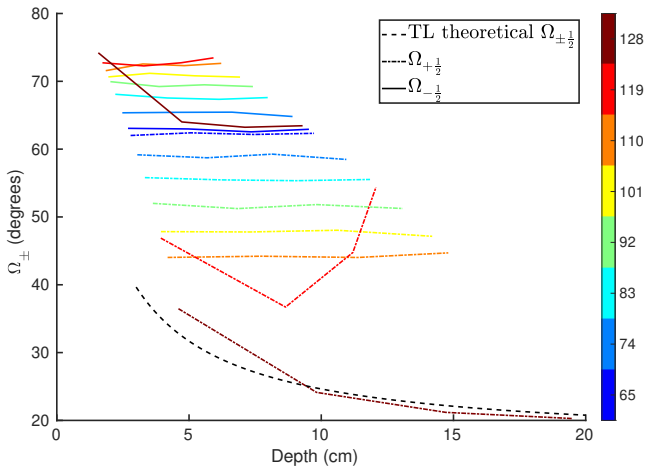

(a) The two one-sided angular FOVs orthogonal (along x) to each emitting element.

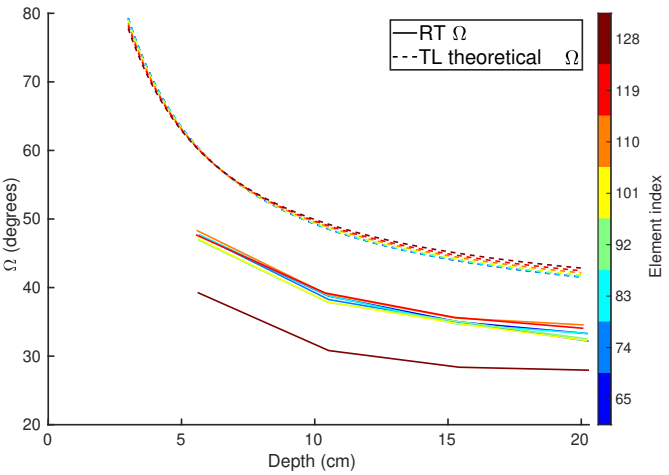

(b) The two-sided angular FOV along (along y) each emitting element.

FIG. 10. The angular FOV predicted orthogonal to (a) and along (b) the emitting elements at varying depth. The angular FOV is predicted using the simulated pressure-fields at arcs predicted by the ray tracing model (RT), and using the theoretical thin lens (TL) value given in (18).

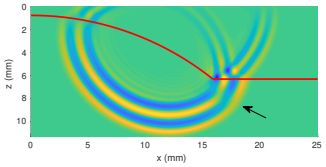

FIG. 11. The position of the pressure wave emitted by element number 128 at time = 8.83 µs. The red line indicates the border between the lens (above) and the water (below). The annotated arrow points to an apparent node in the pressure wave, just below the corner of the lens curvature.

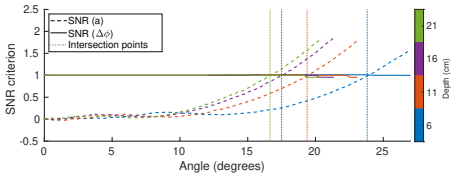

FIG. 12. The variation in SNR($\Delta\phi$) and SNR(a) for the center element at four different depths. The SNR criterion are presented along the positive propagation angles along the y-direction.

alized in Fig. 9a and b, and at a depth of approximately 10 cm, the FOV in the x-direction is 125.3°, while it is 38.8° in the y-direction. As shown in Fig. 9 this difference is prevalent for all of the studied element indexes. The usable FOV varies from 28.5° to 51.2°, which is lower than the typical FOV of commercial convex arrays (GE Healthcare, 2021; Phillips, 2021; Siemens Healthineers, 2021). However, even for element number 128, which has the smallest calculated FOV, the usable FOV is significantly wider than the usable FOV without a lens. At $z = 10.5$ cm, the usable FOV is 7.4 cm, which is 2.9 times wider than without a lens, and, the lensed width increases with depth. When using a lensed RCA for pulse-echo imaging, the usable FOV is limited by the overlap between the usable FOV for the transmitting elements and the receiving elements (Bouzari *et al.*, 2017). Thus, if the usable FOV for the receiving elements is the same as the usable FOV in transmit, the final usable FOV for pulse-echo imaging is limited by the smaller values calculated for the y-direction. However, such reciprocity cannot necessarily be assumed without further study due to the complexity of the refracting lens. In transmit, the emitting angle in the y-direction is assumed to be $\alpha_y = 0$, but when the elements are receiving sound this is not necessarily true. Thus, further study of the receive geometry is needed to conclude on the full usable FOV for a lensed RCA.

In Fig. 10a it is shown that the usable FOV calculated from the simulated pressure fields decreases with depth. Looking at the variation in the two SNR criterion with depth in Fig. 12 reveals that SNR($\Delta\phi$) is relatively constant with propagation angle for all depths, while SNR(a) starts to increase at varying propagation angles, depending on the depth. Thus, it is the amplitude of the pressure wave which makes the SNR criterion fail, rather than phase errors. Therefore, the decline in usable FOV with depth is caused by geometric attenuation of the wave. Simulations by Bouzari *et al.* (2017) and Engholm *et al.* (2018) have suggested that decreas-

ing the lens' radius of curvature will increase the spread of power. Together with the findings in Fig. 12 this indicates that a smaller radius of curvature could be used to increase the FOV in the x-direction.

VI. CONCLUSION

The usable FOV of a 128 + 128 element RCA with a concave diverging lens has been investigated through 3D simulation of the emitted pressure field. A novel method for predicting the position of the emitted wave-front has been presented and its performance has been compared with the thin lens model proposed by Bouzari *et al.* (2017). The comparison has shown that the ray tracing model gives a more accurate prediction of the wave-front position, especially in the dimension laying orthogonal to the emitting element and for emitting elements laying further from the center of the array. This leads to a greater usable FOV. For the edge element the FOV in the x-direction was calculated to be 25.1° greater when using the ray tracing model than the thin lens model. Moreover, this improvement in the accuracy of the prediction of the wave-front will increase the contrast of the images when using the wave-front prediction to make beamformed images from lensed RCAs. Evaluation of the usable FOV for the 128 + 128 element RCA gave an average angular FOV of 122° ± 2° in the direction laying orthogonal to the emitting element, which is approximately twice as large as the typical FOV for commercial convex arrays. If this FOV can be translated to a clinical implementation of pulse-echo imaging, this will greatly improve the applicability of RCA imaging. However, in the direction laying along the emitting element, the usable FOV was found to be more limited, laying between 28.5° to 51.2°. It is not certain if this will restrict the usable FOV for pulse-echo imaging, and further investigation of the ray propagation when receiving the sound is required to establish the FOV for clinical imaging. Nevertheless, even with just 28.5° usable FOV, the lens has significantly increased the volume of the image that the RCA will be capable of making.

ACKNOWLEDGMENTS

This work was financially supported by grant 82-2014-4 from the Danish National Advanced Technology Foundation, by grant 7050-00004B from Innovation Fund Denmark, and by BK Medical, Herlev, Denmark.

The authors would like to acknowledge Kevin Chan, OnScale, for helping setting up the simulations.

Anderson, M. E., McKeag, M. S., and Trahey, G. E. (**2000**). "The impact of sound speed errors on medical ultrasound imaging," J. Acoust. Soc. America **107**(6), 3540–3548.

Bouzari, H., Engholm, M., Beers, C., Nikolov, S. I., Stuart, M. B., Thomsen, E. V., and Jensen, J. A. (**2018**). "Curvilinear 3-D imaging using row–column addressed 2-D arrays with a diverging lens: Phantom study," IEEE Trans. Ultrason., Ferroelec., Freq. Contr. **65**(7), 1182–1192.

Bouzari, H., Engholm, M., Beers, C., Stuart, M. B., Nikolov, S. I., Thomsen, E. V., and Jensen, J. A. (**2017**). "Curvilinear 3-D imaging using row-column-addressed 2-D arrays with a diverging lens: Feasibility study," IEEE Trans. Ultrason., Ferroelec., Freq. Contr. **64**(6), 978–988.

Carpena, P., and Coronado, A. V. (**2006**). "On the focal point of a lens: beyond the paraxial approximation," European Journal of Physics **27**(2), 231–241.

Davidsen, R. E., Jensen, J. A., and Smith, S. W. (**1994**). "Two-dimensional random arrays for real time volumetric imaging," Ultrason. Imaging **16**(3), 143–163.

Démoré, C. E. M., Joyce, A. W., Wall, K., and Lockwood, G. R. (**2009**). "Real-time volume imaging using a crossed electrode array," IEEE Trans. Ultrason., Ferroelec., Freq. Contr. **56**(6), 1252–1261.

Engholm, M., Bouzari, H., Beers, C., Jensen, J. A., and Thomsen, E. V. (**2018**). "Increasing the field-of-view of row-column-addressed ultrasound transducers: implementation of a diverging compound lens," Ultrasonics **88**, 97–105.

Ernst, P. J. (**1947**). "Measurement and specification of ultrasonic lenses," J. Acoust. Soc. America **19**(3), 474–474.

Ferin, G., Dumoux, M. C., Flesch, M., Montauban, E., Lejeune, A., Rosinski, B., Mateo, T., Poree, J., Sauvage, J., Deffieux, T., Pernot, M., Tanter, M., and Nguyen-Dinh, A. (**2018**). "A novel row-column addressed stack architecture for enhanced cardiac imaging," in *Proc. IEEE Ultrason. Symp.*, pp. 1–4.

GE Healthcare (**2021**). "Vscan air data sheet," Technical Report, https://www.gehealthcare.com/-/media/A66296638B1D4D4EA4B9411857A38066.pdf.

Joyce, A. W., and Lockwood, G. R. (**2014**). "Crossed-array transducer for real-time 3D imaging," in *Proc. IEEE Ultrason. Symp.*, pp. 2116–2120.

Margrave, G. F., and Daley, P. F. (**2001**). "Recursive Kirchhoff wavefield extrapolation," CREWES Research Report **13**, 617–646.

Morton, C. E., and Lockwood, G. R. (**2003**). "Theoretical assessment of a crossed electrode 2-D array for 3-D imaging," in *Proc. IEEE Ultrason. Symp.*, pp. 968–971.

Oddershede, N., Hansen, K. L., Nielsen, M. B., and Jensen, J. A. (**2007**). "In-vivo examples of synthetic aperture vector flow imaging," in *Proc. SPIE Med. Imag.*, Vol. 6513, pp. 1–10.

Phillips (**2021**). "C5-2 curved array transducer," Technical Report, https://www.usa.philips.com/healthcare/product/HC989605427371/c5-2-usb.

Rasmussen, M. F., Christiansen, T. L., Thomsen, E. V., and Jensen, J. A. (**2015**). "3-D imaging using row–column-addressed arrays with integrated apodization — Part I: Apodization design and line element beamforming," IEEE Trans. Ultrason., Ferroelec., Freq. Contr. **62**(5), 947–958.

Sampaleanu, A., Zhang, P., Kshirsagar, A., Moussa, W., and Zemp, R. (**2014**). "Top-orthogonal-to-bottom-electrode (TOBE) CMUT arrays for 3-D ultrasound imaging.," IEEE Trans. Ultrason., Ferroelec., Freq. Contr. **61**(2), 266–276.

Seo, C. H., and Yen, J. T. (**2009**). "A 256 x 256 2-D array transducer with row-column addressing for 3-D rectilinear imaging," IEEE Trans. Ultrason., Ferroelec., Freq. Contr. **56**(4), 837–847.

Siemens Healthineers (**2021**). "Transducers ACUSON juniper ultrasound system," Technical Report, https://cdn0.scrvt.com/39b415fb07de4d9656c7b516d8e2d907/bc36bf3cfc798dc7/4a4c338741ff/10042_US_ACUSON_Juniper_1_5_Transducers_-V5_HOOD05162003156124.pdf.

Yen, J. T. (**2013**). "Beamforming of sound from two-dimensional arrays using spatial matched filters," J. Acoust. Soc. America **134**(5), 3697–3704.

Paper 7

Tracking Performance in Ultrasound Super-Resolution Imaging

Iman Taghavi, Sofie B. Andersen, Carlos A. Villagomez Hoyos, Mikkel Schou,
Sigrid Husebø Øygard, Fredrik Gran, Kristoffer L. Hansen, Charlotte M. Sørensen, Michael B. Nielsen,
Matthias Bo Stuart, Jørgen Arendt Jensen

Published in:
Proceedings of the IEEE International Ultrasonic Symposium

Document Version:
Published

DOI:
10.1109/IUS46767.2020.9251605

Tracking Performance in Ultrasound Super-Resolution Imaging

Iman Taghavi[1], Sofie B. Andersen[2,3], Carlos A. Villagomez Hoyos[4], Mikkel Schou[1], Sigrid H. Øygard[1], Fredrik Gran[4], Kristoffer L. Hansen[2], Charlotte M. Sørensen[3], Michael B. Nielsen[2], Matthias B. Stuart[1], Jørgen Arendt Jensen[1]

[1]Department of Health Technology, Technical University of Denmark
[2]Department of Diagnostic Radiology, Rigshospital, Denmark
[3]Department of Biomedical Sciences, University of Copenhagen,
[4]BK Medical, Herlev, Denmark

***Abstract*—Tracking plays an important role in super-resolution (SR) ultrasound imaging, as it improves the quality and sharpness of the final SR images. Moreover, tracking enables quantification of clinically important parameters, such as blood flow velocity. However, the tracking performance degrades in the presence of complex particle patterns and localization uncertainty due to noise and motion. This work presents and discusses multiple approaches for tracking evaluation and compares a nearest-neighbor (NN) with a Kalman tracker through simulations and an in vivo experiment. It is shown that in the presence of a localization uncertainty with a standard deviation (SD) of $\lambda/5$, the bias and SD of the velocity estimates reach -1.04 $\pm$ 0.9 mm/s and -0.12 $\pm$ 0.72 mm/s in the NN and Kalman tracker, respectively (relative to the peak velocity of 10 mm/s). The precision of individual track positions is estimated for an in vivo experiment as 37.95 $\pm$ 21.37 μm and 23.9 $\pm$ 11.82 μm for the NN and Kalman trackers, respectively. The results indicate that the Kalman tracker achieves a better velocity estimation and reduces localization uncertainty.**

I. Introduction

Ultrasound super-resolution imaging (SRI) has been studied by various research groups over the last years [1]–[7]. The approach employs detection and tracking of microbubble (MB) contrast agents to visualize the micro-vasculature including the capillary network. A detector estimates the centroids of the MBs, and several factors including the non-linear imaging scheme, the signal to noise ratio (SNR), complex and nonuniform MB concentrations, and various MB dynamics affect the centroid estimation and tracking of the MB positions. The centroid localization is uncertain, since the above mentioned factors produce non-symmetrical, overlapped, dissimilar, and shifted target spread functions for the various MBs during the scan. These conditions are even worse for in vivo measurements, as several other ultrasound artifacts, organ motion, and uncontrolled MB concentrations depending on the 3D vessel structure, affect the images.

The tracking methods aim to link the detected MBs from frame to frame. The methods range from simple nearest-neighbor (NN) [8] to multi-frame data structure and using explicit motion models (*e.g.* Kalman filtering) [6], [9]–[11].

This work investigates several performance metrics for tracking evaluation. A NN and a Kalman tracker are compared through both simulations with known ground-truth and in an in vivo experiment with unknown ground-truth. Finally, a new tracking strategy that will likely address tracking difficulties in a wide range of scenarios is suggested.

II. Methods

A. Simulation

The simulations were made by generating MB positions, each with uniformly random lifetime and known ground-truth, moving with different velocities across an X-shaped phantom. A random localization error was added to each MB position. The various parameters of the phantom are listed in Table I. The ground-truth tracks with different MB density and trajectories of MBs with localization uncertainty are shown in Fig. 1. These simulations provided a wide range of scenarios, including various MB concentrations, velocities, and localization uncertainties.

TABLE I: Parameters used in the in-silicon X-phantom

Parameters	**Value**
Tube length	10 mm
Tube radius	250 μm & 125 μm
Peak velocity	10 mm/s & 5 mm/s
Velocity profile	Parabolic
Angle between tubes	60°
Point Spread Function (PSF)	Unsymmetrical Gaussian
Axial / Lateral FWHM	0.7λ / 1.5λ
Number of MBs per frame (mean $\pm$ standard deviation (SD))	Very low: 2 $\pm$ 2 Low: 8 $\pm$ 4 Medium: 28 $\pm$ 13 High: 49 $\pm$ 20
Uncertainty in localization (SD of localization error)	Very low: $\lambda/20$ Low: $\lambda/10$ Medium: $\lambda/5$ High: $\lambda/2$

B. In vivo measurement

The in vivo measurement was conducted using a modified BK5000 scanner, and an X18L5s transducer (BK Medical,

978-1-7281-5448-0/20/$31.00 ©2020 IEEE

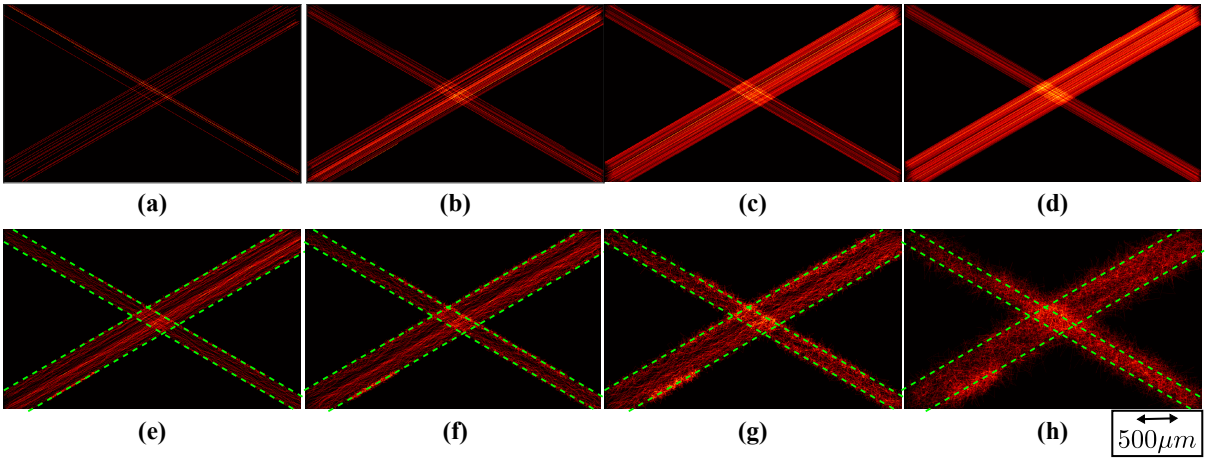

Fig. 1: Ground-truth tracks of various MB density scenarios for a (a) very low (b) low (c) medium or (d) high concentration. The tracks of uncertain MB positions with standard deviation of (e) $\lambda/20$ (f) $\lambda/10$ (g) $\lambda/5$ and (h) $\lambda/2$ for a low-density scenario are shown in the bottom row. The green dash lines show the wall of the tubes.

Herlev, Denmark) was used to record 10 minutes of contrast-enhanced and B-mode frames from a rat kidney with a frame rate of 53.85 Hz. A pulse amplitude modulation sequence was used for imaging with a transmit frequency of 6 MHz (λ = 256 μm). The transmit voltage was low with a corresponding mechanical index (MI) of 0.2 to prevent bursting of the MBs. The MBs (SonoVue, Bracco, Milan, Italy) were injected with a flow-rate of 100 μl/min after a 1:10 dilution.

C. Tracking algorithms

In the NN tracker, the estimated MB positions in the next frame are linked to the MB positions in the current frame based on their minimum distance. Though NN is simple and fast, simple linking of MB positions generates false and flexuous tracks when the localization is uncertain. Considering the MB's smooth movement, more robust tracking is possible via Kalman filtering. This simple movement consideration can be modeled as $\vec{r}(t) = \vec{r}(t-1) + d\vec{r}(t) + \vec{\varepsilon}(t)$, where $\vec{r}(t) = (r_z(t), r_x(t))$ is the position of MB at time t, $d\vec{r}(t) = (dr_z(t), dr_x(t))$ is the displacement of the MB and $\varepsilon(t)$ is the uncertainty in the displacement. This model can be formulated within the Kalman framework as:

$$\begin{cases} \bar{x}(t) = \mathbf{F}x(t-1) + \varepsilon(t) \\ \bar{z}(t) = \mathbf{H}\bar{x}(t) + \nu(t), \end{cases} \tag{1}$$

where $x(t) = [\vec{r}(t), d\vec{r}(t)]^T = [r_z(t), r_x(t), dr_z(t), dr_x(t)]^T$, $\bar{x}(t)$ is the prediction of MB position in the next frame, $\bar{z}(t)$ is the estimated uncertain position,

$$\mathbf{F} = \begin{bmatrix} 1 & 0 & 1 & 0 \\ 0 & 1 & 0 & 1 \\ 0 & 0 & 1 & 0 \\ 0 & 0 & 0 & 1 \end{bmatrix}, \quad \mathbf{H} = \begin{bmatrix} 1 & 0 & 0 & 0 \\ 0 & 1 & 0 & 0 \end{bmatrix},$$

$\varepsilon(t) \sim \mathcal{N}(0, \sigma_\varepsilon^2)$, and $\nu(t) \sim \mathcal{N}(0, \sigma_\nu^2)$.

In this study, the maximum linking distance was 500 μm, and the initial conditions of the Kalman filter were σ_ε = 1 mm and σ_ν = 100 μm. After tracking, the velocity of the MBs was estimated by calculating the time derivative of track positions.

D. Evaluation

The first group of performance metrics, proposed in [12], was based on an assignment problem. To evaluate tracking performance using this approach, estimated tracks were paired with ground-truth tracks based on their minimum distance using Hungarian algorithm [13]. Hungarian algorithm provides fast optimal assignment of the two sets. The gate size is equal to λ, meaning that any tracks outside this gate range were considered as false positive (FP), tracks within the gate range were assumed as true positive (TP) or false negative (FN), if they are paired or unpaired to the ground-truth. The Jaccard Similarity Coefficient (JSC) is defined as JSC = TP/(TP+FP+FN), which determines the similarity of the set of estimated tracks and set of ground-truth tracks. The root-mean-square error (RMSE) of velocity estimates was calculated for each paired track (TP), and the number of unpaired (spurious) tracks was also counted as an extra performance metric. For the paired tracks, JSC of track positions and RMSE of the estimated positions can also be calculated to provide metrics at the position level.

The second performance metric was calculated by considering the known velocity profile of flow in the tubes as a ground-truth. In this approach bias and standard deviation of velocity profiles over different cross sections of the tubes were calculated.

The localization uncertainty in the in vivo data, used as the last performance metric, was estimated by RMSE of a fitted piece-wise least-square line to the MB positions.

III. Results

The super-resolution (SR) images shown in Fig. 2 indicate that the Kalman filter has more smooth tracks in this scenario. All of the assignment-based performance metrics for various density and uncertainty scenarios at the track and position levels are listed in Table II and Table III (the green labels show a better performance). At the position level, the Kalman filter outperformed the NN almost in all scenarios. Notice that the RMSE of the track positions are relevant to the localization

TABLE II: Performance Metrics at Track Level (Color scheme: green → higher performance, yellow → roughly the same).

MB Density	Tracker	Unertainty in Localization											
		SD = $\lambda/20$ = 12.83 μm			SD = $\lambda/10$ = 25.67 μm			SD = $\lambda/5$ = 51.33 μm			SD = $\lambda/2$ = 128.34 μm		
		JSC	Spurious	RMSE	JSC	Spurious	RMSE	JSC	Spurious	RMSE	JSC	Spurious	RMSE
Very low	NN	0.731	14	0.01	0.731	14	0.01	0.731	14	0.05	0.132	250	0.33
	Kalman	1	0	0	1	0	0	1	0	0.03	0.528	34	0.01
Low	NN	0.961	13	3.19	0.953	16	0.01	0.835	64	3.22	0.148	1868	0.34
	Kalman	0.934	23	0.03	0.923	27	0	0.91	32	0.01	0.416	454	0.03
Medium	NN	0.892	104	0	0.839	165	0.02	0.642	478	0.9	0.104	7437	0.17
	Kalman	0.534	435	0.01	0.632	500	0.02	0.595	585	0.04	0.236	2194	0.19
High	NN	0.717	672	0.06	0.634	983	1.02	0.435	2209	0.3	0.095	16226	1.1
	Kalman	0.446	2079	0.04	0.418	2376	0.04	0.388	2681	0.01	0.215	6209	0.9

TABLE III: Performance Metrics at Position Level (Color scheme: green → higher performance, yellow → roughly the same).

MB Density	Tracker	Unertainty in Localization							
		SD = $\lambda/20$		SD = $\lambda/10$		SD = $\lambda/5$		SD = $\lambda/2$	
		JSC	RMSE	JSC	RMSE	JSC	RMSE	JSC	RMSE
Very low	NN	0.639	15.02	0.639	29.49	0.576	52.27	0.127	135.23
	Kalman	1	11.99	1	20.34	0.937	37.63	0.584	88.92
Low	NN	0.754	14.3	0.672	25.12	0.557	38.86	0.154	115.25
	Kalman	0.92	13.96	0.836	22.18	0.788	36.61	0.463	76.55
Medium	NN	0.511	15.54	0.432	15.58	0.354	29.21	0.094	112.72
	Kalman	0.534	13.21	0.493	19.95	0.421	31.83	0.236	77.48
High	NN	0.446	16.52	0.36	22.62	0.266	40.09	0.078	111.92
	Kalman	0.432	15.98	0.38	22.92	0.319	38.99	0.189	79.75

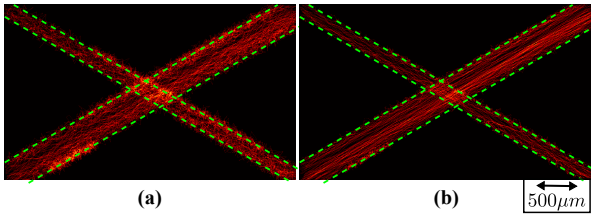

Fig. 2: A comparison between (a) NN tracker, and (b) Kalman tracker for low-density scenario and uncertainty of $\lambda/5$ in the localization.

uncertainty. This will be used later to estimate the uncertainty of localization from the in vivo measurements. At track level, NN achieved a better rank in JSC, and the number of spurious tracks was lower in several scenarios. However, the velocity estimates of paired tracks were more accurate when a Kalman filter was employed. This diverse behavior of trackers through different scenarios is discussed in Section IV. It can be seen that in some scenarios the Kalman filter can reduce the number of spurious tracks by more than 67%.

To avoid the ambiguities in an assignment problem, the estimated velocity profiles over 14 cross-sections of the larger vessel in the final SR image are illustrated in Fig. 3. The velocity estimates and the resolution were improved by the Kalman filter. This shows the superiority of the Kalman over NN in a scenario with high MB concentration and uncertainty in the localization.

While there is no ground-truth for the in vivo measurement, less flexuous tracks are expected for more accurate localization or robust trackers. To measure the precision of the tracks positions, a piece-wise least-square line was fitted to MB positions tracked for more than 5 frames. Table IV lists the mean and SD of the localization error relative to the fitted line after NN and Kalman tracking. It shows that the Kalman filter has reduced the localization uncertainty. Fig. 4 shows SR images produced by the two trackers for 90 seconds of the in vivo data. It is clear that the Kalman tracker outperforms the NN tracker.

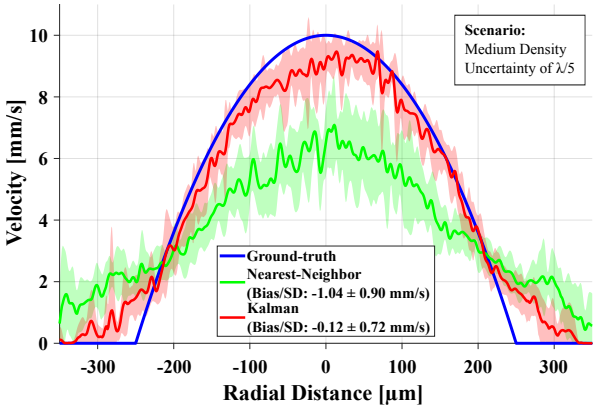

Fig. 3: Velocity estimation statistics over 14 cross-sections of the large vessel for medium density scenario with localization uncertainty of $\lambda/5$. The NN estimates had a bias and standard deviation of -1.04 $\pm$ 0.9 mm/s, while these values for the Kalman estimates were reduced to -0.12 $\pm$ 0.72 mm/s.

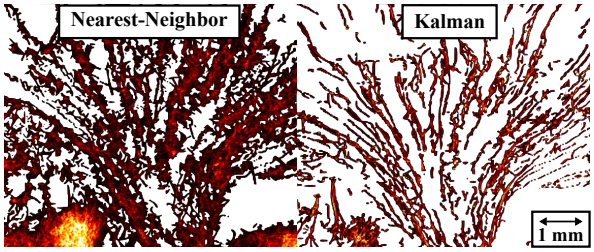

Fig. 4: Super-resolution images of renal inner medulla created using the NN (left) and Kalman (right) trackers. The NN generated a lot of spurious and flexous tracks. However, the Kalman tracker reduced these uncertainties. The structure is clearly distinguishable in the right image, as it is resolved down to 25.6 μm for almost every position.

Finally, velocity SR images of the entire kidney, shown in Fig. 5, demonstrate the difference between two trackers in terms of less spurious and less uncertain tracks.

TABLE IV: Tracking performance on localization uncertainty

Tracker	Precision of individual track positions
NN	37.95 $\pm$ 21.37 μm
Kalman	23.9 $\pm$ 11.82 μm

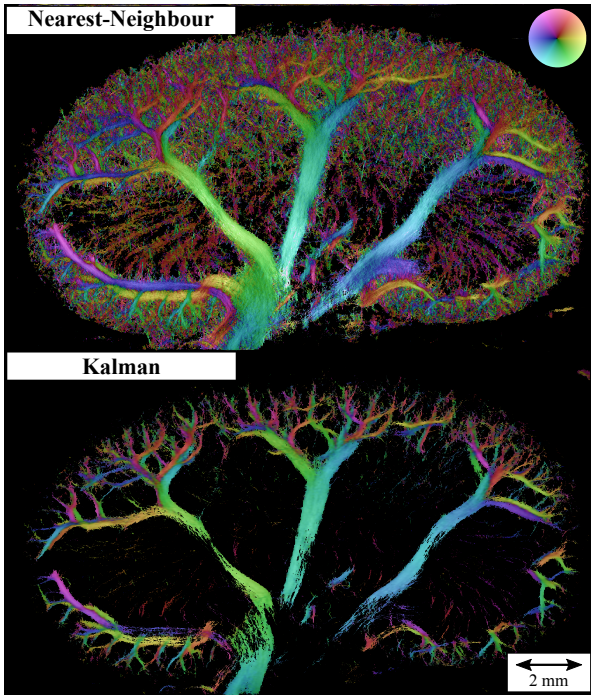

Fig. 5: Velocity SR images of the kidney show renal vascular tree with opposite flows (arteries and veins). The color wheel on top-right corner shows the flow direction of the color-coded tracks.

IV. Discussion

Considering only the JSC and the number of spurious tracks, NN performed better than Kalman in some scenarios. Two key factors explain this behavior of the Kalman tracker. Firstly, based on the definition of optimal assignment, a unique estimated track must be assigned to a ground-truth track. A tracker might estimate a long track with multiple small tracks. In this case, while tracks are correct, the number of spurious tracks will increase, and JSC will decrease. Therefore, these two metrics cannot determine the overall performance of the tracker in all scenarios. Secondly, a single Kalman filter with specific initial conditions is employed for tracking in all scenarios. A Kalman filter might not reach a fair estimate within a short lifetime of these MBs. The question that may arise here is why we do not optimize the tracker for each specific scenario? The reason is that in an in vivo measurement, the tracker has to deal with a wide range of scenarios, as the MBs have uncontrolled concentrations as well as different velocities and flow dynamics when entering the blood stream. All of these scenarios are usually difficult to track with a simple tracking strategy. One solution would be tracking with a hierarchical structure. For example, a Kalman filter with a strict initial condition can apply to track slow flows. Then, the untracked MBs and the track positions with an overestimated velocity can be passed to another Kalman filter optimized to track faster MBs. This can be continued in a hierarchical structure to cover all range of scenarios [14].

V. Conclusion

Several performance metrics for the tracking algorithms in SRI were investigated. It was shown that in the presence of a high localization uncertainty, the Kalman tracker reached a better velocity estimate bias and SD of -0.12 $\pm$ 0.72 mm/s compared to -1.04 $\pm$ 0.9 mm/s in the NN relative to a peak velocity of 10 mm/s. The Kalman tracker reduced the precision of individual track positions in an in vivo experiment to 37.95 $\pm$ 21.37 μm and 23.9 $\pm$ 11.82 μm for the NN and Kalman trackers. Overall, the Kalman tracker was superior, as it estimated velocity with a higher precision and reduced localization uncertainty.

Acknowledgment

This work was financially supported by grant 82-2014-4 from the Danish National Advanced Technology Foundation, by grant 7050-00004B from Innovation Fund Denmark, and from BK Medical, Herlev, Denmark.

References

[1] O. M. Viessmann, R. J. Eckersley, K. Christensen-Jeffries, M. X. Tang, and C. Dunsby, "Acoustic super-resolution with ultrasound and microbubbles," *Phys. Med. Biol.*, vol. 58, pp. 6447–6458, 2013.

[2] M. A. O'Reilly and K. Hynynen, "A super-resolution ultrasound method for brain vascular mapping," *Med. Phys.*, vol. 40, no. 11, pp. 110 701–7, 2013.

[3] Y. Desailly, J. Pierre, O. Couture, and M. Tanter, "Resolution limits of ultrafast ultrasound localization microscopy," *Phys. Med. Biol.*, vol. 60, no. 22, pp. 8723–8740, 2015.

[4] K. Christensen-Jeffries, R. J. Browning, M. Tang, C. Dunsby, and R. J. Eckersley, "In vivo acoustic super-resolution and super-resolved velocity mapping using microbubbles," *IEEE Trans. Med. Imag.*, vol. 34, no. 2, pp. 433–440, February 2015.

[5] C. Errico, J. Pierre, S. Pezet, Y. Desailly, Z. Lenkei, O. Couture, and M. Tanter, "Ultrafast ultrasound localization microscopy for deep super-resolution vascular imaging," *Nature*, vol. 527, pp. 499–502, November 2015.

[6] D. Ackermann and G. Schmitz, "Detection and tracking of multiple microbubbles in ultrasound B-mode images," *IEEE Trans. Ultrason., Ferroelec., Freq. Contr.*, vol. 63, no. 1, pp. 72–82, January 2016.

[7] K. Christensen-Jeffries, O. Couture, P. A. Dayton, Y. C. Eldar, K. Hynynen, F. Kiessling, M. O'Reilly, G. F. Pinton, G. Schmitz, M. Tang *et al.*, "Super-resolution ultrasound imaging," *Ultrasound Med. Biol.*, vol. 46, no. 4, pp. 865–891, 2020.

[8] J. C. Crocker and D. G. Grier, "Methods of digital video microscopy for colloidal studies," *J. Colloid*, vol. 179, no. 1, pp. 298–310, 1996.

[9] O. Solomon, R. J. G. van Sloun, H. Wijkstra, M. Mischi, and Y. C. Eldar, "Exploiting flow dynamics for super-resolution in contrast-enhanced ultrasound," *IEEE Trans. Ultrason., Ferroelec., Freq. Contr.*, vol. 60, no. 10, pp. 1573–1586, 2019.

[10] S. Tang, P. Song, J. D. Trzasko, M. Lowerison, C. Huang, P. Gong, U. Lok, A. Manduca, and S. Chen, "Kalman filter–based microbubble tracking for robust super-resolution ultrasound microvessel imaging," *IEEE Trans. Ultrason., Ferroelec., Freq. Contr.*, vol. PP, no. 99, pp. 1–1, 2020.

[11] W. J. Godinez, M. Lampe, S. Worz, B. Muller, R. Eils, and K. Rohr, "Deterministic and probabilistic approaches for tracking virus particles in time-lapse fluorescence microscopy image sequences," *Med. Image Anal.*, vol. 13, no. 2, pp. 325–342, 2009.

[12] N. Chenouard, I. Smal, F. D. Chaumont, M. Maška, I. F. Sbalzarini, Y. Gong, J. Cardinale, C. Carthel, S. Coraluppi, M. Winter *et al.*, "Objective comparison of particle tracking methods," *Nature methods*, vol. 11, no. 3, pp. 281–290, 2014.

[13] H. W. Kuhn, "The Hungarian method for the assignment problem," *Naval research logistics quarterly*, vol. 2, no. 1-2, pp. 83–97, 1955.

[14] I. Taghavi et al., "In vivo ultrasound super-resolution imaging with motion correction and robust tracking," *IEEE Trans. Med. Imag.*, p. submitted, 2020.